

Master thesis

Ferromagnetic resonance study of epitaxial Fe/Rh layers

Name: Jonas Wiemeler

Major: Physics M. Sc.

Date of submission: 25.07.2022

Supervisor: Prof. Dr. Michael Farle

Contents

1. Motivation	1
2. Theoretical Background	3
2.1. Magnetisation dynamics and ferromagnetic resonance	3
2.1.1. Equation of motion	3
2.1.2. Helmholtz free energy density	6
2.1.3. Ferromagnetic resonance	12
2.2. Spin pumping in ferromagnetic resonance	25
3. Experimental Methods	31
3.1. UHV Chamber	31
3.1.1. Molecular Beam Epitaxy (MBE)	31
3.1.2. Low energy electron diffraction - LEED	33
3.1.3. Auger electron spectroscopy - AES	34
3.1.4. Epitaxial growth	36
3.2. Sample preparation	39
3.3. FMR	40
3.3.1. In-situ FMR / Microwave short	40
3.3.2. Cavity FMR	41
3.3.3. Coplanar waveguide (CPW) FMR	42
3.3.4. FMR Experiments	44
4. Analysis	46
4.1. Rh growth on Fe	46
4.1.1. AES growth dependence	47
4.1.2. LEED	55
4.2. Ferromagnetic resonance analysis	60
4.2.1. Determination of the g-factor and anisotropies	61
4.2.2. Special observations	76
4.2.3. Magnetisation damping and spin pumping	77
5. Conclusions and outlook	88
A. Appendix	91
A.1. Additional Information	91
A.2. VNA-test-sample	91
A.3. Restoration of the evaporation system	93
A.4. Software used	94
A.4.1. FMR-Fit	94
A.4.2. Chamber Software	95

Zusammenfassung

Diese Masterarbeit befasst sich mit der magnetischen Charakterisierung und dem Wachstum von Fe/Rh-Doppelschichten, die auf GaAs(100)-(4x6) als Substrat mittels E-Beam-Verdampfung aufgewachsen sind und mittels ferromagnetischer Resonanz (FMR) gemessen wurden. Im Rahmen dieser Arbeit wurde ein E-Beam-Verdampfer umgebaut und repariert, um die Verdampfung von Eisen und Rhodium zu ermöglichen. Die thermodynamische Wachstumsmodi von Rhodium auf Eisen wurde mittels Auger-Elektronenspektroskopie für Rhodiumdicken unter 1 nm untersucht. Es wurde festgestellt, dass das Wachstum am besten mit dem Modell von Stranski-Krastanov beschrieben werden kann. Die Analyse der Niederenergie-Elektronenbeugung (LEED) unterstützt das epitaktische Wachstum von Rh auf Fe. Es wird angenommen, dass Rhodium für eine Dicke von 1 nm in fcc-Struktur und 45° versetzt zum Eisengitter wächst, was eine Gitterfehlانpassung von etwa $\approx 6\%$ bewirkt.

Die magnetische Charakterisierung umfasst die Bestimmung der magnetischen Anisotropiefelder in der Probenebene, des spektroskopischen g-Faktors und der magnetischen Dämpfung. Hierfür wurden sowohl Multifrequenz-Coplanar-Waveguide (CPW) als auch FMR auf Hohlraumbasis verwendet, wobei mit dem CPW-Aufbau Frequenzen von 1-40 GHz und mit dem Hohlraum-Aufbau X-Band-Frequenzen (≈ 9.5 GHz) abgedeckt wurden.

Es wurde festgestellt, dass die magnetische Anisotropie von Rh(x nm)/Fe(5 nm)/GaAs(100)-(4x6) Doppelschichten schwach von der Dicke x der Rh-Schicht abhängig ist. Die effektive Magnetisierung eines 5 nm großen Fe-Films, der mit Rh bedeckt ist, wurde über einen weiten Bereich der Rhodiumdicke (3 nm - 15 nm) mit $\mu_0 M_{eff} = 1.9 \pm 0.11$ T als konstant bestimmt, während sie für geringere Dicken bis auf 1.83 ± 0.08 T abnimmt. Die uniaxiale Anisotropie in der Ebene $\mu_0 H_{K_{2||}}$ nimmt nicht-monoton von 27 ± 2 mT auf 20 ± 4 mT ab, wenn die Rh-Dicke von 1 bis 15 nm zunimmt, was auf einen möglichen strukturellen Übergang der Rh-Schicht bei etwa 3 nm Dicke hinweist. Das kubische Anisotropiefeld in der Ebene $\mu_0 H_{K_{4||}}$ nimmt mit zunehmender Rh-Dicke linear von 37 mT auf 32 mT ab, mit einer Gesamtänderung von $\Delta\mu_0 H_{K_{4||}} = 12\%$.

Die Magnetisierungsdämpfungskonstante zeigt ein exponentielles Verhalten, das mit der Rhodiumdicke zunimmt, was im Rahmen des Modells des Spinpumpens analysiert wird. Die Rh-Spin-Diffusionslänge von $\lambda_{sd} = 2.68 \pm 1.46$ nm und eine Spin-Mischungsleitfähigkeit von $g^{\uparrow\downarrow} = (2.96 \pm 0.3) \cdot 10^{19} m^{-2}$ wurden gefunden. Da keine frühere Studie zum Spin-Pumping in Rh veröffentlicht wurde, werden diese Werte mit anderen Spin-Sink-Metallen wie Pd (das nächste Element nach Rh im Periodensystem) und Pt verglichen. Rh zeigt eine ähnliche Spin-Diffusionslänge wie Pt. Die Spin-Mischungsleitfähigkeit an der Fe/Rh-Grenzfläche liegt nahe an den berichteten Werten für Fe/Pt-Doppelschichten, ist aber höher als bei Pd, was auf die höhere elektrische Leitfähigkeit von Rh und die Grenzflächenlegierung mit Fe zurückzuführen sein könnte, die die Spinstreuung verringert. Aufgrund der hohen Spin-Mischungsleitfähigkeit ist die Gilbert-Dämpfung im Vergleich zu ungedecktem Fe, das mit In-situ-FMR gemessen wurde, um den Faktor 4.5 erhöht.

Summary

This master thesis deals with the magnetic characterisation and growth of Fe/Rh bilayers grown on GaAs(100)-(4x6) as a substrate via E-beam evaporation and measured using ferromagnetic resonance (FMR). During this thesis, a e-beam evaporator has been rebuild and fixed, to enable the evaporation of both iron and rhodium. The thermodynamic growth mode of rhodium on iron was investigated using Auger electron spectroscopy for rhodium thicknesses below 1 nm. The growth was found to be the best described with the model of Stranski-Krastanov. Low energy electron diffraction (LEED) analysis supports the epitaxial growth of Rh on Fe. It is assumed, that rhodium for a thickness of 1 nm grows in fcc structure and 45° offsetted to the iron lattice, inducing a lattice mismatch of about $\approx 6\%$.

The magnetic characterisation includes the determination of in-plane magnetic anisotropy fields, spectroscopic g-factor and magnetic damping. For this both multifrequency coplanar waveguide (CPW) and cavity based FMR were used, covering frequencies of 1-40 GHz for the CPW setup and X-Band frequency (≈ 9.5 GHz) using the cavity setup.

The magnetic anisotropy of Rh(x nm) /Fe(5 nm)/GaAs(100)-(4x6) bilayers was found to be weakly-dependent on the thickness x of Rh layer. The effective magnetisation of 5 nm Fe film covered with Rh was determined as constant over a wide range of rhodium thickness (3 nm - 15 nm) at $\mu_0 M_{eff} = 1.9 \pm 0.11$ T, while decreasing till 1.83 ± 0.08 T for lower thicknesses. The in-plane uniaxial anisotropy $\mu_0 H_{K_{2||}}$ non-monotonously decreases from 27 ± 2 mT to 20 ± 4 mT when Rh thickness increases from 1 to 15 nm, pointing to possible structural transition of Rh layer occurring at around 3 nm thickness. The cubic in-plane anisotropy field $\mu_0 H_{K_{4||}}$ is found to linearly decrease with increasing Rh thickness from 37 mT to 32 mT with, with a total change of $\Delta \mu_0 H_{K_{4||}} = 12\%$.

Magnetisation damping constant shows an exponential behaviour increasing with the rhodium thickness, which is analysed within the model of spin pumping. The Rh spin diffusion length of $\lambda_{sd} = 2.68 \pm 1.46$ nm and a spin mixing conductance of $g^{\uparrow\downarrow} = (2.96 \pm 0.3) \cdot 10^{19} m^{-2}$ is found. As no earlier study of spin pumping to Rh has been published before, these values are compared to other spin sink metals like Pd (next element to Rh in periodic table) and Pt. Rh shows spin diffusion length similar to that of Pt. Spin mixing conductance on Fe/Rh interface is close to reported values for Fe/Pt bilayers, it is higher than for Pd which might be due higher electrical conductivity of Rh and interface alloying with Fe which reduces the spin scattering. Due to the high spin mixing conductance, the Gilbert damping is increased by a factor of 4.5 compared to uncapped Fe measured using in-situ FMR.

1. Motivation

The alloy FeRh of various Fe compositions has been studied extensively for structural, electrical and magnetic properties. It undergoes a first order magnetic phase transition from antiferromagnetism to ferromagnetism, which can be driven by external magnetic fields, while the transition temperature can be modified by Fe concentration [1] or Ne⁺-Ion induced disorder [2]. This first order phase transition exerts a very large entropy change, which makes a bulk FeRh system suitable for magnetocaloric applications. Because of high prices and limited worldwide supply of Rh, a bulk application would be economically inefficient. Therefore investigation focuses on FeRh thin films, like in the case of HAMR technology [3] to increase the memory density of hard drives. Furthermore the spintronics applicability was investigated for FeRh/Pt thin films. A very low damping of the FM state of about $\alpha = 0.0023$ was found, which offers the usage in spin-orbitronic devices for efficient charge to spin transfer. Furthermore, the damping is greatly enhanced by transitioning into the AFM state, as FM domains in an AFM matrix are subject to very efficient spin pumping [4].

In the case of an equiatomic FeRh thin film, the (111) interface represents Fe and Rh multilayers of monolayer thicknesses [5]. Fe/Rh thin film bilayer systems whose Fe and Rh layer thicknesses are greater, than the monolayer limit were not studied in detail yet. In this work, 5 nm Fe films capped with Rh of thicknesses (1, 2, 3, 5, 10, 15) nm were grown on GaAs(100) substrates using molecular beam epitaxy (MBE) to be studied by ferromagnetic resonance at room temperature.

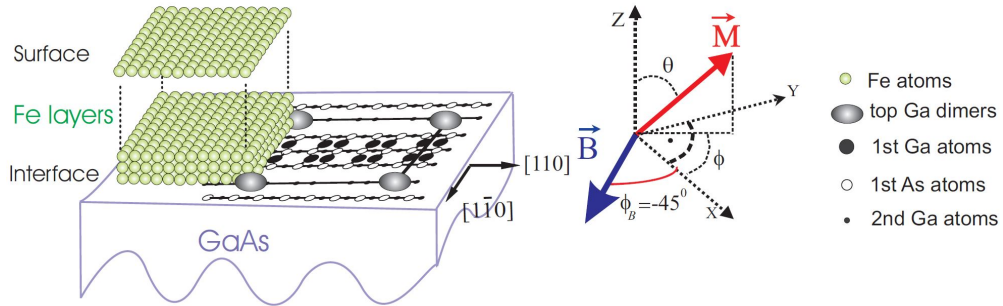


Fig. 1.1.: Schematic representation of Fe growing on GaAs(100)-p(4x6). The picture was taken from [6].

The ferromagnetic substrate layer of GaAs(100)/Fe has been studied in great detail in the past decades. Considering a lattice mismatch of $\approx 1.4\%$, iron is found to grow epitaxially on GaAs(100) in 3D crystallites for the first 5 monolayers (ML), followed by deviated layer-by-layer growth [6, 7]. The magnetic properties¹ of Fe are found to be bulk-like for thicknesses around 5 nm and above, combining a cubic in-plane anisotropy field of around $\mu_0 H_{K4\parallel} = 40$ mT, with saturation magnetisation of about $\mu_0 M_s = 2$ T, a bulk g-factor of $g_{bulk} = 2.09$ and a bulk Gilbert damping of around $\alpha \approx 1.8 \cdot 10^{-3}$. Additionally due to the special structuring of Ga and As, building uniaxial trenches as can be seen in figure 1.1, the overlaying Fe layer experiences a small dislocation along

¹All values with references can be found in the analysis part of this thesis.

one axis. This dislocation effect at the GaAs/Fe interface induces an additional in-plane uniaxial anisotropy, perpendicular in-plane to the axis of the trenches. This anisotropy is highly dependent on the surface quality and Fe thickness and will vanish for sufficiently thick Fe layers. Additionally rhodium nanoclusters, were the first nonmagnetic 4d or 5d metal clusters to show spontaneous ordering [8]. Ferromagnetism in ultra-thin Rh layers grown on Fe was observed using spin polarised photoelectron spectroscopy with magnetic moments of around $1\mu_B$ [9, 10].

Based on this well known system, further investigation of magnetic anisotropy, spin dynamics and spin pumping in Fe capped with Rh thin film layers is performed within this thesis and compared with uncapped and capped Fe/GaAs films.

2. Theoretical Background

2.1. Magnetisation dynamics and ferromagnetic resonance

2.1.1. Equation of motion

Ferromagnetic resonance (FMR) is the phenomenon of a resonance precession of magnetic moments around the effective field axis of a ferromagnet and corresponding absorption of microwave energy. A phenomenological description of FMR can be obtained within a macrospin model: all magnetic moments \vec{m} of a body are normalised across the volume of the body and summed to the macroscopic magnetisation \vec{M} , which represents the magnetic moment of a macroscopic body [11]:

$$\vec{M} = \frac{\sum_{\delta V} \vec{m}}{\delta V}$$

This assumption is valid for of a single domain sample, which is homogeneously magnetised. In this work, thin film samples of a ferromagnetic Fe layer of 5 nm are investigated. For ferromagnets, the electronic wave function overlap of neighbouring electron orbitals creates a strong exchange coupling. This direct exchange coupling creates the situation of minimal potential energy for the case of parallel standing moments, its magnitude for ferromagnets is measured as an exchange constant $J_A > 0$ [11]. The exchange constant of Fe $J_A \approx 2 \cdot 10^{-11}$ J/m together with a saturation magnetisation $M_s \approx 1710$ kA/m, gives rise to the exchange length $l_{ex} = (\frac{J_A}{\mu_0 M_s^2})^{1/2}$, describing the range at which the exchange interaction is dominant over the demagnetisation energy. The exchange length for Fe is approximately $l_{ex,Fe} \approx 2.3$ nm to 3.3 nm [12, 13]. Magnetic films of thicknesses comparable to the exchange length are referred to as ultrathin films. One assumes the exchange coupling to be dominant over the whole sample size, aligning all magnetic moments parallel to each other, enabling the treatment in the model of a macroscopic spin representative for the whole ultrathin film [14]. In this thesis, the 5 nm thick Fe is assumed to be homogeneously magnetised, to allow for a description of a macrospin \vec{M} .

A torque \vec{T} operates on a magnetic moment \vec{m} in an external magnetic field \vec{H}_{ext} [11, 15, 16, 17]:

$$\vec{T} = \vec{m} \times \vec{H}_{ext} \quad (2.1)$$

The angular momentum \vec{L} is related to the torque via $\vec{T} = \frac{d\vec{L}}{dt}$, as a result one can rewrite equation 2.1 to [18]:

$$\frac{d\vec{L}}{dt} = \vec{m} \times \vec{H}_{ext} \quad (2.2)$$

All \vec{m}_i in the macrospin model add up to \vec{M} , following the relation $\hat{m} = -\gamma \hbar \hat{L}$; $\gamma = \frac{g|e_o|}{2m_e c}$ the motion of the magnetisation in an external field is given by:

$$\frac{d\vec{M}}{dt} = -\gamma \vec{M} \times \vec{H} \quad (2.3)$$

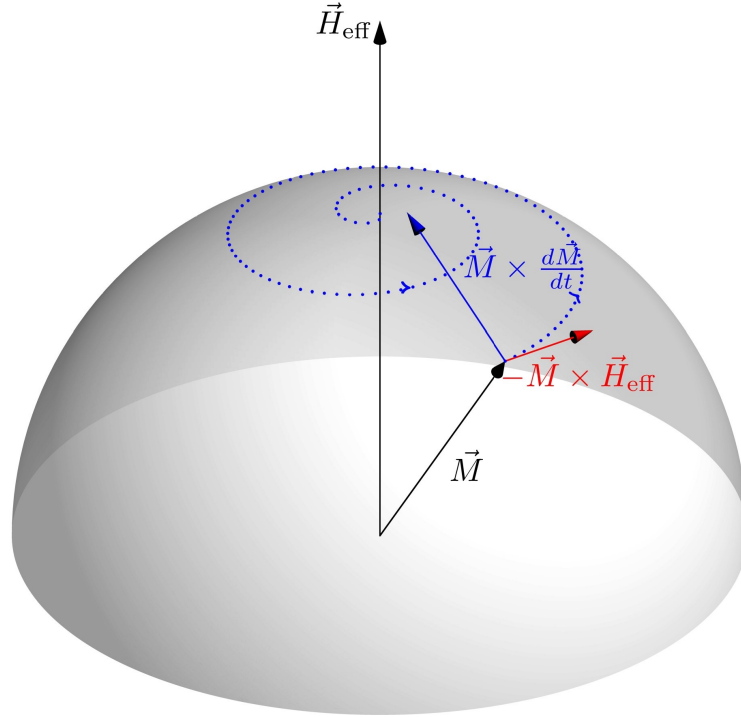


Fig. 2.1.: Schematic diagram of the precession of the magnetisation. The blue arrow is the damping term, that shows the spiral motion of \vec{M} , if external stimulation through microwave fields is neglected. The red arrow is the precession term, driving the magnetisation around an effective magnetic field \vec{H}_{eff} .

The parameter γ is called the gyromagnetic ratio, it is proportional to the Landé g-factor and is the ratio between the spin moment and the magnetic moment. The g-factor of a free electron is $g = 2.00232$. For 3d-elements one expects the ratio of angular momentum to spin moment to be [19]:

$$\frac{\mu_L}{\mu_S} = \frac{g}{2} - 1 \quad (2.4)$$

Spin-orbit interaction bound to the symmetry of the crystal lattice will change not only the value of the g-factor (few percent in the cubic lattice), but will also induce an anisotropic g-factor. As Rado suggested [19, 20], the contributions for the magnetisation parallel to a film surface g_{\parallel} and perpendicular g_{\perp} need to be distinguished. The anisotropic g-factor gives rise to the g-tensor, which for uniaxial symmetry results in [19]:

$$g^2 = g_{\parallel}^2 \sin^2 \theta + g_{\perp}^2 \cos^2 \theta = g_{\parallel}^2 + (g_{\perp}^2 - g_{\parallel}^2) \cos^2 \theta. \quad (2.5)$$

With θ as the polar angle in spherical coordinates.

Equation 2.3 describes the motion of magnetisation from its equilibrium position due to the torque \vec{T} , neglecting dissipation. The damping of the movement is taken into consideration phenomenologically in the Landau-Lifshitz equation (LL equation), which is named after its discoverers [21]:

$$\frac{d\vec{M}}{dt} = -\gamma \vec{M} \times \vec{H} + \frac{\gamma \lambda}{M^2} \vec{M} \times (\vec{M} \times \vec{H}) \quad (2.6)$$

The dissipation parameter with the dimensionality of a magnetic field is known as λ . The damping term becomes bigger than the precession term at sufficiently large values of λ , and the LL equation

becomes physically non-valid. Gilbert introduced a damping component based on viscous damping in 1955, which meets the criterion $d\vec{M}/dt \rightarrow 0$ [16], by using a dimensionless damping $\alpha = \lambda/M$ and replacing the term $(\vec{M} \times \vec{H})$ of the damping with $\frac{1}{\gamma} \frac{d\vec{M}}{dt}$. The Gilbert damping transforms the LL equation into the Landau-Lifshitz-Gilbert equation (LLG equation) [21]:

$$\frac{d\vec{M}}{dt} = \underbrace{-\gamma \vec{M} \times \vec{H}}_{\text{Precession Term}} + \underbrace{\frac{\alpha}{M} \vec{M} \times \frac{d\vec{M}}{dt}}_{\text{Damping Term}} \quad (2.7)$$

The saturation magnetisation M is a crucial prerequisite for this type of magnetisation movement. That is, the magnitude of M is unaffected by the externally applied field or time. This depicts the situation of atomic magnetic moments that are completely parallel. Multiplying the LLG by M scalar further demonstrates this property:

$$\frac{dM^2}{dt} = 0$$

As a result, the magnitude $|\vec{M}|$ remains constant. This vector is also considered in the following course with a stationary point at one of its endpoints. As a result, the non-stationary end has the ability to oscillate. Precession is the name for this type of oscillation. A schematic representation of the precession is shown in figure 2.1. The constant magnitude of the magnetisation creates a unit sphere, visible as the grey sphere, to which the magnetisation will always be perpendicular to.

The term magnetisation damping describes any effects contributing to a relaxation of the magnetisation precession into equilibrium state. This includes spin-flip scattering through s-d exchange interaction, dissipation of energy through generation of eddy currents due to the magnetisation precession and magnon-phonon coupling [14].

The damping, compared to a highly viscous fluid, will reduce the precession cone opening continuously. If one tracks the position of the precessing magnetisation vector, the magnetisation relaxes in a spiral around the effective fields H_{eff} , as shown in figure 2.1. The sum of all internal magnetic fields H_i yields an effective magnetic field H_{eff} in the LLG equation. It is defined as [22]:

$$\vec{H}_{eff} = \vec{H}_{ext} + \vec{H}_{Ani} + \vec{H}_{ex} \quad (2.8)$$

\vec{H}_{eff} consists of three parts: The external applied field \vec{H}_{ext} , the magnetic anisotropy contributions \vec{H}_{Ani} and the exchange field \vec{H}_{ex} created by an internal exchange interaction. The effective field defines the equilibrium position of the magnetisation, thus replaces \vec{H} , in the LLG equation. The LLG equation is changed by \vec{H}_{eff} to [19]:

$$(1 + \alpha^2) \frac{d\vec{M}}{dt} = -\gamma \vec{M} \times \vec{H}_{eff} + \frac{\alpha}{M} \vec{M} \times \frac{d\vec{M}}{dt} \quad (2.9)$$

To account for situations of higher damping, the term $(1 + \alpha^2)$ must be considered. For small damping $(1 + \alpha^2) \approx 1$ and is neglected.

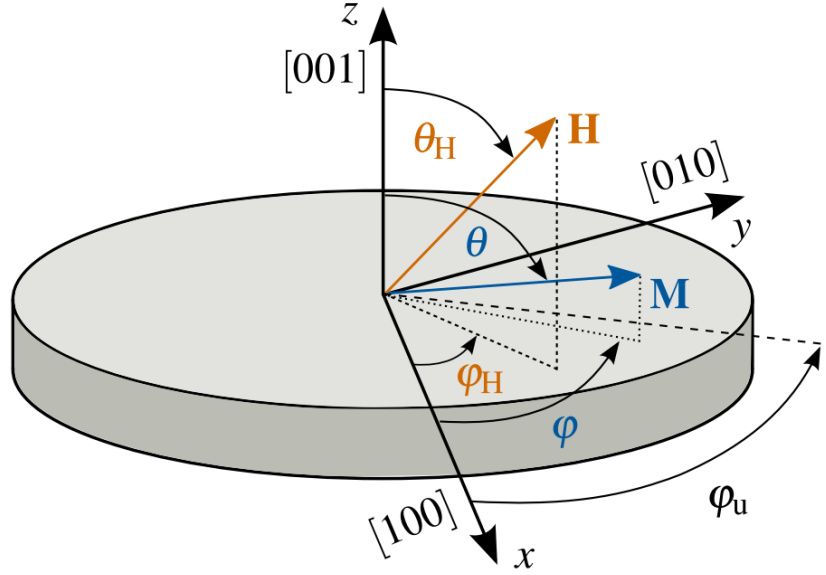


Fig. 2.2.: This figure shows the spherical coordinate system, that is used to derive the phenomenological anisotropy. The field H is the external magnetic field and θ_H, ϕ_H describe the orientation of H . The angles θ, ϕ describe the orientation of the magnetisation M . The x axis is set along the $[100]$ direction. A uniaxial in-plane anisotropy can be oriented with respect to the $[100]$ direction, by the angle ϕ_u . This schematic further explains the meaning of in-plane rotation, in which the field H is varied around the z-axis with $\theta = \text{const} = 90^\circ = \pi/2$ and out-of-plane rotation in which $\phi = \text{const}$ and θ is varied. The picture is adapted from [23]

2.1.2. Helmholtz free energy density

The magnetic anisotropy in terms of a phenomenological model, is described by the Helmholtz free energy density F [16, 24]:

$$F dV = [U - TS] dV \quad (2.10)$$

The internal energy is U , the temperature is T , and the entropy is S . The energy required to move \vec{M} from its equilibrium position is expressed in this value. As a result, a potential landscape, typical for the magnet under examination, is formed by many contributions in F . Magnetic anisotropy contributions are referred to as F_{Ani} . A magnet obtains an extra energy, the Zeeman energy, written as $F_{zee} = -\vec{M} \cdot \vec{H}_{ext}$, when it is exposed to an external magnetic field [11]. The total free energy density is calculated as follows:

$$F = F_{Ani} - \vec{M} \cdot \vec{H}_{ext} \quad (2.11)$$

The qualitative analysis of the magnetic anisotropy energy (MAE) considers two major contributions, the magnetostatic energy due to the shape anisotropy and the magnetocrystalline contribution, arising from dipole-dipole coupling and the spin-orbit interaction, correspondingly. The anisotropy of a magnet may be represented by internal fields derived from the energy landscape F_{Ani} [23]:

$$\vec{H}_{Ani} = -\frac{1}{M} \nabla_m F_{Ani} \quad (2.12)$$

A minimum in the energy landscape defines the equilibrium position of the magnetisation, this orientation is named easy axis. The global maximum of the energy landscape is named hard axis. If there is the case of local maxima, whose height is less than the hard axis, but still higher than the

easy axis, these orientations are named intermediate axis.

In 3d transition metals, the partly filled 3d electron orbitals lay farthest from the nucleus. This means, that they are not significantly shielded from the electrical potentials of other atoms. By summing up all contributions of electrical potential in a three dimensional crystal lattice a inhomogeneous crystal field is created. A description of the magnetisation movement in such crystal fields can be described in crystal field or in the ligand field theory [25]. Although great knowledge of the system under investigation is needed, to compute an anisotropy effect in such theories. Nevertheless they are of great importance for understanding the behaviour of different anisotropy contributions.

Exchange energy

The exchange interaction between two magnetic moments is responsible for ferromagnetism if the exchange constant is $J > 0$. For the exchange energy of magnetic moments (i, j) one considers the Heisenberg Hamiltonian [23, 25]:

$$\hat{H}_{ex} = -2 \sum_{i,j} J_{i,j} \vec{S}_i \cdot \vec{S}_j \quad (2.13)$$

This model becomes anisotropic through different coupling constants in different orientations $J_{x,y,z}$, while the Heisenberg Hamiltonian on its nature is isotropic $J_x = J_y = J_z = J$. The indices i and j represent individual moments, and \vec{S} are the moments spin contribution in the orientation of (x, y, z).

Zeeman energy

The Zeeman energy due to the external field \vec{H}_{ext} acting on \vec{M} is given through the scalar product $\vec{M} \cdot \vec{H}$ in spherical coordinates:

$$\begin{aligned} F_{Zeeman} &= -\vec{M} \cdot \vec{H} = -M_0 \begin{pmatrix} \sin(\theta) \cos(\phi) \\ \sin(\theta) \sin(\phi) \\ \cos(\theta) \end{pmatrix} \cdot H_0 \begin{pmatrix} \sin(\theta_H) \cos(\phi_H) \\ \sin(\theta_H) \sin(\phi_H) \\ \cos(\theta_H) \end{pmatrix} \\ &= -M_0 H_0 [\sin(\theta) \sin(\theta_H) \cos(\phi - \phi_H) + \cos(\theta) \cos(\theta_H)] \end{aligned} \quad (2.14)$$

Magnetostatic energy

The magnetostatic energy is described by the magnetic dipole interaction in a ferromagnet, that is given by its Hamiltonian \hat{H}_{dd} [19]:

$$\hat{H}_{dd} = \frac{1}{4\pi\epsilon_0} \frac{1}{|r_{i,j}|^3} \left[\vec{\mu}_i \cdot \vec{\mu}_j - \frac{3}{|r_{i,j}|^2} (\vec{\mu}_i \cdot \vec{r}_{i,j})(\vec{\mu}_j \cdot \vec{r}_{i,j}) \right] \quad (2.15)$$

The resulting field of dipoles $\vec{\mu}_{i,j}$ at location $r_{i,j}$ is interfering with the external field \vec{H}_{ext} . This creates the macroscopic field \vec{H}_{macro} of a ferromagnet, which can be modelled as: $\vec{H}_{macro} = \vec{H}_{ext} + \vec{H}_{dem}$ [11]. The field \vec{H}_{dem} describes the demagnetisation field, that is counteracting the magnetic field given accordingly to the magnetisation direction.

Magnetic anisotropy energy

Shape anisotropy

When observing a macroscopic magnet, the stray field contribution to the MAE becomes significant. Depending on the shape of the ferromagnet, the long-range nature of the magnetic field induces different demagnetising fields [25, 26]:

$$\vec{H}_{dem} = \underline{\underline{N}}\vec{M} \quad (2.16)$$

The energy contribution to the free energy density can be broken down to the entries of the demagnetising tensor $\underline{\underline{N}}$:

$$F_{dd} = \frac{1}{2}\mu_0 (N_x M_x^2 + N_y M_y^2 + N_z M_z^2) \quad (2.17)$$

Especially in the thin film shape, a sample can be simplified as a spheroid with rotation symmetry around its z-axis. This leads to the simplification of the demagnetising tensor $\underline{\underline{N}}$ to $N_x = N_y = N_{\perp}$ and $N_z = N_{\parallel}$. This assumption modifies Eq.(2.17) to:

$$F_{dd} = \frac{1}{2}\mu_0 |\vec{M}_S|^2 (N_{\perp} \cos^2 \theta + N_{\parallel} \sin^2 \theta) \quad (2.18)$$

In the case of magnetic thin films one can assume the lateral dimensions to be sufficiently larger compared to the samples thickness in order to reduce the demagnetising contribution further to $N_{\perp} = 1$ and $N_{\parallel} = 0$. The shape anisotropy energy contribution for magnetic thin films is now:

$$F_{dd} = \frac{1}{2}\mu_0 |\vec{M}_S|^2 \cos^2 \theta \quad (2.19)$$

This equation only shows influence in the θ direction, which in spherical coordinates is defined by the polar angle θ and in a projection to Cartesian coordinates would refer to an out-of-plane contribution. This means that the shape anisotropy of thin films forces the magnetisation into an orientation parallel to the surface.

Magnetocrystalline anisotropy

The magnetocrystalline anisotropy describes every MAE contribution to the free energy density bound to the crystallographic axes of the magnet. The only origin is the dipole-dipole coupling and spin-orbit interaction (LS coupling). For the spin-orbit contribution one finds its Hamiltonian as [19]:

$$\hat{H}_{LS} = -\frac{\mu_B}{\hbar m_e e c^2} \left(\frac{1}{r} \frac{dV}{dr} \right) \vec{L}_j \cdot \vec{S}_i \quad (2.20)$$

To fully resolve the anisotropy caused by the LS coupling, the LS coupling would have to be calculated over a complete macroscopic system of spins, including the interactions between the moments. A simpler approach is to mirror this behaviour phenomenologically, by the use of a powerseries of \vec{M} projected on the crystallographic axes of the magnet to describe the energy of the anisotropy. This results in a Helmholtz free energy density landscape that mimics the magnetisation's orientational deflection dependence. The magnitude of a MAE contributions is given by the magnetic anisotropy constant K_i corresponding to a distinctly defined orientation. These

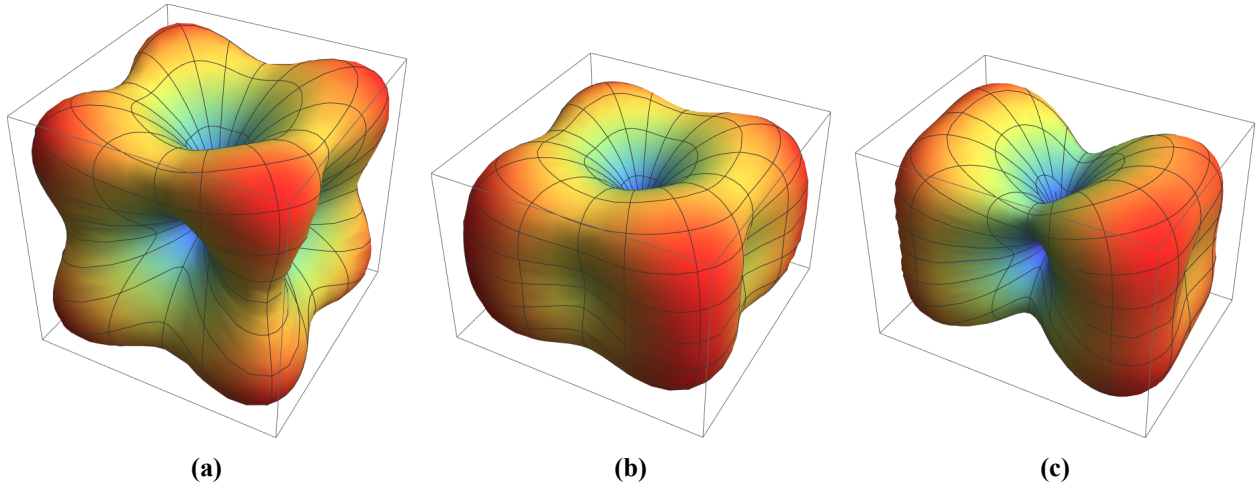


Fig. 2.3.: Phenomenological Helmholtz free energy landscapes for different anisotropy contributions. Figure **a)** is a purely cubic anisotropy potential landscape. Figure **b)** shows a cubic anisotropy tetragonal distorted and figure **c)** shows a cubic anisotropy overlaid by an in-plane uniaxial anisotropy

constants have units J/m^3 . This derivation must be subject to the symmetries of the real crystal structure, and it must, for example, be invariant for all operations that make up the crystal symmetry group [16]. The powerseries of \vec{M} to its distinct axes is given by the direction cosines $\alpha_i = \frac{\vec{M}_i}{|\vec{M}|}$, $i \in 1, 2, 3$, under consideration of $\alpha_1 + \alpha_2 + \alpha_3 = 1$ one finds for a cubic symmetry [26]:

$$F_{cub} = K_4 (\alpha_1^2 \alpha_2^2 + \alpha_2^2 \alpha_3^2 + \alpha_3^2 \alpha_1^2) + K_6 \alpha_1^2 \alpha_2^2 \alpha_3^2 + \dots \quad (2.21)$$

where the symbols α_i describe the direction cosines regarding the [100] orientation and $K_{4,6}$ are the cubic anisotropy constants. Expressed in spherical coordinates F_{cub} changes to [23]:

$$F_{cub} = \frac{1}{4} K_4 (\sin^2(2\theta) + \sin^4(\theta) \sin^2(2\phi)) + \frac{1}{16} K_6 \sin^2(\theta) \sin^2(2\theta) \sin(2\phi) \quad (2.22)$$

The case with a single axis of symmetry is called the uniaxial anisotropy:

$$F_{uni} = K_2 \sin^2(\theta) + K_4 \sin^4(\theta) + K_6 \sin^6(\theta) + \dots \quad (2.23)$$

Taking into account a basal plane, F_{uni} also contributes in the ϕ direction [16]:

$$F_{uni} = K_2 \sin^2(\theta) + K_4 \sin^4(\theta) + K_6 \sin^6(\theta) + K'_4 \sin^4(\theta) \cos(4\phi) \quad (2.24)$$

The names of the anisotropy constants can be changed to correspond to the number of directions contributed to. Instead of its sinusoidal order $K_{2,4,6,\dots}$ the constants will be called $K_{2,4}$, standing for K_2 : two fold symmetry = two contributed directions, K_4 : four fold symmetry = contributing in 4 directions. Additionally this approach further divides the constants into parallel \parallel and perpendicular \perp contribution with respect to the thin film sample surface. This allows for a more precise determination of in-plane \parallel and out-of-plane \perp magnitudes. The uniaxial anisotropy, therefore will be split in $F_{uni,\parallel}$ and $F_{uni,\perp}$ [19]:

$$F_{uni,\parallel} = -K_{2,\parallel} \alpha_1^2 = -K_{2,\parallel} \sin^2(\theta) \cos^2(\phi - \phi_U) \quad (2.25)$$

$$F_{uni,\perp} = -K_{2,\perp} \alpha_3^2 - K_{4,\perp} \alpha_3^4 = K_{2,\perp} \sin^2(\theta) - K_{4,\perp} \cos^4(\theta) \quad (2.26)$$

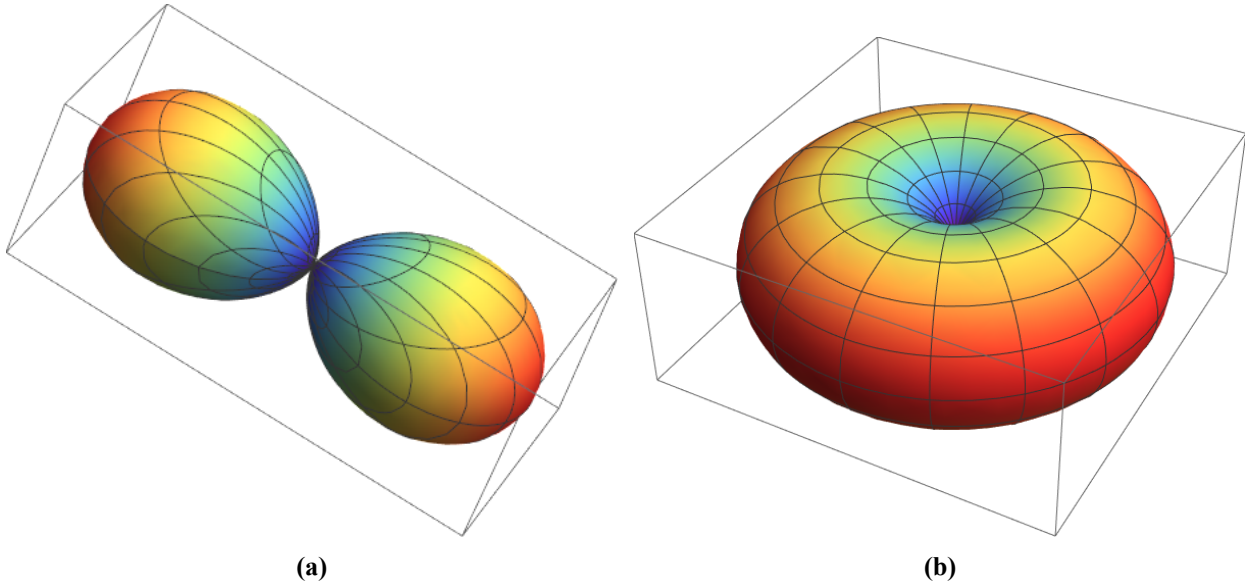


Fig. 2.4.: Helmholtz free energy landscape for uniaxial anisotropies F_{uni} . Figure a) shows the uniaxial anisotropy for a negative free energy density $F_{uni} < 0$ and figure b) for positive $F_{uni} > 0$.

The angle ϕ_U sets direction of the easy axis in respect to the orientation $[100]$ and therefore defines the direction of the influence. Additionally, this simplifies the description of a tetragonal distorted crystal lattice, in which the cubic anisotropy constants $K_{4,\perp,\parallel}$ are of unequal magnitude [23]:

$$\begin{aligned}
 F_{tet} &= K_{2\perp} \alpha_3^2 + \frac{1}{2} K_{4\perp} \alpha_3^4 + \frac{1}{2} K_{4\parallel} (\alpha_1^4 + \alpha_2^4) \\
 &= K_{2\perp} \sin^2(\theta) - \frac{1}{2} K_{4\perp} \cos^4(\theta) - \frac{1}{8} K_{4\parallel} (3 + \cos(4\phi)) \sin^4(\theta)
 \end{aligned} \tag{2.27}$$

The free energy landscapes can be plotted in 3D-spherical-coordinates. Figure 2.3 shows the cubic anisotropy in 2.3a, which can be deformed vertically by a tetragonal distortion for figure 2.3b. The case for a cubic anisotropy, that is distorted in-plane by a uniaxial anisotropy, can be found in 2.3c. The uniaxial anisotropy for either positive or negative free energy density can be found in 2.4b and 2.4a. Their shape does not change for in-plane or out-of-plane direction, thus this figure is representative for uniaxial anisotropy in general.

In ligand field theory, the energy levels of the electrons are determined by the sum of the electrostatic potentials Φ over nearest neighbours: $K = \sum_i^N e \cdot \Phi(|\vec{r}_i|)$. For a cubic symmetry in spherical coordinates the crystal field is as follows:

$$K = \frac{35}{4} \frac{q_{ion}}{a^5} \left(x^4 + y^4 + z^4 - \frac{3}{5} r^4 \right) \tag{2.28}$$

Whereas q_{ion} describes the charge of the ligand, r_i describes their position and a is the distance between the ligands. By perturbation of the potential K non vanishing contributions to the magnetic anisotropy energy are found. In second order perturbation a uniaxial contribution is found to be of orders $K_2 \approx 1 \text{ meV}$, the cubic contribution vanishes. For fourth-order perturbation the cubic contribution is found to be of orders smaller, $K_4 \approx 0.2 \mu\text{eV}$. The reason for the big discrepancy between uniaxial and cubic energy magnitude, is the quenching of orbital moments in cubic systems. This means, the d orbitals in distinct axes orientations d_{xy}, d_{yz}, d_{xz} are found to have the

least energy due to crystal field splitting. These orbitals are preferred over for example the $d_{x^2-y^2}$ orbital. The orbital moment along the quantisation axis z is found to be:

$$\langle |\hat{L}_z| \rangle = \langle d_{xy} | \hat{L}_z | d_{xy} \rangle = \langle d_{yz} | \hat{L}_z | d_{yz} \rangle = \langle d_{xz} | \hat{L}_z | d_{xz} \rangle = 0 \quad (2.29)$$

This means the angular momentum along the z -axis is vanishing and the total angular momentum is only defined by the spin momentum. In reality however tetragonal distortion and asymmetries give rise to a unquenching, resulting in spin orbit interaction [19], which leads to a small decrease in ground state energy and a fourth order perturbation cubic energy contribution is achieved. The effect of the small energy contribution for cubic symmetry for the magnetic anisotropy can be seen in smaller effect on the resonance positions. As an example, K_{uni} , in the free energy model, can reach values of several 100 kJ/m³ and higher. The corresponding resonance positions can reach fields in the range of Tesla. The cubic anisotropy K_{cub} can reach values of 10 kJ/m³ and produce resonance fields of several 100 mT.

To get a thorough description of a crystal's free energy density, all the symmetry terms that are important for the system in a phenomenological study are summed up. Due to the enormous lateral extension in proportion to the thickness of the studied thin films, a significant demagnetising field is expected in Fe and Rh bilayers, causing a large uniaxial anisotropy parallel to the surface. Fe has a cubic symmetry, which might be tetragonally distorted due to effect of strain at the interface with substrate and direct contact with Rh, which has a higher lattice parameter. The system's total free energy density is as follows:

$$F = F_{dd} + F_{uni,\parallel} + F_{Zeeman} + F_{tet} \quad (2.30)$$

This leads to the total free energy density [23]:

$$\begin{aligned} F &= F_{dd} + F_{uni,\parallel} + F_{tet} + F_{Zeeman} \\ &= -\frac{1}{2}\mu_0 M^2 \sin^2(\theta) - K_{2,\parallel} \sin^2(\theta) \cos^2(\phi - \phi_U) \\ &\quad + K_{2\perp} \sin^2(\theta) - \frac{1}{2}K_{4\perp} \cos^4(\theta) - \frac{1}{8}K_{4\parallel}(3 + \cos(4\phi))\sin^4(\theta) \\ &\quad - MH [\sin(\theta) \sin(\theta_H) \cos(\phi - \phi_H) + \cos(\theta) \cos(\theta_H)] \end{aligned} \quad (2.31)$$

In FMR experiments, without knowledge of the saturation magnetisation, one can not disentangle M_s and $K_{2\perp}$. Therefore the so called effective magnetisation M_{eff} is introduced [23]:

$$\mu_0 M_{eff} = \mu_0 M_s - \frac{2K_{2\perp}}{M_s} \quad (2.32)$$

The reason for the entanglement lies in the shape anisotropy and the uniaxial anisotropy perpendicular to the film surface. Both contribute to the same effect $\propto \sin^2(\theta)$, just that the magnitude of the shape anisotropy is given by the saturation magnetisation, while the strength of the uniaxial anisotropy is given by the anisotropy constant $K_{2\perp}$. Only the clear determination of M_s , for example using SQUID magnetometry, allows to evaluate the value of $K_{2\perp}$. Additionally equation 2.12 can be expressed in terms of the anisotropy field deduced from the total free energy density F , as follows [23]:

$$\mu_0 H_{K_i} = \frac{2K_i}{M_s} \quad (2.33)$$

This expresses the magnitude of each anisotropy parameter in units of Tesla. It allows for direct comparison, with external applied fields. This enables a easier discussion of the strength of the anisotropy in a magnet.

2.1.3. Ferromagnetic resonance

Resonance condition

The derivation of the resonance condition and of the Lorentzian line shape is taken from literature [16, 26, 27, 28]. In FMR, a ferromagnet absorbs energy from a time-varying magnetic field $h(t)$ in a resonant manner. The magnetic field part of electromagnetic radiation in various frequency bands is used for experimental observation of FMR in this work. The magnetisation and effective field are modulated by the microwave field in the following way

$$\vec{H}(t) = H_{eff} + \vec{h}(t) \quad \text{and} \quad \vec{M} = M_0 \vec{e}_z + \vec{m}(t) \quad (2.34)$$

In the following we assume that $h(t) \ll H_{ext}$ and $m(t) \ll M$. The initial condition at $t=0$, derived by substituting equation 2.34 into the LLG, is determined to be $\vec{M} \times \vec{H}_{eff} = 0$ approximating only time invariant contributions. When the pure AC contributions $\vec{m}(t) \times \vec{h}(t)$ are negligibly small, the linearised form of the LLG is derived using the bilinearity of the cross product and $dM/dt = 0$ and $\vec{M}_0 = M_0 \vec{e}_z$, as follows:

$$\frac{\partial \vec{m}(t)}{\partial t} + \gamma \vec{m}(t) \times \vec{H}_{eff} + \frac{\alpha}{|M|} \vec{m}(t) \times \vec{M}_0 = -\gamma \vec{M}_0 \times \vec{h}(t) \quad (2.35)$$

The time-dependent contributions can now be represented harmonically in sinusoidal form, with the complex amplitudes \tilde{m} and \tilde{h} representing a circularly polarised wave:

$$m'' = \tilde{m} \exp\{i\omega t\}, \quad h'' = \tilde{h} \exp\{i\omega t\}$$

In the LLG this yields:

$$i\omega \vec{m}(t) + \gamma \vec{m}(t) \times \vec{H}_{eff} + \frac{i\omega\alpha}{|M_0|} \vec{m}(t) \times \vec{M}_0 = -\gamma \vec{M}_0 \times \vec{h}(t) \quad (2.36)$$

The linear approximation of the equation of motion is useful for observing motion at tiny amplitudes and deflections. When the linearised equation of motion is projected onto the axes of the Cartesian coordinate system, contributions are found in the X , Y , and Z directions; if the magnetisation and therefore the effective field are aligned parallel to the Z -Axis $\vec{H}_{eff} || \vec{e}_z$, the results are:

$$\begin{aligned} X : \quad & i\omega m_x + \gamma m_y H_{eff} + \frac{i\omega\alpha}{|M|} m_y M_0 = \gamma M_0 h_y \\ Y : \quad & i\omega m_y + \gamma m_x H_{eff} - \frac{i\omega\alpha}{|M|} m_x M_0 = -\gamma M_0 h_x \\ Z : \quad & i\omega m_z = 0 \end{aligned} \quad (2.37)$$

With solution of $m(t)$ as:

$$\begin{aligned} m_x &= \chi h_x + i\chi_a h_y \\ m_y &= -i\chi_a h_x + \chi h_y \\ m_z &= 0 \end{aligned} \quad (2.38)$$

Here $\chi = \frac{\gamma M_0 \omega_H}{\omega_H^2 - \omega^2}$ and $\chi_a = \frac{\gamma M_0 \omega}{\omega_H^2 - \omega^2}$ and $\omega_H = \gamma H_{eff} + i\omega\alpha$.

We obtain the following representation by separating the imaginary component of ω_H and therefore of χ, χ_a from the real part:

$$\begin{aligned} \chi &= \chi' - i\chi'' \quad \text{and} \quad \chi_a = \chi'_a - i\chi''_a \\ \chi' &= \frac{1}{D} \gamma M_0 \mu_0 \omega_H [\omega_H^2 - (1 - \alpha^2) \omega^2] \\ \chi'' &= \frac{1}{D} \gamma M_0 \mu_0 \omega \alpha [\omega_H^2 + (1 + \alpha^2) \omega^2] \\ \chi'_a &= \frac{1}{D} \gamma M_0 \mu_0 \omega [\omega_H^2 - (1 + \alpha^2) \omega^2] \\ \chi''_a &= 2\alpha \gamma M_0 \mu_0 \omega^2 \omega_H \\ D &= [\omega_H^2 - (1 + \alpha^2) \omega^2]^2 + 4\alpha^2 \omega^2 \omega_H^2 \end{aligned} \quad (2.39)$$

The solutions may alternatively be put in tensor form using $\vec{m} = \underline{\chi} \cdot \vec{h}$. As a solution of the linearised equation of motion of the magnetisation, the high-frequency tensor $\underline{\chi}$ is obtained:

$$\begin{pmatrix} m_x \\ m_y \\ m_z \end{pmatrix} = \begin{vmatrix} \chi & i\chi_a & 0 \\ -i\chi_a & \chi & 0 \\ 0 & 0 & \chi_{||} \end{vmatrix} \cdot \begin{pmatrix} h_x \\ h_y \\ h_z \end{pmatrix} \quad (2.40)$$

For the sake of completeness a longitudinal contribution $\chi_{||} > 0$, parallel to the magnetisation orientation, for sufficiently small damping is added to the tensor:

$$\chi_{||} = \frac{i\gamma\alpha M_0}{\omega - i\alpha M_0 \mu_0 \omega_H / (\mu_0 M_0)} \quad (2.41)$$

In the background of the macrospin model with a uniformly saturated magnetisation, this contribution is neglected. Figure (2.5) shows the susceptibility of a ferromagnet presented as the real and imaginary parts behaviour for external fields $H \in (0, 0.6)$ T. By stimulating the magnet with a time dependent magnetic field $h(t)$ of an adequate frequency and applying a time constant magnetic field H_{ext} , a rapid maximisation of the imaginary part of χ'' can be observed. This sudden maximum point accompanies a maximum response of the ferromagnet to the external time dependent field $h(t)$, which is known as the ferromagnetic resonance. This response can be interpreted as the deflection into a precession motion, as described by the LLG equation 2.9, around the equilibrium position, which is given by H_{eff} . The ferromagnet is constantly absorbing energy from the magnetic field $h(t)$, without the magnetisation damping the magnetisation would never stop precessing and eventually flip its direction on the quantisation axis. With damping enabled, the precession cone opening, which means the angle of deflection around H_{eff} , will become stationary at a fixed deflection angle, under constant microwave irradiation. One has to note, that this situation in reality is not the case. Due to the dragging effect in intermediate orientations between crystallographic

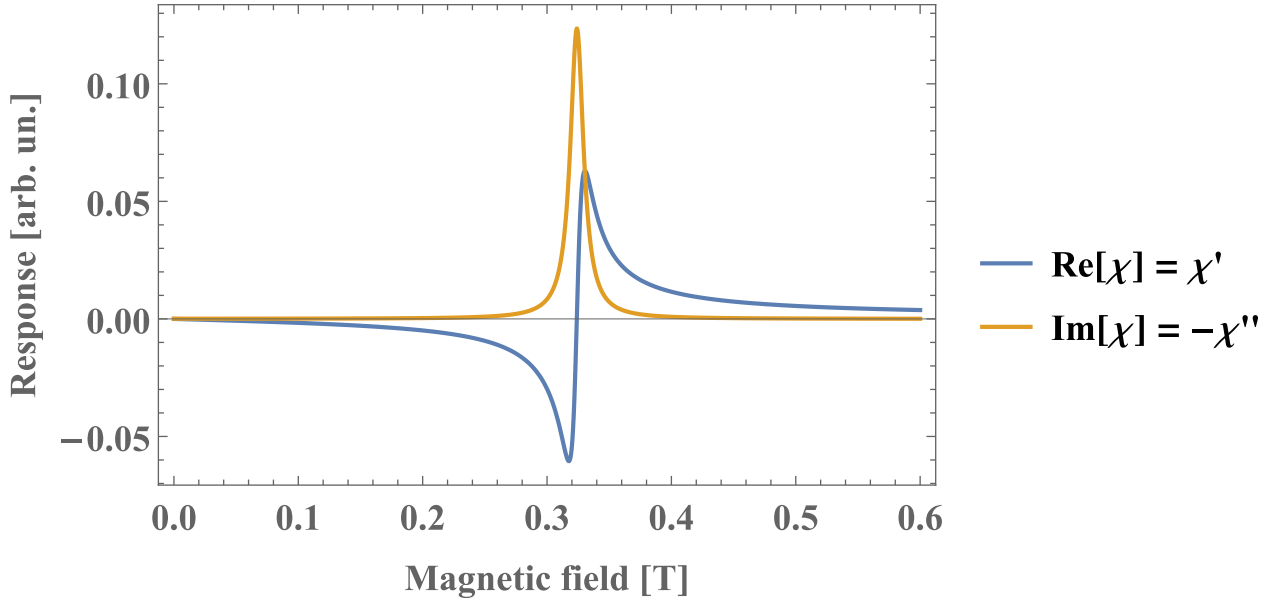


Fig. 2.5.: Resonant response of the magnetic susceptibility for the case of ferromagnetic resonance. The susceptibility was calculated according to equations 2.39 using $M_0 = 0.0016$ T a damping of $\alpha = 0.01$, a frequency of 9.54 GHz and a g-factor $g = 2.1$. Only the resonance for positive fields is shown, in negative applied fields $H \in (-0.6, 0)$ T, due to the square law dependency on ω_H , a solution of the magnetic susceptibility can be found as well. This negative resonance mirrors the resonance of positive fields.

axes, the precession might be elliptically distorted. This distortion was neglected for the sake of this derivation, but should be mentioned in the case of a real world experiment. At resonance, χ'' , χ_a'' become maximal, and χ' changes sign. In the damped case, the resonance condition is as follows [16]:

$$\omega_{res} = \frac{\omega_H}{1 + \alpha^2} = \frac{\gamma \mu_0 H_{eff} + i\omega\alpha}{1 + \alpha^2} \quad (2.42)$$

If the damping α is assumed to be sufficiently small, the above condition is simplified to [15]:

$$\omega_{res} = \gamma \mu_0 H_{eff} \quad (2.43)$$

There are now two ways to achieve the resonance condition in the experiment. The external field is kept constant in the first. The outcome is ω_{res} , a resonance frequency determined by Eq.(2.43). The second approach keeps the frequency constant while varying the field, resulting in a resonant field H_{res} :

$$\frac{\omega}{\gamma} = \mu_0 H_{res} \quad (2.44)$$

The second method was used in the FMR experiments of this thesis. The resonance field is defined by the magnetic anisotropy of the given system and its magnitude in a certain spatial orientation. As already noted, the MAE of a magnet can be illustrated by the Helmholtz free energy density F . A resonance condition with respect to the MAE can be found using the so-called Smit-Beljers-Suhl (SBS) approach [29, 30], considering the change of the total energy of a magnetic dipole for a infinitesimal small deflection derived in spherical coordinates. The assumption of small deflection, or small precession cone, is valid under consideration of FMR using a microwave power, which is small enough to assume linear FMR. The deflection is proportional to the damping and microwave

power and is usually found to be in the range of few degrees $\rho \approx 6^\circ$ for frequencies of about 9 GHz [31], which is small enough to consider small angle approximations. Additionally it is assumed, that the microwave field penetrates the sample homogeneously, which is valid under consideration for thin films of lateral diameters smaller than the wavelength of the microwave. In the case of GHz radiation, the wavelength is in the range of cm. With lateral sample dimensions of 4mm x 4mm, complete coverage of the sample in one wave period is achieved. These considerations give rise to the energy landscapes Hessian matrix, due to the small angle approximation of the precession, whereas the determinant reflects the resonance condition, and the Smit-Beljers-Suhl approach for FMR resonance condition, if the damping is approximated as $1 + \alpha = 1$, is found as follows [29, 30]:

$$\omega_{\text{res}} = \pm \frac{\gamma}{M \sin(\theta)} \sqrt{\frac{\partial^2 F}{\partial \theta^2} \frac{\partial^2 F}{\partial \phi^2} - \frac{\partial^2 F}{\partial \theta \partial \phi}} \quad (2.45)$$

Additionally Baselgia points out the Smit-Beljers-Suhl approach to have singularities at $\theta = 0^\circ$ orientation [32]. Together with the ability of a total disentanglement of all anisotropy contributions of F to $\frac{\gamma}{M}$ he proposes a modified resonance condition using the notation $\frac{\partial F}{\partial(\theta, \phi)} = F_{\theta, \phi}$ as:

$$\omega_{\text{res}} = \pm \frac{\gamma}{M} \sqrt{F_{\theta\theta} \left[\left(\frac{F_{\phi\phi}}{\sin^2 \theta} + \frac{\cos \theta}{\sin \theta} F_{\theta} \right) - \left(\frac{F_{\theta\phi}}{\sin \theta} - \frac{\cos \theta}{\sin \theta} \frac{F_{\phi}}{\sin \theta} \right)^2 \right]} \quad (2.46)$$

According to the resonance condition, equation 2.45 or 2.46, the resonance position $\omega_{\text{res}}/\gamma$ is directly related to the Helmholtz free energy density at the orientation of the magnetisation. In the FMR experiment, to extract the anisotropy out of the resonance condition, an angular dependence of the resonance field must be investigated in several directions (in-plane, out-of-plane rotation), which can be used to resemble the free energy landscape. The position of the magnetisation in spherical coordinated is given by polar and azimuthal angle $\theta_M \in [0, \pi]$, $\phi_M \in [0, 2\pi]$. Measurements are usually performed with one of these angles fixed while second one is varied. For the case of an in-plane (IP) angular dependence the polar angle θ is fixed to $\theta = \pi/2$. The angle ϕ is then varied in a certain range, usually $0^\circ - 180^\circ$ is enough, but full 360° would reflect the whole IP case. For the case of out-of-plane measurements (OOP), the ϕ angle is fixed, usually to 0° , and θ is varied. In case of an IP measurement one has to imagine a cut into the free energy landscape as it is shown in figure 2.3a. This cut is shown in figure 2.6a. In the experiment, one follows the curvature at the edge of the cut, which is highlighted in red. Projected into Cartesian coordinates, shown in figure 2.6b, this depicts the angular dependence of the IP free energy density, which can be directly transformed to the angular dependence of the FMR resonance condition following Eq. 2.45, plotted in figure 2.6c. As the external magnetic field in the experiment is varied, the equilibrium position of the magnetisation is changed according to the free energy density. To extract the anisotropy fields out of the angular dependence of the resonance position, equation 2.45 solved for H , one must find the equilibrium positions of the magnetisation for each measurement point. These can be determined by the condition:

$$\frac{\partial F}{\partial \theta} \stackrel{!}{=} 0 \quad \frac{\partial F}{\partial \phi} \stackrel{!}{=} 0 \quad (2.47)$$

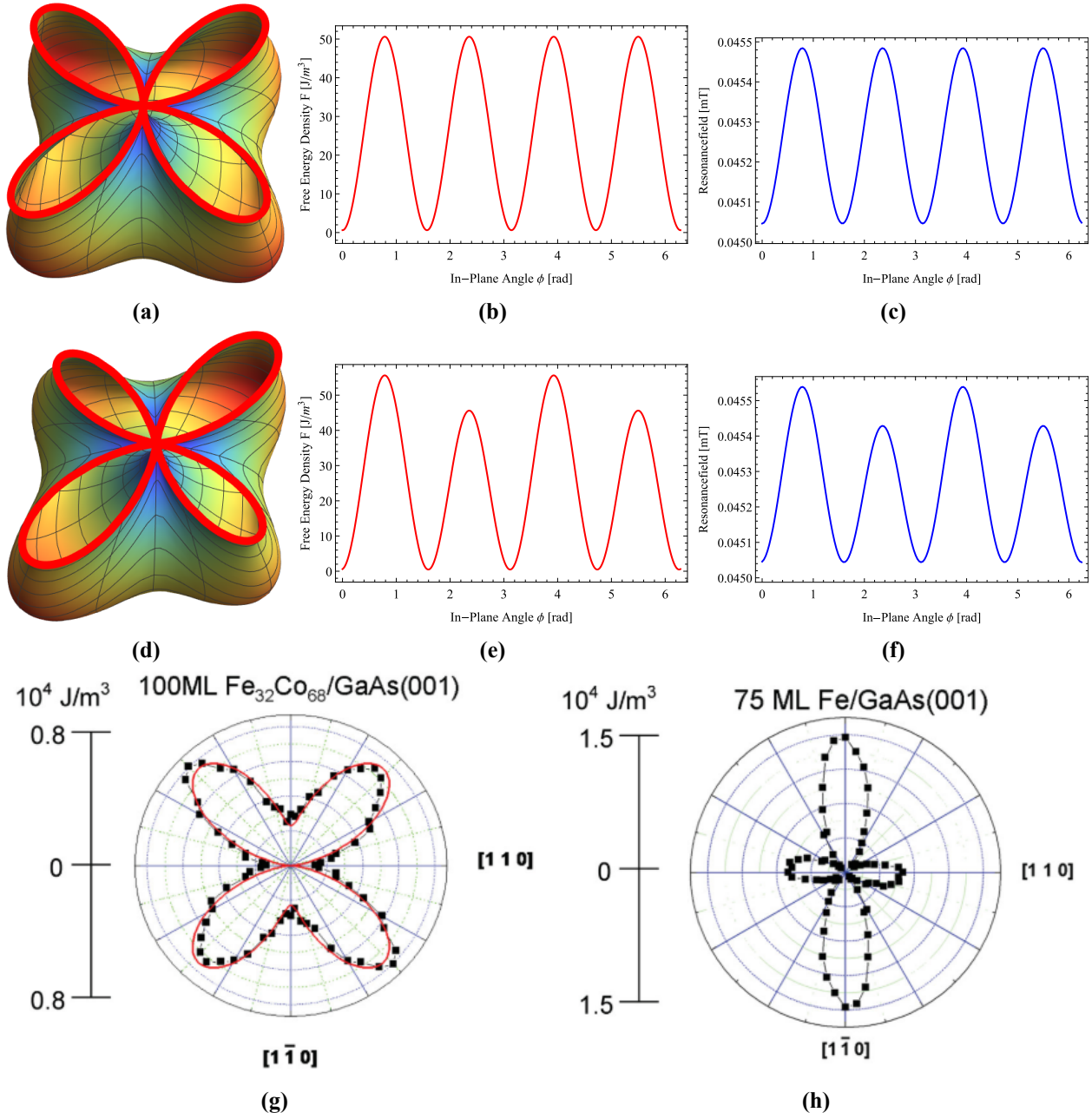


Fig. 2.6.: These figures show the free energy landscape cut **a)** and **d)**, like an in-plane, $\theta = \pi/2$, FMR measurement would produce. The values projected in 2D are presented in **b)** and **e)**. From these values the resonance field using the SBS resonance condition Eq. 2.45 seen in **c)** and **f)** can be determined. For figures a) to c), a pure cubic crystal was assumed. In figures d) to f) the cubic crystal was overlaid by an additional in-plane uniaxial anisotropy with easy axis at $\frac{3}{4}\pi$. Pictures g) and h) show a cubic anisotropy of Fe superimposed by a uniaxial anisotropy due to the growth on GaAs with ZnS structure. The magnitude of the superimposed uniaxial anisotropy becomes smaller, as Fe thickness increases. This is due to a increasing volume anisotropy, compensating the ZnS structure effect. This can be seen for a cubic anisotropy of Fe overlaid by measurement points in a polar plot in figure g). This figure reflects the situation in figures a) - c). For sufficiently thin Fe films on GaAs a additional uniaxial anisotropy is present, as seen in figure h). This figure reflects the situation of figures d) - f). Taken from Bayreuther [33].

A minimum position is found, if the Hessian matrix is positive definite. This means every eigenvalue must be positive and the following condition applies:

$$\partial_{\theta\theta}F\partial_{\phi\phi}F - \partial_{\theta\phi}F\partial_{\phi\theta}F > 0, \quad \partial_{\theta\theta}F > 0 \quad (2.48)$$

The conditions can be numerically solved, by minimising F with regards to θ and ϕ using a minimisation solver, for example the `scipy` minimisation tool kit for Python or the `FindMinimum` solver for Mathematica. In this work, two programs/approaches to fitting the anisotropy parameters and minimising the free energy density were used. The most robust and most precise approach was written by Dr. Benjamin Zingsem in Mathematica. There, a large table of variables are generated according to a variables range and stepsize. This table includes every combination of parameters which then were included into the free energy density and minimised, with regards to θ and ϕ . With the obtained equilibrium angles, the set of anisotropy parameters is then put into the resonance condition equation 2.45 or 2.46. For each change in parameters, especially the external field, the equilibrium position needs to be reevaluated. With one set of anisotropies the angle is changed for a full rotation in certain angle steps. For each angle step a resonance position is found, creating a calculated angular dependence according to the given set of anisotropies, frequency, g-factor and saturation magnetisation. By iterating with a decreasing parameter range and stepsize for the anisotropy parameters, a precise and converging result can be obtained. This algorithm was transferred to Python, to make use of the convenience of one single infrastructure of a fitting graphical user interface, seen in appendix A.4. Additionally a gradient descent algorithm was implemented utilising the maximum likelihood functionality of the Levenberg-Marquardt least linear squares fitting routine. Although a convergence is not guaranteed, the anisotropy parameters obtained using this method lay in close proximity or overlap with those of the Mathematica approach, with the benefit of at least 10 times decrease in computation time.

In the case of a frequency dependent FMR experiment, magnetic field-swept spectra are taken at different frequencies between 0-40 GHz. Additionally the angles ϕ and θ are fixed in one direction. In this work, frequency dependent measurements were done using a coplanar wave guide (CPW) setup and fixing the sample orientation in IP direction, $\theta = \pi/2$, in the hard axis Fe[110] and intermediate axis Fe[1 $\bar{1}$ 0] orientation. By fixing the angles to constant values in the experiment, one cannot obtain a detailed analysis of the anisotropies present. On the other hand, such experiments enable the determination of the gyroscopic splitting factor γ . Since γ includes

$$\gamma = \frac{g\mu_B}{\hbar} \quad (2.49)$$

where μ_B is the Bohr magneton, \hbar is the reduced Planck constant and the Landé g-factor of the ferromagnet can be extracted from the resonance positions frequency dependence. The relationship between frequency and resonance position can be described by the Kittel equation for fixed IP position [15, 34]:

$$f(H_{res}) = \frac{g\mu_0\mu_B}{h} \sqrt{(H_{res} + H_1(\phi))(H_{res} + M_{eff} + H_2(\phi))} \quad (2.50)$$

This equation is the analytical solution of the resonance condition for FMR for the so-called aligned mode. Here the so called dragging effect is neglected and ϕ_H, θ_H are set to $\phi_H = \phi, \theta_H = \theta$. Here $H_{1,2}$ denotes the in-plane anisotropy fields and h is the Planck constant. One has to note, that a precise calculation can also be obtained using the general resonance condition 2.46. In both models the anisotropies will change the curvature and slope of the square root function, directly

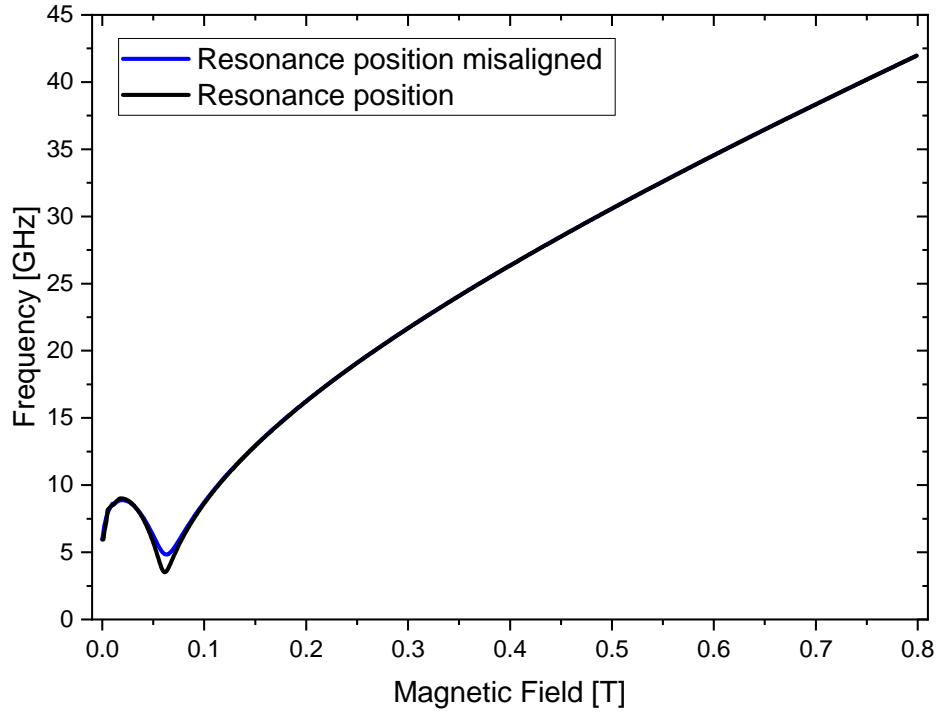


Fig. 2.7.: Calculated resonance positions for a frequency dependent FMR experiment oriented in the hard axis, for a Fe/GaAs(100) film this correlates to the [110] direction. The blue line shows the situation of the resonance positions for a very small misalignment around the hard axis of $\Delta\phi = 1.3^\circ$. Parameters of the film are given in the text.

influencing the fit. By taking the square of both sides, the square root can be cancelled and better fits are achieved.

Additionally, as long as \vec{H}_{ext} stays sufficiently small, the equilibrium position does not have to be parallel to the external field $M \parallel \vec{H}_{ext}$. A non-parallel standing M may exert additional resonance solutions, resulting in the so-called non-aligned modes [26]. These can be calculated following the equation 2.46 for a given system of magnetic parameters and solving for equilibrium positions given by equation 2.47. For the in-plane hard axis orientation $\theta = \pi/2, \phi = \pi/4$ (Fe-[110] direction) of a ferromagnetic thin film with a saturation magnetisation of 1.8 kA/m, $g = 2.11$, and anisotropy constants $K_{2\parallel} = 21000 \text{ J/m}^3$, $K_{2\perp} = 315000 \text{ J/m}^3$, $K_{4\parallel} = 31000 \text{ J/m}^3$, $\phi_U = 3/4\pi$ and $K_{4\perp} = K_{4\parallel}$ one solves the resonance equation for a given set of fields $H \in (0, 0.8) \text{ T}$ resulting in a resonance position shown in figure 2.7. The non-aligned mode is visible as an additional resonance positions ("hook") in low fields of $H \in (0, 0.1) \text{ T}$ and for low frequencies $f \in (2, 10) \text{ GHz}$. Furthermore, figure 2.7 shows a very high sensitivity of the non-aligned mode to a misposition in ϕ . The blue curve shows the resonance dispersion for a small angle shift of $\Delta\phi = 1.3^\circ$. The minimum position of the hook will shift to higher frequencies, as the angle is changed out of the hard axis orientation. Therefore by calculating the non-aligned mode for a given system and comparing it to measurements, the ϕ misalignment can be determined very precisely. The hook of the non-aligned mode is further shown in more detail in figure 2.8 for a sample consisting of GaAs(100) / 4 nm Fe / 0.76 nm Rh. This figure shows frequency dependent measurement at room temperature, in which the intensity was represented by colour accordingly to a scale on the right. The two horizontal lines of different colour represent measurements at constant frequency. At 13GHz, only one resonance position can be found. By setting the frequency constant and varying the ϕ angle, a in-plane angular dependence is obtained. The angular dependence at 13GHz is marked by the yellow star.

This in-plane angular dependence is the measurement of the same sample as seen in the detailed non-aligned mode figure. Because the 13GHz measurement is out of the non-aligned mode regime, a simple four-fold overlaid by a two-fold behaviour is seen. Which is to be expected in Fe films of thicknesses of around 4 nm on GaAs(100), as can be seen in figure 2.6h. By fixing the frequency to about 9.4 GHz, as represented by the green line, three resonance positions are obtained. One at very low fields around 5 mT, the second at about 50 mT and the resonance of the aligned mode at 120 mT. With fixed green position, the ϕ angular dependence is shown in figure 2.8b. Both 13 GHz and 9.4 GHz measurements show a four-fold cubic anisotropy. The most pronounced difference between 13 GHz and 9.4 GHz dependence is the appearance of resonance loops in the hard axes ($[1\bar{1}0]$, $[11\bar{0}]$) not overlaid by the additional two-fold uniaxial anisotropy. These loops originate from the non-aligned modes, that for specific angles exert multiple resonance. These loops can also be calculated, as shown in figure 2.8c.

Absorption lineshapes

During resonance the value of χ is [16]:

$$\begin{aligned} \chi'_{res} &= \frac{\gamma M_0}{2\omega_H} & \chi''_{res} &= \frac{\gamma M_0}{2\alpha\omega} \\ \chi'_{a,res} &= 0 & \chi''_{a,res} &= \frac{\gamma M_0}{2\alpha\omega_H} \end{aligned} \quad (2.51)$$

To extract the shape of the absorption curve one approximates the linearised solutions of the equation of motion Eq.(2.38) for fields and frequencies in close range around the resonance position Eq.(2.44) [16]:

$$\begin{aligned} \frac{\chi'}{\chi''_{res}} &\approx \frac{\chi'_a}{\chi''_{res}} \approx \frac{(\omega - \omega_H)}{\alpha\omega_H(1 + (\frac{\omega - \omega_H}{\alpha\omega_H})^2)} = \frac{\beta}{1 + \beta^2} \\ \frac{\chi''}{\chi''_{res}} &\approx \frac{\chi''_a}{\chi''_{res}} \approx \frac{1}{1 + (\frac{\omega - \omega_H}{\alpha\omega_H})^2} = \frac{1}{1 + \beta^2} \end{aligned} \quad (2.52)$$

with $\beta = \frac{\omega - \omega_H}{\alpha\omega_H}$. The shape of these formulas is equivalent to the natural Lorentzian absorption curve [35]:

$$f(\omega) = \frac{1}{(\omega^2 - \omega_0^2)^2 + \gamma^2\omega_0^2} \quad (2.53)$$

The linewidth of this absorption is defined as the distance between the points, where the intensity reaches half of its maximum: $\chi'' = \chi''_{res}/2$:

$$\Delta\omega = 2\alpha\omega \quad \mu_0\Delta H = \frac{2\alpha\omega}{\gamma} \quad (2.54)$$

During the FMR experiment one does not measure the absorption directly, but rather its derivative to the externally applied field $d\chi''/dH$. Therefore, additionally the linewidth is given in terms of peak-to-peak linewidth instead of the previous full-width-half-maximum: $\Gamma = \frac{1}{\sqrt{3}}\Delta H_{FWHM}$ [19]. The Lorentzian derivative using the peak-to-peak linewidth is as follows [23]:

$$\frac{dL}{dH} = -\frac{A(2(H_0 - \Gamma))}{\pi H_R^3 \left(\frac{(H_0 - \Gamma)^2}{H_R^2} + 1 \right)^2} \quad (2.55)$$

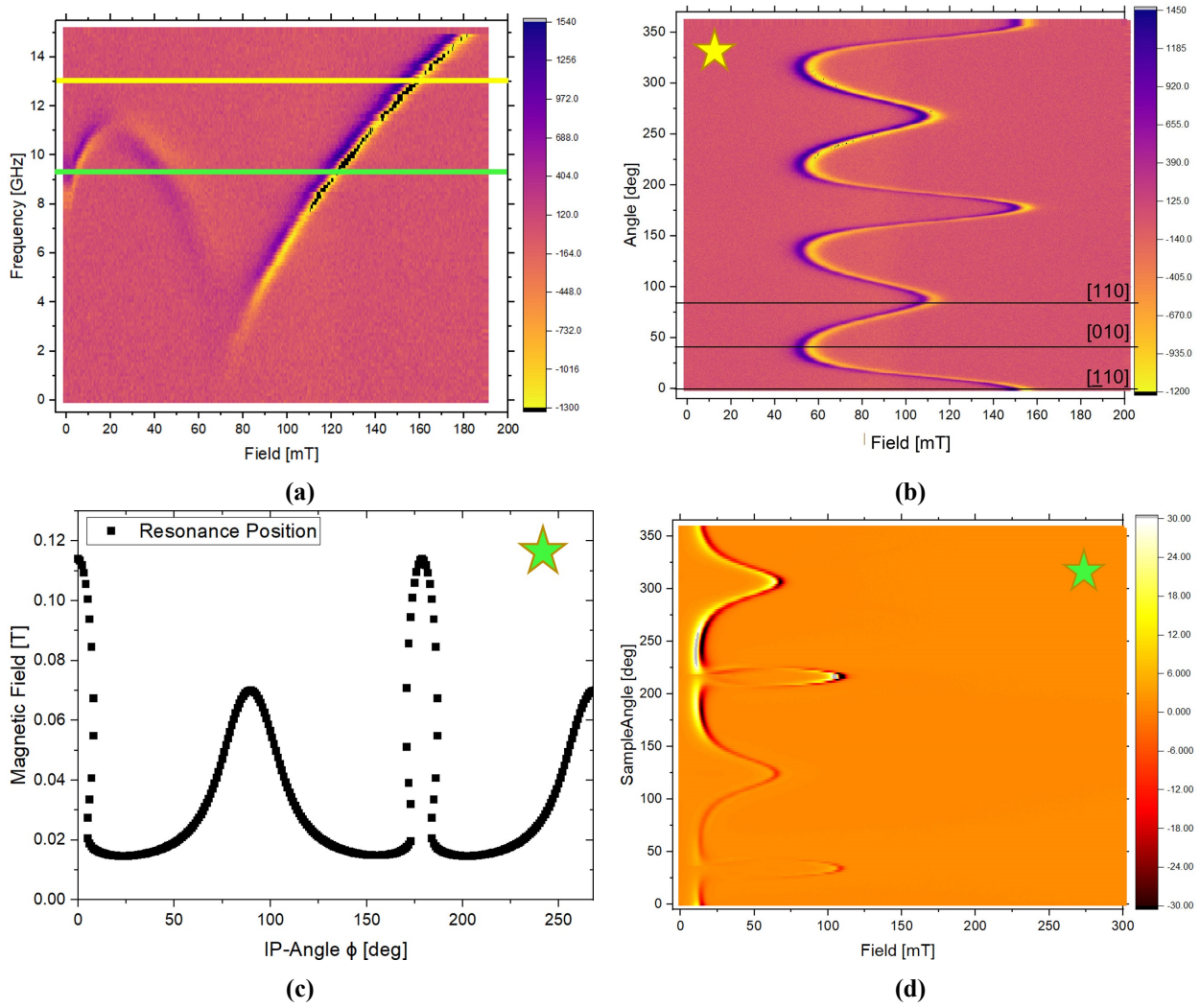


Fig. 2.8.: FMR experiments for sample GaAs(100) / 4 nm Fe / 0.76 nm Rh. Based on a frequency dependence **a)**, the non-aligned modes can be made visible, following the green curve, in 9.4 GHz cavity angular dependence measurements **d)**. Following the yellow at 13 GHz **b)**, the FMR lies out of the non-aligned mode regime, resulting in undisturbed angular dependencies. From anisotropy parameters extracted from the 13 GHz measurement, the resonance loops originating from the non-aligned modes can be calculated **c)**.

Parameter A denotes an amplitude scaling factor, H_R is the resonance position and Γ is the peak to peak linewidth.

Microwave absorption in a conducting ferromagnet was studied by Flovik et al. [36]. During absorption, additional eddy currents are generated inside the magnet due to the possible high conductivity. These also induce time-dependent alternating current, the intensity of which is determined by the material conductivity and thickness. The Lorentz absorption curve natural lineshape is distorted by the extra AC field. In comparison to the Lorentz curve, it produces an asymmetric signal with an offset resonance position and linewidth. To be considered for an application, the material must be thinner than 50 nm. In contrast to the derivation of the standard Lorentzian lineshape, Flovik et al. use an extended form of microwave excitation:

$$\begin{aligned} h_{ac}(t) &= \vec{h}_{MW} \exp\{i\omega t\} + \vec{h}_{ind} \exp\{i(\omega t - \phi)\} \\ &= \vec{h} \exp\{i\omega t\} [1 - \beta_i] \end{aligned} \quad (2.56)$$

Here \vec{h} denotes the sum of the amplitudes of all exciting fields $\vec{h} = \vec{h}_{MW} + \vec{h}_{ind} \cos \beta$. The parameter β with its x- and y- contributions $\beta_i = (\beta_x, \beta_y)$ is called the asymmetry parameter, which indicates the relative magnitude ratio of both fields and their phases to each other in the x/y direction. It is defined as: $\beta = \vec{h}_{in} \sin \phi / (\vec{h}_{MW} + \vec{h}_{ind} \cos \phi)$. This parameter is often called α as well. This is attributable to a similar study of the microwave absorption by conduction electrons in a diffusive model by Dyson in 1955 [37]. A so-called Dysonian lineshape describes the asymmetric absorption regarding an asymmetry parameter α [38]. When the induced field equals zero, β equals zero, and the asymmetric contribution vanishes. The same happens when the phase difference approaches 0. The magnetisation is set along the Z-axis in the same way as for the Lorentz derivation, but with the addition of a time-dependent variable:

$$\vec{M}(t) = M_0 \vec{e}_z + \vec{m} \exp\{i\omega t\} \quad (2.57)$$

Now the high frequency susceptibility for small excitations is determined by $\vec{m} = \underline{\chi} \cdot \vec{h}$. Together with $\omega_0 = \mu_0 \gamma H$ and $\omega_M = \gamma M_0$ one finds:

$$\underline{\chi} = \begin{vmatrix} \chi & i\chi_a \\ -i\chi_a & \chi \end{vmatrix} \quad (2.58)$$

And the elements:

$$\chi = \frac{(1 - i\beta_i)\omega_M(\omega_0 + i\alpha\omega)}{\omega_0^2 - \omega^2(1 + \alpha^2) + 2i\alpha\omega\omega_0} \quad \chi_a = \frac{(1 - i\beta_i)\omega_M\omega}{\omega_0^2 - \omega^2(1 + \alpha^2) + 2i\alpha\omega\omega_0} \quad (2.59)$$

Now consider the microwave absorption P in a volume V :

$$P_{abs} = \frac{1}{2} \text{Re} \left\{ \int_V i\omega (\underline{\chi} \cdot \vec{h}) \cdot \vec{h}^* dV \right\} \quad (2.60)$$

The comparison of the above values with those of the pure Lorentz curve reveals the unique feature of this derivation. Another Lorentz curve is added by the additional AC field created by eddy currents. Due to out-of-phase fields, the expression consists of a symmetrical Lorentz absorption and an asymmetrical dispersive part proportional to β . The final expression for the lineshape given

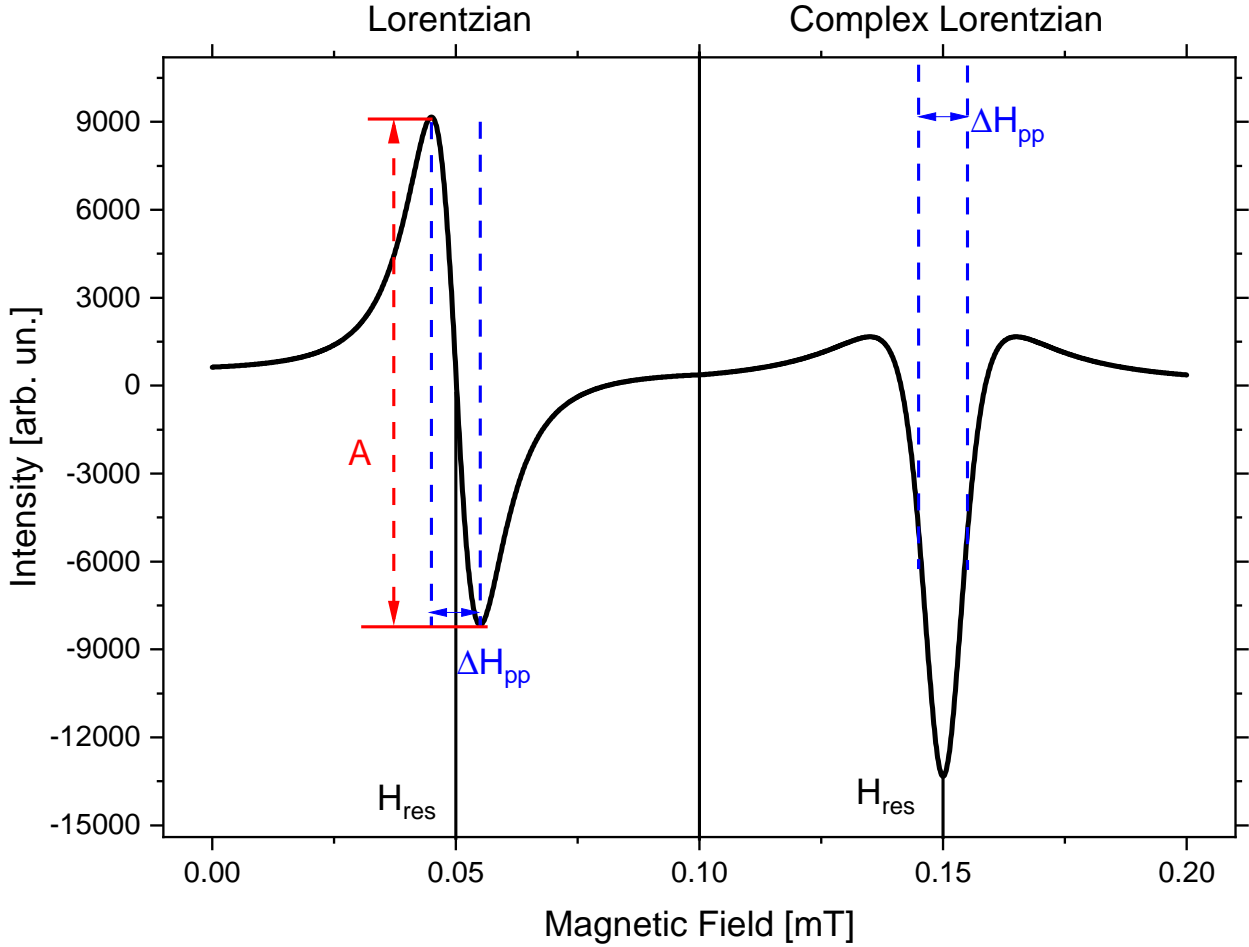


Fig. 2.9.: Lorentzian lineshape in comparison to a Flovik/Complex-Lorentz lineshape. For the Flovik line, a high asymmetry was chosen (Complex Lorentz of $\phi = 3\pi/2$), to enhance the difference to the Lorentzian shape. The parameters chosen to plot these functions were: $A = 1$, $\Delta H_{pp} = 0.01$ mT, $H_{res} = H_R \in \{0.05, 0.15\}$

by Flovik et al. is:

$$\text{Im}\{\chi\} = A \frac{1 + \beta_i(H_R - H_0)/\Gamma_H}{(H_R - H_0)^2 + (\Gamma_H/2)^2} \quad (2.61)$$

Parameter A is the amplitude factor, H_R is the resonance field, H_0 denotes the external field and Γ_H is the full width half maximum (FWHM) linewidth, that is converted to a peak-to-peak linewidth γ according to the same relation as for the Lorentzian linewidth. As for the Lorentzian shape, in equation 2.55, the Flovik shape needs to be expressed as the first derivative regarding the external field, to match the FMR experiments in which a lock-in amplifier measures the first derivative of the imaginary high frequency susceptibility:

$$\frac{d}{dH_0} \text{Im}\{\chi\} = A \left[\frac{-\beta/\Gamma}{(H_R - H_0)^2 + (\Gamma/2)^2} + \frac{2(H_R - H_0)[1 + \beta(H_R - H_0)/\Gamma]}{[(H_R - H_0)^2 + (\Gamma/2)^2]^2} \right] \quad (2.62)$$

Figure 2.9 shows the difference between Flovik and Lorentzian lineshape. It should be noted that the Flovik line for $\alpha = 0$ represents a Lorentz line, since the asymmetric component vanishes.

Additionally for CPW measurements, explained in chapter 3.3.4, in difference to the conven-

tional FMR setup, where the lineshapes express absorption or dispersion, in the CPW measurements the resonance response is measured. To obtain a resonance position the effective impedance of the sample needs to be considered [23]. This has been done by linking the scattering parameter $S_{i,j}$ of, for example a VNA setup, to the impedance of the system from which the magnetic susceptibility can be derived. For the case of a quasi static transmission measurement, without any reflection, the connection between susceptibility and scattering parameter is found to be $\chi(H) \approx -2\chi_0 S_{1,2}$ [39]. Parameter χ_0 is a substitute for all parameters needed to express χ in the conventional case. In order to derive a universal function, Körner motivated the CPW lineshape to be compatible with both absorption and dispersion effects [23]. He uses a phenomenological complex Lorentz Ansatz:

$$L = \frac{A_{compl}}{\Delta R + i(H - H_R)} \quad (2.63)$$

Using a linewidth ΔR , that translate to that of a Lorentzian linewidth as: $\Delta R = \frac{\sqrt{3}}{2}\Gamma$. By multiplying the Ansatz with a phase parameter ϕ one obtains the final complex Lorentzian:

$$\begin{aligned} \frac{dL_{complex}}{dH} = A_{complex} & \frac{\sin(\phi)(0.75\Gamma^2 + (H - H_R)^2) - 2(\sqrt{3}/2\Gamma \cos(\phi))}{(0.75\Gamma^2 + (H_0 - H_R)^2)^2} \\ & + \frac{(H_0 - H_R) \sin(\phi)(H_0 - H_R)}{(0.75\Gamma^2 + (H_0 - H_R)^2)^2} \end{aligned} \quad (2.64)$$

Due to the most general assumption of a simple phase factor ϕ in the derivation, this lineshape can be used for a broad range of cases, in which a asymmetric lineshape needs to be fitted. In principle every deviation from a perfect symmetric Lorentzian is achievable using this complex Lorentzian. Although the physical origin of the asymmetry needs to be critically discussed.

In the further course, the peak-to-peak linewidth Γ is referred to as ΔH or ΔH_{pp} .

Magnetisation damping

The linewidth of a FMR absorption is defined by the relaxations process of the precession into equilibrium position, its behaviour over changing frequency, and therefore different precession cones, gives rise to the magnetic precession damping parameter α . The peak-to-peak linewidth correlation to the damping is explained as follows [29]:

$$\Delta H_{pp}^{Gilbert} = \frac{1}{\sqrt{3}} \frac{\alpha}{|\partial\omega/\partial H|} \frac{\gamma}{M_S} \left(\frac{\partial^2 F}{\partial \theta^2} + \frac{1}{\sin^2 \theta} \frac{\partial^2 F}{\partial \phi^2} \right) \quad (2.65)$$

By orienting a frequency dependent measurement in a crystallographic orientation, such as the hard axis, the dragging effect will be minimised, and equation 2.65 can be simplified to:

$$\mu_0 \Delta H = \frac{4\pi\alpha_{eff}}{\gamma} f + \mu_0 \Delta H_0 \quad (2.66)$$

This formula consists of ΔH_0 , the inhomogeneous linewidth broadening and the total damping parameter α_{eff} , which consists of several contributions. A disentanglement would consider every contribution to the linewidth [40]:

$$\Delta H = \Delta H_{TMS} + \Delta H_{Mosaicity} + \Delta H_{Gilbert-dragging} + \Delta H_{Spin-Pumping} \quad (2.67)$$

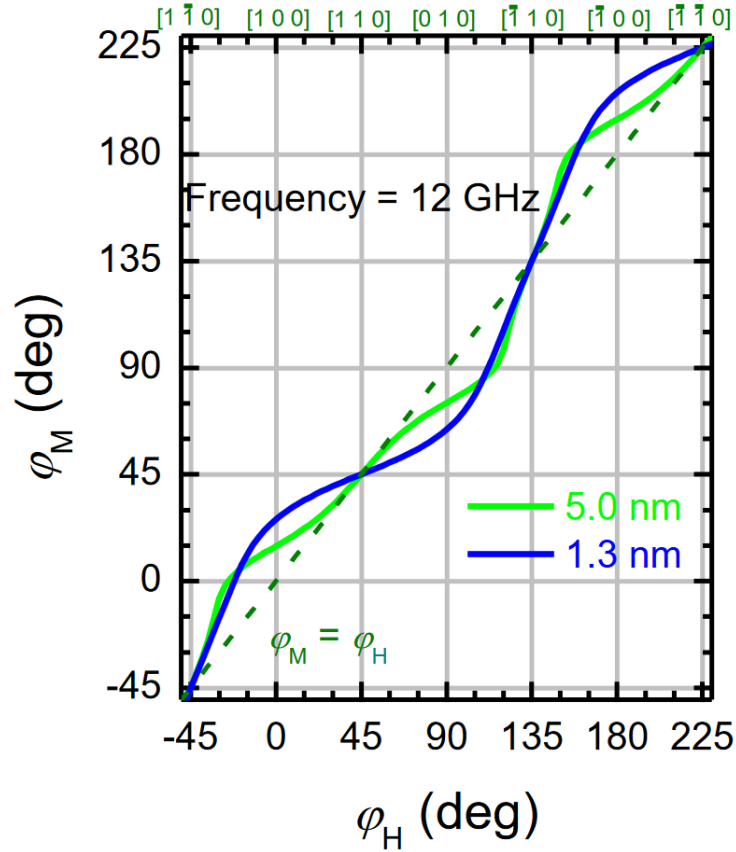


Fig. 2.10.: The dragging effect of ultrathin Fe films on GaAs(100). Figure has been taken from supplementary materials of [41]. The solid light green line shows the dragging effect of a 5 nm Fe film. The green dashed line displays the situation without dragging. At hard axes points ($[110]$, $[1\bar{1}0]$, $[\bar{1}10]$), the green, blue and the dashed green line are crossing, marking the points where the dragging effect vanishes in the experiment.

The term TMS stands for Two-Magnon-Scattering and represents the scattering of magnons from the uniform $K=0$ mode into a mode of unequal wavevector $K \neq 0$ but equal energy at defect points in the crystal. The term of mosaicity includes effects, that change the magnetic properties, such that multiple different resonance conditions can be achieved, constantly increasing the linewidth. Since these effects can appear unbounded to any symmetry they contribute to the inhomogeneous broadening factor ΔH_0 . For magnetic films with non-vanishing magnetocrystalline anisotropy, like in the case of Fe, and sufficiently small external magnetic fields, the magnetisation will not always align with the externally applied field. This results in a elliptical distortion of the precession cone, artificially broadening the linewidth in orientations in between the easy or hard axes. This effect is called the dragging effect. High magnetic fields will align the magnetisation to be parallel again, this would be the case for the hard axis. It can be analytically accounted to by minimising the free energy density, like explained above, resulting in angles θ for OOP and ϕ for IP of the magnetisation M , that deviate from the angles θ_H and ϕ_H from the external magnetic field H . The influence of the dragging effect on a experiment can be evaluated by the relation [40, 41]:

$$|\phi_H - \phi_M|$$

If $|\phi_H - \phi_M| = 0$, the magnetisation M always points in the same direction as the external field

H. For dragging enabled, one finds $|\phi_H - \phi_M| \neq 0$, the dragging effect of 5 nm Fe thin films on GaAs(100) was determined by Chen [41]. In figure 2.10, the dragging effect is shown for the case of an ultrathin film of Fe thickness 1.3 nm and 5 nm Fe. Additionally as a reference they added the case of no dragging effect, visible as the darker green dashed line. However the dragging effect will be reduced, when the sample is oriented in distinct crystallographic orientations, like hard axis, intermediate axis or easy axis. Because of this, for each frequency dependence an angular dependence was done, to identify the hard and intermediate axes with a resolution of 0.5° .

The precession damping has a maximum contribution, partly due to the dragging effect, while the magnetisation is not pointing in distinct crystallographic orientations as well. In case of the easy axis, the precession has a higher damping, than compared to the harder axes, because the magnetisation has to be moved out of the energetic minimum to energetically higher orientations. Since the magnetisation strives to reach the position of minimal energy, phenomenologically speaking, an additional damping will occur. For the case of the hard axis, the magnetisation is already oriented in a maximum of the free energy density. With the same argumentation as before, the magnetisation precession is less damped, as it is energetically more favourable for it to be in the precessing state around the hard axis.

The non-local Gilbert damping originating from spin pumping changes its magnitude over the thickness of the added non-ferromagnetic metal layer. Therefore by assuming $\Delta H_{TMS} + \Delta H_{Mosaicity} + \Delta H_{Gilbert-dragging}$ to be constant over all samples, changes to α_{eff} can be analysed according to the spin pumping theory discussed in chapter 2.2. This assumption is valid under consideration, that every sample consists of the same 5 nm Fe layer. In total, the damping contribution will change over the sample number, due to effects of GaAs(100) interface quality and evaporation rate. It is assumed, that these changes are minor and will be included in the error of the final α_{eff} .

A multifrequency measurement improves the damping determination, as higher frequencies lower the precession opening, reducing the magnetisation deflection out of the equilibrium position. Therefore any anisotropic contribution in deflection along the precession path gains less influence. Even additions of higher order anisotropies not accounted for in the free energy model are reduced. In this thesis frequency-dependent FMR experiments were done for microwave frequencies ranging from 0 to 40 GHz, which is sufficient enough, to bring the equation 2.50 into the linear square root regime, for the anisotropies in the present Fe system. Since the resonance positions frequency dependence is linearly proportional to the g-factor, the linear square root regime will increase the sensitivity of the g-factor determination.

2.2. Spin pumping in ferromagnetic resonance

All magnetic moments in a ferromagnet (FM) are coupled to one another, so a deflection of one moment causes deflection of all moments. If a ferromagnet is in precession, all moments precess approximately equally. Non-ferromagnetic metals (often referred to as "normal" metals or NM), on the other hand, have no parallelising coupling between their magnetic moments and thus can deflect in any direction. In contrast to ferromagnets, spin information in the form of spin waves is not transported throughout the body, but is lost due to intrinsic scattering processes based on electrical conductivity and spin-orbit coupling. The spin diffusion length λ_{sd} is the characteristic length, or range, of the propagation of spin information in normal metal. This length is in the range of a few nanometres for normal metals with high spin-orbit coupling, such as Pt ($\lambda_{sd} \approx 1$ nm), but can easily reach several hundred nanometres for copper or silver [42]. Tserkovnyak et al. 2002 [43, 44] were the first to model spin pumping as a phenomenon of spin scattering at the interface between

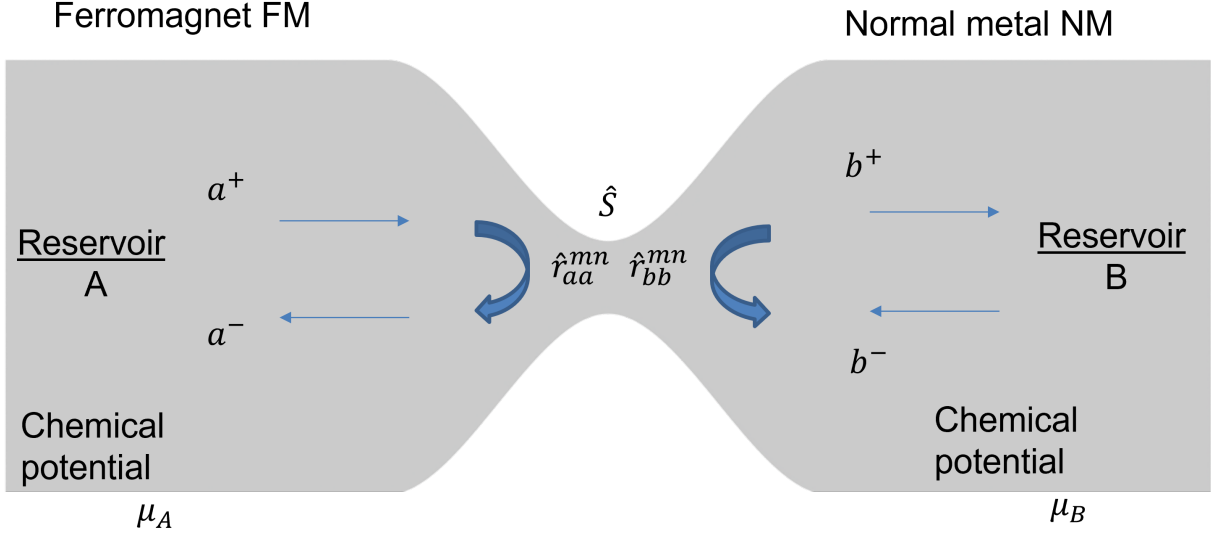


Fig. 2.11.: A quantum channel that connects two spin reservoirs A and B, which represent a ferromagnet and a regular metal, respectively.

the FM and the NM. This model is based on the Landauer-Büttiker formalism of parametric electron pumping, which considers spin scattering in quantum channels rather than electron scattering at the interface, as shown in Fig. 2.11. The following derivation is based on this theory and can be found in [14, 43, 44, 45, 46] for greater detail.

The reflection coefficients $\hat{r}_{aa,bb}$ represent the scattering of spin waves a , b of the respective reservoirs A, B at the contact point. a^+ represents an outgoing wave starting from reservoir A, that hits the boundary layer and is reflected, but also transmitted, according to \hat{r}_{aa} . In reservoir B, this transmitted part is denoted by the symbol b^+ . The same consideration applies to spin accumulation at the interface in reservoir B, where b^- is the outgoing wave whose transmitted part, $\hat{t}_{ba,ab} = 1 - \hat{r}_{bb,aa}$, adds up with the reflected part of a^+ to form the scattered wave a^- . The sum of all reflection and transmission coefficients at an interface m,n yields a $2N \times 2N$ scattering matrix \hat{S} , where N denotes the number of quantum scattering channels.

$$\hat{S} = \begin{pmatrix} \hat{r}_{aa} & \hat{t}_{ab} \\ \hat{t}_{ba} & \hat{r}_{bb} \end{pmatrix} \quad (2.68)$$

Now consider the chemical potentials of both $\mu_{A,B}$ reservoirs. In the parametric electron pumping, there are no electrons flowing across the interface, when $\mu_A = \mu_B$ is in equilibrium. Translated to the spin pumping, this means, that no spin information is pumped from the ferromagnet into the non-ferromagnetic metal. This equilibrium is disrupted in the Landauer-Büttiker formalism by applying an external voltage δV . Following that, the chemical potentials change in proportion to the applied voltage:

$$E = qV = e\delta V = \mu_A - \mu_B \quad (2.69)$$

In the Landauer-Büttiker formalism, charge carriers are then exchanged until the so-called quasi Fermi energies μ_a and μ_b form inside the channels. However, because these are unequal for each reservoir, due to different Fermi levels of each of the metals in the bilayer system, one obtains a potential difference $\delta\mu_{ab} = \mu_a - \mu_b \neq 0$, which, depending on the scattering matrix and transmission,

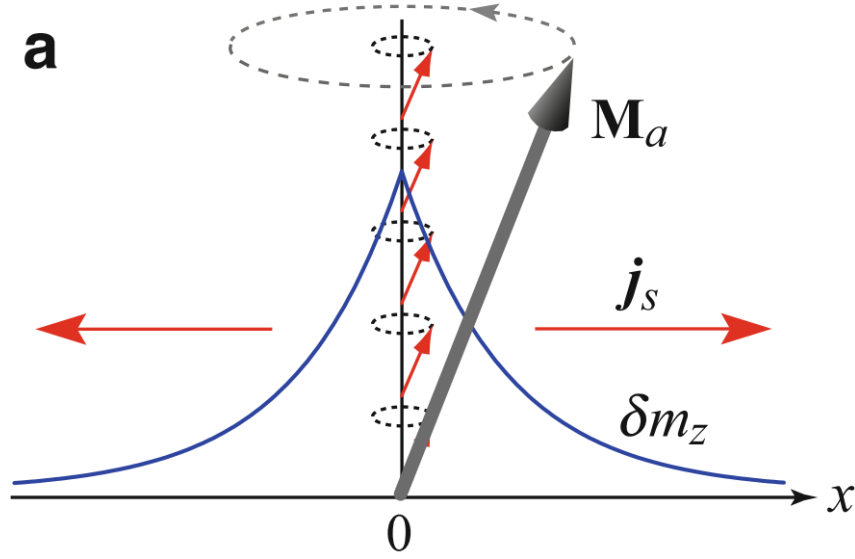


Fig. 2.12.: Schematics of spin accumulation due to the precession of the magnetisation, taken from literature [47]. The magnetisation $\vec{M}_a(t)$, at a fixed time, is found to point at a specific value on the x-axis. The spin accumulation can now be described as the difference of spin polarised chemical potential $\delta\mu_s$ due to an inhomogeneous distribution of the value of the magnetisation between the present direction and its opposite site at a fixed time. In this figure the opposite site is modelled as $x < 0$. The model described by Takahashi, the blue line represents the spin accumulation δm_z for a precessing magnetisation of unfixed time. The resulting spin current is named \vec{j}_s .

leads to a current δI :

$$\begin{aligned} \delta I = G\delta V &= \frac{2e}{h} \delta\mu_{ab} \sum_{n \in a} \sum_{m \in b} |S_{nm}|^2 \\ &= \frac{2e}{h} \delta\mu_{ab} \sum_{n \in a} \sum_{m \in b} |t_{nm}|^2 \end{aligned} \quad (2.70)$$

The conductivity is represented by G , the channels are represented by n and m , and the elementary charge is represented by e . The spin polarisation $\hat{\sigma}$ is used to parameterise the scattering states of the scattering matrix in order to apply this formalism to spins. The resultant current I_s is expressed in a spin state σ, σ' determined by the spin polarisation.

$$I_s = \frac{e}{h} \delta\mu_{s,ab} \sum_{n \in a} \sum_{m \in b} |t_{n\sigma m\sigma'}|^2 \quad (2.71)$$

The scattering from channel m in state σ' to channel n in spin state σ is now described by the transmission probability $t_{n\sigma m\sigma'}$. This current flows only if a potential difference $\delta\mu_{s,ab} = \mu_{s,a} - \mu_{s,b} \neq 0$ prevails, similar to the previous consideration. The potentials $\mu_{s,ab}$ now also take into account the reservoir's spin state.

Without an externally applied voltage at a temporally constant magnetisation, no polarised charge current flows through the boundary layer in a bilayer system consisting of a ferromagnet and a normal metal. A flow of pure spin angular momentum, modelled as spin current, can be generated if the magnetisation now begins to precess uniformly due to, for example, a ferromagnetic resonance precession. The distribution of spin information and the resulting spin accumulation is based on this effect. Due to the exchange interaction, ideally all magnetic moments of the FM precess parallel to

each other in uniform resonance mode. The spins of the FM point periodically towards and away from the NM if we consider the time dependence of the magnetisation at a fixed location, such as the interface to the NM, see figure 2.12. A spin accumulation at the interface is the result of this local temporal change in magnetisation. The chemical potentials change periodically with the same frequency but different phases. The phase difference results in a potential difference $\delta\mu_{s,ab}(t) \neq 0$; $\overline{\delta\mu_{s,ab}} = 0$, allowing a pure spin current to flow through the interface and accumulating at the interface region in the NM. The spin accumulation μ_s is therefore given by the potential difference of FM to NM and, because of spin flip scattering, is also dependent on the distance x to the interface:

$$\mu_s(x) = \frac{\cosh \kappa(x - L)}{\sinh \kappa L} \frac{2\vec{I}_s}{\hbar N S D \kappa} \quad (2.72)$$

In this equation, ω is the precession frequency, L describes the thickness of the NM layer, N is the density of states for one spin orientation only, S is the interface area, D is a diffusion constant to describe the propagation of spin angular momentum into the NM and κ is the spin flow wave vector $\kappa = \frac{1}{\lambda_{sd}} \sqrt{1 + i\omega\tau_{sf}}$ dependent on the spin diffusion length λ_{sd} and the spin flip rate τ_{sf} . For the case of a uniform precession of the magnetisation parallel to the interface, Tserkonvyak et al. discovered the following pumped spin current:

$$I_s^{Pump} \hat{\sigma} = \frac{\hbar}{4\pi} \left(A_r \hat{m} \times \frac{d\hat{m}}{dt} - A_i \frac{d\hat{m}}{dt} \right) \quad (2.73)$$

where $\hat{m} = \frac{\vec{M}}{M_s}$ is the magnetisation direction's unit vector, and $\hat{\sigma}$ is the polarisation of the pumped spin current. The spin angular momentum \vec{s} is oriented in the opposite direction as $\hat{\sigma}$. A perfect spin bath was assumed when Eq. 2.73 was derived. This means that the entire spin current pumped into the NM is absorbed immediately, and that the entire flux of pumped spins always flows perpendicular to the interface minimising a possible spin accumulation. In reality, pumped spins in an NM relax by spin-flip processes. The spin-preserving range, or spin-diffusion length λ_{sd} , in the NM reflects the intensity of these processes' influence. A finite spin angular momentum is created in the event of sufficiently large λ_{sd} , i.e., spin information accumulates in the NM at the interface to the FM. Due to energy conservation, the pumped spin current would be pumped back into the FM if spin relaxation mechanisms were not present. As a result of the established equilibrium of pumped I_s^{Pump} and back-pumped current I_s^{Back} , the total spin current I_s^{tot} would extinguish: $I_s^{tot} = I_s^{Pump} - I_s^{Back} = 0$. As a result, spin-flip relaxation at the interface and in the NM are critical features in spin pumping, to reduce the magnitude of the back pumped current. Backscattering is a type of scattering whose strength is defined by the ratio $\epsilon = \frac{\tau_{el}}{\tau_{sf}}$, the rate of elastic spin scattering τ_{el} , and the spin-flip scattering τ_{sf} . The spin current in the NM relaxes more efficiently as ϵ increases, thus the backflow to the FM is decreased.

Using the relation $D = v_F^2 \sqrt{\frac{\tau_{el}\tau_{sf}}{3}}$ we find the spin diffusion length expressed by the Fermi velocity v_F with Eq.2.72 to be:

$$\lambda_{sd} = v_F \sqrt{\frac{\tau_{el}}{3} \tau_{sf}} \quad (2.74)$$

Now the strength of the backflow current I_s^{Back} pumped by the spin accumulation can be described

by a backflow parameter β :

$$\beta = \frac{\tau_{sf} \delta_{SD} / \hbar}{\tanh L / \lambda_{sd}} \quad (2.75)$$

The absolute pumped spin current I_s^{tot} can be put into the form of Eq. 2.73 in that the spin pumping conductance A now also takes into account β . One defines $\tilde{A} \equiv A(\beta) \equiv \tilde{A}_r + \tilde{A}_i$:

$$I_s^{Pump} \hat{\sigma} = \frac{\hbar}{4\pi} \left(\tilde{A}_r \underbrace{\hat{m} \times \frac{d\hat{m}}{dt}}_{\text{Parallel to Gilbert damping}} - \tilde{A}_i \underbrace{\frac{d\hat{m}}{dt}}_{\text{Parallel to Precession}} \right) \quad (2.76)$$

The equation 2.76 can then be added to the Landau-Lifshitz-Gilbert equation, using $\hat{M} = \vec{M}/M_s$, as follows:

$$\begin{aligned} \frac{d\vec{M}}{dt} &= -\gamma\mu_0 \vec{M} \times \vec{H}_{eff} + \frac{\alpha}{M_s} \left(\vec{M} \times \frac{d\vec{M}}{dt} \right) + I_s^{Pump} \hat{\sigma} \\ &= -\gamma\mu_0 \vec{M} \times \vec{H}_{eff} + \frac{\alpha}{M_s} \left(\vec{M} \times \frac{d\vec{M}}{dt} \right) \\ &\quad + \frac{\gamma\hbar}{4\pi M_s V_{FM}} \left(-\tilde{A}_i \frac{d\vec{M}}{dt} + \tilde{A}_r \vec{M} \times \frac{d\vec{M}}{dt} \right) \end{aligned} \quad (2.77)$$

By comparing the spatial orientations of the added terms Eq.(2.76), one notices that the term $\propto \tilde{A}_r$ is parallel to the Gilbert damping term, thus changing the damping of the FMR. The other term $\propto \tilde{A}_i$ is parallel to the precession term and has an influence on the measured gyromagnetic ratio and thus on the precession. In the FMR experiment, the fraction \tilde{A}_r leads to an increased damping, therefore to a broadening of the absorption line width, while \tilde{A}_i changes the precession cone and thus the resonance field. The components $\tilde{A}_{r,i}$ can be merged to:

$$\tilde{A} \equiv \tilde{A}_r + i \tilde{A}_i = g^{\uparrow\downarrow} = \text{Re}\{g^{\uparrow\downarrow}\} + i \text{Im}\{g^{\uparrow\downarrow}\} \quad (2.78)$$

The dimensionless parameter $g^{\uparrow\downarrow}$ is the so-called spin mixing conductance, which describes the spin-dependent transport of the spin current through the interface of the bilayer and can be calculated via the transmission and reflection probabilities. In the case that the FM is much thicker than its transverse spin relaxation coherence length, the influence on the precession by $\text{Im}\{g^{\uparrow\downarrow}\}$ is negligible and as an approximation $g^{\uparrow\downarrow} = \text{Re}\{g^{\uparrow\downarrow}\}$ applies. The spin coherence length indicates the range of influence of a precessing spin having a precession phase different from that of the entire body. Thus, if this length is large, this precessing spin has a higher influence on the total precession of the magnetisation, than a smaller length, under constant dimensions of the ferromagnet. The spin current Eq. 2.76 is thus reduced to:

$$I_s^{Pump} \hat{\sigma} = \frac{\hbar}{4\pi} \text{Re}\{g^{\uparrow\downarrow}\} \left(\hat{m} \times \frac{d\hat{m}}{dt} \right) \quad (2.79)$$

The effect that spin pumping has on the FMR can thus be seen, approximately, only through the absorption line broadening as a result of the increased Gilbert damping. Another way to detect spin pumping is through the inverse spin Hall effect. This enables spin information to be converted into

electron transport, which is why a voltage perpendicular to the pumping direction can be measured in the case of a pumped spin current. With the g-factor g of the bilayer system, μ_B the Bohr magneton, M_s the saturation magnetisation, t_{FM} the thickness of the ferromagnet and t_{NM} the thickness of the normal metal, the contribution to the Gilbert damping α by spin pumping is valid under consideration of the backflow as follows [43, 48]:

$$\begin{aligned}\alpha &= \alpha_0 + \alpha_{sp} \\ &= \alpha_0 + \frac{g\mu_B}{4\pi M_s t_{FM}} g^{\uparrow\downarrow} \left(1 - \exp\left\{-2\frac{t_{NM}}{\lambda_{sd}}\right\} \right)\end{aligned}\quad (2.80)$$

For NM thicknesses t_{Rh} smaller than the spin diffusion length, the pumped spins cannot fully dissipate into the NM, resulting in spin current capable of reaching the NM to vacuum interface [49]. This causes some spin current to be reflected and pumped back into the FM, reducing the overall damping. The exponential term in Eq.(2.80), originally proposed as $1/\tanh -2t_{Rh}/\lambda_{sd}$ as it says in Eq.(2.75) by Tserkovnyak [43] and modified to include non-elastic scattering of electrons [48] in Pd bilayers to the appearance of the exponential dependency, accounts for the back pumping of spins.

Another equivalent modelling derives the spin transport into the NM via the exchange coupling of the localised d-electrons of the FM with the conduction band s-electrons of the NM and could be labelled as dynamic RKKY exchange coupling [50]. It turns out that Bergers model is equivalent to the Tserkovnyak model, by renormalising the parameters, one obtains an equivalent contribution to the Gilbert damping Eq. 2.80. Due to the consideration of the conduction band s-electrons, the spin pumping effect now additionally shows a proportionality to the electrical conductivity [47].

3. Experimental Methods

3.1. UHV Chamber

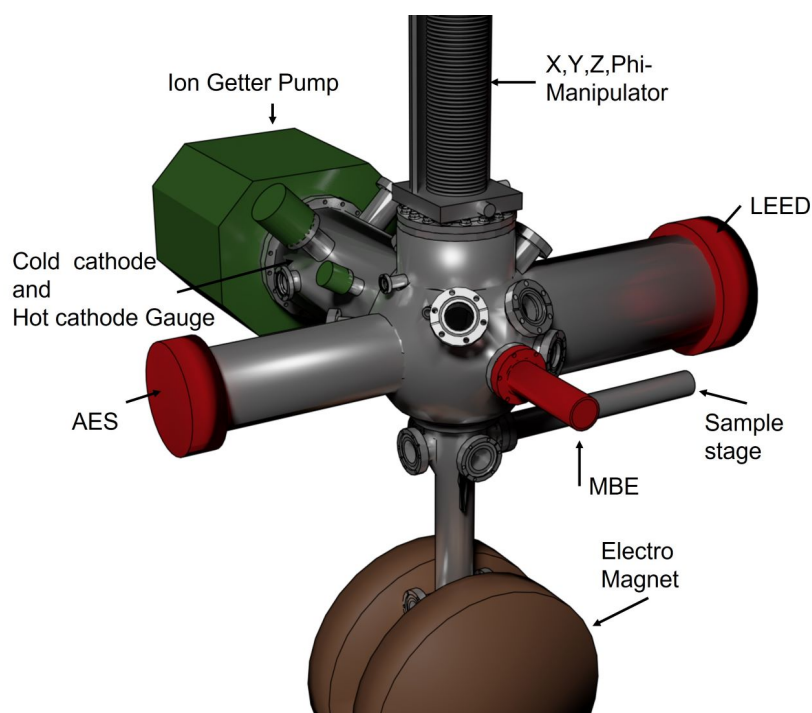


Fig. 3.1.: The simplified 3D model of the ultra high vacuum chamber used in this work.

An ultra high vacuum chamber with a base pressure of $<5\text{E-}11$ mbar ($5\text{E-}9$ Pa) and lower was used to prepare the samples and perform some of the characterisation. This chamber was designed specifically for in-situ ferromagnetic resonance characterisation of magnetic thin films. It is made up of two discrete chambers that can be vented and pumped separately. This allows for easy sample or substrate transfer while maintaining the 10^{-11} mbar main vacuum. A small E-Beam evaporator is included in the main chamber to epitaxially grow materials onto a substrate mounted on a vertical manipulator. Auger electron spectroscopy (AES) and low-energy electron diffraction (LEED) can be used to characterise sample growth. The AES and LEED are positioned in such a way that reflection high energy electron diffraction (RHEED) can be performed with a primary electron beam of 3-5 keV.

3.1.1. Molecular Beam Epitaxy (MBE)

Molecular beam epitaxy is a physical vapour deposition (PVD) technique. The materials, in shape of thin rods $\approx 1\text{-}4$ mm diameter, are heated under ultra high vacuum conditions using electron bombardment to exert a high vapour pressure of their gaseous phase. Diffusion transports the

atoms/molecules across the vacuum to be deposited via condensation on a cooler surface, ideally one with matching crystal lattices. By condensation, the atoms orient themselves on the substrate surface to minimise the surface, interface and volume free energies. Depending on their relative magnitude, different growth modes need to be distinguished. As these energies are subject to change for different adsorption thicknesses, the process of ordering over time can change and several different growth modes can be achieved. Furthermore the surface and interface energies as well as lattice constants are temperature dependent, meaning different growth characteristics can be obtained for different temperatures. The MBE system used during this thesis utilises a mini E-Beam evaporator called "OS-Vap 4P" manufactured by Oxford Scientific. It is a 4 pocket evaporator, that allows the deposition of 4 different materials, but only one pocket may be utilised for evaporation at a time. All samples have been produced using this MBE evaporator for growth on substrates at room temperature.

A first task was to setup rhodium in the evaporator and make it usable as a running system in combination with Fe, as rhodium had never been used in this chamber before. The 4 evaporator's pockets were filled with the following materials: rhodium, iron, silver, platinum. A high voltage of +1.25kV is applied to the evaporation material, that is Fe and Rh of high purity (Rh: 3N, Fe: 5N) metallic rods with a diameter of 3mm for Fe and 2mm for Rh. A high current of 5 - 7 A is applied to a tungsten filament located directly above the metal rods. This will heat up the tungsten filament to the point of thermal emission of electrons, which are accelerated to the metal rod at a positive potential. Emitted electrons heat up the evaporation material to a desired temperature. From a vapour pressure diagram Fig. 3.2, one can identify the optimal temperature for deposition rate. The deposition rate is measured as $\left[\frac{\text{\AA}}{\text{min}} \right]$ and can be monitored a crystal quartz monitor. A quartz crystal oscillate at different frequencies depending on its mass. By depositing a metal on its surface, this frequency changes according to the mass flow of the incoming metal atoms, which is calibrated as the deposition rate. The optimal rate is determined, by increasing the filaments current and measuring the film thickness with the thickness monitor.

A second indirect deposition monitor is the flux electrode. This electrode is placed at the opening of the evaporator and a small bias voltage of -30V is supplied. During the evaporation, some atoms are ionised by the electron beam. The amount of positive ions is assumed to be proportional to the metal vapours pressure. At a constant emission rate, this enables the indirect measurement of the evaporation rate, by simply measuring the current of the flux electrode [51]. This current is of the order of nanoamperes and will be influenced by residual gas atoms sublimating from the evaporator itself, creating a noise background leading to imprecise rate evaluations. A much easier and more reliable way for the determination of rate is the combined measurement of quartz thickness monitor and flux electrode creating a flux calibration, that relates a specific flux value to a specific rate. The reason we want to neglect the quartz thickness monitor, is the invasive part of its presence. During a measurement the quartz needs to be aligned parallel and in close proximity to the sample substrate, to get the most precise rate determination. This positioning, especially in the present chamber arrangement, blocks the possibility of direct AES or RHEED measurements of the evaporated sample. Therefore a sample growth dependence, to identify growth modes would not be possible.

Figure 3.2 shows the phase diagram of iron between 0 and 3500 K and 10^{-10} and 10^5 mbar. The region of interest in MBE is beginning at $1\text{E-}9$ mbar of pressures. In this region Fe is sublimating and hot atoms can diffuse through the vacuum onto a substrate to condensate on. By regulating the evaporant temperature, various deposition rates are achieved. For optimal we used around 0.7 \AA/min .

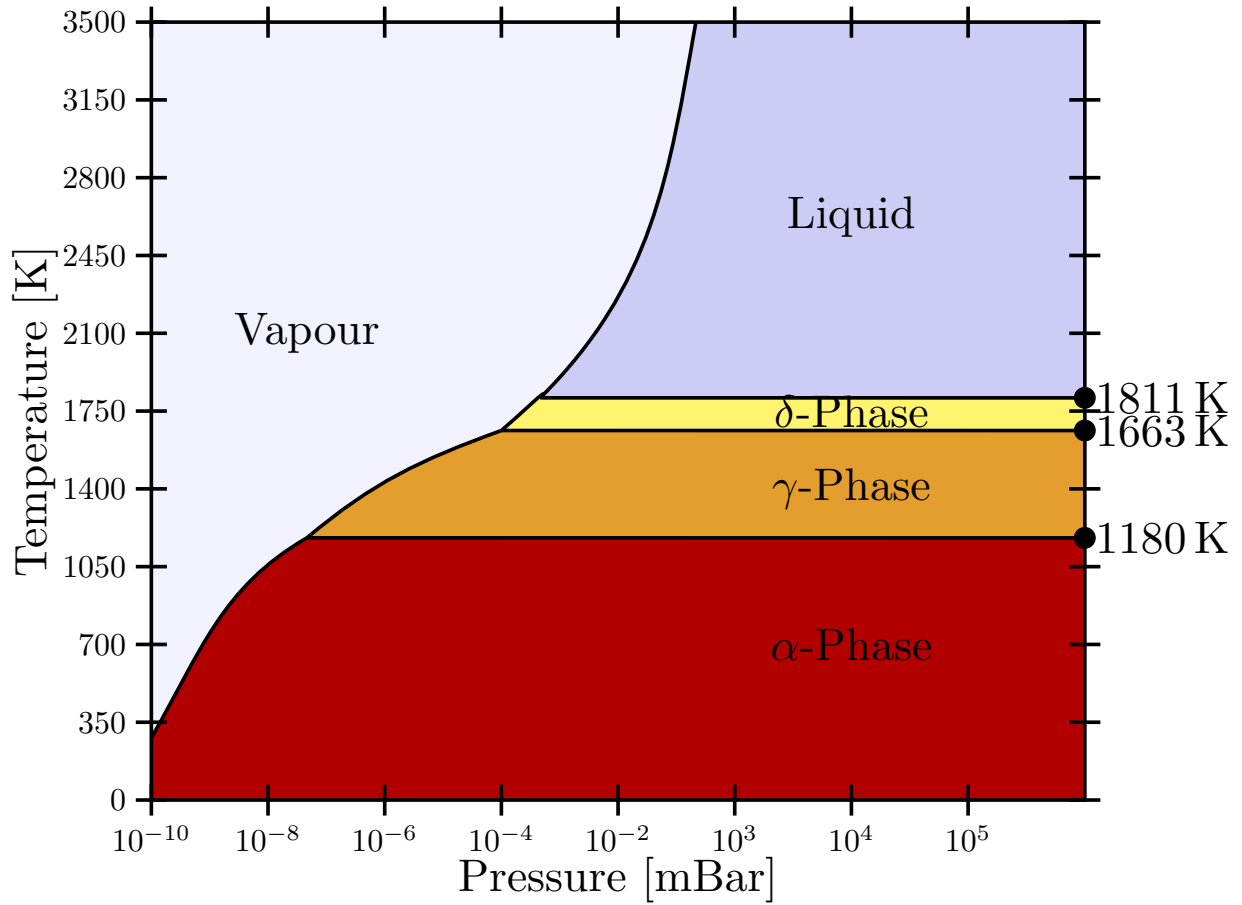


Fig. 3.2.: Approximated phase diagram of pure iron. Different crystallographic phases are present such as bcc- α -Iron, fcc- γ -Iron and bcc- δ -Iron, as well as the states of aggregation, solid, liquid and most importantly the vapour phase. The region of interest in MBE is the range around 800K, producing vapour pressures of about $10^{-10} - 10^{-8}$ mbar. The diagram was recreated with data from [52].

3.1.2. Low energy electron diffraction - LEED

The LEED measurement was used to further determine the surface crystal structure after the sample preparation. Electrons in the range of 1 - 1000 eV were used, that offer a inelastic mean free path of less than 2 nm of surface penetration depth. According to the wave-particle duality, the electrons can also be described as waves with wavelengths according to De broglie as $\lambda = \frac{h}{\sqrt{2mE}}$, whereas λ denotes the wavelength, h is the Planck constant, m is the mass of the electron and E is the applied energy. With incidence perpendicular to the sample surface the elastic scattering at the surface symmetry creates an interference pattern according to the Laue-Law:

$$\vec{G}_{h,k,l} = \Delta\vec{k} = \vec{k}' - \vec{k}_0 \quad (3.1)$$

$\vec{G}_{h,k,l}$ is the reciprocal lattice vector, \vec{k}' is the wave vector of scattered electrons and \vec{k}_0 is the wave vector of the incoming electrons. The Laue-Law describes the points of constructive interference for the case, that the change in wave vector $\Delta\vec{k}$ is exactly a multiple of the reciprocal lattice vector $\vec{G}_{h,k,l}$ of the underlying reciprocal crystal symmetry. This law can be visualised by the Ewald sphere construction. For the case of a surface, the missing periodicity at the vacuum interface can be modelled as a lattice with infinite lattice spacing, this creates so called Laue-Rods/Cylinders,

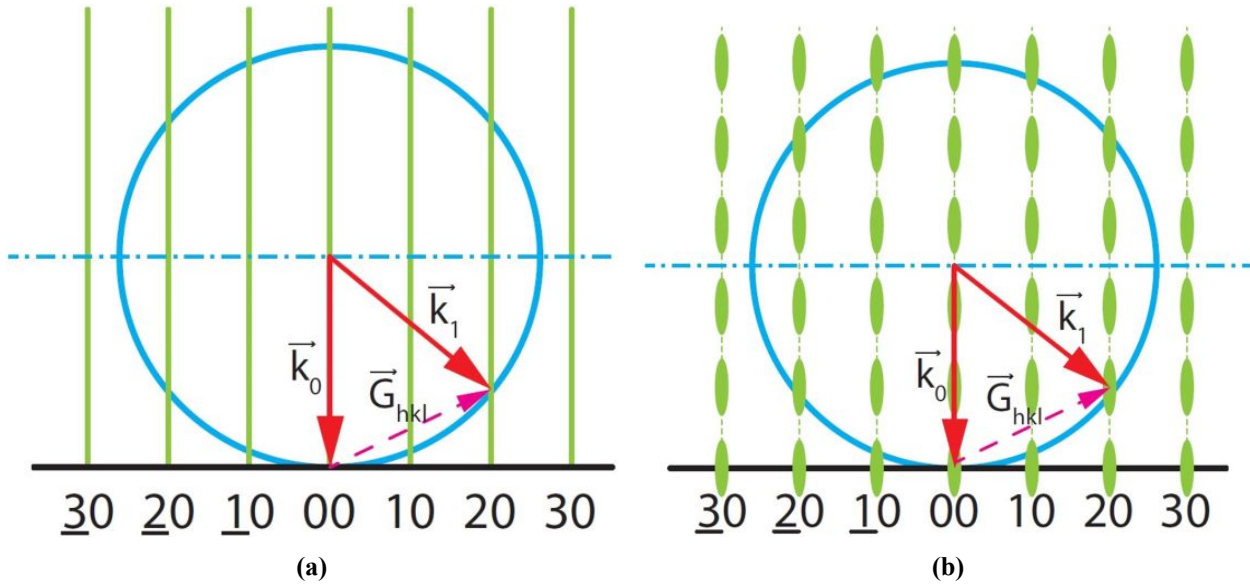


Fig. 3.3.: Ewald construction for the Laue-Law at the surface of a lattice. The green vertical lines show the Laue-Rods, that are created due to missing crystal periodicity to the vacuum. Pictures were taken from [53].

seen in figure 3.3 a). Due to inelastic scattering or too high energies, at which the electrons can penetrate the surface and scatter again at a volume symmetry, the Laue-Rods get broadened in the symmetry of the reciprocal volume crystal, which can be seen in figure 3.3 b). The radius of the blue circle marks the energy of the incoming electrons. As the electrons \vec{k}_0 get elastically scattered, the wave vector orientation will change, but not its magnitude and \vec{k}' emerges. In elastic scattering the electron energy does not change (constant $|\vec{k}|$) and interference maxima are found at the blue circle when it crosses the Laue rods. For the case of broadened Laue-Rods, the interference condition is met more often, as the intersection is not point-like anymore, which gives rise to broadened intensity peaks at the LEED screen. The LEED pattern quality gives information on the crystal surface quality. The LEED dot size reflects the extend of perfect surface crystal periodicity, while the background illumination, due to diffuse scattering, gives rise to point defects, in which the symmetry is disturbed and unordered interference's with the Ewald sphere are found.

3.1.3. Auger electron spectroscopy - AES

The Auger electron spectroscopy was used to identify the chemical structure of the samples surface. It can also be used as a tool for growth mode investigation. The morphology of the growing film gives rise to different AES intensity ratios (adsorbate/substrate elements). The AES spectrometer of this chamber, is a Staib Instruments DESA 100 cylindrical mirror analyser and offers electron voltages from 1 - 5000 eV.

In figure 3.4, the AES process in two steps can be seen. The picture describes the excitation / relaxation process with emission of a fluorescence photon and the right image shows the conventional Auger process with the emission of a characteristic Auger electron. A high energy electron excites a core level electron "K" to level "M". From this excited state, the electron can relax back to the ground state in two mechanism. The first one is by emitting a photon of characteristic wavelength, based on the difference of energy levels $\Delta E = E_M - E_K = h\nu$, whereas ν denotes the frequency of the photon. The second relaxation process, is the Auger process, visible in the right

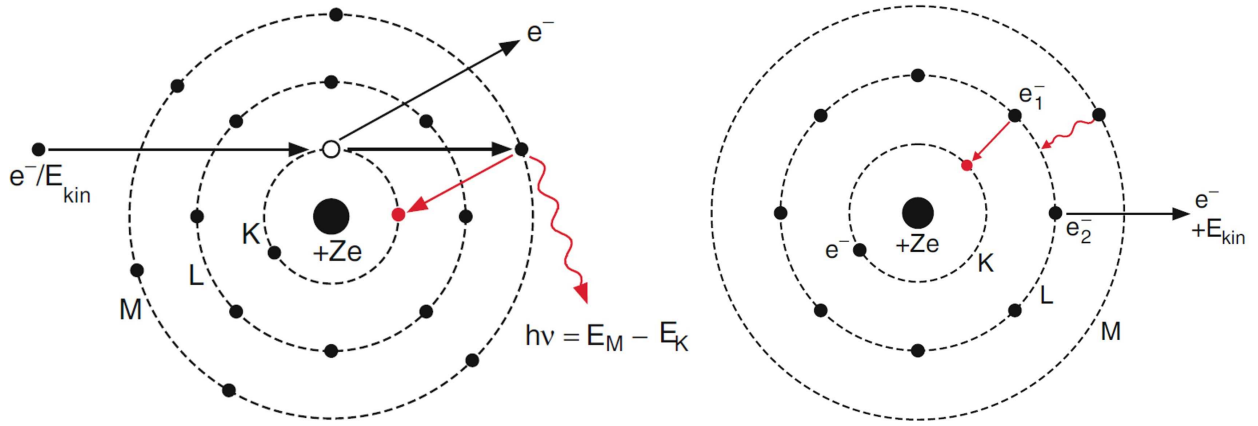


Fig. 3.4.: Auger-process: The left picture shows the excitation of energy E_{kin} . The created electron hole is filled by relaxation under photon emission of a characteristic wavelength. The right picture, begins in the excited state and displays the Auger-Process of radiationless relaxation and emission of an Auger-Electron. Picture taken from [54].

figure of 3.4. In both types, the incoming high energy electron kicks the K electron out of the atom, the thus created electron hole is filled by the radiationless transfer of an electron e_1 of the L-shell. The energy difference ΔE between E_K and E_L is passed to another electron e_2 . If the energy is sufficiently high $\Delta E > E_B$, the binding energy E_B is overcome and the electron is released with a residual kinetic energy E_{kin} . This electron is called the Auger electron and has a kinetic energy, characteristic of each element, which can be determined using an electron spectrometer. The general Auger process condition is as follows

$$E_{kin} = E_i - E_K - E_B \quad (3.2)$$

Where E_i denotes the energy of the i-th energy level.

Increasing atomic diameter $d_s \rightarrow$

Increasing atomic diameter $d_d \downarrow$

	bcc	Fe	Cr	V	Mo	W	Nb	Ta	Li	Na	Eu	Ba	K	Rb	Cs
fcc															
Ni	☆	☆	☆	☆	★ ₁	☆	☆								
Co	☆	☆	☆	☆	☆	☆	☆								
Cu	□☆	□☆	☆	☆	★ ₁	☆	☆								
Rh	□	□	□☆	★ ₂	★ ₂	☆	☆								
Ir	□	□	□☆	★ ₂	★ ₂	☆	☆								
Pd	□	□	□	★ ₂	★ ₂	☆	☆								
Pt	□	□	□	★ ₂	★ ₂	☆	☆	☆							
Al	□	□	□	□	□☆	☆	☆	☆							
Au	□	□	□	□	■ ₁	☆	☆	☆							
Ag	□	□	□	■ ₇	■ ₁	☆	☆	☆							
Pb	◇△	△	△	△	▲ ₄	□	□	□	☆						
Th	◇△	◇△	△	△	▲ ₆	□	□	□	☆	☆	☆				
Ce	◇△	◇△	△	△	△	△	□	□	☆	☆	☆				
Yb	◇	◇	◇△	◇△	◇△	△	△	△	□☆	☆	☆				
Ca	◇	◇	◇△	◇△	◇△	△	△	△	□	☆	☆	☆			
Sr			◇	◇	◇	◇△	◇△	◇△	□	□	☆	☆	☆		

Tabulation of all f.c.c.-b.c.c. metal pairs; subscripts d and s refer to deposit and substrate, respectively. The deposit planes which are expected to be parallel to (001)s planes are indicated as follows: ☆—(110); □—(001); △—(111); ◇—(001)₄₅. Systems studied experimentally are indicated by closed symbols accompanied by reference number(s). For the alignment of deposits, see text. (1) Bruce and Jaeger (1978); (2) Bruce and Jaeger (present work); (3) Jowett, Dobson and Hopkins (1969); (4) Bauer *et al.* (1975); (5) Gorodetskii and Yas'ko (1972); (6) Estrup, Anderson and Danforth (1966); (7) Hartig, Janssen and Venables (1978).

Fig. 3.5.: Predicted and measured metal on metal growth taken from [55]. According to these calculations, Rh(001) is expected to grow parallel to Fe(001) plane.

3.1.4. Epitaxial growth

A detailed study of metal on metal growth was done by Bruce [55] in 1979, predicting the growth of many fcc-bcc and hcp-(fcc/bcc) metal on metal combinations, among others also Rh on Fe, which is expected for Rh to grow parallel to Fe(100) plane, figure 3.5. The epitaxial creation of metallic films is considered as a condensation process onto a substrate. The condensation process might be explained by quasi-equilibrium processes. Furthermore, epitaxy is split into two systems, homoepitaxial and heteroepitaxial systems. The homoepitaxial system represents the evaporation of the same elements as substrate and evaporant, while heteroepitaxial describes systems where evaporant and substrate are of different elements. In terms of neglecting inter diffusion in these systems, three different main growth mechanisms can be found:

Frank-van der Merwe (FM) Perfect layer by layer growth producing very homogeneous layers

Stranski-Krastanov (SK) Deviation from perfect layer growth. Crystallites (mountains of adsorbate) form on top of closed layers

Volmer-Weber (VW) Crystallites grow from the beginning producing a very rough surface

The following consideration can be found in [56]. By neglecting energies occurring because of boundary conditions, like edge energies, as well as the shape and size effects of the surface energies a growth mode is predicted by the net energy Δ :

$$\Delta = \sigma_{film} + \sigma_{interface} - \sigma_{substrate} \quad (3.3)$$

where σ_x with $x \in \{film, interface, substrate\}$ are the specific free surface energies. For $\Delta > 0$ Volmer-Weber describes the state where the energy contribution of the evaporant $\sigma_{film} + \sigma_{interface}$ is larger than the energy contribution of the substrate $\sigma_{substrate}$. This indicates the situation for energy minimisation for clustering of many atoms into crystallites, exposing as much of the substrate surface as possible.

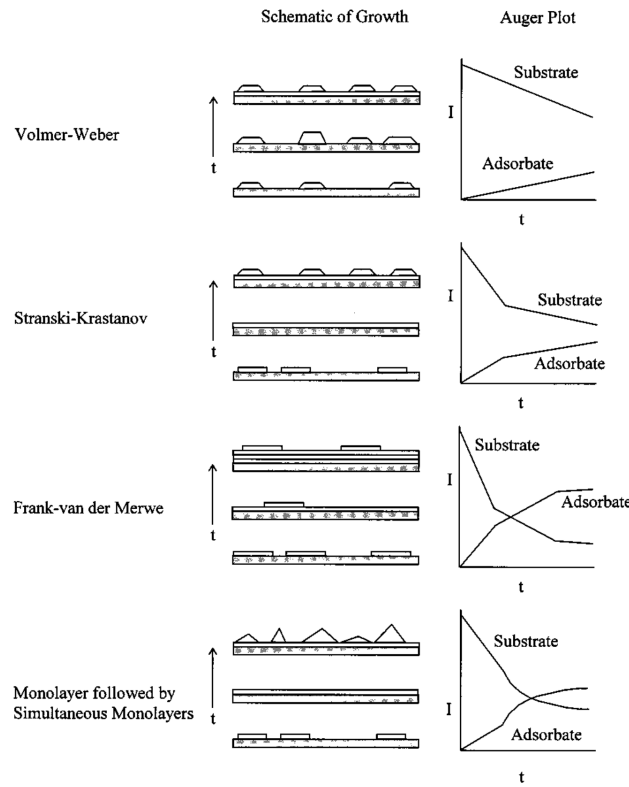


Fig. 3.6.: Schematic description of the growth and corresponding AES intensity dependencies, taken from [57]

larger than $\sigma_{substrate}$. To qualitatively investigate the growth mode of a system it is possible to utilise chemical surface analysis methods, such as AES. This measurement method makes use of the inelastic scattering of the electrons attenuating the Auger electron flux escaping the surface or volume parts of the investigated film. This attenuation strongly depends on the electron energies, this enables a simplification of the consideration by neglecting material specific parameters. Ossicini describes the AES signal depending on the coverage of the substrate with an evaporated material [58]. The ratio of peak-to-peak intensities of the element-specific AES signals will change during the evaporation process. The substrate signal is expected to decrease, while the adsorbant is expected to increase over evaporation time. The dependence on either substrate or adsorbant intensity over evaporated adsorbant thickness or evaporation time, will give rise to the momentary growth mode. In figure 3.6, the schematics of the AES intensity dependence over evaporation time is shown. The attenuation of the electron beam might be described by the inelastic mean free path λ of electrons. For each monolayer formed, the Auger electron intensity shall be multiplied by a factor:

$$w = \exp\left\{-\frac{d}{\lambda}\right\}$$

Other solutions for $\Delta \leq 0$ were found by Frank-Van der Merwe and Stranski-Krastanov. The differences lie in the conditions under which the individual monolayers grow. For FM mode, each layer is assumed to fullfill $\Delta \leq 0$. This is only the case if the substrate element and the evaporant element are very similar in material properties. This means that these two elements have approximately the same energies: $\sigma_{film} \approx \sigma_{substrate}$ reducing the interface contribution to zero $\sigma_{interface} \approx 0$. For homoepitaxial systems this consideration holds for every thickness. In the case of a heteroepitaxial system, the FM condition can only be fulfilled for a small number of monolayers, until σ_{film} and $\sigma_{interface}$ gained enough influence, that Eq. 3.3 changes its sign and crystallite growth becomes dominant. Last effect was described by SK growth. Neglected effects, such as interface alloying or interface diffusion, play a big role in changing the energy contributions. According to Bauer et al. [56], the stronger the interfacial alloy, the more energy is gained by the formation of the interface, hence the more negative $\sigma_{interface}$ is, the more favourable 2D layer growth becomes, even if σ_{film} is much

, where d is the thickness of the layer. Now Ossicini defines a weighted ratio of intensity, to eliminate a dependence of the measurement on the incident beam intensity I_0 :

$$R = \frac{I_a}{S_a} / \frac{I_s}{S_s} = \frac{I_a S_s}{I_s S_a} \quad (3.4)$$

The intensity of the substrate and the adsorbate are described by $I_{s,a}$, respectively. Parameters $S_{a,s}$ are characteristic factors of each element proportional to the cross-section of the scattering process. The attenuation factors are now split according to substrate w_s and adsorbate w_a :

$$w_a = \exp\left\{\frac{-d}{\lambda_a}\right\} \quad w_s = \exp\left\{\frac{-d}{\lambda_s}\right\}$$

In the **Frank-van der Merwe** growth mode the film is composed of h complete monolayers plus top most layer filled by a fraction x : $0 \leq x \leq 1$. For FM they obtain a ratio R_{FM} :

$$R_{FM} = \frac{xw_a^h + \frac{1-w_a^h}{1-w_a}}{w_s^h \left(\frac{1}{1-w_s}\right) - x} \quad (3.5)$$

In the sub-monolayer regime $h=0$, the FM mode enables the determination of the substrate coverage x , by means of a single AES spectra:

$$x = \frac{1}{1-w_s} \frac{R}{1+R}$$

The ratio R_{VW} for the **Volmer-Weber** growth is:

$$R_{VW} = \frac{x(1-w_a^h)(1-w_s)}{(1-x+xw_s^h)(1-w_a)}$$

In the case of **Stranski-Krastanov** growth, the VW and FM ratios are combined and one gets:

$$R_{SK} = \frac{1-x+xw_a^h + x \left(\frac{1-w_a^h}{1-w_a}\right)}{(1-x+w_s^h) \frac{w_s}{1-w_s}}$$

As the number of evaporated atoms increases, the Volmer-Weber intensity ratio R_{VW} increases the slowest and approaches a saturation, as complete monolayer coverage might not be found, leaving parts of the substrate exposed as the adsorbant crystallites grow in height. As the intermediate case of Volmer-Weber and Frank-van der Merwe, the Stranski-Krastanov mode ratio R_{SK} increases faster than VW but slower than FM mode, considering an initial layer growth followed by the formation of crystallites. In comparison to the FM mode, this leads to a bigger difference in the ratio R for larger coverages. For $h = 0$ R_{FM} has to be used, but for $h > 0$ R_{SK} is valid. The Frank-van der Merwe growth has the highest increase of R over the deposition of the adsorbant, due to the most efficient growth in terms of reducing the exposed substrate area.

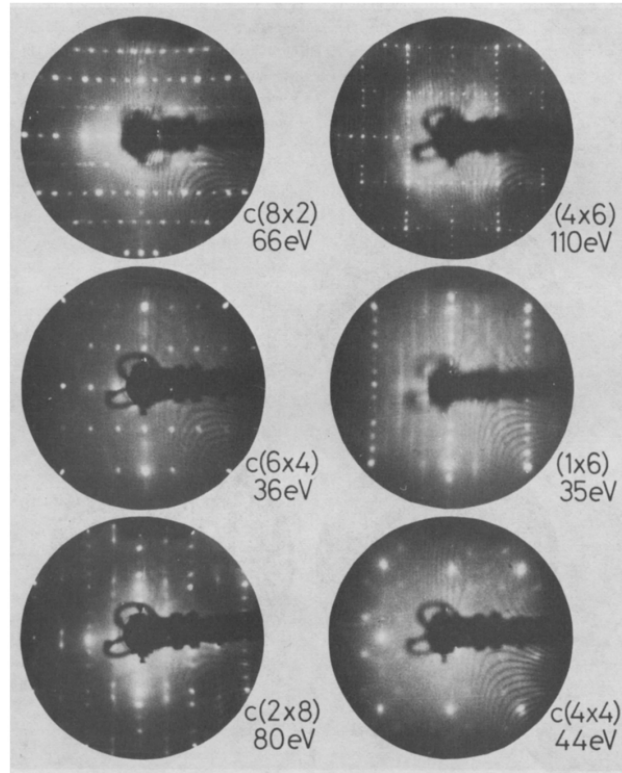


Fig. 3.7.: A collection of LEED patterns for GaAs(100) taken from literature [59]

3.2. Sample preparation

The substrate layer of GaAs(100) needs to be prepared using a certain procedure, to produce the (4x6) superstructure. The GaAs(100) surface has a variety of different superstructures like c(8x2), c(6x4), (1x6), c(2x8) and c(4x4), that can be seen in figure 3.7.

As found by Xue et al. [60], the real (4x6) superstructure of GaAs is a superposition of (2x6) and (4x2) structures, creating a pseudo (4x6) symmetry. According to this definition, all of the mentions of a (4x6) structure refer to the pseudo structure p(4x6). In their STM studies, they report about the Ga and As surface concentrations of each structures. It turns out, that the surface Ga concentration increases in the order of the (2x6), (4x2), and (4x6) phases. The GaAs superstructure is of great importance for the magnetic properties of a Fe thin film layers grown on top of it. Besides the growth properties of Fe on each individual GaAs structures, the Ga concentration on the surface layer plays a significant role. By creating a Ga-rich and As-poor surface, the probability of As diffusion into an Fe layer on top is minimised. In that context, the more Ga is exposed on a substrate surface, the higher the purity of the evaporated Fe films and less As will influence the magnetic properties of this layer. A Ga-rich surface minimises the emergence of magnetic dead layers due to the creation of $Fe_3Ga_{2-x}As_x$ compounds at the surface and up to 40 monolayer into the sample. The inter-diffused As will quench the magnetic moments of Fe due to p-d hybridisation [61]. This Fe-GaAs compound exerts only half of the saturation magnetisation of pure Fe and would therefore have a big influence on properties like magnetic anisotropy and spin dynamics in general [62, 63].

For studies of magnetic properties of Fe grown on GaAs, the focus lays in preparing the (4x6) superstructure. Many preparation recipes exist, which do not differ greatly from each other. The standard approach in literature is to start with degasing the GaAs(100) at temperatures of 400-500 °C, followed by Ar^+ -ion sputtering at 0.5 - 1 keV for several minutes and an annealing process

at temperatures of up to 600 °C [49, 63, 64, 65, 66]. The preparation recipe for substrates prepared in this work is as follows:

Ex-Situ preparation The GaAs(100) substrates were pre-cut to a size of 4x4 mm² and were taken from a wafer. The individual samples are covered with a thin protective layer, that is removed by ultra-sonic washing in pure Ethanol for 10 min at room temperature. The clean substrates were then mounted onto the sample holder using a heat conducting silver adhesive. To fully cure the adhesive the substrates were heated to temperatures of 150 °C for 15 min, before insertion into the transfer chamber to be pumped to pressures of 10⁻⁷ mbar.

Ar⁺-ion sputtering After the transfer into the main ultra-high-vacuum chamber, Argon gas of a partial pressure of 1.2 · 10⁻⁶ mbar was inserted into the chamber and the sample was sputtered at sputter energies of 1 keV. Simultaneously to the sputtering, the sample is heated to a temperature of 670 °C with a heating rate of about 20 °C/min.

Soft sputtering As soon as the sample temperature of 670 °C was reached, the sputter energy was reduced to 0.5 keV and the temperature was kept constant for further 30 minutes.

Annealing After the 30 minutes of soft sputtering, the sputter gun was completely shut off and the substrates were annealed for additional 30 minutes at a temperature of 670 °C. The pressure during annealing usually was at 5E-9 mbar.

At the end of each sample preparation the superstructure quality was investigated using LEED and the chemical surface composition was checked using AES for impurities like carbon or oxygen. If both LEED and AES show a clean GaAs(100)-p(4x6) surface, the substrate was used to grow Fe.

3.3. FMR

3.3.1. In-situ FMR / Microwave short

After a sample has been created, its position in the chamber can be lowered to a point known as the glass finger. This includes a microwave short that causes a magnetic field oscillating perpendicular to the current flow due to an oscillating current. This microwave short acts as a source of AC magnetic field required for in-situ FMR characterisation. An electromagnet can be placed around the glass finger since it is suitably thin. FMR can be performed in the so-called reflectance mode by lowering the sample into close contact to the short. The reflected microwave power varies according to the ferromagnet's state. The microwave energy is absorbed by the magnet when it is in resonance, which is recorded as a drop in reflected microwave power. The microwave short setup is a multi-frequency setup that can measure FMR at frequencies ranging from 1 to 20 GHz. Up to 26 GHz frequencies are also achievable, however non linearities in absorption linewidth and amplitude are present [53]. The manipulator can be used to adjust the orientation of the sample on the microwave short by keeping the frequency constant, allowing for not only frequency dependent FMR but also angular dependent FMR. As a result, the samples can be evaluated not only for damping and g-factor, but also for anisotropies. However, this measurement method had to be neglected, as the repair of the MBE system took too much time and sample preparation as well as FMR measurements needed to be done as fast as possible.

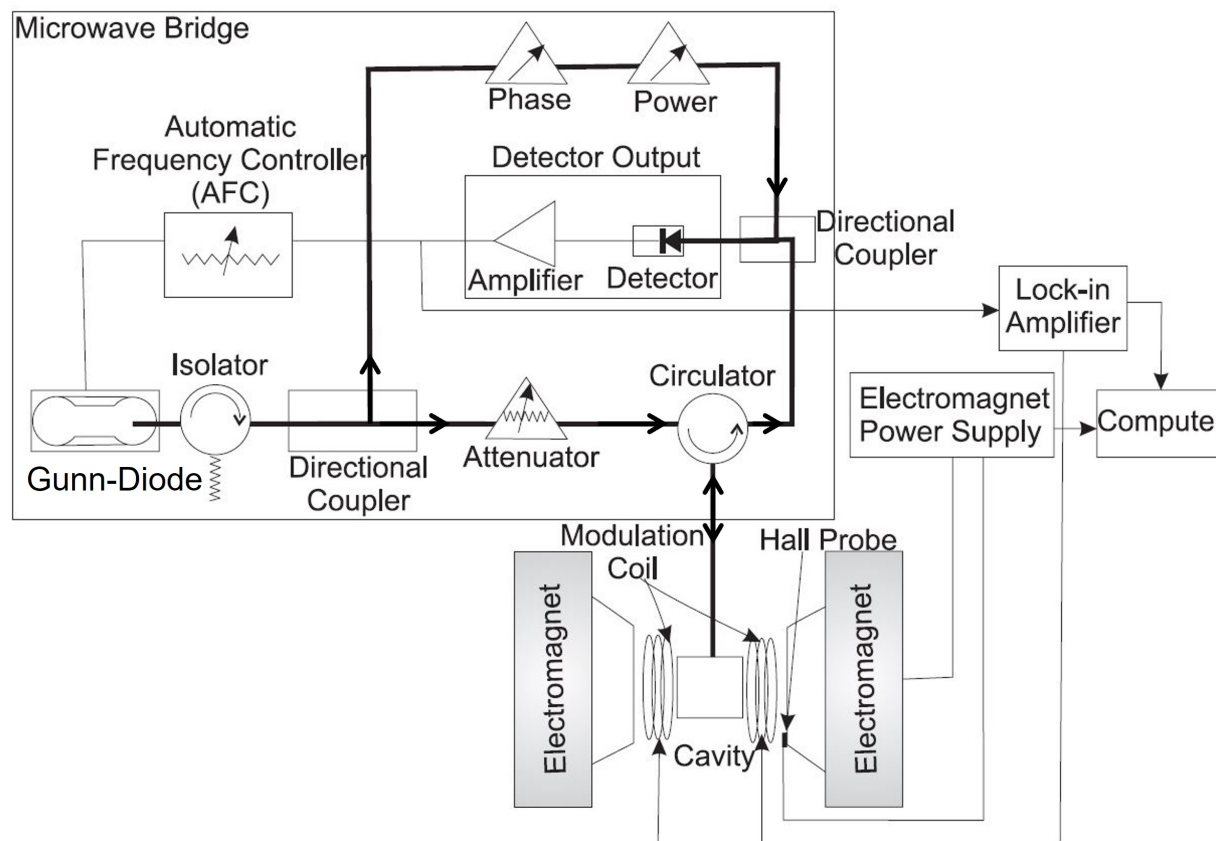


Fig. 3.8.: Schematic representation of a Bruker Elexsys E500 EPR setup. The EPR setup can be used for FMR experiments, as both effect can be measured by resonant absorption of microwave energy. As a microwave source, a Gunn-Diode is used. However, the present measurement arrangement of X-Band microwaves can also be achieved by using a Klystron microwave source. The thicker black lines represent the path of the microwaves, while the arrows indicate the propagation direction. Picture based on [6]

3.3.2. Cavity FMR

The cavity based FMR, like the MW-Short FMR, is a technology that uses microwave reflectance measurements to detect a resonance. The dimensions and filling of a microwave cavity will define the standing waves that form inside. Over the length of the measurement, this results in a fixed frequency. Figure 3.8 shows the schematic setup. The microwaves are produced by a Gunn-diode, which produces microwaves with a maximum power of 200 mW in the X-Band frequency range of $\approx 9 - 10$ GHz. A microwave guide transports the microwaves from the microwave bride to the cavity, as can be seen in the top left of the schematics figure 3.8. The microwaves travel from the source to the main cavity across a directional coupling element, that splits the incoming microwaves into two paths. The main path includes the passing of a attenuator, whose purpose is to damp the microwave power in steps of 1 dBm, from 200 mW at 0 dBm to a complete blockage for 60 dBm and higher. After damping, the microwaves are transferred over a circulator to the main cavity. A so-called iris-screw is positioned near the microwave aperture of the cavity. This screw has a metal terminating cap and is composed of a non-conductive plastic. The cavity's impedance can be matched to the waveguide's impedance by adjusting its height. No microwaves are reflected from the cavity back to the circulator, if complete matching is ob-

tained. The microwave distribution is disrupted when a dielectric sample is placed in the cavity, for this case the cavity must be retuned. In the case of ferromagnetic resonance, if a sufficiently large external magnetic field is provided, the samples resonance condition is achieved and Eq.2.45 is fulfilled. The precessing magnetisation absorbs energy from the microwaves this modifies the cavity impedance, causing microwaves to be reflected out of the cavity. The reflected microwaves travel to the circulator, in which they are only passed in a single direction to the detector. The circulator, as seen in figure 3.9, in the shape of a ferrite circulator is a passive microwave component, that can split the microwave, for example originating from cavity **D**, into parts $\pm J$ of unequal magnitude and phase. The positive part reaches the Diode **I** and can be measured. An additional part $+J$ of the same magnitude as the negative part $-J$ reaches port **A**. Due to destructive interference, because of the opposite phases, the signal at **A** will vanish. Therefore reflected microwaves from **D** will only be transferred to the Diode **I**. On the other hand microwaves from **A** are only passed through port **D** and vanish in **I**. If **I** were to exert microwaves, microwaves from **A** would only pass through port **D** and vanish in **I**; microwaves from **I** would only pass through port **D** and vanish in **F**. The purpose of the circulator is to act as a one-way street for microwaves, with this it can be also used as a kind of isolator. By grounding the cavity connection, reflected microwaves will be passed to the ground potential and will not harm the Gunn-Diode.

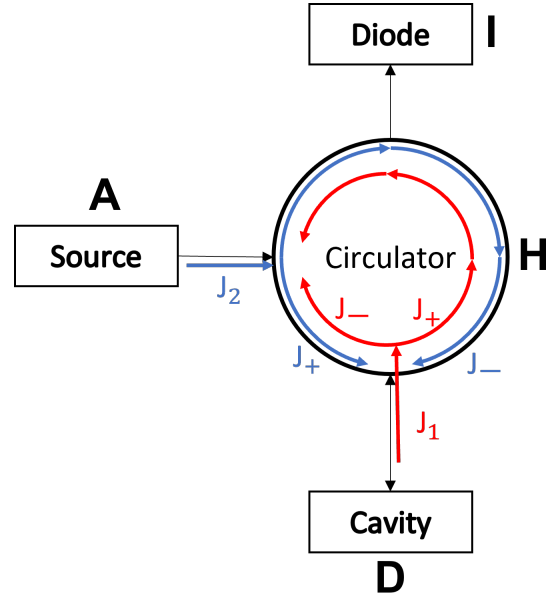


Fig. 3.9.: Schematics of a circulator. Recreated according to [67]

Once the microwaves got reflected and passed through the circulator, their reflected power can be measured as a current between 0 and 400 μA in the detector, consisting of a microwave diode appropriate for X-band frequencies. Now the second path of the directional coupler becomes important. The secondary microwaves get attenuated and phase matched to the main path microwaves. Their purpose is to serve as a bias microwave power to drive the microwave detector diode into a maximum sensitivity regime. The sensitivity is proportional to the incoming microwave power and peaks at $\approx 180 - 200 \mu\text{A}$ diode current. The sensitivity reduces as the square root of the power, and the system acts in the linear square root regime for $\approx 200 \mu\text{A}$ and above. Furthermore a small pair of coils is built inside the walls of the main cavity, parallel to the external magnet coils. The modulation coils are a pair of coils that modulate the outside magnetic field with a calibrated amplitude of 0 - 15 G or 0 - 0.0015 T and a modulation frequency of 100 kHz. This modulation allows a lock-in amplifier to be used, boosting the SNR and thus the sensitivity. Under ideal conditions, this device is capable of measuring samples with a number of spins in the region of $10^{14} - 10^{12}$ [28], and is predestined to measure ultrathin magnetic films with a thickness of 5 nm or less.

3.3.3. Coplanar waveguide (CPW) FMR

For the broadband FMR measurements, a coplanar waveguide (CPW) setup was used. In figure 3.10, the schematics of a CPW are shown. A stripline transports an oscillating current, over which

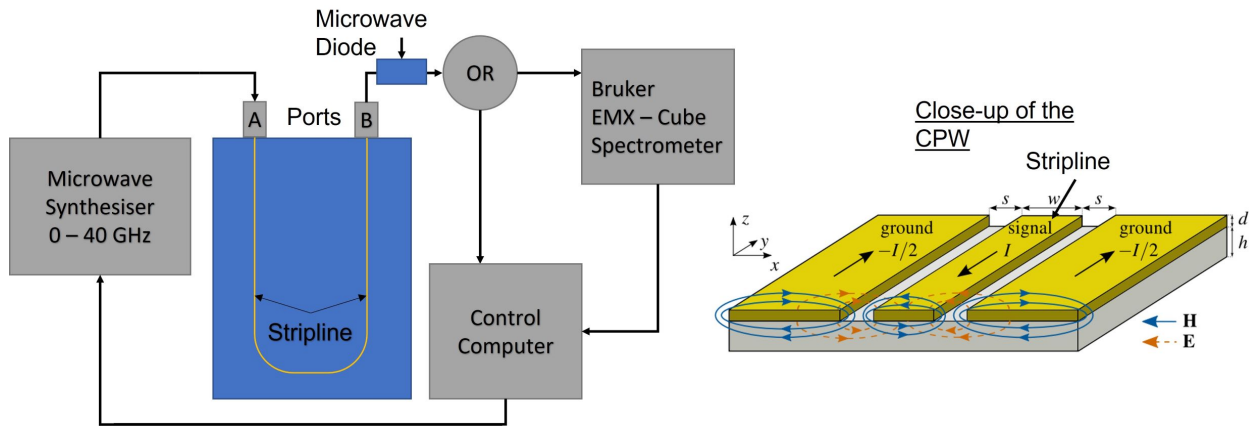


Fig. 3.10.: Schematic representation of the CPW FMR setup. On the left side, the overall setup without the magnet and the modulation coils is shown. The right picture shows a close-up of the CPW stripline with the electric and magnetic field portion distribution of the flowing signal. The right picture was taken from [23].

the oscillating electric field creates a magnetic field perpendicular to the flow direction, as shown in the right close up picture of the stripline. Other than the setups for a microwave short or the cavity setup, this measurement method relies on a transmission measurement instead of reflection. The current sent through the stripline is generated by a Rhode & Schwarz SMB100A microwave synthesizer, that allows the generation of frequencies up to 40 GHz with a maximum output power of 17 dBm. The microwave current is applied at either port **A** or port **B**. For demonstration purpose, port **A** was chosen to be the microwave input. When a sample is placed on the stripline and both ground potentials are touched, but not the stripline itself, it is in close contact with the changing magnetic field of the stripline. If the sample is brought to resonance by applying an external magnetic field, the FMR precession absorbs energy from the oscillating magnetic field of the stripline, causing the flowing current to be attenuated. The flowing current is constantly converted to a voltage by a microwave diode at port **B**. In a measurement, the current is flowing to the Bruker EMX-Cube spectrometer, in which it is measured using a lock-in amplifier. Similarly to the cavity FMR, the resonance absorption is field modulated by external modulation coils at a modulation frequency of 13 kHz.

As the microwave current is generated in the microwave synthesizer, only one frequency may be generated at a time. This means, a controller is needed, to change the frequencies after each field-swept FMR measurement. This task is done by a separate computer, that watches the state of the EMX spectrometer and switches the frequencies appropriately after each measurement. In the schematic figure 3.10, an "OR" element is seen. This part represents the switching of the output port, to either the computer or the spectrometer. If the connection is applied to the computer, a Keithley 2000 multimeter measures the voltage and sends the information to the computer. This needs to be done in the sense of a calibration measurement. The microwave output power depends on the microwave frequency. As the dependence is subject to change for different cable placements, calibration measurements need to be done after each construction of the setup.

A calibration measurement can be seen in figure 3.11. First, the frequency is swept across a defined frequency range, usually 0 - 40 GHz in steps of 0.001 GHz. For each frequency step, the diode voltage is measured, the corresponding plot can be seen in 3.11 a). From this data, oscillating minima and maxima are obtained, from which in a defined window size local maxima are extracted. These can be seen as red dots in both 3.11 a) and zoomed in b). A second frequency sweep is done,

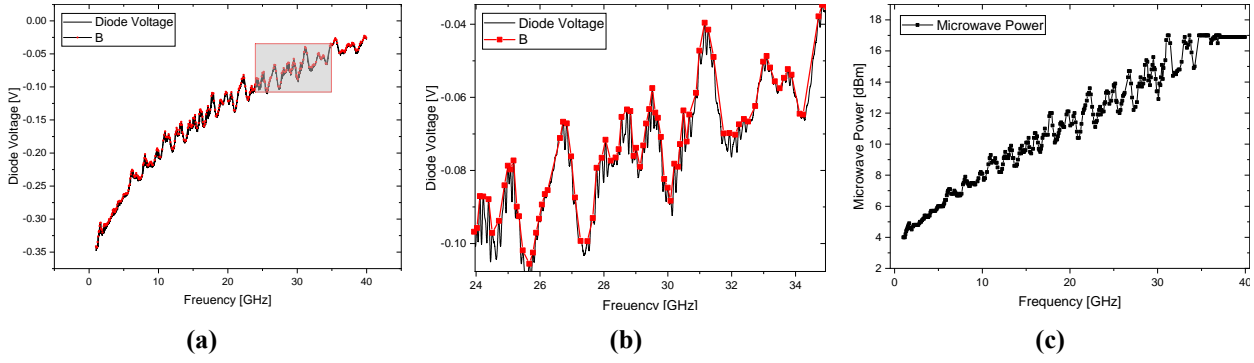


Fig. 3.11.: Calibration measurement for frequency dependent FMR using either a CPW or a microwave short. Figure **a)** and **b)** show the uncalibrated diode voltage over the applied frequency with constant microwave power of 5 dBm. The red dots, that are better resolved in figure **b)**, are the local maxima of the diode voltage for a specific frequency range. Figure **c)** shows the microwave power for each of the local maximum points required to achieve a constant diode voltage of -0.3 V.

in which the frequency is set to each local maxima point. In this second sweep, for each local maxima, the output power of the microwave synthesizer is changed, until a diode voltage of -0.3 V is found. This results in a frequency-power calibration to keep the diode voltage output constant. The determined $f(\text{dBm})$ curve can be seen in figure 3.11 c), note, that the synthesizer for frequencies above 30 GHz cannot supply the needed microwave power to reach -0.3 V at the diode, so that the power has been set to the maximum value. Regardless of transmission setup or reflection setup, the calibration measurement is always done after the setup

3.3.4. FMR Experiments

The field sweep method of FMR experiments also referred to as conventional FMR setup, has a very good signal-to-noise ratio (SNR). The reason for the increased sensitivity lies in the construction of the measurement. A cavity resonator is used that delivers very constant frequencies with the help of standing waves. This minimises the influence of frequency errors and the slightest distortion of the cavity results in a measurable signal. If a ferromagnetic material is in resonance, it reflects the microwaves from the cavity onto a diode. Important for a cavity based FMR experiment is the quality factor of the cavity itself. It is used to characterise the cavity sensitivity and is defined by [68]:

$$Q = 2\pi \frac{\text{Stored energy inside the cavity } W_R}{\text{Energy consumption per period}} = \frac{\omega W_R}{P} \quad (3.6)$$

This Q includes several different contributions, like ohmic losses at the inner metallic surfaces Q_ω , losses due to the connection towards the microwave generator and their coupling elements Q_K , as well as losses from dielectric elements such as the sample and sampleholder Q_ϵ and losses due to the absorption of the magnetic layer under investigation Q_χ . All contribution can be summarised in the quality factor of the empty cavity, or the unloaded Q -factor, Q_U :

$$\frac{1}{Q_U} = \frac{1}{Q_\omega} + \frac{1}{Q_K} + \frac{1}{Q_\epsilon} + \frac{1}{Q_\chi} \quad (3.7)$$

In the case of this thesis a cavity with $Q_U = 3000$ was used. For the resonant case of the ferromagnetic sample, the factor Q_χ will change according to:

$$Q_\chi = \omega \frac{W_R}{P_\chi} \quad (3.8)$$

where P_χ is the energy absorbed by the sample in resonance per period. The absorbed energy will be converted to Joule heat due to the magnetic damping. Using the Poynting vector to calculate the absorbed energy of the sample, the quality factor Q_χ can be found to be:

$$Q_\chi = \frac{1}{2\mu_0} \frac{\int_{V,cavity} b_1^2 dV}{\int_{V,sample} \chi'' b_1^2 dV} \quad (3.9)$$

This equation sets the quality factor Q_χ in direct correlation to the magnetic susceptibility of the sample and the magnetic induction b_1 of the microwave field inside the cavity. For sufficiently small samples, that the microwave distribution will be homogeneous over the whole sample, one can find the reflectivity coefficient Γ of the cavity in terms of the imaginary part of the sample susceptibility:

$$\Gamma = \frac{1}{2} Q_U \frac{\int_{V,sample} \chi'' b_1^2 dV}{\int_{V,cavity} b_1^2 dV} \quad (3.10)$$

This is an integral over the sample and cavity volume V_s, V_c . The reason for the derivation of this reflectance coefficient lies in the measurement setup, in which the FMR can be determined by the intensity of reflected microwaves out of the microwave cavity. These reflected microwaves are then measured using a microwave diode, that converts the incoming microwaves into a current. Important for the conversion is the Signal-to-Noise-Ratio (SNR) one can obtain in this measurement setup, which can be defined as the ratio of voltage drop at the diode V_{ref} and the thermal noise voltage at the diode V_{noise} :

$$SNR = \frac{V_{ref}}{V_{noise}} = \frac{\Gamma \sqrt{P_{in}}}{\sqrt{4k_B T \Delta\nu}} \quad (3.11)$$

The SNR is linearly proportional to the reflectance and with this the imaginary part of the susceptibility χ'' , while only scaling in a square root law of incoming microwave power P_{in} . The parameter $\Delta\nu$ describes the bandwidth of the diode in units of Hz. In the case of ferromagnets the magnetic susceptibility is extremely high in comparison to paramagnets, for the case of electron paramagnetic resonance (EPR). This means, in FMR experiments the SNR is usually expected to be very high, according to the magnitude of the susceptibility. In the real experiment the signal will be field modulated by utilising small external modulation coils of frequency of 100 kHz. The modulation enables the usage of an lock-in amplifier enhancing the SNR.

4. Analysis

This chapter deals with the discussion of the results obtained from the experiments. It starts with the investigation of the Rh growth on Fe investigated by AES intensity comparisons, supported by interpreting LEED patterns of the prepared GaAs(100) substrates as well as both Fe and Rh LEED pictures. Following the growth determination, the magnetic characterisation starts by acquiring the saturation magnetisation of all prepared thin film samples. It then continues with the interpretation of FMR spectras taken as angular dependent as well as frequency dependent experiments, to extract magnetic damping, magnetic anisotropy and g-factor for all samples individually. Additionally the thickness dependent damping is interpreted in terms of a spin pumping effect assuming the model discussed in the theoretical background of chapter 2.2.

The samples are divided into two groups, designated as batch-1 and batch-2, both grown on $4 \times 4 \text{ mm}^2$ GaAs(100) substrates from two different wafers. The difference between the wafers is in age, substrate thickness and polish. The wafer from batch 1 has a thickness of 0.4 mm, is polished on the top and etched on the bottom; it was purchased in 2013. A new wafer with a thickness of 0.62 mm and polished top and bottom was purchased from the same manufacturer. Each batch consists of 6 samples with different Rh thicknesses. Each sample was prepared following the same recipe for GaAs(100) preparation to achieve the 4×6 superstructure. The substrate preparation was always followed by the evaporation of 5 nm Fe, except for the sample of batch-1 with 1 nm Rh, where due to complications with the Rh evaporation system, the Rh layer has been evaporated roughly 24 hours after the deposition of the Fe layer. During this break, the Fe film has been exposed to a vacuum with pressure gradually decreasing from 5×10^{-9} mbar to 5×10^{-11} mbar. Such delays due to problems with the evaporation system occurred several times during the work of this thesis, a more detailed description of the problems can be found in the appendix A.3.

In total 16 samples have been prepared and are discussed in the following of this chapter. For batch-1 and batch-2 the samples contain GaAs(100)- 4×6 / 5 nm Fe / {1, 2, 3, 5, 10, 15} nm Rh. Additionally four more samples have been prepared during the course of the AES intensity growth dependencies consisting of three samples with GaAs(100)- 4×6 / 4 nm Fe / {0.36, 0.5, 0.76} nm Rh and a single GaAs(100)- 4×6 / 5 nm Fe / 2 nm Rh thin film. The thicknesses were determined using a MTM-10 quartz crystal monitor system from TecTra [69]. This offers a resolution of 0.1 nm in the case of a perfectly calibrated tooling factor. The tooling factor for this work has not been determined, an older standard value for this particular system was used, that can be found in [53]. Since the tooling factor could have changed over time, the measured thicknesses go in hand with a large phenomenologically derived error of 0.5 nm or greater.

4.1. Rh growth on Fe

In this section the growth of Rh on Fe is investigated, by comparing the AES peak to peak intensities of 302eV Rh and 703eV Fe signals over the evaporated Rh thickness. In the end the produced layers were scanned using LEED, to hint surface periodicity and defect density. An AES growth determination with substrate and Fe preparation takes more than 14 hours per measurement, depending on the Rh step size. Therefore, only four experiments were performed.

4.1.1. AES growth dependence

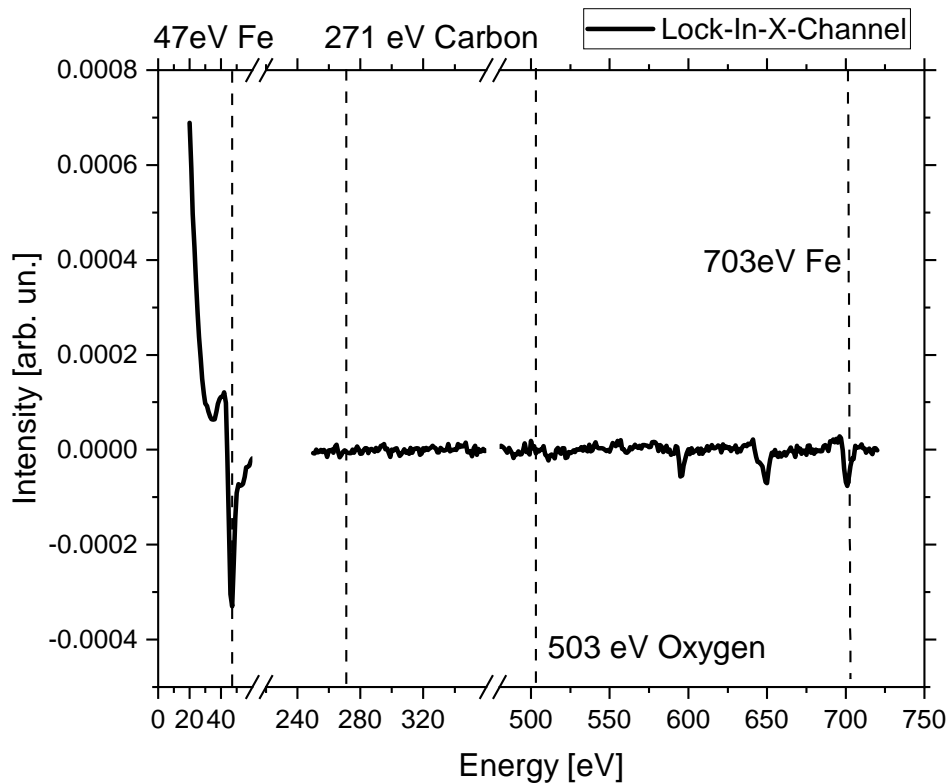


Fig. 4.1.: Example of a freshly prepared Fe layer AES spectra. Impurities like Carbon and Oxygen have been marked, as well as the very surface sensitive low energy Fe peak at 47 eV and the 703 eV peak. The measurement was taken under parameters creating a sample current $> 1 \mu\text{A}$

As described in chapter 3.1.4, the way how the Rh atoms will align themselves on a Fe substrate layer can be determined by AES investigations. For this GaAs(100)-4x6/4, 5 nm Fe films were prepared to serve as a substrate layer for Rh atoms. In total there were four AES growth studies conducted during this work, three of which were made using 4 nm Fe and one with 5 nm Fe. Nevertheless the approach stayed constant for all films. For the AES experiments of 4 nm Fe a primary electron beam of energies of 3 keV was used utilising emission currents in the range of $I_{Em} = 3.6 \text{ mA}$. This results in a sample current of approximately $0.8 \mu\text{A}$. For the 5 nm Fe sample the AES setup was adjusted to exert sample currents of $\approx 5 \mu\text{A}$, that were achieved using emission currents of about $I_{Em} = 20 \text{ mA}$. The energy analyser was calibrated using the so-called elastic peak, which was found to be already operating at its optimum and did not need to be readjusted.

For all films, the Fe layer was first measured using AES in the range of 10-1300 eV, to find the chemical purity on the surface layer. Impurities like carbon at 271 eV or oxygen at $\approx 500 \text{ eV}$ could not be found, directly after evaporation, see figure (4.1). Additionally for the last two growth studies, the intensity change of low energy Fe peak at 47 eV has also been measured. This peak, due to its low energy, is extremely surface sensitive. The Auger electrons originating in this energy region are of low kinetic energy. Their inelastic mean free path can be roughly estimated by $\lambda = 143/E^2 + 0.054\sqrt{E}$ to be 0.4309 nm at around 40 eV and 1.43205 nm at 703 eV [70]. The dependence is shown in figure 4.2. The thickness sensitivity is therefore limited to about 4 Å, meaning

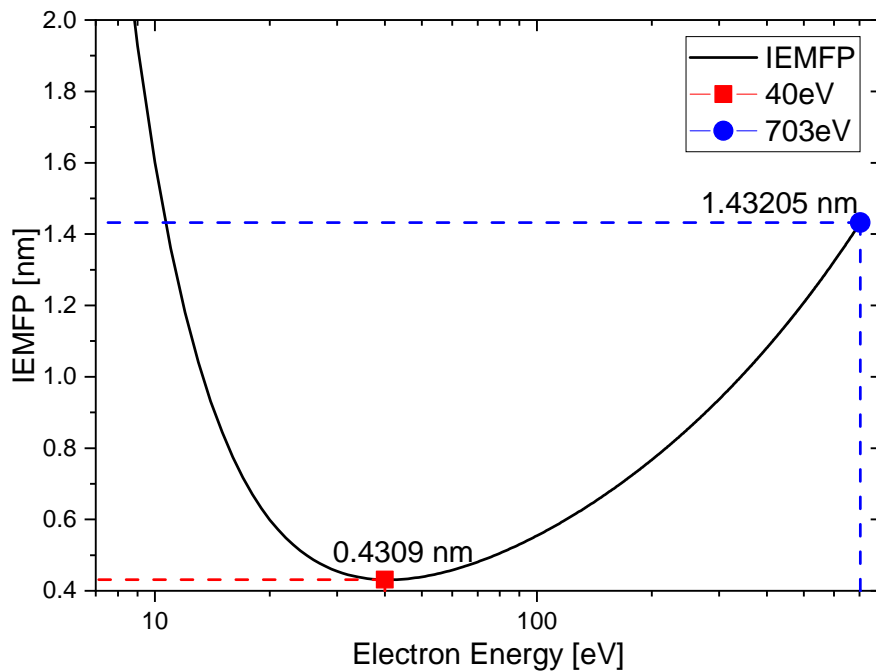


Fig. 4.2.: A rough estimation of the inelastic mean free path of an electron plotted and highlighted for low and higher energy peak of Fe. The graph was calculated according to data from [70].

that the measured low energy electrons can only be created in the top most layer, otherwise they would scatter and lose their energy. Any adsorbate will increase the path to the vacuum, greatly reducing the amount of electrons contributing to this peak. Once a complete adsorbate monolayer was formed, the low energy peak should vanish.

At an energy of 40 eV, Rh has a low energy peak too. By measuring the low energy range, both Fe and Rh surface contribution can be determined, leading to a high sensitivity to growth in the limit of a few monolayer thicknesses. The only measurement where the surface peaks were investigated in is the 0.2 Å dependence.

In the further studies the energetically higher peaks were taken into account. For Rh the peak at 302 eV and for Fe at 703 eV was scanned and analysed. To make the intensities comparable, all elements found in [71], were normalised to the intensity of Ag and given a scaling factor. According to this the Fe peak needs to be multiplied by a factor 2.5 to compare it to the Rh peaks. With reference to the clean Fe surface peak named I_0 , Rh was evaporated with a rate of 0.6 Å/min. At a defined thickness step, for example 0.1, 0.2, 0.3 or 0.5 Å the sample was rotated from the evaporation position to the AES position and was probed for 280-320 eV Rh and 480/680-720 eV Fe position. During the AES measurements, the intensities were extracted manually and plotted, to have a quick comparison of the last step.

The cycle of evaporation and AES experiments was continued until the Rh signal was saturated and the Fe signal could no longer be distinguished from the background noise. In the AES growth experiments, both deposition time and Rh thickness dependent measurements were performed to compare and verify the final thickness of the grown layers.

All growth experiments can be found in figure 4.3, these figures show highlighted areas of repeating shapes and patterns. The 0.1 Å Rh per step dependence is seen in figure 4.3a. In this study the quartz crystal thickness monitor was used to determine the evaporated Rh thickness. In addition to the oscillating element, the thickness sensor consists of a sheet of metal with a 4x4 mm hole next to the quartz oscillator. This hole serves as a mask behind which the sample is positioned to protect

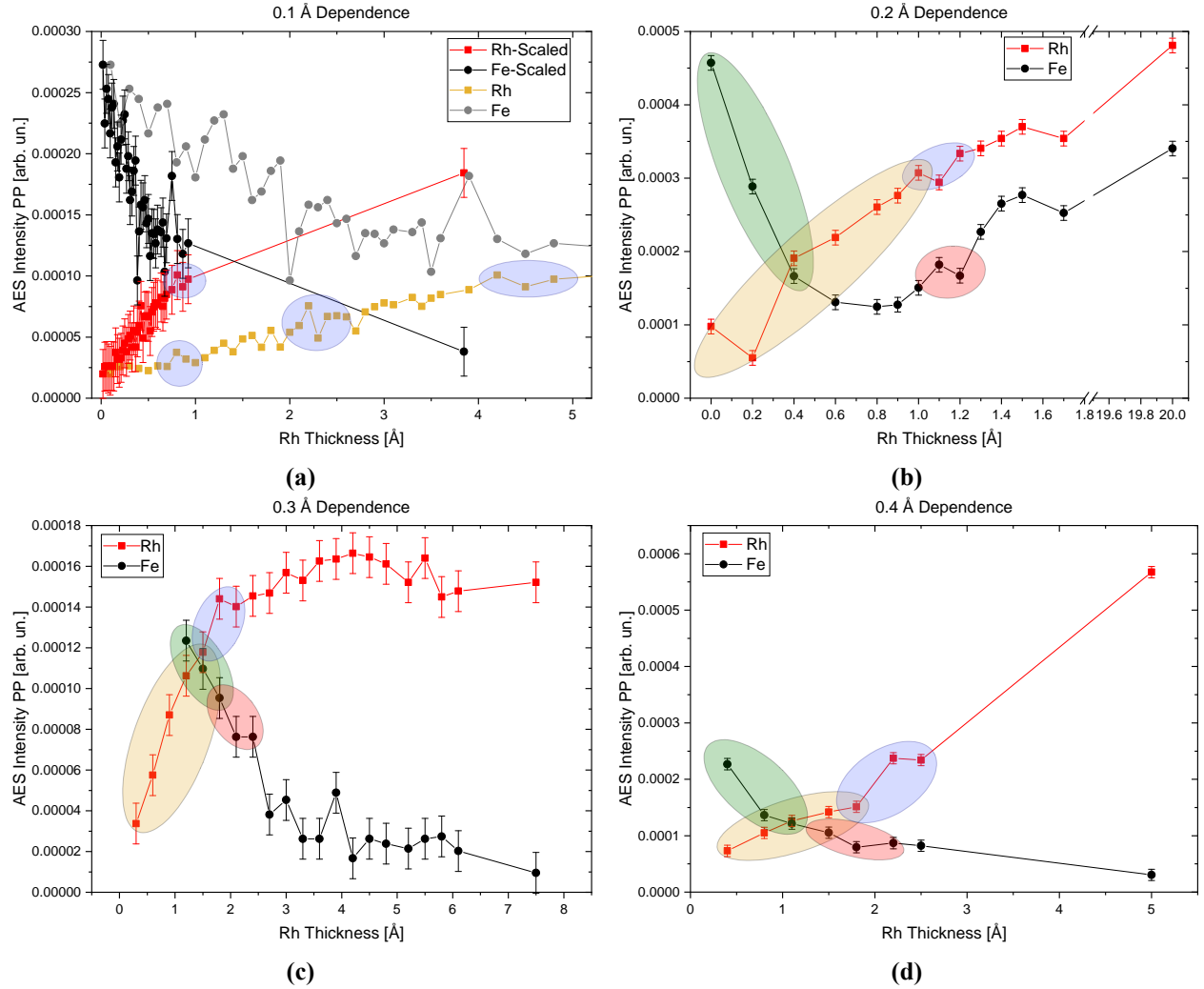


Fig. 4.3.: All AES growth studies made during this thesis. The highlighted areas mark repeating patterns. The error of the intensities is determined to be the size of the symbols in the plots and lay in the area of $\pm 1\text{E-}5$. Figure **a)** shows the 0.1 Å per evaporation step dependence of AES peak to peak intensities. For this study in particular, the thickness error is significant. Figure **b)** shows the 0.2 Å Rh per step measurement. This study was performed with an increased electron beam current, resulting in higher AES intensities, reducing the noise. The 0.3 Å Rh per step measurement is shown in figure **c)**, the first three data points of the Fe intensity are missing. In the measurement of figure **d)** the Rh was evaporated in steps of 0.4 Å. After reaching 2.4 Å, the study was stopped and continued on the next day to evaporate a total Rh thickness of 5 Å.

the sample holder in the evaporation process. In the case of this study, the positioning behind the mask was not optimal, blocking about 1/6th of the sample homogeneously over the whole evaporation period. The blocked area is visible by eye as a black shadow on the substrate, see appendix figure A.4.

The original data can be seen as orange for Rh and grey for the Fe signal. At about 4.6 Å, the AES study was stopped and additional Rh was evaporated, until a total thickness of 2 nm was reached. In the data analysis the crossing point of Fe and Rh intensities was determined to be at 7.3 Å, that in context to other AES studies, shows an increase by a factor of 5. By disregarding the thickness information and overlaying this data to the other studies, it was possible to scale the thickness reading, so that the Fe and Rh intensity slopes were matching. It was found, that a scaling factor of 5.2 for the x-axis, is sufficient to scale the measurement and make it comparable to the others. The scaled data is visible as black for Fe and red for Rh. The crossing point of the scaled data lays at 1.42 Å. Overall the sample has a high noise contribution, which might be explained with the thickness offset and the blocking of sample area. Nevertheless the Rh intensities show a linear increase from a minimum value of 2E-5 to a maximum value of 1E-4. The Fe intensity seems to be a linear decrease in the beginning, decreasing from 2.75E-4 to about 1.4E-4. After this point, the intensity seems to change its slope, but due to the absence of further measurement points no clear trend can be seen. Besides the main AES study, that took place until 1 Å, as for the scaled dependence, the growth had been continued to reach a desired thickness of 2 nm Rh. In the scaled format this thickness would correspond to about 4 Å. Including this point into the observations, a change in the trend of Rh and Fe intensities can be seen. For Fe the intensity change might be interpreted as an exponential decay or a power law, in order to reach the last data point. In the case of Rh an exponential saturation could explain the further path.

Furthermore the 0.2 Å Rh per step dependence is shown in figure 4.3b. In difference to the other growth measurements, this experiment was performed on 5 nm of Fe as a substrate layer and with a lower AES-grid voltage, than previous dependencies (2.25 instead of 2.73, the values express the value of a potentiometer and do not correspond to any unit), boosting the sample current into the regime of 4-5 μA and therefore increasing the AES signal strength with costs of electron beam divergence. The quartz oscillator was used to track the Rh thickness during evaporation. The increment of 0.2 Å could not be held for all measurement points, due to thermal fluctuation of the oscillator. Interestingly the Fe signal seems to decrease exponentially in the range from 0 Å to 0.9 Å to a intensity value about 4 times less as the maximum value at 0.0 Å. The Fe intensity then starts increasing, with roughly the same slope as the intensity of Rh. After 1.7 Å of Rh, the study was stopped and a final evaporation was done to reach at total thickness of 2 nm Rh. The Fe signal intensity seems to increase again to a second order maxima of 3.4E-4 at 2 nm of Rh thickness.

The 0.3 Å Rh per step measurement is shown in figure 4.3c. In total 7.6 Å of Rh was evaporated in this study. The thickness has been tracked by calibrating an evaporation rate, that was measured over a period of ten minutes, to a specific E-Beam flux value. The rate was determined to be 0.76 Å/min. With respect to this value, the E-Beam shutter was opened for 24 seconds for each step to reach the needed 0.3 Å. Due to difficulties in the Rh evaporator, the flux was irregularly decreasing during the deposition. Because of this, the filament current and the high voltage supply to the Rh rod needed continuous adjustments during the time of this experiment, to keep the Rh rate constant.

The initial increase of Rh can be interpreted as linear till 1.8 Å with a total intensity change of about 7 times the minimum value. After the linear increase, the slope changes and the thickness dependence becomes more comparable to an exponential saturation of a value of 1.6E-4, with a small decrease at about 5 Å, that keeps the intensity rather constant on a level of 1.4E-4. The Fe

thickness dependence however shows a linear decrease with intensities from $1.3\text{E-}4$ to $7\text{E-}5$ in the thickness range of 1 \AA to 2.5 \AA and then starts to decrease exponentially until 7.6 \AA with an intensity down to $1\text{E-}5$. Additionally the measurement point of Fe at 4 \AA shows a jump in intensity from $2\text{E-}5$ for 3.7 \AA to $5\text{E-}5$ for 4 \AA , back to $1.5\text{E-}5$ for 4.3 \AA . This does not fit into the overall dependence and does not lay in between the error bar of this measurement. One might explain this by a small change in positioning of the AES electron beam or changes to the electron beam current, since the emission current will change with time, one needs to readjust the parameters.

The 0.4 \AA Rh per step dependence is shown in figure 4.3d. This AES study was performed without the quartz thickness monitor and the thicknesses were obtained through a calibration of E-Beam flux. The intensity of the Fe peak decreases from $2.25\text{E-}4$ at 0.4 \AA to $3\text{E-}5$ at 5 \AA . The overall dependence could be interpreted as an exponential decay. The Rh intensities on the other hand show a dependence, that could be approximated linearly from 0.4 \AA with $7.5\text{E-}5$ to 1.9 \AA with $1.5\text{E-}4$. From this point to the maximum of $5.5\text{E-}4$ at 5 \AA , the dependence seems to be linear again with a change in slope. One has to note, that from 2.5 \AA till 5 \AA the amount of measurement points is too small to conclude a dependence.

In all subfigures of figure 4.3, repeating patterns are marked in the colours blue, green, yellow and red. The areas marked by a blue circle represent a sudden change in intensity of Rh out of the previous behaviour. The measurement data points after this change usually fall back into the initial dependence. In all experiments, it is only one measurement that is shifted to higher intensities. A similar effect can be seen in the areas marked in red. There, for the Fe intensities, either the point in the middle of the circle is shifted to higher intensities or the point at the end is shifted to lower intensities. The shift of an Rh measuring point almost always occurs in the same thickness as the Fe point changes, which could indicate a possible correlation between these points.

The green circles mark the initial dependence of the Fe signal. With the exception of the dependence of 0.1 \AA this can always be approximated with a linear slope; whether this dependence is exponential or linear is disputed. The same applies to the Rh output curve marked in the yellow areas.

The red and blue areas can possibly be explained by a readjustment of the AES electron beam parameters. During the course of the AES measurements, the filament current decreases. To compensate for this decrease, the filament current or grid voltage is adjusted to achieve a general emission current of $I_{Em} = 3.3\text{ }\mu\text{A}$ and $I_{Em} = 18\text{ }\mu\text{A}$ for the 0.2 \AA dependence. When matching has occurred, the intensity of the measured AES signal is increased compared to the previous measurement point. This is due to a higher emission current as a result of a small offset error during manual and inaccurate adjustment. A physical origin cannot be ruled out, such as a rearrangement of the Rh atoms at the surfaces, perhaps due to crystallites forming too thin and too fast thus eventually collapsing. No complete explanation for the origin of the red and blue areas can be derived from these measurements.

In addition to the higher energy peaks, the lower energy surface peaks were also investigated for the 0.2 \AA dependence. The evaluated peak-to-peak intensity of 40 eV Rh and 47 eV Fe is shown in figure 4.4a. For Fe, the intensity decreases exponentially to zero at about 1.5 \AA . For Rh, it increases exponentially up to 1.5 \AA but does not reach saturation. It increases to a maximum value of $3.4\text{E-}3$ at a thickness of 20 \AA . Since points are missing in between, no clear dependence can be established for the last part.

To draw conclusions about the nature of Rh growth on the Fe substrate layer, one has to compare the AES dependence experiments with theory and literature. From the theoretical point of view, one has to determine the slope of the Rh and Fe intensity curves. Thermodynamically, three main growth modes can be distinguished [57]. The Volmer-Weber (VM), Frank-van-der-Merwe (FM)

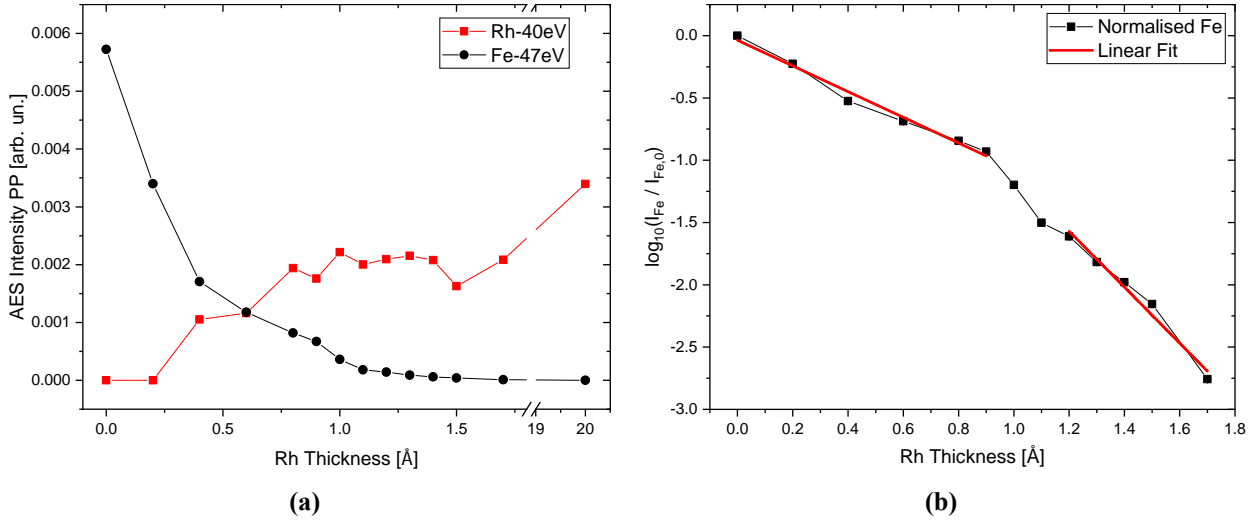


Fig. 4.4.: AES surface peak intensities as a function of 0.2 \AA . The intensity error is smaller or comparable to the point size of the measurement points. The Rh points in particular show large fluctuations that cannot be attributed to the noise or error of the signal. This is due to a large background that does not change the Rh value linearly. Figure **a)** shows the peak-to-peak AES intensity of Rh and Fe, while Figure **b)** shows the logarithm of the normalised Fe surface peak intensity. The linear fits are intended to highlight the areas of interpreted linear dependence.

and the Stranski-Krastanov (SK) modes.

The VM mode describes the growth of crystallites on a substrate layer. These crystallites are comparable to mountains or large adsorbate clusters. In this growth mode, the AES intensities of the substrate layer decrease most slowly and the adsorbate intensities increase most slowly. Due to the formation of crystallites, complete coverage may not be present in the ultra-thin layers.

The complete opposite of VM is the FM mode. This describes perfect layer-by-layer growth, where one monolayer forms and only when a complete monolayer has formed does the second monolayer begin to grow. This reduces the AES intensities most rapidly. Each time a monolayer has formed, the slope of the curves changes. During the growth of a monolayer, the intensities increase or decrease linearly with the evaporation time.

The SK mode is a combination of both VM and FM. It describes the case of a initial layer-like growth with fastly decreasing linear slopes, that turn into the formation of crystallites, which greatly reduces the slope of the intensities to be more compatible with a VM curve. In reality, however, no absolute perfect growth can be achieved. Bryant et al. [57], also suggest a small deviation of the SK growth, which they call the monolayer followed by simultaneous monolayer growth. In this model, like in SK, a first monolayer forms perfectly, but after this, several monolayers will form separately at once. In difference to SK, these monolayers will partly close over the evaporation time, reducing the AES intensity slope from FM to an exponential dependence after the first monolayer.

From all dependencies and especially the experiments without the usage of the quartz crystal monitor, one finds the crossover point of Fe and Rh to be roughly around 1.5 \AA . Assuming Rh to have a bulk crystal lattice parameter of 380.4 pm and Fe to have a bulk lattice parameter of 287 pm [72], Rh could potentially have a minimum lattice mismatch to Fe, if it grows 45° rotated on Fe: $\sqrt{2} a_{Fe} = 405 \text{ pm}$. The lattice mismatch in this case will be 6.17% . Assuming the volume of a Rh unit cell to be constant and Fe not deforming while Rh is condensing on top of it, one can find the approximated atomic distance out of geometric consideration to be 167.8 pm or 1.678 \AA . In this scenario, the Rh lattice will be compressed and is referred to as tetragonally distorted. Furthermore,

by assuming an fcc lattice, the Rh atoms will be closely packed. This will result to an atomic monolayer thickness of about $t_{mono} = \sqrt{3/4a^2} = 1.453 \text{ \AA}$. Since this value does not account for tetragonal distortion, a smaller value is expected and is approximated as $t_{mono} = 1.4 \text{ \AA}$.

The crossing point is suspiciously close to the assumed monolayer thickness. Theoretically, a monolayer with perfect layer growth can be defined as a change in the linear slope of either the substrate or the adsorbate, which cannot be fully determined in the present experiments. This indicates a growth that deviates from a layer growth, since no definite monolayer can be determined by a change in the slope. In the case of the 0.3 \AA dependence, a linear slope can be assumed for Rh from 0 \AA to about 2 \AA . After this approximately linear slope, the dependence saturates similarly to an exponential function. This indicates a change in the slope at about 2 \AA and a deviation from perfect layer growth. At the same time, Fe also decreases linearly and rapidly up to 2 \AA followed by a change in slope that is best described as saturation rather than a complete disappearance of intensity. This could be explained by Fe atoms in the near-surface region.

For the low energy peaks (figure 4.4a), that are very sensitive to changes to the surface, one can see a fast decrease of Fe intensity. The decrease of Fe until the vanishing point at about 1.5 \AA points to the creation of at least one full monolayer of Rh. A logarithmic dependence of the normalised Fe intensity over the Rh thickness can give rise to a better determination of possible layer growth, as can be found in figure 4.4b. For FM growth, the normalised Fe intensity without a log-scale, during formation of a single monolayer, would be a linear slope. As the monolayer is completed the slope will change, while the dependence is still linear (as shown in the schematics 3.6). In the FM mode, the change in slope determines the monolayer thickness. By assuming SK or monolayer followed by monolayer growth, the dependence would be exponential in which a log-scale gives rise to the change in slopes. This was done in figure 4.4b. In this case the regions from 0 \AA to 0.9 \AA and from 1.1 \AA to 1.7 \AA are assumed to be linear, as represented by the linear fits. The intersection of the linear fits lies around 1 \AA . That implies the formation of two monolayers of Rh, with a thickness of about 1 \AA .

In addition, the 0.2 \AA dependence shows an increase in Fe signal intensity. A description of this phenomena could be the intermixing of Fe into the Rh layer. This is especially of importance, with regards to an alloy formation of FeRh. Since the 702 eV Fe peak is increasing until 2 nm Rh and the surface peak of 47 eV in figure 4.4a vanishes, one has to assume, that no clear Fe surface layer was formed and the majority of Fe atoms contributing to the 702 eV for high Rh thickness is originating from below a closed Rh surface layer. Which supports the theory of intermixing of Fe into Rh for this particular sample. If the Fe was grown on a rough substrate surface of GaAs(100), it might not form a perfect layer at 5 nm final thickness. This could potentially create crystallite like mountains of Fe atoms with deep valleys. If Rh is evaporated, they will first fill up the valleys leading to a fast reduction of Fe surface peak intensity, with a constant change in slope as Rh is building up. This constant change of slope might be the reason for an exponential decay of the Fe surface layer intensity. Furthermore, if the Fe mountain peak is covered with Rh, the surface peak will vanish, but the higher energy peak will still contribute to an AES signal. The exponential decay of the Fe signal further suggests a monolayer followed by monolayer or further layer-by-layer deviated growth. An exponential, but still vanishing dependence of Fe, would therefore hint at several Rh layers forming at once, but closing at sufficiently high amount of deposited Rh (suggested by the comparison to schematics 3.6). This suggests the growth mode to be SK or monolayer followed by simultaneous monolayers. A clear differentiation between multi monolayer growth or crystallite growth, with this AES study, cannot be made. However, literature studies of Rh growth on Fe(100) have been made.

Busch et al. [10] investigated the growth of Rh on Fe(100) using AES and SPLEED measure-

ments. They found the "heteroepitaxial growth of Rh on Fe(100) at room temperature to deviate from a perfect pseudomorphic layer-by-layer growth". The growth begins layer-by-layer like and transforms into a growth governed by roughness with several layers exposed. Furthermore, through SPLEED they could find a Rh spin polarisation in the first few monolayers, whose strength is decreasing with increasing Rh thickness. This finding overlaps with previous spin polarisation experiments conducted on Rh and Fe systems, by Kachel et al. [9]. Both studies find Rh being polarised in the ultrathin film limit of a few monolayers. Although giving different origins of this polarisation effect, Kachel explains the origin of spin polarisation and ferromagnetism in monolayer Rh, to be the 3d- 4d band hybridisation between Rh and Fe, supported by ab initio calculations. On the other hand Busch observed a similar polarisation effect explained by an intermixing or interdiffusion effect of Fe into Rh, which was taken into account through simulations. Their polarisation might originate from a very rough growth of Rh and the ability of Fe to form an alloy with Rh. Additionally the alloy formation in Fe and Rh multilayers was studied in [73] using Mössbauer spectroscopy to investigate the hyperfine fields. They argue, that Fe and Rh potentially like to intermix with an interface alloy formation due to a wide solubility range of both Fe and Rh phase diagrams for low temperatures at 4.2 K. They observed the formation of both FCC-RhFe and BCC-FeRh alloy at the multilayer interfaces, with unclear thicknesses in the range of several Å. For the Rh growth mode determination, another study conducted by Pfandzelter [74] using grazing scattering of 50 keV He projectiles, repeatedly found Rh to initially grow in a layer-by-layer manner followed by multilayer growth.

In summary all of the above studies suggest a deviation of perfect layer growth. In contrast to the thermodynamic growth theories this could be an approximation of the SK growth of crystallites on monolayers or monolayers followed by simultaneous multilayers.

Based on the fast decrease to saturation of Fe and the fast increase of Rh, in the limit of the first monolayers of the studies in this thesis, these findings might be best described as an inefficient layer-by-layer growth. These studies, being only conclusive for the low Rh thickness range, give no result for the change in growth properties for higher thicknesses. Based on the fact, that a crossing point of Fe and Rh intensities is visible in most of the studies and the position of which lays close to the monolayer regime, a Volmer-Weber growth mode can be excluded from consideration. In the VM mode few layers form to a completion and especially the Fe surface peak would not vanish in ranges of the assumed first two monolayers, as it does in 4.4a. The growth might be best described in the theory of SK or monolayer followed by multiple monolayer growth, while the latter seems to be more likely in the case of the 0.3 Å dependence, based on the obtained results. Although, a clear differentiation, especially for the case of films thicker than the limit of one to two monolayers, can not be conducted based on the presented experiments. All experiments would need to have more data points with less noise and higher thicknesses to completely identify the final growth mode, ideally up to several nm of thickness.

Nevertheless, the results of this study have a very similar outcome to the determination of the growth mode of Rh on Fe to literature. Kachel [9], Busch [10] and Pfandzelter [74] suggest a Rh growth deviating from perfect layer-by-layer symmetry. While not explicitly naming any growth mode, literature explains the Rh surface to be very rough with multiple layers exposed, that in the theory of growth mode models, would fit into the category of Stranski-Krastanov growth, supported by studies made in this thesis.

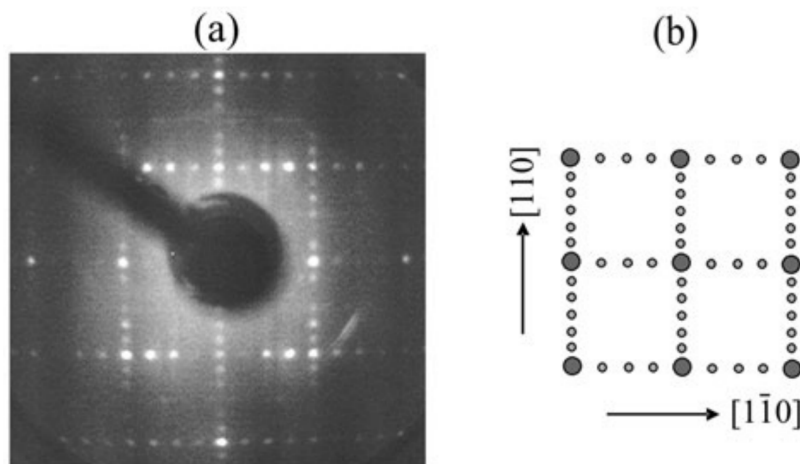


Fig. 4.5.: Example picture of a perfect GaAs(100) 4x6 LEED pattern at 124 eV. Taken from literature [64]

4.1.2. LEED

During the AES studies and sample preparation, LEED pictures were taken as the final step of a sample preparation. This includes LEED on GaAs(100), 5 nm of Fe and x nm of Rh. For batch-1, the LEED power supply was not working for a majority of samples, therefore the only LEED pictures available from this batch were made for the samples of 5 nm and 15 nm of Rh. The LEED images were taken using a ErLEED 100 optics from SPECS in combination with a CCD camera from JAI. The LEED energies and images were adjusted and obtained by in manual mode. A Python script to control the LEED power supply and obtain images from the CCD camera was written to the end of this thesis, but due to time reasons no IV-LEED experiment could be made.

LEED pictures of GaAs(100)

The LEED pictures for the GaAs(100) substrate, taken in this thesis after the substrate preparation steps to produce a (4x6) superstructure, showed the pattern visible in figure 4.5, with deviations in LEED dot intensities.

As already was mentioned, the substrates between Batch-1 and Batch-2 are from different GaAs(100) wafer. The Batch-2 wafer was a newly bought one. No difference between these wafers was assumed. Practically all samples in between one wafer, show a very similar pattern, that is different from the samples of the other wafer, whilst still representing a (4x6) superstructure. It must be pointed out, that for batch-1 only 2 samples could be measured with LEED, which is why batch-1 is underrepresented in order to be able to make a meaningful statement about all samples.

The Batch-1 wafer is referred to as wafer-1, an example LEED image can be seen in figure 4.6a. It was taken at a LEED energy of 150 eV and has very dominant horizontal lines of symmetry 4. Additionally it shows weak vertical lines, that represent a symmetry of 2. This implies the creation of a GaAs(100)(4x2) superstructure. For lower energies the (4x6)-pattern could not be seen. In contrast to this, the wafer-2 samples like figure 4.6b, taken at 118 eV, show a more pronounced square like pattern, in which the (4x6) symmetry is clearly visible. For higher energies at about 150 eV, around the same as in figure 4.6a, the same (4x2) symmetry is achieved. This shows, that the surface of films with a (4x6) pattern, comparable to figure 4.5, are of higher quality.

Based on the LEED patterns, the Ga surface concentration of wafer-1 films is assumed to be roughly the same as for wafer-2 samples, based on the fact, that both superstructure symmetries are

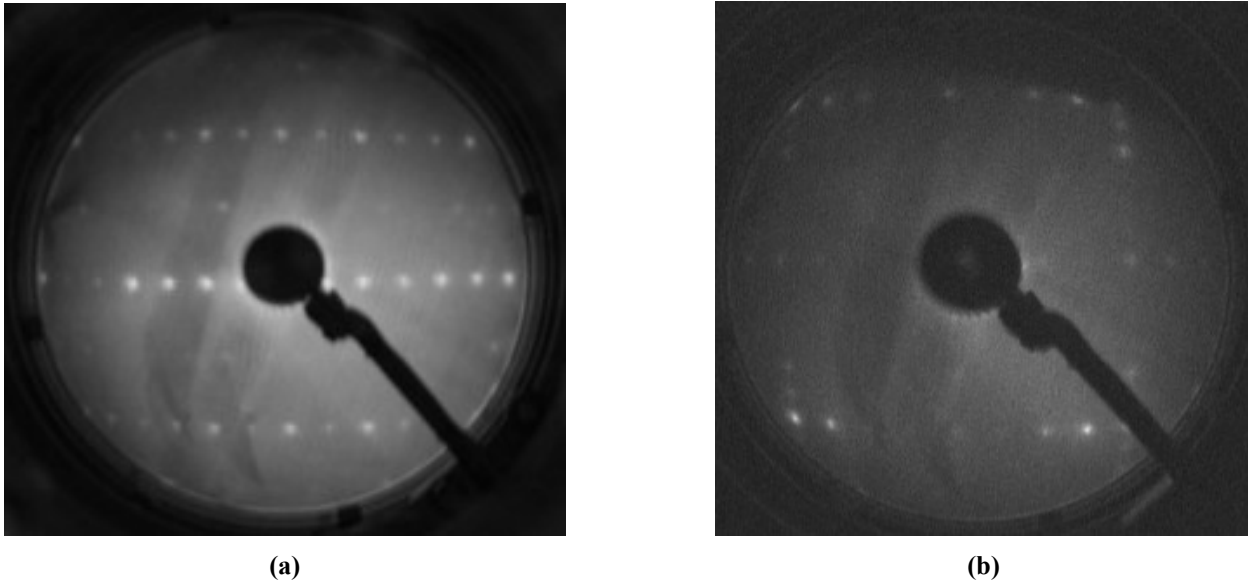


Fig. 4.6.: Example LEED pictures of prepared wafer-1 and wafer-2 substrates. Figure **a)** shows the GaAs substrate for Fe the of 0.4 Å Rh AES dependence at 150 eV, In figure **b)** the GaAs substrate of the 2 nm Rh sample of Batch-2 at 118 eV is presented.

present for the p(4x6) superposition. Though, no big change in magnetic anisotropies is expected for Fe layers thicker than 15 ML on either a (2x4) or p(4x6) rich substrate, as has been shown for the additional uniaxial and cubic anisotropy of Fe on (4x2)- and (2x6)-GaAs(100) [65]. The real origin of the difference in the surface quality, although the recipe of sample preparation stayed the same, is unknown. Assumptions can be made:

Sputter gun Between batch-1/wafer-1 samples and batch-2/wafer-2 samples, the sputter gun and LEED power supply were repaired and exchanged. Especially the sputter gun, after the usage of a few minutes, exerted a "Filament Fail" - error, whilst still functioning, as measured of a sample current of about 1 μA .

Sample annealing For annealing the sputtered GaAs substrates were heated to temperatures of about 960 K. During the course of this thesis, the sampleholder including the heater has been renewed. Because this heater is handmade, small deviations in positioning and mounting are possible, among which the difference of the K-type thermocouple position would play the biggest role in the determination of temperature. However, the possible temperature difference is not expected to be significant, since the sampleholder is made of Cu which is characterised with excellent thermal conductivity.

Wafer quality Any change in contaminant ratio between the batches can not be excluded. Since the age difference of both wafers is in the range of about 10 years, differences in the cutting misalignment or surface polishing might be present. Even the growth method might have varied, producing slightly different substrates.

LEED pictures of 5 nm Fe

It has been shown in several papers, that Fe grows epitaxially on GaAs(100) surfaces intially in the Volmer-Weber growth mode following to layer-by-layer like growth for higher thicknesses [75, 76]. Despite initial growth in crystallites, LEED patterns can be observed. The films grown on

top of the GaAs(100)-p(4x6) substrate surface are of symmetry Fe(100). In figure 4.7a a literature example of Fe/GaAs(100)-p(4x6) is shown [76]. Some example LEED patterns observed during the sample preparation are shown in 4.7b.

In comparison to literature, the example LEED pattern of a 5 nm Fe film used in this thesis, shares a very similar LEED symmetry. In the case of figure 4.7b, LEED pictures were taken up until a maximum LEED voltage of 1000 eV. The symmetry of these patterns is clearly visible until 650 eV. After this, for 895 eV and for 1004 eV, a similar symmetry to 650 eV is visible, which could also be interpreted as background noise or residual luminosity of the fluorescent LEED screen. The fact, that a symmetry can be seen at least up to 650 eV with relative small dot sizes being distinctly differentiable from the background brightness, points to a surface lattice with a low roughness and high periodicity. A comparable LEED pattern of Fe was achieved for samples 1 nm, 3 nm of Batch-2. For the samples of 5 nm, 10 nm and 15 nm, Fe patterns were visible but not as defined and sharp as compared to figure 4.7b at 118 eV.

LEED pictures of Rh grown on Fe, in various thicknesses

The LEED pictures of Rh after evaporation can be found in figure 4.9. Overall, the LEED patterns of Rh were more difficult to obtain. From batch-1 only the 15 nm rhodium sample shows a weak symmetry at 289 eV as can be seen in figure 4.9a on the top left. For batch-2, samples with 1, 2 and 3 nm Rh showed the best patterns, with roughly the same pattern quality, of differences only in stability to higher LEED energies above 400 eV. Samples 5, 10 and 15 nm deviate from these pictures as can be seen in the middle pictures. While more diffuse spots were observed, the symmetry kept the same.

In figure 4.9b a direct comparison of Rh to Fe LEED patterns is presented. The sample shown is the 2 nm Rh sample, that has been already discussed for Fe patterns. At the same LEED energies, Rh shows roughly the same LEED pattern as Fe. The only noticeable difference, is the spot intensity, sharpness of peaks and dependence on the LEED energies higher than 500 eV. An AES measurement was done to confirm the existence of a Rh layer (figure 4.10). The AES analysis shows the Rh high energy peaks at 300 eV and the low energy surface peak at 40 eV. A small peak at 703 eV can be interpreted as Fe peak. In the context of a 2 nm Rh layer and a electron mean free path of about 1.43 nm at energies of 700 eV, as can be found from 4.2, this Fe peak could originate from underlying Fe capped by Rh. The Rh AES intensity, especially the surface peak, suggests a clean Rh surface, ruling out an effect of mispositioned substrate or other problems during evaporation.

This finding confirms, that the LEED patterns presented in figure 4.9b are originating from a Rh surface. The matching patterns can be interpreted as fcc Rh growing with a 45° rotation on the bcc-Fe lattice. Usually high strain of the first few monolayers is expected, as of a lattice mismatch of about 6 %. This strain should relax in higher Rh thicknesses, forming bulk like Rh structures.

Thus, the LEED experiments further suggest an epitaxial growth of Rh on Fe, especially in the case of 1 nm LEED patterns as they present the least thickness and are more affected by interface effects. Strain at the interface would then be considered as epitaxial strain from heteroepitaxial crystal growth.

Together with the LEED image on the 50 hour old 5 nm Rh batch-2, the AES scan of figure 4.10 suggest very little surface oxidation effects of Rh. This might be due to the very high vacuum ($2\text{E}-9$ mbar to $5\text{E}-11$ mbar in 8 hours, then continuously at $5\text{E}-11$ mbar), as less amount of residual material can be adsorbed. adsorbate s consisting of oxygen should be visible in the AES scan at an 24+ hours old sample. The fact, that oxygen peaks can not be seen points out a high vacuum

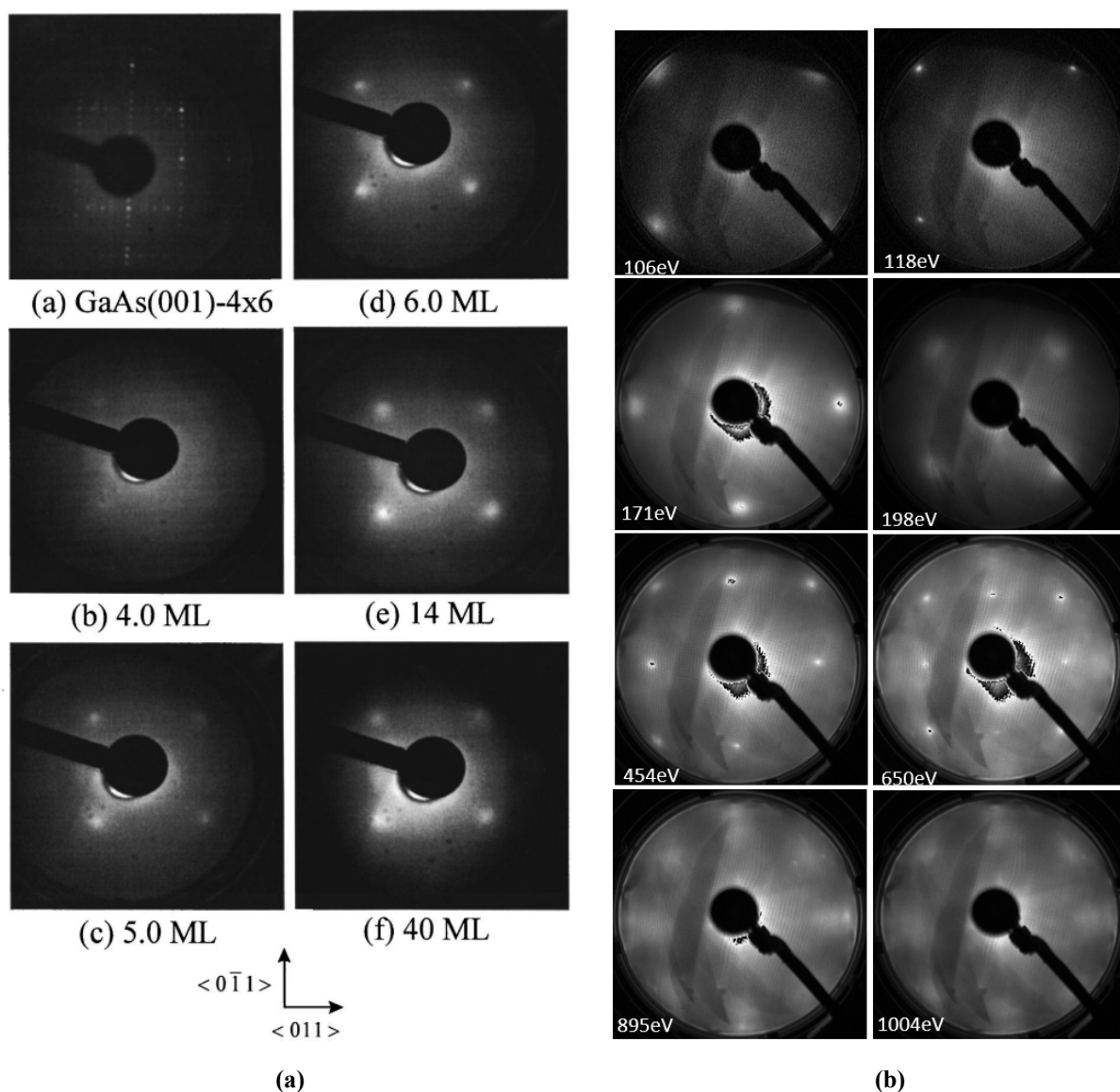


Fig. 4.7.: Figure a) shows the LEED images for prepared GaAs(100)-p(4-6) at 135 eV and Fe layers at 120 eV, taken from [76]. Example LEED pictures of a 5 nm Fe film, directly after evaporation, are found in figure b). This Fe belongs to the 2 nm Rh sample of Batch-2.

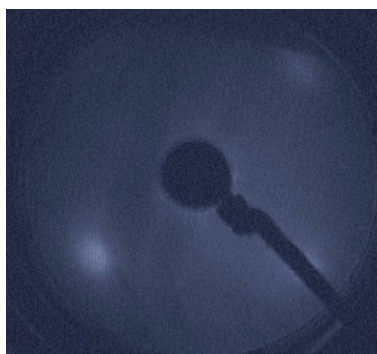


Fig. 4.8.: Example LEED picture for Fe films with worse pattern as for 2 nm Rh sample of Batch-2 in figure 4.7b. The sample shown in the picture is the Fe layer of the 5 nm Rh Batch-2 sample at 149 eV. The picture has been enhanced in brightness and contrast, to make the dots visible

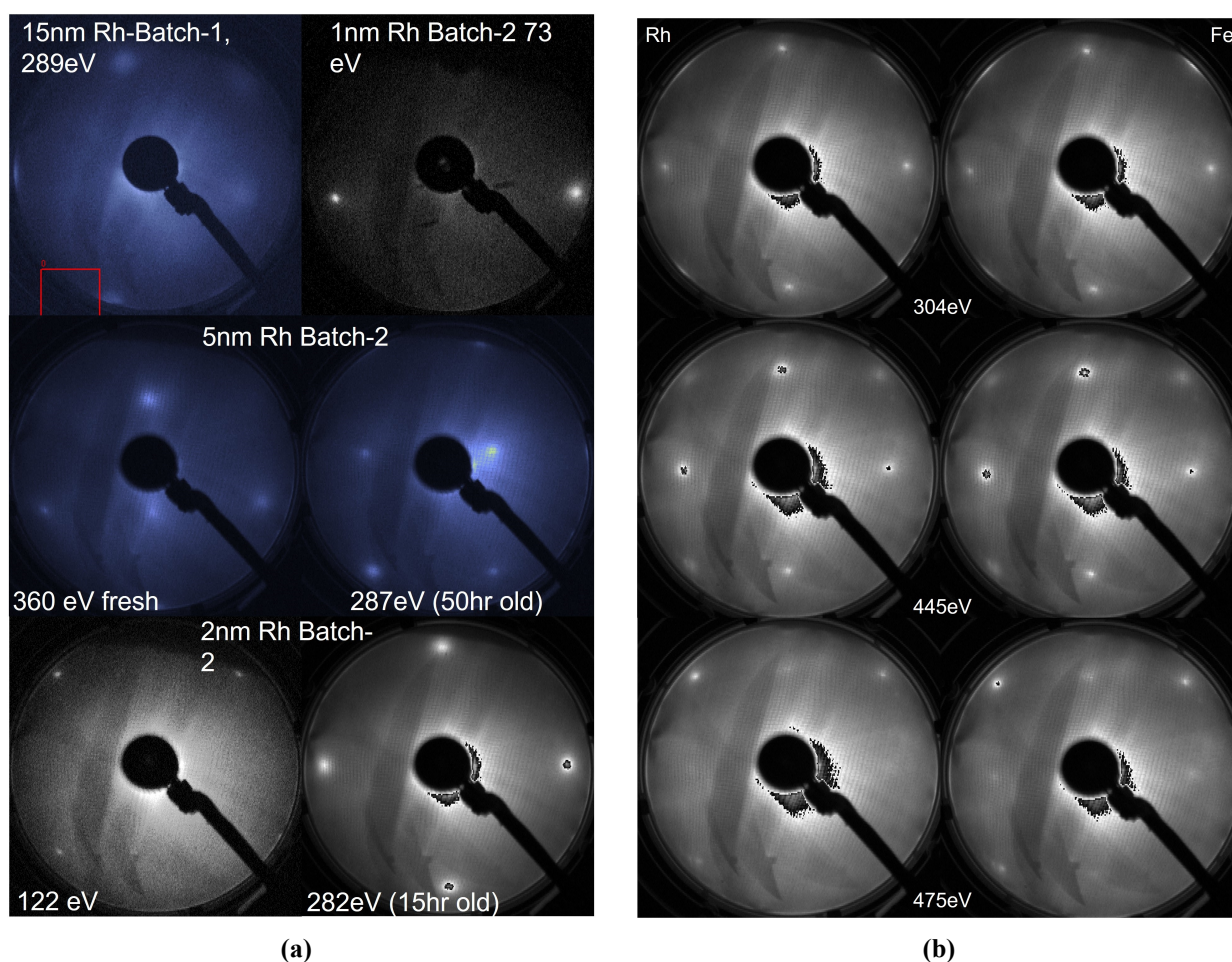


Fig. 4.9.: LEED images of **a)** Rh, and **b)** a comparison between Rh and Fe at the same energies of 2 nm Rh Batch-2 sample. Besides 289 eV of 15 nm Rh Batch-1 no picture was enhanced. The red box is a residual box from the LEED acquisition software used in the beginning and was not placed to focus on this area in particular. In the pictures of 5 nm Rh Batch-2 a misalignment of the sample holder is present.

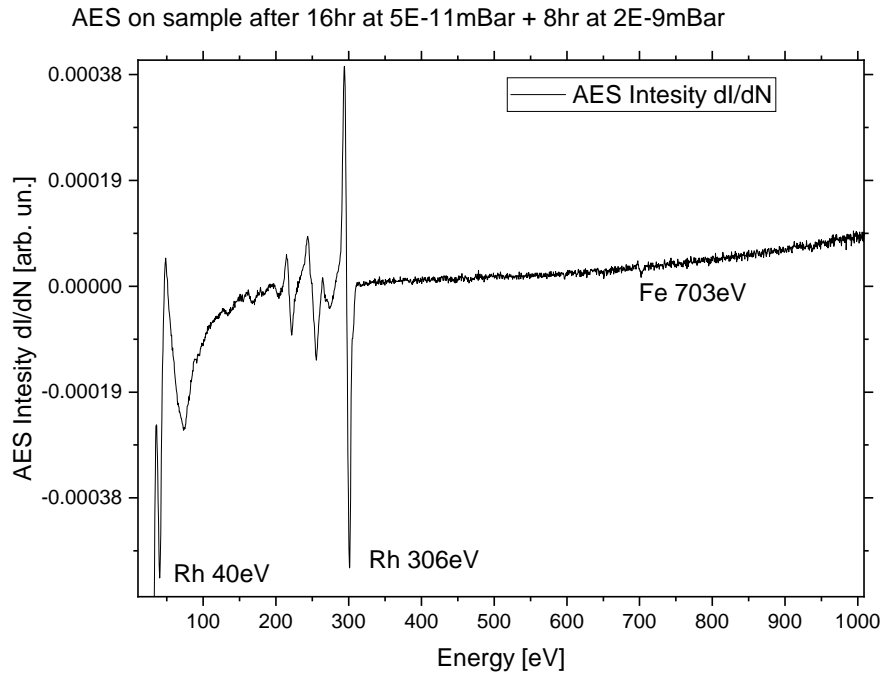


Fig. 4.10.: Analysis of the 2 nm Rh batch-2 surface using AES-spectroscopy. This measurement was done utilising a sample current of $4.5 \mu\text{A}$.

quality or high oxidation resistance of Rh.

Additionally, the AES scan plus the 50 hour old LEED patterns of 5 nm Rh batch-2, suggest very little surface oxidation effects of Rh. This might be due to the very high vacuum, as less contaminants can be adsorbed. Adsorbates consisting of oxygen should still be visible in the AES scan at an 24+ hours old sample. The fact, that these cannot be seen points to a high vacuum quality or high oxidation resistance of Rh.

4.2. Ferromagnetic resonance analysis

The FMR analysis deals with the extraction of the resonance line of both angular and frequency dependent FMR measurements. Further, the lineshape gives rise to several more detailed analyses of magnetic anisotropies, g-factor and magnetic damping. The chapter starts by extracting the g-factor of each sample out of frequency dependencies in both hard and intermediate direction, which is later used for both anisotropy and damping determination. All measurements were done at room temperature. The term "hard axis" refers to the $[110]$ and $[\bar{1}\bar{1}0]$ crystallographic orientations of Fe, the "intermediate axes" have an offset of 90° to the hard axes, therefore refer to orientations $[\bar{1}10]$ and $[1\bar{1}0]$.

Cavity based angular dependencies at about 9.5 GHz were done for all samples. Frequency-dependent measurements have been performed for all samples of Batch-1 and Batch-2 except 15 nm Rh Batch-2. After evaporation of all samples the FMR characterisation took place. There were many difficulties in recording frequency dependencies with the CPW-FMR setup. Due to a failing magnet power supply, that has been repaired several times during this thesis, frequency dependent characterisation got delayed for several months and finally could not be conducted for 15 nm Rh batch-2 sample and only partly for 2 nm Rh batch-2, in which the intermediate axis could only be characterised up to 22 GHz. A VNA based FMR setup has been tested for 5 nm Rh batch-2,

whose outcome is presented in the appendix A.2, but due to limited time no further measurements or analysis could be done.

4.2.1. Determination of the g-factor and anisotropies

The CPW setup was used to obtain both frequency dependence and angular dependence measurements. The frequency dependent measurements were taken using the field sweep method of obtaining a ferromagnetic resonance. In these the frequency is set constant and the field is varied from 0 to 900 mT in 4096 points. For each point, the field is kept constant for twice the duration of the lock-in amplifier time constant of $TC = 40 \mu s$. In comparison to the magnetisation deflection, which happens in orders of nano seconds, the change in external field can be considered as static. This means, although the external field is changed in steps of micro seconds, the system can still be considered as saturated and static and the Smit-Beljers-Suhl and LLG equation applies. Regarding the 4096 field steps, assuming a small linewidth of about 3 mT, results in about 13 points per line-shape, which is sufficient enough to reproduce a resonance line without distortion. After a field sweep the frequency is increased in steps of 0.5 GHz until 40 GHz are reached.

The angular dependences, using a CPW, were measured using a goniometer and a stepper motor controlled by the Bruker acquisition program. The sample was mounted onto a plastic sample holder and placed on top of the CPW with a layer of parchment paper to protect both sample and CPW stripline while the sample is turning. Under a constant frequency of 13 GHz an angular dependence was acquired by sweeping the field from 0 to 300 mT and changing the sample angle in steps of 5° or 1° after each field sweep. A full angular dependence consists of a full rotation of 360° . Another angular dependence was done after the first one, to fully identify the hard and intermediate axes of a sample. These second "axis search" measurements were done with a angle resolution of 0.5° per step to search the distinct crystallographic axes, like hard and intermediate axes. This means every CPW frequency measurement with fixed axes has a angle offset of $\Delta\phi = \pm 0.5^\circ$.

A frequency dependent measurement oriented in hard axis direction can be seen in figure 4.11. This sample was prepared in the course of batch-1 and has a 5 nm Fe base layer on GaAs(100) of wafer-1 measured at room temperature with a Rh thickness of 2 nm. In this graph, the Y-Axis is the Frequency in GHz, the X-Axis is the magnetic field value in T and the colour value is the intensity of the absorption signal according to the scale on the top side. The resonance positions can be seen as the change from dark orange to yellow. The hook between field 0 - 100 mT and 0 - 10 GHz represents the non-aligned mode. In this region multiple resonances at the same frequency can be found. Their origin lies, as the name suggests, in a fulfilment of the resonance condition, where the magnetisation is not aligned with the externally applied field, as described in chapter 2.1.3. The resonance position of the individual spectra can be fitted using the Flovik lineshape or the complex Lorentzian lineshape described in chapter 2.1.3, latter has been used, due to the property of the complex Lorentzian of being less error prone in fitting algorithms. Using the resonance position of these lineshapes, one can fit the g-factor as a function of the frequency dependence of the resonance positions $f(H_{res})$ equation 2.50. The resulting fit parameters are g, M_{eff} , H_1 and H_2 . The anisotropy fields H_1 and H_2 are superimposed with many different anisotropy contributions and are fitted to compensate the residual slope of the square root behaviour. Furthermore the orientation is set constant, in which the determination of orientation dependent parameter is bound to a big error. Therefore the g-factor was first extracted from the frequency dependence and afterwards the angular dependence was used to determine the anisotropies of the films with respect to their previously fitted g-factor. This procedure was iteratively repeated to acquire a complete set

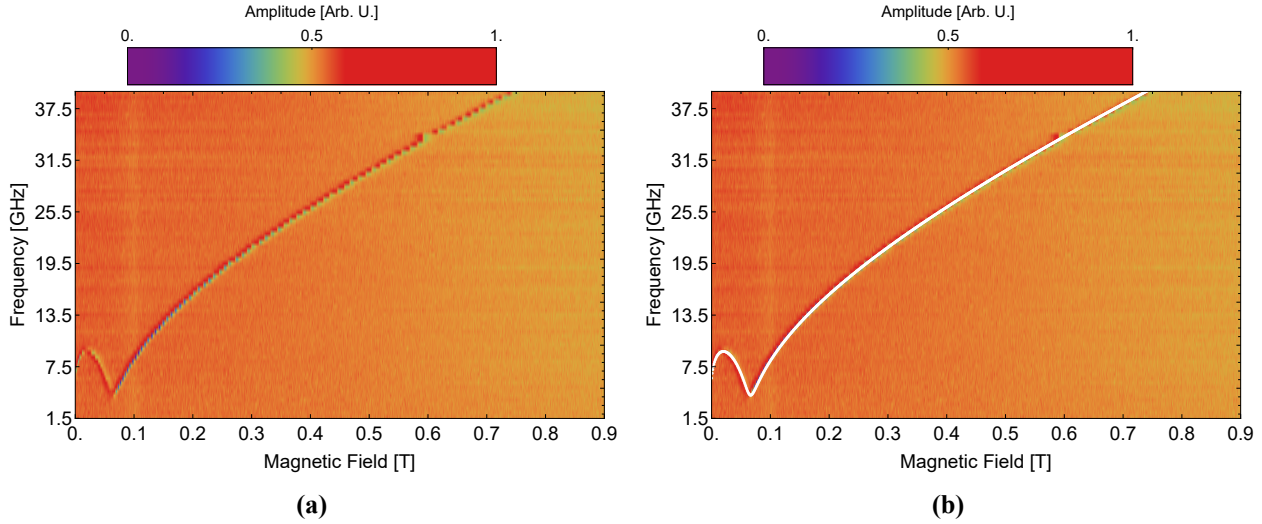


Fig. 4.11.: In figure **a**) a in-plane CPW-FMR frequency dependence measurement, oriented in hard axis Fe[110], is visible. Figure **b**) shows the calculated and overlaid resonance position, according to an iterative fitting method of anisotropies, misalignment and g-factor. The sample shown is 2 nm Rh of batch-1. The anisotropy was determined to be $K_{2\perp} = 340000 \pm 50000 J/m^3$, $K_{2\parallel} = 22000 \pm 2000 J/m^3$ and $K_{4\parallel} = 33813 \pm 1500 J/m^3$. The g-factor is $g = 2.11 \pm 0.02$ and additionally a hard axis misalignment of $0.01 \text{ rad} \approx 0.57^\circ$ was found.

of parameters (g-factor, M_{eff} , anisotropies) consistently describing a full data set (frequency- and angular-dependent measurements).

The g-factors of each sample were evaluated for both intermediate and hard axis. For the hard axis, the results can be seen in table 4.1 and figure 4.12. The results for the intermediate orientation can be found in table 4.2 and are plotted in figure 4.13.

The 0 nm Rh point in the tables and the green triangle in the figures represent an uncapped 5 nm Fe film. This reference film was grown on the same chamber with the same equipment as all of the other samples by Babli Bhagat [77]. The substrate is GaAs(100)-p(4x6) and is from the same wafer as the substrates of batch-1. Additionally a reference literature value can be seen as the orange star in both hard and intermediate plots. The literature value of $g_{\text{lit}} = 2.11 \pm 0.008$, was measured on GaAs(100)-(2x4) superstructure with an Fe thickness of 5 nm capped with 3 nm of Al [41]. Frequency dependent measurements were done in [110] and $[\bar{1}\bar{1}0]$. The individual g-factors were evaluated to be constant and the authors believe the g-factor to be isotropic.

For batch-1 the 1 nm Rh sample shows the highest g-factor with a value of $g = 2.13 \pm 0.03$ for the hard axis and $g = 2.19 \pm 0.2$ for the intermediate orientation. For both batches in hard axis, a initial slope of the g-factor, in the range of 1 to 2 nm of Rh thickness is visible. For higher Rh thicknesses, the g-factor dependence on Rh can be assumed to be constant within the error bars. For batch-1 samples, the average g-factor is $g = 2.11$ and for batch-2 without 15 nm Rh the average g-factor is $g = 2.104 \pm 0.0054$. By neglecting the batch-1 1 nm Rh point, the average g-factor is reduced to $g = 2.108 \pm 0.0083$. From these two datasets, the overall g-factor for the hard axis [110] orientation is $g = 2.106 \pm 0.009$. The reference point at $g = 2.117 \pm 0.002$ is out of reach for the average value in the limits of the standard deviation. The g-factor dependence on Rh shows a positioning around 2.11, which leads the average value of $g = 2.106 \pm 0.009$ to describe this sets of data more accurately.

In comparison to the hard axis, the intermediate axis g-factors are very stable around the uncapped reference sample of $g = 2.103 \pm 0.001$. The maximum deviations from $g = 2.1$ for batch-1

Table 4.1.: The g-factors for all samples in **hard axis** [110] orientation evaluated as a fit of the frequency dependence of the resonance field according to the Kittel equation 2.50. The 15 nm Rh sample of batch-2 could not be measured in a frequency dependence. The g-factor is assumed to be constant over all samples, therefore the g-factor of 15 nm was assumed to be $g = 2.11$ for further angular dependent anisotropy estimation.

Rh-Thickness [nm]	0	1	2	3	5	10	15
Batch-1:	2.117 ± 0.002	2.13 ± 0.03	2.11 ± 0.02	2.1 ± 0.015	2.1 ± 0.03	2.11 ± 0.03	2.12 ± 0.05
Batch-2:	2.117 ± 0.002	2.11 ± 0.02	2.1 ± 0.02	2.1 ± 0.01	2.11 ± 0.02	2.1 ± 0.03	assumed to be 2.11

is visible in the 1 nm Rh sample with a g-factor of $g = 2.19 \pm 0.2$ and for batch-2 the 2 nm Rh sample with a value of $g = 2.12 \pm 0.02$. The average value for batch-1 excluding 1 nm Rh is $g = 2.108 \pm 0.011$ and for batch-2 a average value of $g = 2.1 \pm 0.013$ is found. In the case of the intermediate axis, the reference uncapped value is met perfectly with an average g-factor of both batches of $g = 2.104 \pm 0.005$.

The comparison of both hard axis and intermediate axis g-factors shows only a small difference, that lays in the standard deviation of the measurement points. For this system of thin film Fe/Rh samples an anisotropic g-factor, in in-plane orientation, is not present. The absence of an anisotropic in-plane g-factor, in context of the ratio between spin magnetic moment and angular magnetic moment as described in equation 2.4, points to the fact, that the difference in LS-coupling must be near equal, or very small, in the hard and intermediate orientations of this cubic crystal. This also might point to a high cubic crystal quality, as lateral distortions would give rise to a unquenching of orbital moments in certain orientations along the distortions. Effects like band hybridisation and crystal distortion might also explain the initial slopes visible in the 1 nm and 2 nm Rh samples (figure 4.12 and 4.13).

As already pointed out, the LS-coupling will affect the g-factor. In the case of Rh thin film layers on Fe and by assuming the SK-growth mode, the first few monolayers should cover the Fe surface completely. With a thickness of 1 nm Rh, the effects like band hybridisation or stress on either Fe or Rh crystal lattice might not be saturated yet, giving rise to an increase or decrease of the g-factor and anisotropies. At a certain thickness however these effects should be saturated and should not change over additional Rh thickness. This might explain, why the g-factor values stay rather constant after a thickness of 3 nm, with an increase of the error bar due to experimental circumstances. A interpretation of 1 nm Rh of batch-1 should be taken with care. This sample has in both hard and intermediate orientations not only a very big error bar, but also a very high value compared to other samples. This can be explained by the circumstances of how the sample was produced. While the evaporation of 5 nm Fe was flawless, the evaporator had a malfunction with Rh and had to be repaired before continuation of the sample growth. The repair took one day, during which the 5 nm Fe layer was exposed to a increasing vacuum of $5\text{E-}9$ mbar after evaporation, to $5\text{E-}11$ mbar after repair and bake out of the evaporator. By assuming an exponential decay in vacuum pressure, the pressure can be modelled as: $p(t) = c \exp\{-\lambda t\}$. The coverage in Langmuir can be modelled as: $L(t) \approx 4/3 \cdot 10^{-6} \cdot t \cdot p(t)$. By assuming an exposure time of 60000 s, the coverage of the Fe surface assuming a perfect sticking coefficient, might be in the range of 1.06 L. This means approximately one monolayer of adsorbate has been formed on the Fe surface in the ideal case, before evaporating Rh. Furthermore, the 1 nm Rh layer might not be sufficient enough to act as a protection layer to prevent oxidation of Fe. In general the role of Rh as a protection layer has not been investigated, but by the fact, that Rh is a precious metal growing epitaxially on Fe, a protective behaviour might be assumed.

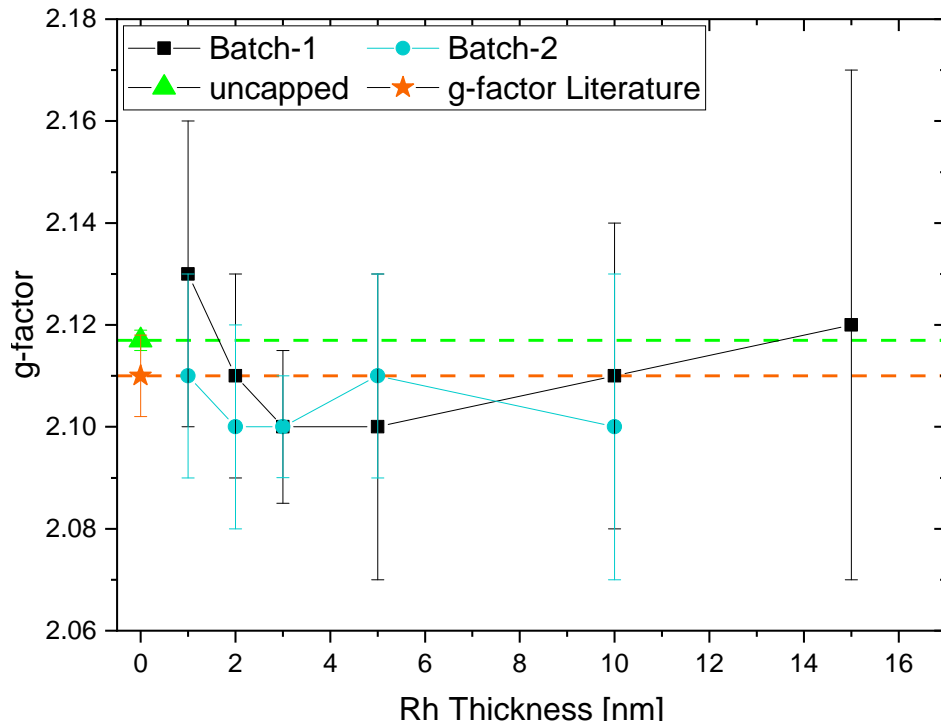


Fig. 4.12.: Plot of the g-factors for **hard axis** [110]. A uncapped reference sample of 5 nm Fe on GaAs(100)-(4x6) was added as the green triangle at $g = 2.12$. Furthermore, a value taken from literature $g_{lit} = 2.11 \pm 0.008$ is presented as an orange star [41]

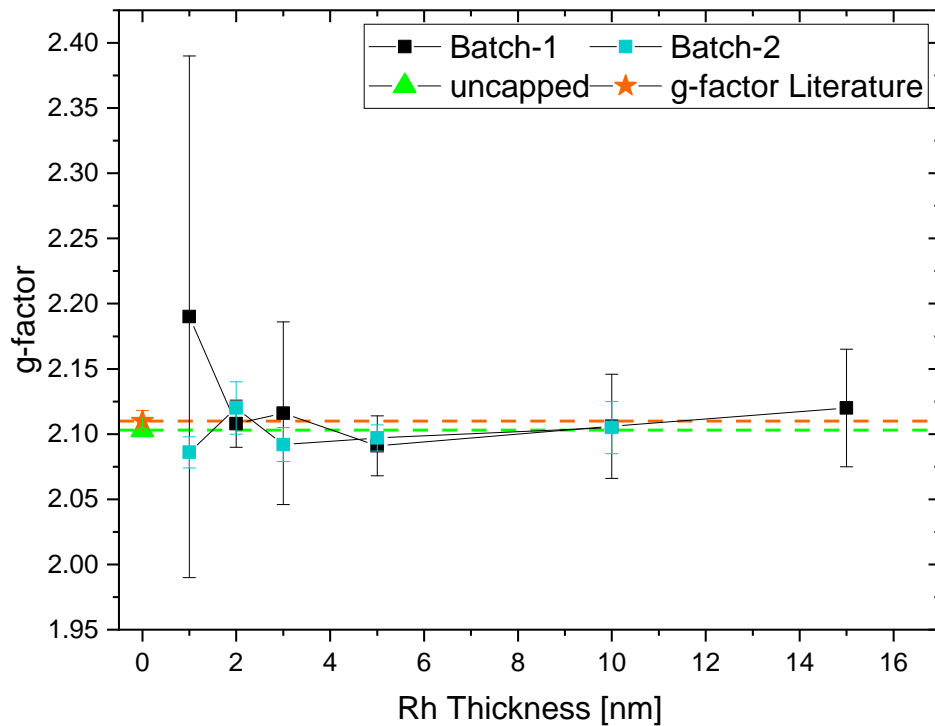


Fig. 4.13.: Plot of the g-factors for **intermediate axis** [110]. A uncapped reference sample of 5 nm Fe on GaAs(100)-(4x6) was added as the green triangle at $g = 2.1$. Furthermore, a value taken from literature $g_{lit} = 2.11 \pm 0.008$ is presented as an orange star [41]

Table 4.2.: The g-factors for all samples in **intermediate axis** $[110]$ orientation evaluated as a fit of the frequency dependence of the resonance field according to the Kittel equation 2.50. The 15 nm Rh sample of batch-2 could not be measured in a frequency dependence. The g-factor is assumed to be constant over all samples, therefore the g-factor of 15 nm was assumed to be $g = 2.1$ for further angular dependent anisotropy estimation.

Rh-Thickness [nm]	0	1	2	3	5	10	15
Batch-1:	2.103 ± 0.001	2.19 ± 0.2	2.108 ± 0.018	2.116 ± 0.07	2.091 ± 0.023	2.106 ± 0.04	2.12 ± 0.045
Batch-2:	2.103 ± 0.001	2.086 ± 0.012	2.12 ± 0.02	2.092 ± 0.013	2.097 ± 0.01	2.105 ± 0.02	assumed to be 2.1

In the further analysis, the individual g-factors of each sample were used, instead of the estimated mean values of $g_{hard} = 2.106 \pm 0.009$ and $g_{intermediate} = 2.104 \pm 0.005$.

Determination of the anisotropies

A qualitative analysis of the IP anisotropies was done by iteratively interpreting both cavity and CPW angular dependencies and CPW frequency dependence. This includes using the anisotropies from the angular dependence together with the g-factor of the resonance position of the frequency dependence to calculate the resonance position for a frequency dependent measurement. This was done by solving the Basalgia-equation (2.46) for ω and fixing the angles to $\theta = \pi/2$ as well as $\phi = \pi/4$, this results in the Fe IP-[110] direction. For a given set of field points $H \in (0, 0.9)$ T, a resonance position ω_{res} could be found according to the anisotropy and g-factor. By fitting this outcome to the obtained frequency dependent resonance positions of the respective sample, also including the non-aligned modes, using slightly different anisotropy parameters and including a hard axis offset, a new set of anisotropies might arise. This newly obtained set is then used to reevaluated the angular dependence. By iteration, a optimal set of anisotropy parameters can be obtained. One has to note, that the ω_{res} -fit-to-measurement iteration was not automatised, due to missing time to program and test a fitting algorithm. This means the calculated resonance positions were overlaid with the measurement data by manually. The errorbars of the manually fitted parameters were appropriately adjusted.

In the FMR experiment, the anisotropy can only be obtained as an anisotropy field. However, in the anisotropy fitting methods, utilising a fixed saturation magnetisation, the anisotropy parameters are extracted. To compare the strength of the anisotropy contributions, the anisotropy parameters were converted back to anisotropy fields $\mu_0 H_{K_i}$ expressed in Tesla, according to equation 2.33. For this and further analysis, the saturation magnetisation was set constant to $M_s = 1800$ kA/m or $\mu_0 M_s = 2.01$ T.

In the case of batch-1 samples, all samples were measured at least once in an in-plane cavity angular dependence at frequencies of about 9.5 GHz. This means the resonance positions in hard axes orientations are superimposed of multiple resonance positions due to the non-aligned modes, as already explained in figure 2.8, creating loop-like resonance dependencies. In order to rule out errors during fitting, for batch-2 additional CPW based angular dependencies at 13 GHz were made, in which the non-aligned mode is not present anymore.

This means for batch-1 the anisotropies were evaluated from two measurements, one frequency dependence and one IP angular dependence, while batch-2 samples had three measurements, two IP angular and one frequency dependence. Out-of-plane (OOP) angular dependencies were only done for samples 2 nm and 5 nm Rh of batch-1. As will be shown later with support of the OOP measurements, the hard axis resonance position of the samples lays in the range of 2.2 T and above. For this current setup, the water cooled magnet can only reach such field with great distress of the

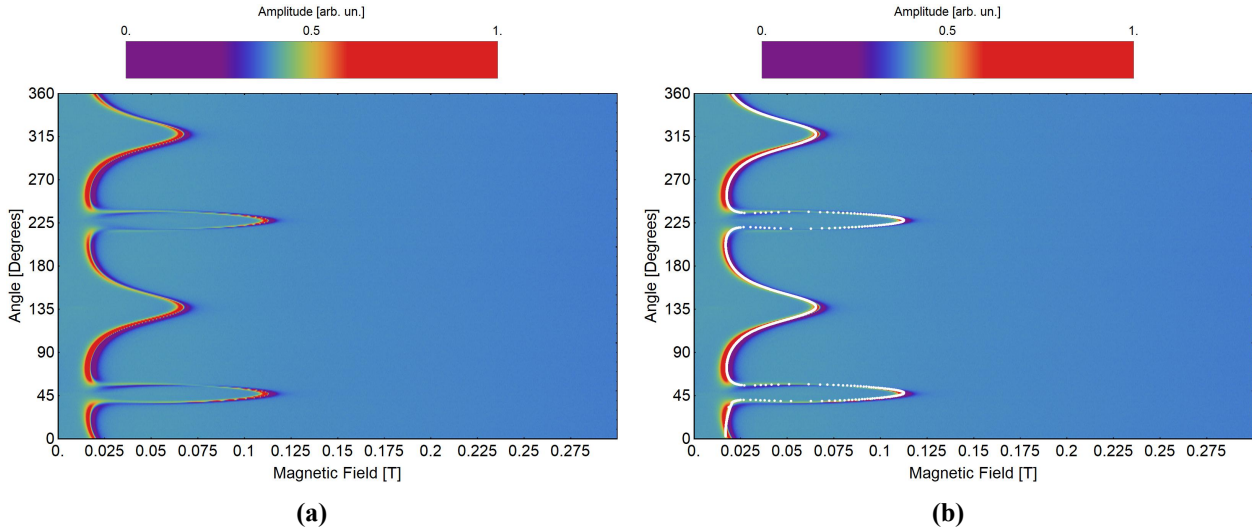


Fig. 4.14.: In figure **a)** a in-plane cavity angular dependence measurement of 2 nm Rh of batch-1 is shown. The angle was varied from 0° to 359° in 1° steps. For each step the external field was varied from 0 to 0.3 T in steps of 2048 points and a microwave frequency of $f = 9.543$ GHz was used. The hard axes at 45° and 225° correspond to Fe $[110]$ and $[\bar{1}\bar{1}0]$ directions. Figure **b)** shows the calculated resonance position as white dots; the non-aligned mode loops are calculated as well. The anisotropy was determined to be $K_{2\perp} = 340000 \pm 50000 J/m^3$, $K_{2\parallel} = 22000 \pm 2000 J/m^3$ and $K_{4\parallel} = 33800 \pm 1500 J/m^3$. The g-factor is $g = 2.11 \pm 0.02$.

power supply, which has to be driven up to 120% capacity to reach 2.15 T. To protect the system, no further OOP measurements were done on these samples. This means the OOP anisotropy parameter $K_{2,\perp}$ can not be evaluated precisely. Furthermore parameter $K_{4,\perp}$ shows no effect in IP direction and can only be evaluated from OOP measurements. In the following this parameter was set constant to $K_{4,\perp} = K_{4,\parallel}$ and $K_{2,\perp}$ was evaluated with a big error. Taking the 2 nm Rh sample of batch-1 as an example, the anisotropy parameters were extracted as follows: First the cavity angular dependence was used to extract a series of three sets of anisotropy parameters. For this the Baselgia equation, including the Helmholtz free energy density (2.31), was solved for the field H . This field represents the resonance field at a constant frequency. While solving for the equilibrium positions, as described in chapter 2.1.3. Each set was slightly offsetted in the ϕ angle used for the calculation, which produces a slight deviation in anisotropy values. By combining all values, a mean value plus additional error could be evaluated. According to these values, the resonance position can be evaluated and overlaid with the angular dependent measurement, as shown in figure 4.14. In order to account for the resonance loops in 45° and 225° ($[110]$ and $[\bar{1}\bar{1}0]$) in the angular dependence, the resonance positions can not be calculated easily by the angular dependent resonance condition of equation 2.46. To account for the non-aligned modes, the frequency dependence was calculated for each angle $\phi \in (0, 359)$ in steps of 0.2° . This creates a 3 dimensional dataset of both angle and frequency varied resonance position, as can be seen in figure 4.15. By interpolating between the resonance positions and extracting intercepting points with a line of constant frequency in the dataset, the resonance position together with the resonance loops can be found as multiple intersections of the dataset with the constant frequency. A qualitative analysis includes the comparison of calculated lines with extracted resonance position of the angular dependence.

Using this method, two sets of anisotropy parameters are found, one for the cavity based angular dependence and one set for the frequency dependence. The data can be found in table 4.3. The IP anisotropies are found to overlap for both frequency and angular dependence. In contrast,

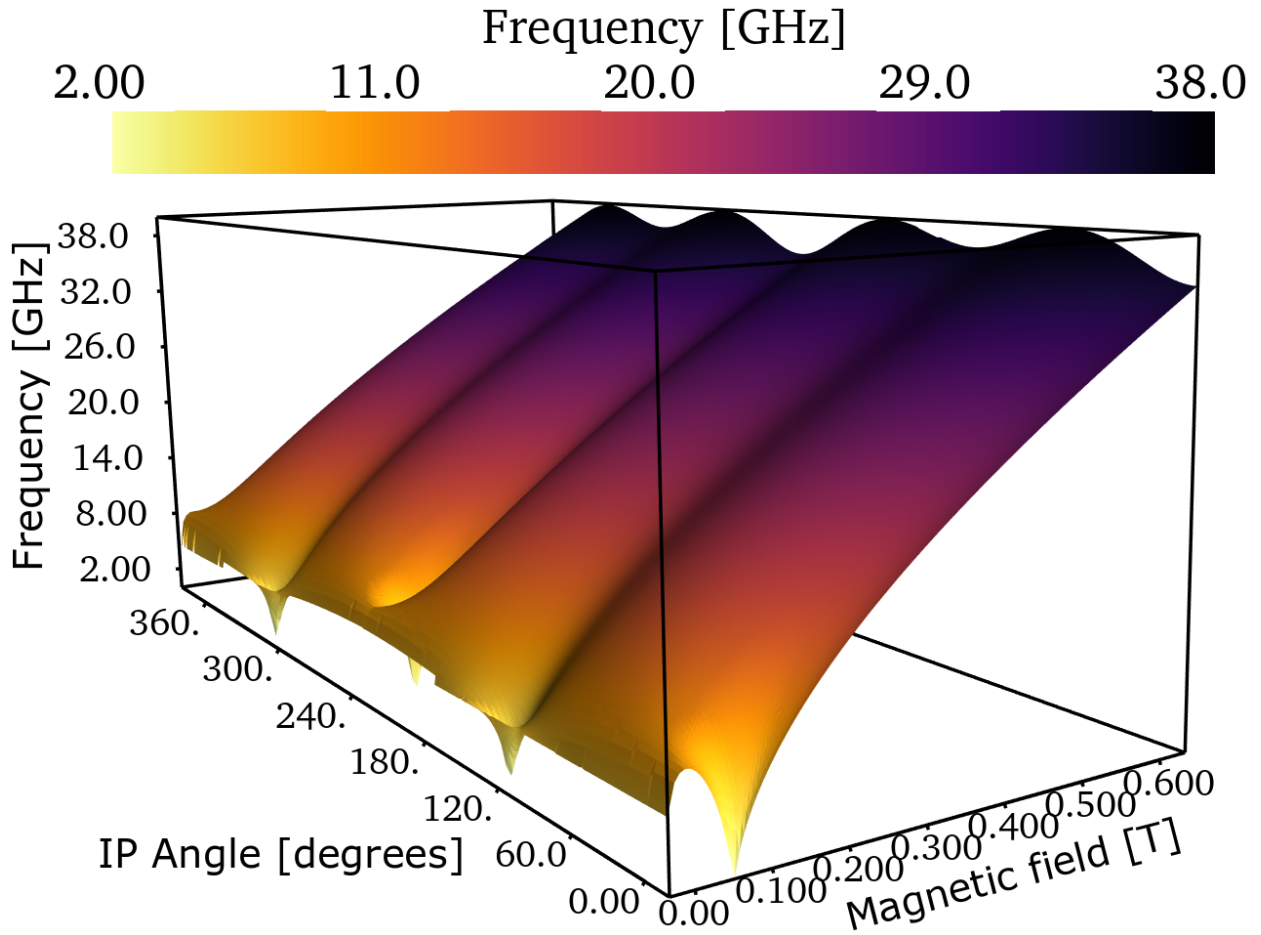


Fig. 4.15.: This 3D plot shows the angular and frequency dependence on the resonance position. The field was varied between 0 to 0.6 T in steps of 0.001 T. The resonance frequencies were calculated for each field step. This was done for angles from 0° to 359° in steps of 0.2°. As anisotropy parameters, the anisotropies of 2 nm Rh of batch-1 were taken. If one keeps the frequency constant, which would create a 2D plane in the XY orientation, the intersections with this plane would correspond to the angular dependence matching the constant frequency. For the case of non-aligned modes, multiple intersections are found, corresponding to multiple resonance positions at one angle, creating the resonance loops. One could explain this 3D plot as the angular dependence of the frequency dependence of the FMR as seen in figure 2.7. The minima positions (cones) at 0° and 180° show the hard axis non aligned modes. For 90° and 270° the intermediate axis can be found.

Table 4.3.: Anisotropy fields for two methods of anisotropy estimation. The values belong to sample 2 nm batch-1. As the names suggest, $\mu_0 H_{K_{2,4||}}$ are the anisotropy field of anisotropy parameters $K_{2,4||}$. The parameter $K_{2\perp}$, as described in chapter 2.1.2, is described in term of M_{eff} . Cavity ϕ -Fit stands for the anisotropy of the cavity angular dependence, while CPW f-Fit stands for the anisotropies obtained through aligning the resonance frequency to the measurement data.

Anisotropy-Field [mT]	$\mu_0 H_{K_{2 }}$	$\mu_0 H_{K_{4 }}$	$\mu_0 M_{eff}$ [T]
Cavity ϕ -Fit	23.33 ± 2.22	36.66 ± 1.11	1.873 ± 0.111
CPW f-Fit	24.44 ± 2.22	36.66 ± 1.11	1.884 ± 0.111
Final Values	23.88 ± 1.11	36.66 ± 0.55	1.878 ± 0.055

the OOP parameters were as closely approximated as feasible, without the usage of OOP angular dependencies.

A OOP measurement can be found in figure 4.16. The resonance position of this sample is higher than 2.2 T, this can be seen at 83 ° and above. Since the magnet cannot reach values higher than 2.2 T, the hard axis position is cut off and only the maxima of the absorption derivative is visible. By fitting the visible part of the absorption line, one can estimate the hard axis position, which is the case for the black data points. Due to a very high linewidth, in the region 1.8 T to 2.15 T, the resonance position could not be determined precisely and had been neglected. With the fit, shown in figure 4.17, it is now possible to estimate the value of $K_{4\perp}$. The IP anisotropy parameter and $K_{2\perp}$ stayed unchanged in this OOP anisotropy fit. The value of $\mu_0 H_{K_{4\perp}}$ is estimated to be $\mu_0 H_{K_{4\perp}} = -22 \pm 11$ mT. With this value in combination with the IP parameters, the resonance position is calculated to be 2.23 T in the highest point. This calculation was overlaid with the measurement and can be found in figure 4.17 as well. To estimate the possibility of further OOP

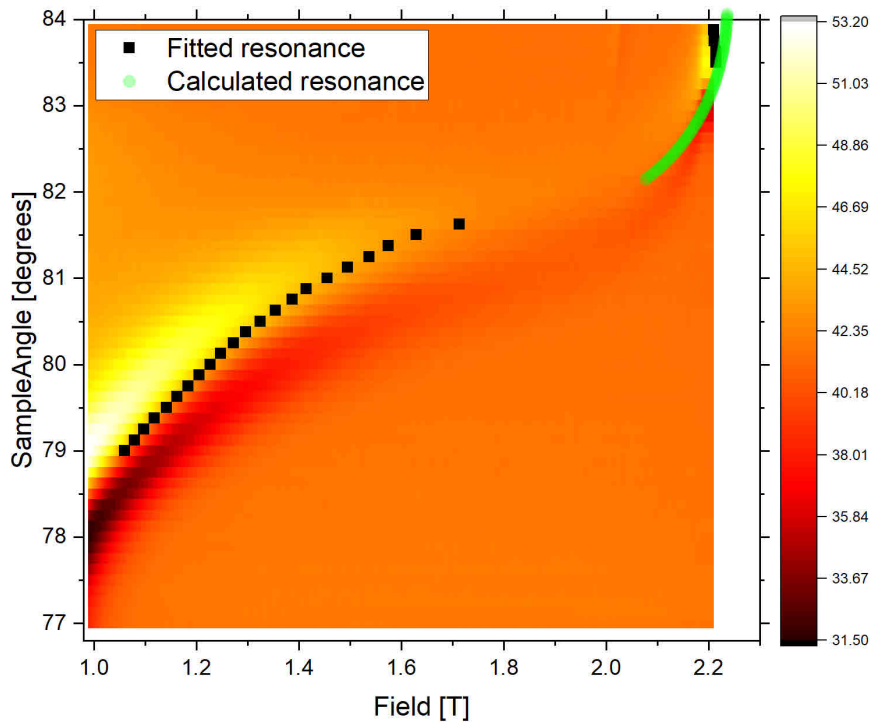


Fig. 4.16.: High field angular dependent measurement from 1.0 T to 2.2 T of 2 nm Rh batch-1. The resonance position was fitted and plotted as the black point. The error of the fit lays in the size of the points. Additionally from a set of anisotropies, $K_{2\perp} = 340000 \pm 50000 J/m^3$, $K_{2\parallel} = 22000 \pm 2000 J/m^3$, $K_{4\parallel} = 33800 \pm 1500 J/m^3$, $K_{4\perp} = -20000 \pm 10000 J/m^3$ and $g = 2.11 \pm 0.02$, the resonance position was calculated and plotted as green points.

measurements, one can discuss the $K_{2\perp}$ values for all samples of this work.

All anisotropy parameters were converted to their corresponding anisotropy field and plotted against literature values, shown in figures 4.18, 4.19, 4.20. These figures are split into two regions: the blue region combines all sample measured in-situ, while the green region combines samples measured ex-situ. The values obtained in this work were measured ex-situ, but are overlaid in both in-situ and ex-situ indicator regions. The first 7 literature samples, were produced in the same or in a equivalent vacuum chamber, as of this work. The values of Zakeri (the first two points), were taken from [78], the points (3,4) are from [77], the next three points (5,6,7) were taken from [79], the point of Madami (8) was taken from [80], the values for Chen (9) were taken from [41], point

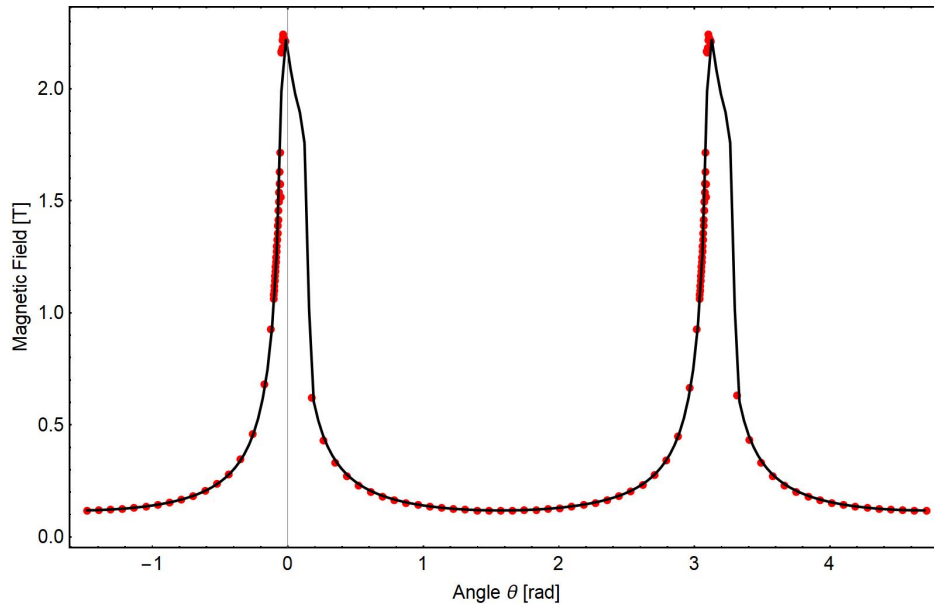


Fig. 4.17.: Out of plane anisotropy fit of 2 nm Rh. The angle $\phi_H = \pi/4$ was set constant and θ was varied. The black line is the calculated value of the resonance position, while the red points show the fitted resonance position. This measurement is a combination of 2 measurements. The magnetic field can only be varied in sweep ranges of 1.2 T. For the higher field portion a second measurement was done only around one hard axis, this measurement is visible in figure 4.16. From both measurements the resonance position was extracted and overlaid. Because the hard axis needs higher fields than the magnet can create, the resonance positions in the distinct hard axis orientation $\theta \in (0, \pi)$ is just an estimate. A value of $K_{4\perp} = -20000 \pm 10000 \text{ J/m}^3$, which corresponds to an anisotropy field of $\mu_0 H_{K_{4\perp}} = -22 \pm 11 \text{ mT}$, was found

(9) was taken from [14], the point (10) from Montoya can be found in [49] and the point (11) from McPhail can be found in [81]. All values can be found in table 4.5.

Discussion of $\mu_0 M_{eff}$

The OOP anisotropy parameter of batch-1 and batch-2 samples was converted to the effective magnetisation $\mu_0 M_{eff}$, shown in figure 4.18. With the exception of 1 nm Rh of batch-1, all values are roughly positioned around $1.89 \pm 0.02 \text{ T}$. A small increase of 0.06 T in values from 1 nm to 3 nm Rh can be seen for both batches. For Rh thicknesses above 3 nm the dependence seems to be constant. Most of the literature values, in the error, are positioned around $\mu_0 M_{eff} = 1.9 \pm 0.05 \text{ T}$. However, the ex-situ points are slightly more scattered, than the in-situ values. It has to be noted, that the first samples were produced and measured in roughly the same experimental setup, therefore reducing the scattering of the values obtained from the in-situ experiments. In the comparison of literature to batch-1 and batch-2 samples, the effect of a similar FMR system can be assumed again, as the batch-1 and batch-2 values match the literature scattering of $\mu_0 M_{eff} = 1.9 \pm 0.05 \text{ T}$ with the exception of 1 nm Rh of batch-1. This outlying point, can again be attributed to the manufacturing error already described in the case of the g-factor determination. The anisotropy parameter $K_{2\perp}$ is surface sensitive. A oxidation or capping layer on the Fe surface layer changes the coordination number, due to the transition from layer to layer to vacuum. By additionally including changes to the saturation magnetisation, the demagnetisation effects will increase or decrease depending on the magnetisation change. This effect might be seen in the low Rh thicknesses of 1 nm and 2 nm

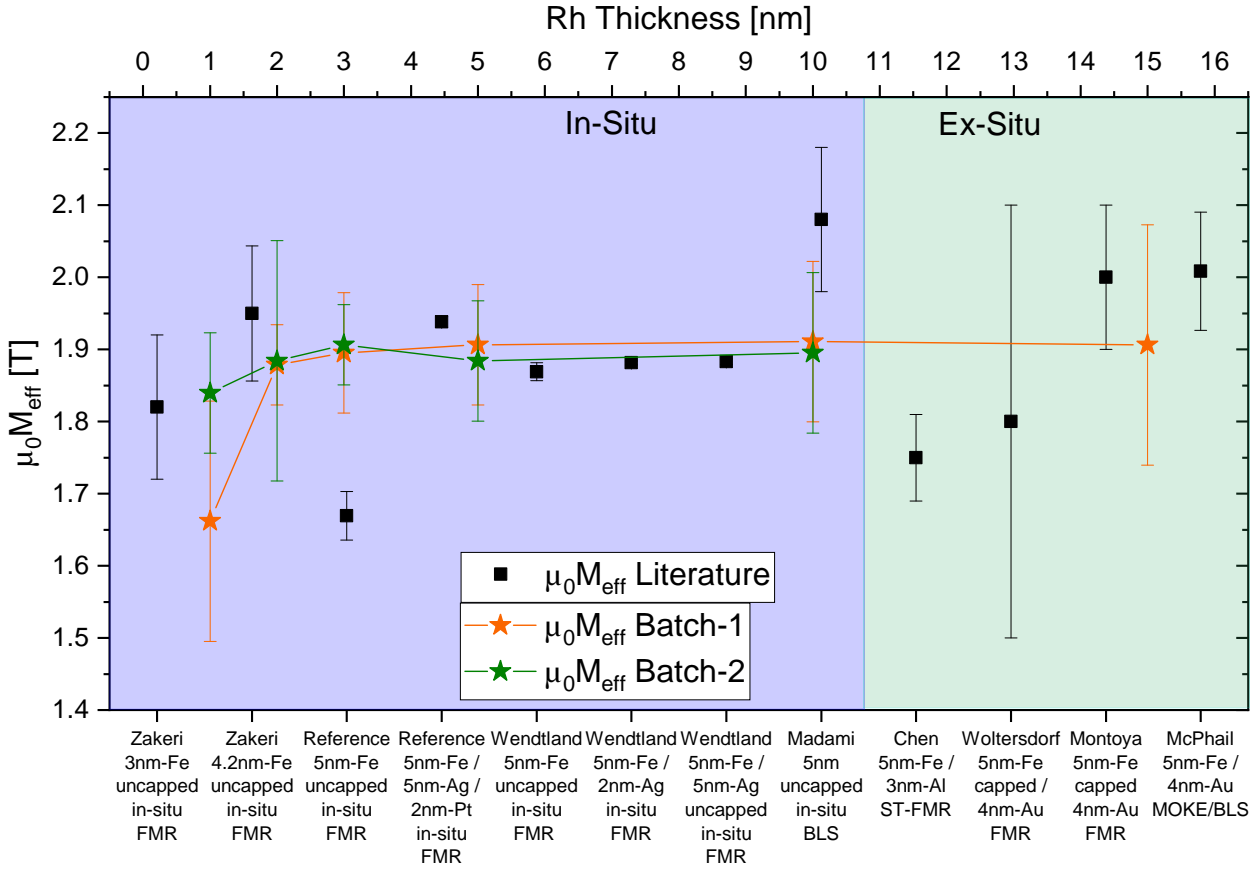


Fig. 4.18.: Comparison of effective magnetisation M_{eff} values between data from this work and literature. The bottom x-axis shows the origin of the literature data and the black points the corresponding value, while the top x-axis shows the Rh-thickness and the green symbols show the values of batch-1 samples, while the orange symbols show the values of batch-2. Furthermore, the literature is split in: In-Situ, marked by the blue region, and Ex-Situ, marked by the green region.

samples. The initial slope before reaching the saturated value could be an effect of Fe oxidation, as Rh, despite growing epitaxially on Fe, might not be a suitable capping layer in the region below 2 nm thickness. Such an effect might be seen already in the anisotropy determination process. For batch-1, the 1 nm sample was prepared mid to end of January and has been measured in ex-situ cavity based FMR end of January, resulting in a $K_{2\perp}$ value of $420 \pm 30 \text{ kJ/m}^3$. About one month later in end of March, the same sample was remeasured again in cavity FMR and a value of $K_{2\perp} = 545 \pm 50 \text{ kJ/m}^3$ is obtained, supported by frequency dependent measurement, from the end of March, whose fitting and calculation gives rise to a value of $K_{2\perp} = 550 \pm 50 \text{ kJ/m}^3$. All values can be found in table 4.4. While the $K_{2\perp}$ values change by 35 % in the course of one month. The IP parameter in the same amount of time change only by 10 %, which lays in the fitting error. A very similar behaviour can be seen for all 1 nm and 2 nm Rh thickness samples of both batches, whereas the thinner 1 nm samples show a higher deviation, than the 2 nm samples. All thicker samples seem not to be affected, as the change lays in the fitting error. A Rh polarisation effect modifying the saturation magnetisation, inducing a change in $K_{2\perp}$, should be not ruled out, although the change in other IP anisotropy field values, that are also dependent on the saturation magnetisation, is small enough to be considered in the fitting error. This assumption is also supported by measurements of a controlled oxidation effect on thin Fe films [82]. Kebe et al. found, that the IP anisotropy will not change in the range of 1-10 L of oxygen exposure, while the OOP parameter $K_{2\perp}$ reduced by 40%

Table 4.4.: Time dependence of the anisotropy parameter of 1 nm Rh batch-1.

Anisotropy-Parameter[kJ/m^3]	$K_{2\parallel}$	$K_{2\perp}$	$K_{4\parallel}$
Cavity ϕ -Fit - end of January	25 ± 1	420 ± 40	26 ± 1
Cavity ϕ -Fit - end of March	26.5 ± 1	545 ± 50	27 ± 1
CPW f-Fit - beginning of April	23 ± 2.5	550 ± 50	26 ± 2

in the first 3 L. This can be translated to a decrease of the effective magnetisation as a reduction in saturation magnetisation. One has to note, that Kebe et al. used several monolayers of Fe, in which surface effects have a bigger magnitude as compared 5 nm films with bigger volume. Nevertheless, a reduction of effective magnetisation, which can be seen for 1 nm Rh samples, will most likely be the result of the oxidation effect of Fe layers, as supported by FMR measurements one month apart. The OOP resonance position will change according to the magnitude of the effective magnetisation. Higher $\mu_0 M_{eff}$ will result in higher OOP resonance positions. Returning to the OOP magnetic field discussion, because the $\mu_0 M_{eff}$ value of all samples are in roughly the same region, a very similar OOP resonance position can be assumed. According to the 2 nm Rh batch-1 sample, this resonance position is located in the region of $\mu_0 H_{res} = 2.23$ T. Based on these considerations it is assumed, that the OOP hard axis resonance positions can not be safely determined with the current setup. Either the magnet power supply is operating on a critical level or the magnetic field can not be driven sufficiently high enough to catch the hard axes positions of other samples. Based on this assumption no further analysis of $K_{4\perp}$ took place.

Discussion of $\mu_0 H_{K_{2\parallel}}$

The anisotropy fields of the in-plane uniaxial anisotropy can be found in figure 4.19. Both batches show a initial decrease to a minimum at 3 nm Rh. The minimum at 3 nm Rh batch-1 shows a reduction of 50 % to the value of batch-2 and about 60 % difference to the surrounding samples. For samples thicker than 3 nm Rh, batch-1 suggests a linear increase with increasing Rh thickness, that in the fitting error can also be seen in batch-2. The slope of the increase is very small in comparison to the initial decrease, with a value of roughly $0.23 \pm 0.01 kJ/m^3 \cdot nm^{-1}$ for batch-1. Due to this small change, taking into account the errobar, the dependence for thicker films is assumed to be constant. Furthermore, by comparing the values of same thickness in between the batches, it is noticeable, that the distance from batch-1 to batch-2 values is constant. The distance can be calculated to be $\Delta\mu_0 H_{2\parallel} = 4 \pm 1$ mT. This means both batches show the same dependence on Rh thickness but are offsetted by 4 mT.

The values of this work compared to literature of the same system and the uncapped in-situ BLS measurement (points 1 - 7 + 8) lay closer together, than the literature values of ex-situ measurements (9-12). To explain the changes in $\mu_0 H_{K_{2\parallel}}$, it is wise to remember the origin of this anisotropy. The Fe layer exhibits a nearest neighbour dislocation at the interface to the GaAs(100) surface [7]. Regardless of the superstructure, the GaAs surface can be described by a furrow-like structure, that will increase the distance of Fe atoms in the range of 0.02 \AA for 2 monolayer of Fe along the furrow. This creates a magneto-elastic anisotropy energy for an in-plane lattice shear [49, 83]. This interfacial expansion will lose its influence with increasing Fe volume, as can be seen in the figure 2.6g. From the observations in this work, there is a constant distance between batch 1 and batch 2, which could indicate a change in the GaAs surface between the batches. In this case, an explanation could lie in the GaAs(100) wafers used. Charge 1 and Charge 2 wafers differ in terms

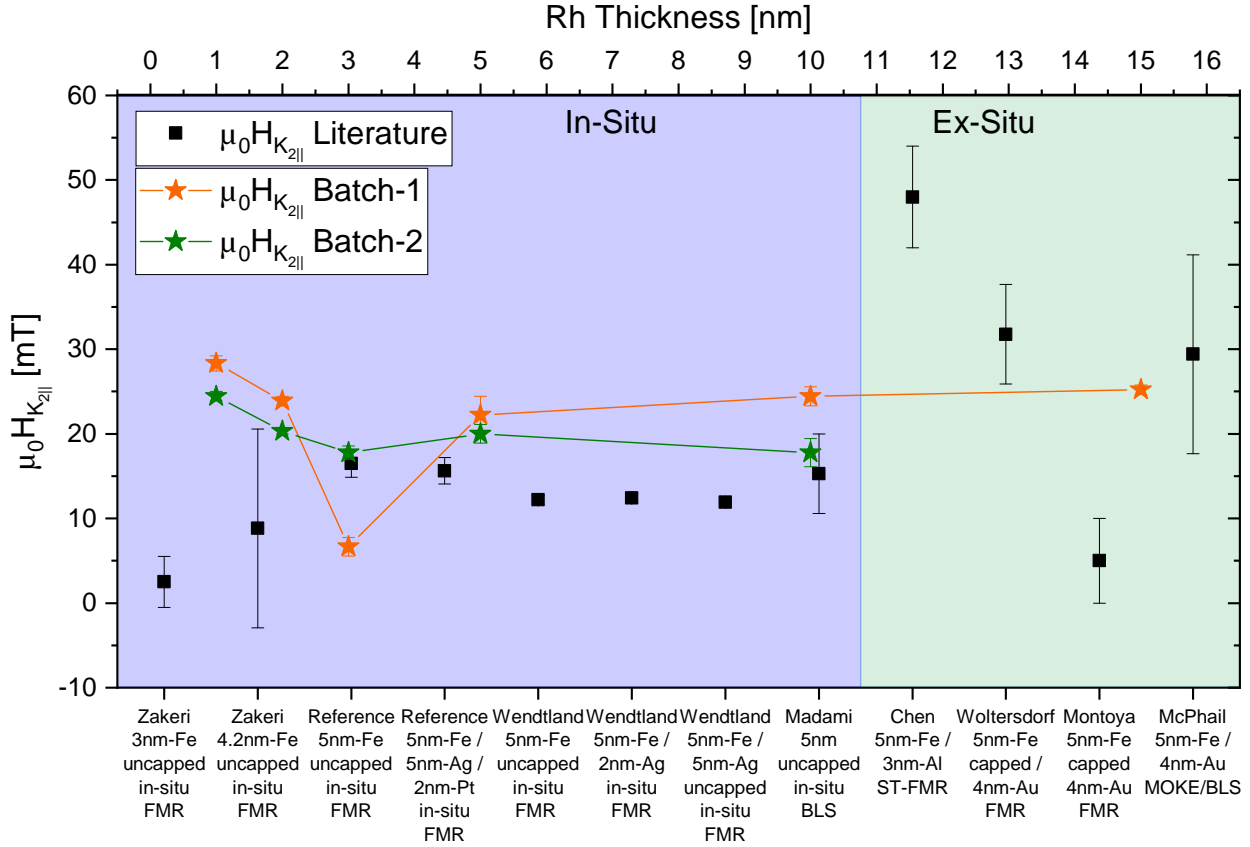


Fig. 4.19.: This figure presents the IP uniaxial anisotropy field $\mu_0 H_{K_{2||}}$ in [mT]. As for the effective magnetisation (figure 4.18), the literature is shown in black and the measurement data is presented in orange for batch-1 and green for batch-2.

of age and thickness. This means that they may also differ in crystal or cut quality and purity. As the dislocation effect is low, a better surface quality could result in a higher uniaxial contribution. The effects of surface preparation must also be considered, as high surface roughness reduces the depth of the furrows and thus weakens the dislocation effect. For batch-1 and batch-2 the preparation procedure was the same, but due to missing LEED pictures of batch-1 no surface quality comparison can take place. Nevertheless, the surface roughness will not be constant in between the batches and therefore can be ruled out for the discussion of a constant offset of $\Delta\mu_0 H_{2||} = 4 \pm 1$ mT. To conclude, the origin of this offset can not be determined precisely, it is obvious, that the GaAs substrate must play a role, but the reason for the influence can not be determined further.

Furthermore it can be noted, that oxidation of the superficial Fe layer is not affecting this uniaxial anisotropy. This is due to the origin of $\mu_0 H_{K_{2||}}$ to be an interface effect of GaAs/Fe, that at sufficiently high volumes of Fe will not be affected by Fe surface effects. This can be proven by comparing batch-1 1 nm Rh to batch-2 1 nm Rh. As already pointed out, $\mu_0 M_{eff}$ will be reduced by oxygen exposure, which was clearly the case for batch-1 1 nm Rh sample. In the case of $\mu_0 H_{K_{2||}}$ however, the value is unaffected and fits into the further thickness dependence. This proves the uniaxial effect to be surface independent. With this reasoning, further effects of epitaxial deformation of Rh on Fe can be excluded, as these would be superficial and would not affect the GaAs/Fe interface. Furthermore, Rh on Fe is expected (and proven by LEED) to grow in a cubic lattice, similar to Ag, which has no additional in-plane uniaxial anisotropy.

Discussion of $\mu_0 H_{K_{4\parallel}}$

The Rh thickness dependence of the $\mu_0 H_{K_{4\parallel}}$ anisotropy field can be seen in figure 4.20. By excluding 1 nm Rh of batch-1, the thickness dependence of batches is assumed to be identical for both batches. According to batch-2, the dependence start with a maximum value of $\mu_0 H_{K_{4\parallel}} = 37.22 \pm 0.83$ mT, and decreases linearly to a value $\mu_0 H_{K_{4\parallel}} = 32.66 \pm 0.33$ mT for 15 nm Rh. The reduction results in a overall change of 16% over 15 nm of Rh thickness. In comparison to literature values, a value range $\mu_0 H_{K_{4\parallel}} = 37 \pm 4$ mT will cover a majority of literature points, including these from batch-1 and batch-2. The 1 nm Rh batch-1 sample repeatedly shows a big offset to the other batch and other values of the dependence. It has an offset of 20% to the 1 nm Rh sample of batch-2. Due to Kebe et al. reporting no change in IP-anisotropy constants for multiple Langmuir of oxygen

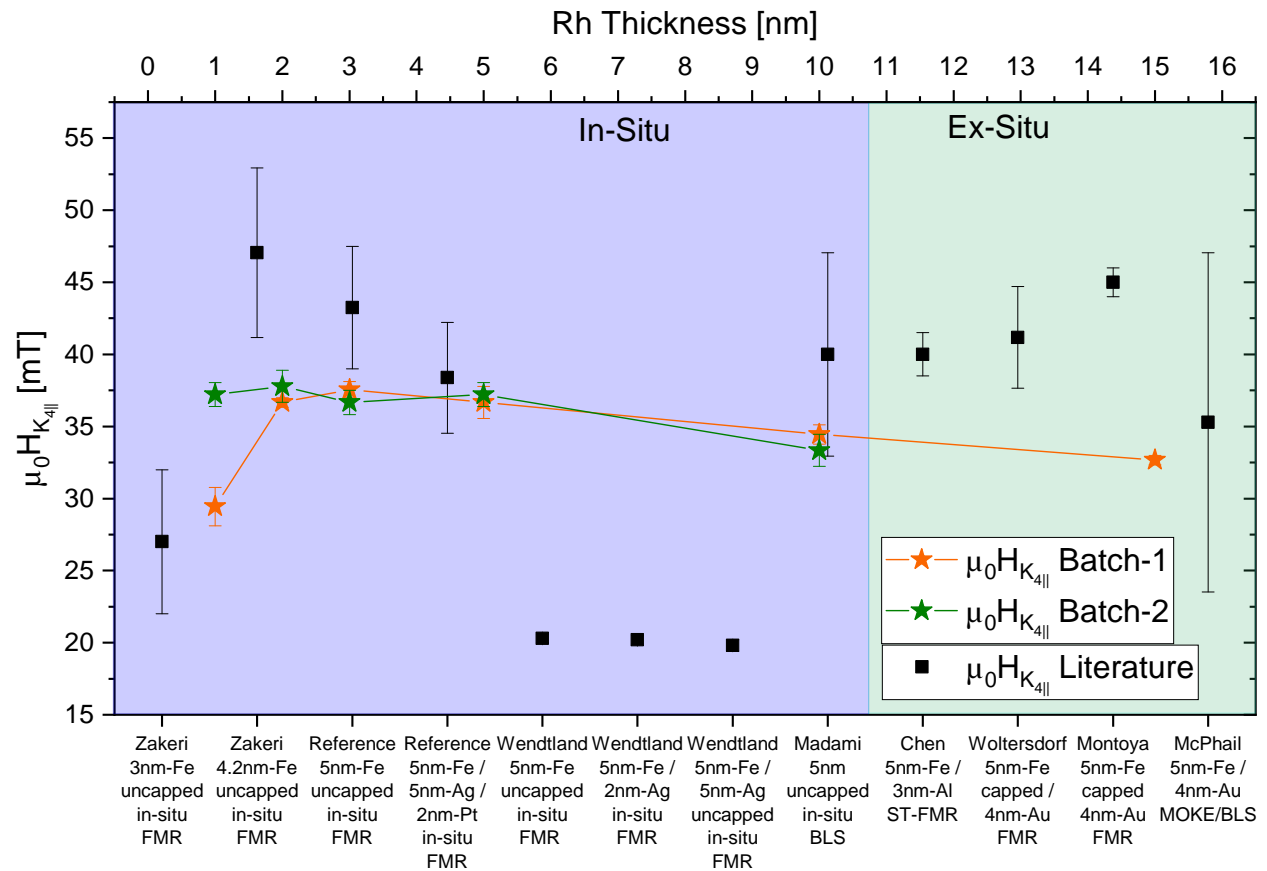


Fig. 4.20.: The figure shows the cubic in-plane anisotropy field $\mu_0 H_{K_{4\parallel}}$. The colour coding follows the same structure as previous comparisons.

exposure [82], the offset of the 1 nm Rh sample can not be explained purely by oxidation effects. The real origin cannot be determined, but assumption can be made. Based on [82], there is little to no effect of oxidation to cubic anisotropy for pure Fe surfaces. The oxidation for low dosages is creating FeO compounds on the surface. The offset might be explained by a missing interface alloying of Fe and Rh, due to a FeO protection layer. According to Hanisch et al. [73], Fe/Rh multilayer like to alloy at the interface. The interface alloying reduces the interface free energy, or depending on the adsorbate thickness the surface free energy. This can support a layer-by-layer growth mode, as it is energetically more suitable to grow in a layer manner, than in crystallites. Assuming that the amount of interfacial alloy decreases with a gradient across the substrate thickness for layer-by-layer growth, one could assume a smooth transition between substrate and adsorbate.

The alloy composition would change along the gradient, e.g. like substrate/substrate alloy/50-50 alloy/adsorbate alloy/adsorbate. In this case, the lattice constant could also change smoothly along this transition. This means an epitaxial strain due to lattice mismatch is minimised, and the over- and underlying crystal structures of adsorbate and substrate is distorted by a minimum. By assuming interface alloying for Fe/Rh bilayers, the cubic anisotropy will be affected, as alloying will distort the underlying Fe symmetry. One might assume, the small linear decrease of cubic anisotropy to be an effect of this alloying, in which the Rh gains influence over the Fe crystal with increasing thickness. Due to a smooth transition of lattice parameters the strain is minimised and the reduction of the cubic anisotropy happens in small portions. If in this assumption, the Fe layer is protected for example by FeO compounds, which might not be able to alloy with Rh, the smoothing of the lattice parameter can not take place and the grown Rh has more influence on the Fe lattice. This follows a quenching or unquenching of the orbital moments, which gives rise to changes in the cubic anisotropy. However, the quenching or unquenching, which for now was assumed to be in the interface region, must take place over a broad range of the volume crystal, to be dominant over the volume effects and therefore to be seen as a change in cubic anisotropy. By regarding, that only one Langmuir, one monolayer, of oxygen was adsorbed and that the Rh thickness is only 1 nm, quenching is unlikely to be the explanation of this effect, as the Fe thickness is 5 times larger than the Rh layer and volume anisotropy would dominate. A clear conclusion about the origin of this change in cubic IP anisotropy cannot be given. One possibility would be the impact of a strain that the Rh causes to the Fe lattice, which rises with thickness.

Furthermore, it was pointed out in the discussion of $\mu_0 H_{K_{2\parallel}}$, that the 3 nm Rh sample of batch-1 shows the minimum of the dependence with a jump of values to the neighbours of 50%. Based on the FMR analysis, no complete origin of this effect can be found either. However based on the value $\mu_0 H_{K_{4\parallel}}$ for 3 nm, which perfectly fits in the dependence of surrounding thickness values, it is assumed to be a GaAs/Fe interface effect. Unfortunately no LEED pattern is available for the GaAs surface of this sample, as could give rise to a estimation of surface roughness. Assuming a high surface roughness, the symmetry of the dislocation of GaAs to Fe might be scattered and the uniaxial in-plane anisotropy might be reduced. Due to a high volume of the Fe layer, the effect of the interface roughness to the cubic anisotropy might be negligible.

To conclude, the magnetic anisotropy of the Fe/Rh bilayer system shows a small dependence on Rh thickness. The effective magnetisation is constant over a wide range of Rh thickness with a mean value of $\mu_0 M_{eff} = 1.9 \pm 0.11$ T, which is in line with other data obtained from literature. Additionally based on the effective magnetisation dependence, one can assume a protection layer effect of Rh on Fe at thicknesses of 2 nm and above. The uniaxial in-plane anisotropy $\mu_0 H_{K_{2\parallel}}$, although being a pure interface effect, shows a dependence of Rh thickness, by initially decreasing until a minimum at 3 nm Rh of $\mu_0 H_{K_{2\parallel}} = 6 \pm 1$ mT and then increasing to a constant value of $\mu_0 H_{K_{2\parallel}} = 22 \pm 1$ mT for 5 nm Rh batch-1. For batch-2 the initial decrease until 3 nm is less pronounced, with a value of $\mu_0 H_{K_{2\parallel}} = 17 \pm 2$ mT followed by the increase of 5 nm of $\mu_0 H_{K_{2\parallel}} = 20 \pm 1$ mT. Furthermore a difference in substrate quality can be seen by comparing both batches. The difference in quality gives rise to a constant $\mu_0 H_{K_{2\parallel}}$ offset of $\Delta\mu_0 H_{K_{2\parallel}} = 4 \pm 1$ mT. The cubic anisotropy field decreases linearly over the Rh thickness with a overall decrease of $\Delta\mu_0 H_{K_{4\parallel}} = 16\%$, when the Rh thickness is increased from 1 to 15 nm. Both batches show the same dependence with overlapping values. The data of Fe/Rh bilayers fits into the literature values by assuming a literature range of $\mu_0 H_{K_{4\parallel}} = 37 \pm 4$ mT, which shows, that the effect of Rh on the cubic anisotropy is small.

Table 4.5.: All anisotropy fields used in the discussion.

Anisotropy-Fields [mT]	$\mu_0 H_{K_{2 }}$	$\pm \mu_0 H_{K_{2 }}$	error	$\mu_0 M_{eff}$ [T]	$\pm \mu_0 M_{eff}$ error [T]	$\mu_0 H_{K_{4 }}$	$\pm \mu_0 H_{K_{4 }}$	error
Batch-1 1 nm Rh	28.33	0.88		1.66	0.16	29.44	1.33	
Batch-1 2 nm Rh	23.88	0.55		1.87	0.05	36.66	0.33	
Batch-1 3 nm Rh	6.66	1.11		1.89	0.083	37.55	0.55	
Batch-1 5 nm Rh	22.22	2.22		1.90	0.08	36.66	1.11	
Batch-1 10 nm Rh	24.44	1.11		1.91	0.11	34.44	0.66	
Batch-1 15 nm Rh	25.22	0.55		1.90	0.16	32.66	0.33	
Batch-2 1 nm Rh	24.44	0.55		1.839	0.08	37.22	0.83	
Batch-2 2 nm Rh	20.33	0.33		1.88	0.16	37.77	1.11	
Batch-2 3 nm Rh	17.77	0.77		1.90	0.055	36.66	0.83	
Batch-2 5 nm Rh	20	1.11		1.88	0.08	37.22	0.83	
Batch-2 10 nm Rh	17.77	1.66		1.89	0.11	33.33	1.11	
Batch-2 15 nm Rh	/	/		/	/	/	/	
Zakeri 3nm-Fe uncapped in-situ FMR [78]	2.5	3		1.82	0.1	27	5	
Zakeri 4.2nm-Fe uncapped in-situ FMR [78]	8.82	11.76		1.95	0.09	47.05	5.88	
Reference 5nm-Fe uncapped in-situ FMR [77]	16.5	1.62		1.66	0.03	43.25	4.25	
Reference 5nm-Fe / 5nm-Ag / 2nm-Pt in-situ FMR [77]	15.62	1.56		1.93	0.007	38.37	3.83	
Wendtland 5nm-Fe uncapped in-situ FMR [79]	12.2	0.5		1.86	0.01	20.3	0.3	
Wendtland 5nm-Fe / 2nm-Ag in-situ FMR [79]	12.4	0.5		1.88	0.002	20.2	0.3	
Wendtland 5nm-Fe / 5nm-Ag uncapped in-situ FMR [79]	11.9	0.5		1.88	0.003	19.8	0.4	
Madami 5nm uncapped in-situ BLS [80]	15.29	4.705		2.08	0.1	40	7.05	
Chen 5nm-Fe / 3nm-Al ST-FMR [41]	48	6		1.75	0.06	40	1.5	
Woltersdorf 5nm-Fe capped / 4nm-Au FMR [14]	31.76	5.88		1.8	0.3	41.17	3.52	
Montoya 5nm-Fe capped 4nm-Au FMR [49]	5	5		2	0.1	45	1	
McPhail 5nm-Fe / 4nm-Au MOKE/BLS [81]	29.41	11.76		2.008	0.08	35.29	11.76	

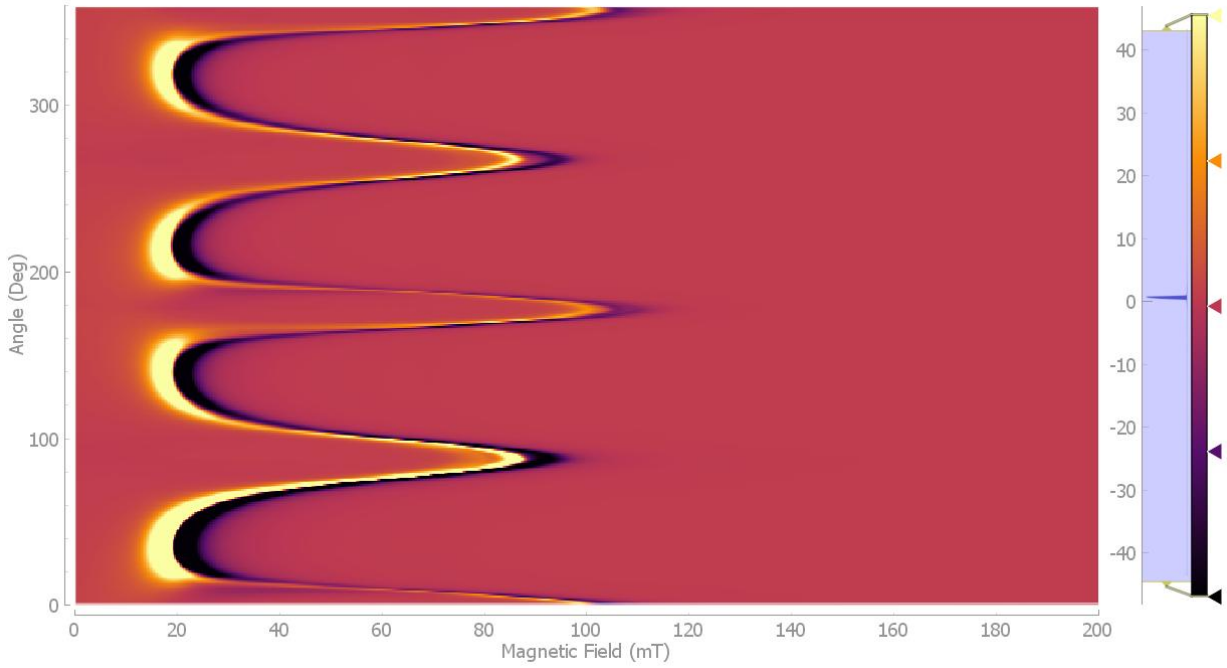


Fig. 4.21.: The colour plot of the angular dependent cavity based FMR measurement for 3 nm Rh of batch-1. The data was obtained in in-plane orientation at room temperature and at a frequency of 9.54 GHz. The colourbar on the right sets a colour value to the FMR intensities. The light blue region defines the colour mapping, in which a histogram of the intensities is plotted.

4.2.2. Special observations

As of the results from $\mu_0 H_{K_{2\parallel}}$ in figure 4.19, the batch-1 sample of 3 nm Rh shows a sudden decrease in the anisotropy field value by a factor of about 4 to the surrounding samples. As this change can only be seen in the uniaxial in-plane anisotropy field, it is evident, that this change must originate from the GaAs/Fe interface. To rule out errors in anisotropy determination, the FMR angular dependence was remeasured twice and the measurement of highest signal-to-noise ratio is presented in figure 4.21. As can be seen from this figure, the hard axis [110], lays approximately at 0° and has a hard axis resonance position of about 105 mT. The intermediate axis, is positioned 90° turned from the hard axis, with a resonance field of 90 mT. The difference of the hard axis position to the intermediate position is given by the strength of the in-plane uniaxial anisotropy. Just by interpreting the angular dependence colour plot, one can already identify a low magnitude of $\mu_0 H_{K_{2\parallel}}$. In comparison to 2 nm Rh of batch-1 in figure 4.14a, where the intermediate axis has a resonance position of about 75 mT and the hard axis at about 110 mT, the influence of this low $\mu_0 H_{K_{2\parallel}}$ value can be seen. It is now evident, that the origin lies in the $\mu_0 H_{K_{2\parallel}}$ strength. A very high roughness of the GaAs could reduce this anisotropy. However, it will also increase the formation of Fe-Ga-As compounds, reducing the saturation magnetisation. The roughness effect might be excluded, as the effective magnetisation compared to surrounding samples does not change. Further a interpretation might be given by structural changes of the rhodium itself. It could be, that thicknesses of around 3 nm are right at the edge of a structural phase transition, maybe due to release of epitaxial stress. This might also explain the slight increase of the uniaxial anisotropy for thicker films. Compared to batch-1, the batch-2 3 nm Rh sample does not show similar decrease in uniaxial anisotropy. However it still represents a local minimum, after which the values are increasing again. This means, considering a thickness error of 0.5 nm, this sample is shortly before or after

the assumed transition, deviating from the batch-1 sample. The structural transition might also explain the behaviour of the in-plane cubic anisotropy field $\mu_0 H_{K_{4||}}$, that is initially increasing until 2 nm Rh, followed by a change at 3 nm and then decreasing for 5 nm and thicker Rh layers. This roughly correlates to both batches. A reduction of cubic anisotropy can be achieved by quenching the atomic orbitals. Samples of Rh thickness higher than 5 nm might exert less stress on the Fe crystal lattice, that an unquenching of orbitals is reduced. However, this is highly speculative and has no real justification. No clear origin can be determined without additional experiments.

Besides the splitting of the resonance position into multiple resonances for several measurements, as for example in figure 4.21 in the second intermediate orientation at about 275° , a second angular dependence can be observed for fields 100 mT to 200 mT with a symmetry, that is shifted by 45° . An overview of pronounced signals, in addition to the Fe signals discussed above, can be found in figure 4.22. The additional signal is present in all of batch-1 samples, including the samples using the substrate of wafer-1. This signal cannot be found in the samples of batch-2. For the 5 nm Rh sample figure 4.22c shows two additional signals: A cubic signal is visible in the background with a extremely low intensity and additionally a much more pronounced uniaxial signal with hard axis above 200 mT can be found.

Appearance of an additional signal always shifted by 45° to the main resonance of Fe, points to cubic symmetry and, therefore, might be related to the crystal structure. The fact, that the Rh crystal grows 45° degrees shifted to Fe leads to the assumption, that this signal originates from a polarised Rh layer at the Fe interface. These signals hard axes resonance positions also seem to be independent on the Rh thickness, as they can all be approximately found at around 170 mT for all samples, which supports the assumption of an origin at the Fe/Rh interface. However, this cannot explain why no such signal was found for batch-2 samples. Since the only difference between batch-1 and batch-2 samples is the substrate wafer, the difference must lie in the way how Fe is growing on each of the two wafers, as this might produce a rougher layer along one batch. With a rougher surface, the interfacial alloying could be enhanced, or more Rh atoms could be found near Fe than in the surface, increasing the amount of polarised atoms. The alloying assumes a creation of a Fe/Rh crystal lattice, that includes the appearance of a crystal symmetry 45° rotated to Fe. Another possibility which shall not be discarded is, that the signal-to-noise ratio could be too small for batch-2 samples to detect the signal. Therefore the additional signal might be overlooked.

4.2.3. Magnetisation damping and spin pumping

As described in chapter 2.1.3, the linewidth of a FMR resonance line gives rise to the relaxation times of the magnetisation precession. To reduce artificial broadening through dragging contributions, the frequency dependent measurements were conducted in hard axes orientations $[110]$ and $[1\bar{1}0]$. This enables the usage of equation 2.66, in which the linewidth depends linearly on the applied frequency, with the Gilbert damping α as the slope. As the frequency increases, the precession cone opening decreases and the resonance position shifts to higher fields. This reduces the influence of dragging contributions for higher frequencies onto the linewidth. Every additional dragging effect through mispositioning can be further reduced by taking higher frequencies into account. In the determination of damping of samples of batch-1 and batch-2, the dataset was adjusted to neglect non-linear low frequency linewidth enhancements. In most cases, this was the case for frequencies up to 10 GHz, resulting in a dataset of IP measurement frequency data from $\approx 10 - 40$ GHz, that was used for fitting the Gilbert damping.

Disorder at the Fe/GaAs interface induces a change in LS-coupling as symmetry relations are broken. This changes the electron band structure at the interface following a change in relaxation

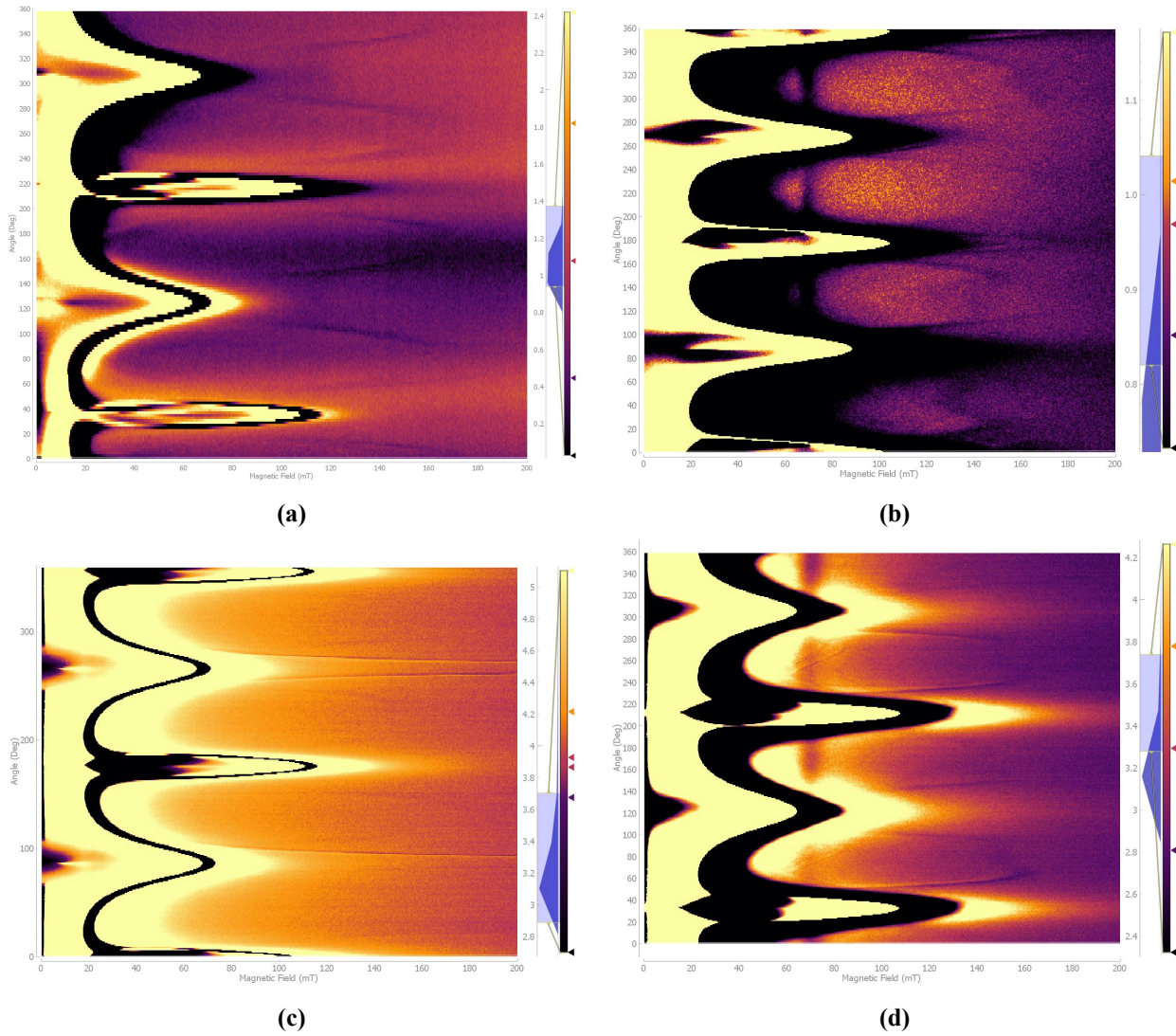


Fig. 4.22.: Additional signals, that were found in in-plane cavity angular dependent FMR experiments on batch-1 samples and samples with the same wafer as batch-1. All measurements were performed at room temperature in an X-Band cavity. Figure **a)** shows the measurement of 0.76 nm Rh on 4 nm Fe using the GaAs from wafer-1. In figure **b)** the measurement of 3 nm Rh batch-1, focused on a very tiny intensity range. For figure **c)**, the measurement of 5 nm Rh batch-1 can be found, while figure **d)** shows the angular dependence of 15 nm Rh batch-1.

Table 4.6.: Literature damping values for bulk or 5 nm thick Fe layers.

Literature	α [10^{-3}]
Frait bulk [84]	1.8
Bhagat bulk[85]	2.4 ± 0.3
Montoya IP 5 nm-Fe [49]	1.7 ± 0.5
Montoya OOP 5 nm-Fe [49]	2.4 ± 0.2
Woltersdorf bulk [14]	2
Reference-[110] 5 nm-Fe [77]	1.25 ± 0.2
Reference-[110] 5 nm-Fe [77]	1.75 ± 0.1

processes and therefore a change in damping. Since the Fe layers were grown according to the same recipe for both batches, the disorder effect is assumed to be constant. Furthermore, due to the appearance of the additional uniaxial anisotropy $\mu_0 H_{K_2\parallel}$ one would also expect to see an anisotropic Gilbert damping in Fe/GaAs(100) as suggested by [41]. However, the effect is very sensitive to the Fe thickness. Chen et al. found the anisotropic effect to vanish for thicknesses above 15 monolayers (≈ 2.1 nm) of Fe. This implies that for Fe thicknesses of 5 nm no anisotropic damping should be present. To compare the effect of Rh capping on the damping, the Gilbert damping values are compared to the Gilbert damping $\alpha_{0,Bulk}$ of Fe with 0 nm Rh, see table 4.6. The damping values obtained from linear fitting are presented in figure 4.23 for the hard axis and figure 4.24 for the intermediate axis. In these graphs, the 0 nm point corresponds to the reference point of the corresponding orientation, see table 4.6. These points represent the damping values, that were obtained for uncapped Fe films produced using the same recipe for Fe evaporation, Fe thickness, substrate preparation and same measurement setup as all samples capped with Rh. As they lay in close proximity to the literature values, they were used for further investigations.

Both intermediate and hard axis orientations show an increase of damping with capping of Rh. For the hard axis of batch-1 a increase of a factor of 5.8 from 0 to 15 nm is observed. The dependence on Rh shows a saturation of damping at 5 nm Rh. For samples from batch-2, the saturation effect can not be seen. Although the 15 nm point of batch-2 is missing, a increase until 10 nm Rh is seen, but due to the missing 15 nm point, no saturation can be assumed. By including the 0 nm point, the dependence of both batches seems to be exponential, whereas batch-2 shows a lower deviation from a exponential function, than batch-1. The same can be seen from the damping dependence of the intermediate axis. Batch-2 shows a clear curvature with increasing Rh thickness. By excluding the 1 nm point of batch-1 a similar behaviour is seen. Furthermore the 15 nm point of batch-1 suggest no saturation until 15 nm. By including error bars, the saturation similar to the hard axis case, can be assumed at 5 nm. Across all batches and all axes, the increase in damping up to 10 nm Rh has a mean factor of 4.53, from $\alpha_0 = 1.5 \cdot 10^{-3}$ to $\alpha_{10nm} = 6.8 \cdot 10^{-3}$.

To investigate a possible anisotropic damping, both hard axis and intermediate axis need to be compared. A comparison can be found in figure 4.25. For batch-2, figure 4.25b, besides 2 nm Rh, no difference can be found. Furthermore, the logarithmic x-scale shows a linear dependence on Rh thickness, while for batch-1 samples the noise is increased and the points do not overlap as good as for batch-2. A linear slope in batch-1 data is not as pronounced as it is in batch-2, one could assume no dependence at all. Nevertheless all points of both batches, lay in their error bars. According to this no anisotropic damping can be found in this data. The error is too high in order to conclude about any anisotropy in these datasets. Additionally the linear fit of linewidth over frequency gives rise to the inhomogeneous broadening ΔH_{inhom} . These values can be found in figure 4.26. Both

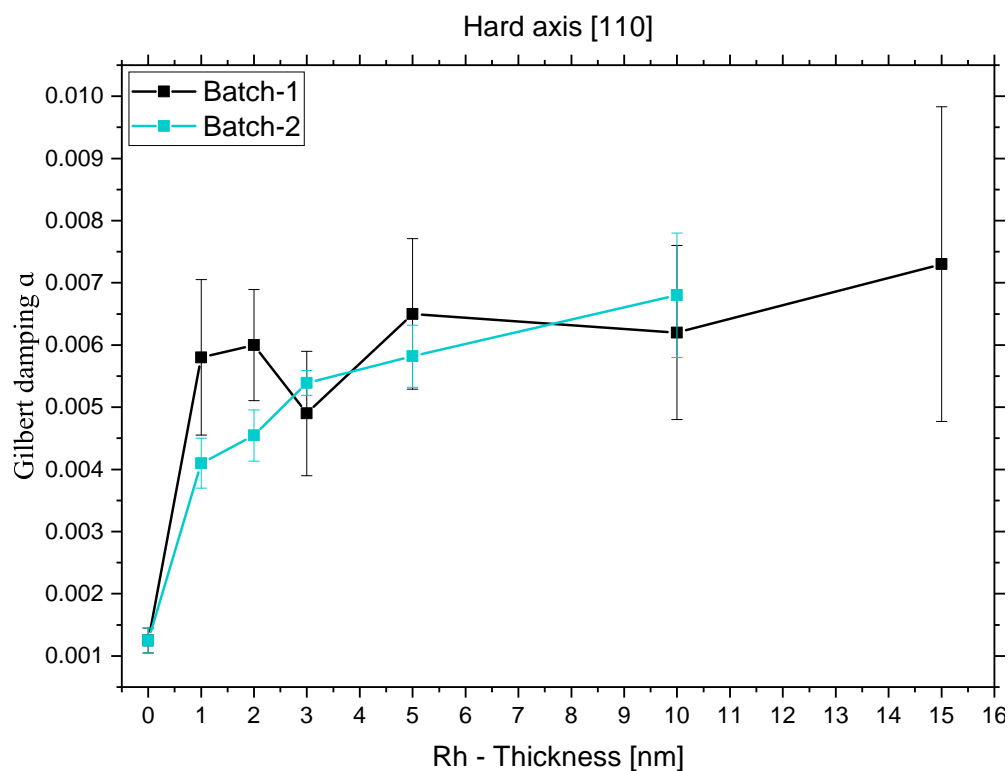


Fig. 4.23.: Gilbert damping in hard axis orientation of batch-1 and batch-2.

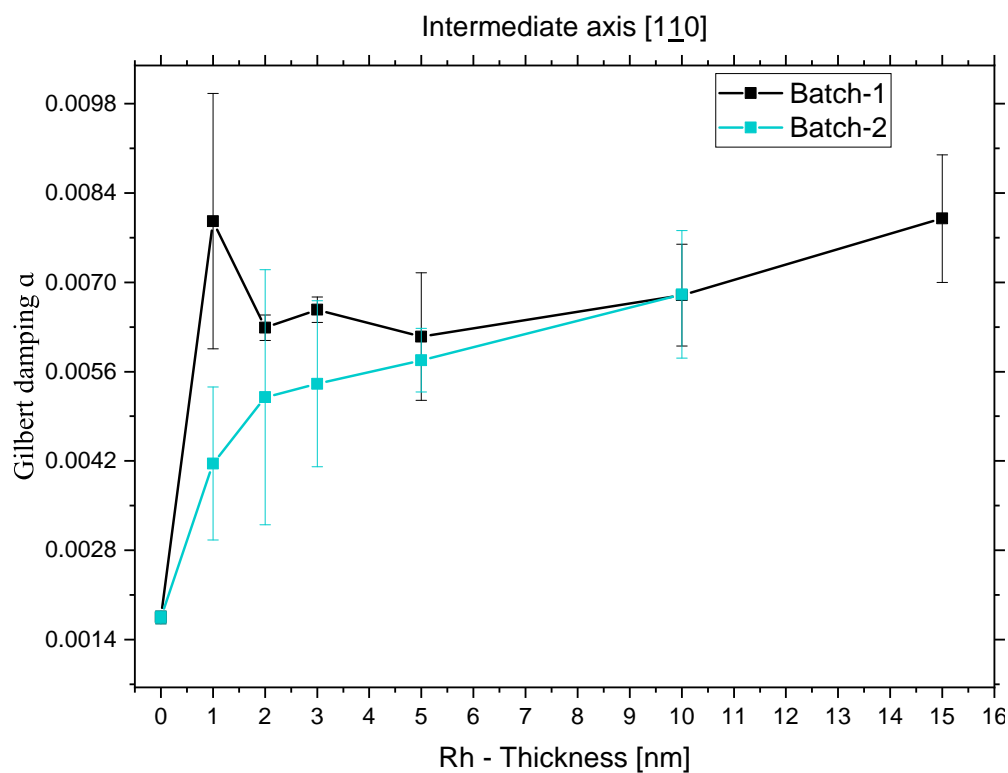


Fig. 4.24.: Gilbert damping in intermediate axis orientation of batch-1 and batch-2.

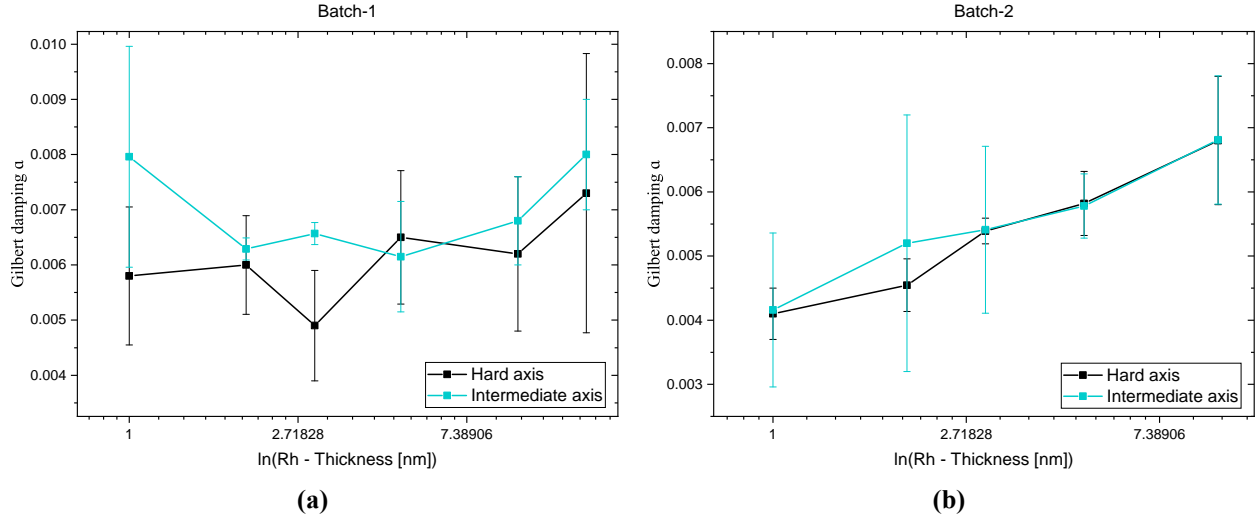


Fig. 4.25.: Comparison of the Gilbert damping in between the batches. The x-axis additionally is scaled using the natural logarithm. Figure **a)** shows the samples of batch-1, while figure **b)** shows the samples of batch-2

Table 4.7.: From fitting obtained Gilbert damping values for all samples. The values are given in $[10^{-3}]$.

Rh thickness [nm]	Batch-1 [110]	Batch-2 [110]	Batch-1 [110]	Batch-2 [110]
0	1.25 ± 0.2	1.25 ± 0.2	1.75 ± 0.1	1.75 ± 0.1
1	5.8 ± 1.25	4.1 ± 0.4	7.96 ± 2	4.16 ± 1.2
2	6 ± 0.89	4.55 ± 0.41	6.29 ± 0.2	5.2 ± 2
3	4.9 ± 1	5.39 ± 0.2	6.5 ± 0.2	5.41 ± 1.3
5	6.5 ± 1.21	5.82 ± 0.5	6.15 ± 1	5.78 ± 0.5
10	6.2 ± 1.4	6.8 ± 1	6.8 ± 1	6.81 ± 1
15	7.3 ± 0.25	/	8 ± 1	/

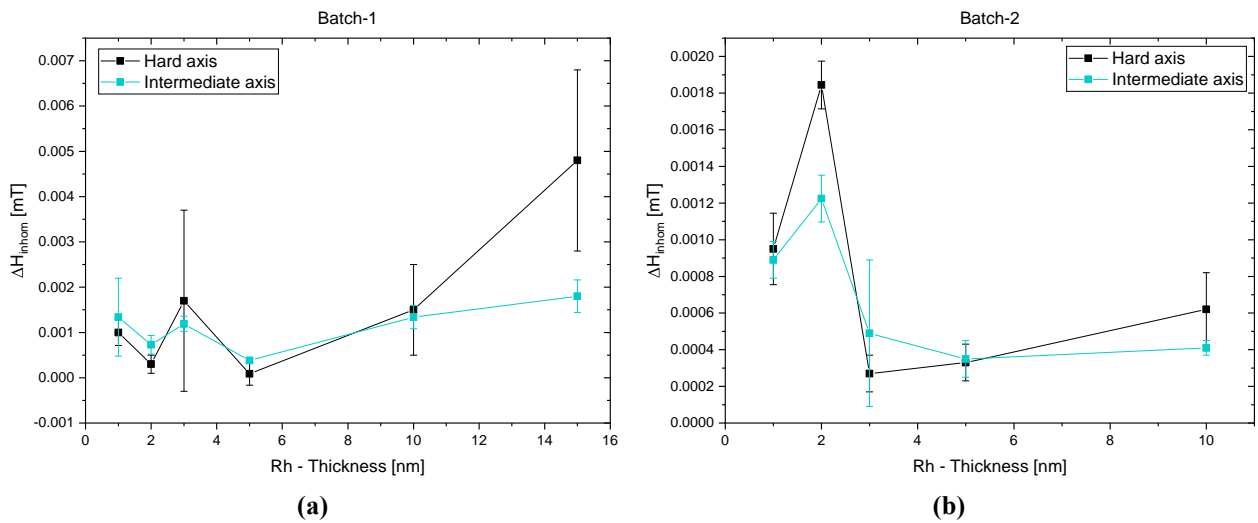


Fig. 4.26.: In homogeneous broadening of batch-1 **a)** and batch-2 **b)**. This value is obtained, as the constant linewidth offset in the linear damping fit.

batches show a very similar behaviour of inhomogeneous broadening with increasing Rh thickness. The broadening is initially decreasing until a Rh thickness of 3 nm, after which it starts increasing again until 10 or 15 nm Rh. Additionally for 3 nm Rh of batch-1, the inhomogeneous broadening shows a local maxima. In the ideal case of no measurement or fitting error, the inhomogeneous broadening should be isotropic, due to its origin of having no symmetry relation. This can be seen in both batch-1 and batch-2, as the intermediate axis closely relates to the hard axis. Regarding the oxidation of 1 nm Rh batch-1, no increase in inhomogeneous broadening can be seen. In the error it is comparable to the 1 nm Rh point of batch-2. In the sense of one monolayer of oxidation, this means the inhomogeneous broadening is a volume effect, that at sufficient thicknesses will suppress surface effects.

To explain the Gilbert damping dependence on the Rh thickness, the spin pumping effect can be used. As described in chapter 2.2, in the diffusive spin pumping model by Tserkovnyak, the Gilbert damping is enhanced exponentially with the thickness of the added normal metal layer. The observed damping is now referred to as α_{eff} , while α_0 represents the bulk Fe damping without any interface to a non-ferromagnetic ("normal") metal NM. The analysis of the spin pumping includes the determination of the spin diffusion length λ_{sd} , characteristic for the NM ability to transport spin information, and the spin mixing conductance g_{eff} , which is a interface dependent parameter defining the spin transport efficiency across the interface layer. To determine these parameters, the Gilbert damping dependence is fitted according to equation 2.80. This has been done in two different approaches.

The first approach includes weight base fitting. In this fitting, the error of the measurement points is accounted for by multiplying a weight factor to the least-squares determination: From $residuals^2 = (model^2 - data^2)$ to $residuals^2 = (model^2 - data^2) \cdot w^2$, increasing the residuals according to the w -factor given. The weights can now be defined differently for example: $1/w$ or $1/\sqrt{w}$, both result in slightly different fitting parameters. As the standard deviation of each parameter is increased, the parameter space of possible values is increased. One could model the number of possible parameters as a Gauß distribution, whose variance is modified by the weighting. The weights will therefore increase the width of the normal distribution and therefore increases the parameter space of possible values. Utilising the maximum-likelihood method, it is now possible to find a optimal value for each parameter, minimising the residual square error.

The second approach includes *weighted orthogonal distance regression*, ODR in short. This algorithm is an enhancement of the weighted fitting, by also including weights for the x-axis values. This means, in the case for the spin pumping fit, the Rh thickness error can be included into the regression. The thickness error of 0.5 nm was assumed in order to account for possible deviations due to calibration of quartz monitor tooling factor.

Additionally for batch-1, the 1 nm point was found to produce nonphysical values and high errors. Two more sets of fits were created, in which this point was included and excluded, resulting in two further sets of values. From all results, the mean value and the standard deviation is calculated, as a representing value for a variety of possible fit parameters. Similar situation holds for batch-2, in there the 15 nm point of batch-1 was taken to complete the dataset.

The fitted values together with mean and standard deviation can be found in tables 4.9 and 4.10. For batch-1 the hard axis orientation yields a spin diffusion length $\lambda_{sd} = 2.15 \pm 1.3$ nm with an effective spin mixing conductance $g^{\uparrow\downarrow} = (3.03 \pm 0.23) \cdot 10^{19} m^{-2}$, while the intermediate orientation yields $\lambda_{sd} = 2.2 \pm 0.87$ nm and $g^{\uparrow\downarrow} = (2.9 \pm 0.1) \cdot 10^{19} m^{-2}$. Note, that for the intermediate axis, the disturbance of the 1 nm Rh point was too big. Therefore only the values from the "1 nm excluded fit" were taken, with the standard deviation from the whole system. The results show almost no difference in the parameters in between hard axis and intermediate axis of batch-1. The anisotropy

in spin pumping in hard and intermediate axes, including the error, might be not ruled out according to this data.

The spin diffusion length of batch-2 is consistently higher from that of batch-1. The mean values of hard axis are $\lambda_{sd} = 3.46 \pm 1.22$ nm and $g^{\uparrow\downarrow} = (2.94 \pm 0.1) \cdot 10^{19} m^{-2}$. For the intermediate axis one finds $\lambda_{sd} = 4.1 \pm 0.95$ nm and $g^{\uparrow\downarrow} = (2.78 \pm 0.19) \cdot 10^{19} m^{-2}$. For this batch, the consideration of the 15 nm Rh point led to an increase of about 40% in mean λ_{sd} in comparison to the Excluded values, while $g^{\uparrow\downarrow}$ only differs by 11%. This increase can be traced back to the contributions of the parameters to the exponential function. The reciprocal spin diffusion length changes the slope of the increase, while $g^{\uparrow\downarrow}$ defines the amplitude. By including the 15 nm point, the α dependence is not saturated anymore, decreasing the slope of the exponential function and therefore increasing the value of λ_{sd} . The amplitude changes less because the y-error produces a wider range of possible values. By including the x-error in the ODR fit, both effects can be combined and the result is a value with moderate change. This is the reason why the ODR fit sometimes has a large offset from the weighted values.

Separately determining the mean and the standard deviation of the parameters for hard and intermediate axis, yields:

All Hard axis: $\lambda_{sd} = 2.68 \pm 1.46$ nm and $g^{\uparrow\downarrow} = (2.96 \pm 0.3) \cdot 10^{19} m^{-2}$

All Intermediate axis: $\lambda_{sd} = 2.62 \pm 1.7$ nm and $g^{\uparrow\downarrow} = (2.82 \pm 0.15) \cdot 10^{19} m^{-2}$

However, this is the mean of batch-1 in combination of batch-2. As can be seen from the value tables 4.9 and 4.10 as well as from comparing the alpha dependencies of batch-1 to batch-2, it becomes apparent, that batch-2 samples show a better thickness dependence in terms of interpreting a exponential function into these points. This leads to the assumption, that batch-2 represents the spin pumping effect in Fe/Rh bilayer better than batch-1. Based on this, the complete mean values for spin diffusion length and spin mixing conductance should be taken with care. This follows the mean values:

Batch-2 Hard axis: $\lambda_{sd} = 3.46 \pm 1.2$ nm and $g^{\uparrow\downarrow} = (2.94 \pm 0.34) \cdot 10^{19} m^{-2}$

Batch-2 Intermediate axis: $\lambda_{sd} = 4.1 \pm 0.95$ nm and $g^{\uparrow\downarrow} = (2.78 \pm 0.29) \cdot 10^{19} m^{-2}$

Since there exists a relative big error between both batches, the spin pumping parameters cannot be determined precisely. To account for the error, the mean values of both batch-1 and batch-2 are used in the further comparison.

From these values, the spin pumping effect is calculated and overlaid with the corresponding axes in figure 4.27. To set the Fe/Rh bilayer results into a perspective, the spin pumping parameters can be compared to literature values of comparable elements. For this, the literature values were chosen to roughly correlate, to this works bilayer system. This means literature values on spin pumping in FMR on Substrate/Fe/NM layers, see table 4.8.

Rhodium has the atomic number 45 in the periodic table, the direct neighbours are ruthenium (44) and palladium (46). The spin pumping effect is dependent on the interface quality and the LS-coupling of the normal metal (NM) element. For example, elements with high spin orbit coupling tend to have a smaller spin diffusion length λ_{sd} , as spin scatter effects are dependent on the coupling forces, that tend to be higher for higher LS-coupling. This can be seen for Fe/Pt or Py/Ta spin pumping experiments, in which the spin diffusion length is estimated to be in the range of 1.5 - 3 nm, depending on the coupling to the ferromagnet. Palladium, which has a higher LS-coupling than rhodium and smaller than platinum is found to be around 5.5 nm. In this context rhodium would be expected to have an even higher spin diffusion length of > 5 nm, like it can be assumed

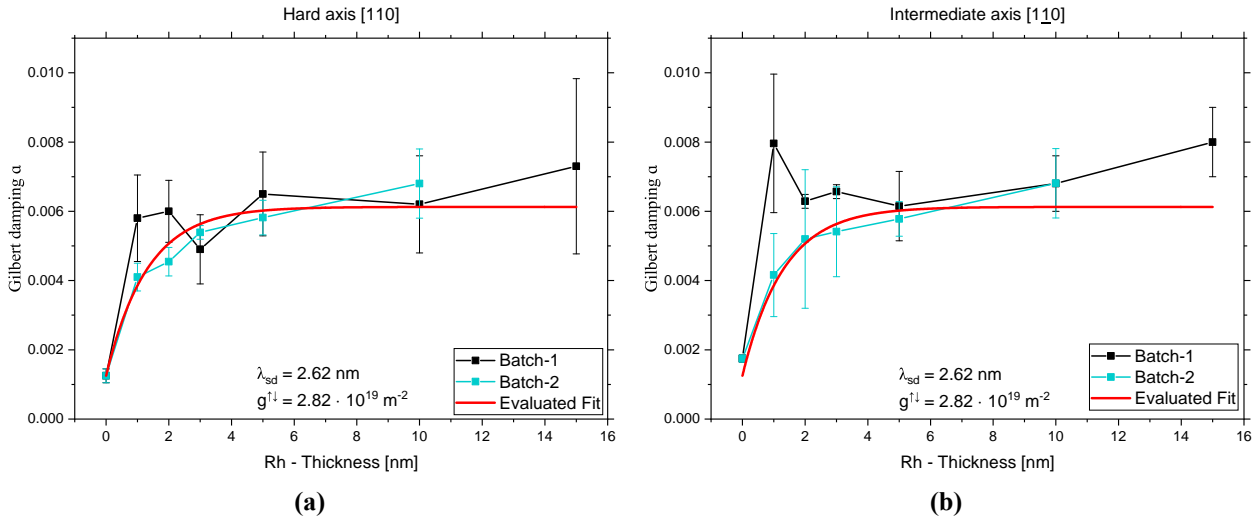


Fig. 4.27.: Evaluation of the spin pumping parameters for hard and intermediate axes of both batches. Figure **a)** shows the hard axis spin pumping, overlaid with a model evaluation of presented parameters. Figure **b)** shows the the spin pumping data of the intermediate axis, overlaid by the evaluated model of same parameters. By the assumption of isotropic spin pumping, one set of parameters should fit both intermediate and hard axis direction.

for ruthenium, that has a spin diffusion length of 14 nm at 4 K (while this value is at 4 K, it might not be comparable as spin scattering is reduced). However a value of $\lambda_{Rh} = 3.46 \pm 1.2 \text{ nm}$ for batch-2 is found, which is close to the value range of platinum. This means rhodium would have a much higher LS-coupling, than reported. This points to other effects than just LS-coupling to describe the dependence on the spin diffusion length to a element. In general every effect enhancing the spin scattering and therefore contributing to the loss of spin information in a NM must be enhanced in rhodium. One possible explanation could be the magnetic proximity effect at the interface of Fe to Rh. Like in Fe / Pd layers, Rh is ferromagnetically ordered for monolayer thicknesses [86, 87, 88]. This leads to an increased damping, artificially reducing the spin diffusion length due to an enhanced exchange stiffness, as the slope of the Gilbert damping α dependence on Rh thickness is increased. However, as can be seen in figure 4.27, the batch-2 dependence seems not to be saturated at 10 nm Rh thickness as the spin pumping fit would suggest. This means, that the value of $\lambda_{Rh} = 2.65 \pm 1.7$ could be underestimated. All in all the error in the Gilbert damping determination needs to be reduced to precisely determine the spin diffusion length.

Furthermore, the spin mixing conductance $g^{\uparrow\downarrow}$ shows similar values to platinum as well. The value of $g^{\uparrow\downarrow}$ for Fe/Rh bilayers is roughly $g_{Rh}^{\uparrow\downarrow} = (2.9 \pm 0.3) \cdot 10^{19} \text{ m}^{-2}$, while Fe/Pt or even Py/Pt bilayers can be placed in the range $g_{Pt}^{\uparrow\downarrow} = (2.8 \pm 0.6) \cdot 10^{19} \text{ m}^{-2}$. In the context of spin pumping this means, the pumping of spin currents across the Fe/Rh interface is more efficient, than in the interface Fe/Pt. This can have multiple reasons. The interface quality is of high importance for spin transport between two layers of different elements. It has been assumed by [89] that the interface roughness modifies the spin transport. For a high roughness, the spin mixing conductance is increased. The authors justify this effect, by considering the spin transport in an tunnel effect manner. With high roughness, the potential barrier at the interface exerts a lower gradient, than in the case of an perfect interface quality. This results into more spins transmitting from the FM into the NM, therefore increasing the transport efficiency. In the case of Fe/Rh a gradient in the potential barrier might be justified by interface alloying, creating a smooth transition from Fe-potential to Rh-potential maximising the spin transport. Furthermore it has been shown, that spin

mixing conductance in the model of dynamic RKKY is proportional to the electrical resistivity. By comparing the resistivity of Rh $\rho_{Rh} = 43.3 \text{ n}\Omega\text{m}$ to Pt $\rho_{Pt} = 106 \text{ n}\Omega\text{m}$ it is apparent [72], that Rh (bulk) is twice more conducting as Pt, which supports the assumption of an increased spin mixing conductance in Rh.

As the spin pumping parameters were fitted using different fitting approaches, the spin mixing conductance did not change as much as the spin diffusion length did. This points to a reduced error in the determination of $g^{\uparrow\downarrow}$. Nevertheless, a more precise determination could be done by reducing the noise of the damping values with larger Rh thicknesses, or an ferromagnetic layer thickness dependence, in which t_{Rh} is set constant and the Fe thickness is varied. This will give a linear dependence of equation 2.80 over the reciprocal Fe thickness t_{Fe} .

To conclude, the Fe/Rh bilayer system shows the spin pumping effect, in which a ferromagnet injects spin current into a normal metal. Multiple fits were done with changing parameters, generating a set of possible values, to describe possible errors. It was found, that rhodium as the normal metal layer has a spin diffusion length of $\lambda_{sd} = 2.65 \pm 1.7 \text{ nm}$ and the interface to Fe exerts a spin mixing conductance of $g^{\uparrow\downarrow} = (2.89 \pm 0.36) \cdot 10^{19} \text{ m}^{-2}$. To set these values in relation with existing data, rhodium shows a similar behaviour to platinum. Different than expected, rhodium shows a lower spin diffusion length than palladium and a spin mixing conductance, which is similar to that of platinum. The latter might be enhanced due to interface alloying or due to the fact, that rhodium has a very high conductivity. Within the errorbar no anisotropic spin pumping was found, although one might interpret the values of batch-2 as anisotropic. Further measurements need to be done to fully understand the saturation behaviour of the damping dependence and to reduce the error to allow a determination of anisotropy in spin pumping. Especially according to Cahaya et al. [90], the spin pumping efficiency is governed by crystal field effects in Ferromagnetic Insulators / Normal Metal bilayer systems. This means a fundamental anisotropy of the spin pumping effect has its origin in the crystal fields. Based on this one might assume, that this theory is applicable to 3d / 4d metal bilayer systems. This means if the crystal field shows a deviation from a cubic symmetry, the spin pumping efficiency and therefore, the spin mixing conductance, might be anisotropic. In the case of GaAs/Fe, a deviation of cubic in-plane symmetry arises at the interface through dislocation of the Fe layer, creating the additional uniaxial anisotropy. The crystal field, giving rise to the anisotropy, according to Cahaya, should give rise to an anisotropic spin mixing conductance as well. Based on the data from batch-2, $g^{\uparrow\downarrow}$ changes from hard axis $g^{\uparrow\downarrow} = (2.94 \pm 0.34) \cdot 10^{19} \text{ m}^{-2}$ to $g^{\uparrow\downarrow} = (2.78 \pm 0.29) \cdot 10^{19} \text{ m}^{-2}$ in the intermediate orientation. The difference of $\Delta g^{\uparrow\downarrow} = 0.16 \cdot 10^{19} \text{ m}^{-2}$ lies in both error bars and an assumption of a possible anisotropy should be taken with care.

Table 4.8.: Table of values for spin pumping in different systems.

Material	λ_{sd} [nm]	$g^{\uparrow\downarrow}[10^{19}m^{-2}]$	Reference
GaAs(100) / 5 nm Fe[110] / Rh	2.68 ± 1.46	2.96 ± 0.3	This work
GaAs(100) / 5 nm Fe[1 $\bar{1}$ 0] / Rh	2.62 ± 1.7	2.82 ± 0.15	This work
Si / 10 nm Fe / Pd	5.4	1.1 ± 0.13	[91]
GaAs(100) / 12 ML Fe / Pd	5.6	0.874	[49]
GaAs(100) / 16 ML Fe / Pd	5.1	0.9	[14]
MgO / 5 nm Fe / Pt	1.5 ± 0.4	3.4 ± 0.4	[92]
MgO / 12 nm Fe / MgO / Pt	3.5 - 10	$(2.7 \pm 0.8) - (4.9 \pm 0.5)$	[93]
GaAs / 16 ML Fe / Au / Ag	245 ± 30	1.1	[94]
Py / Pt	3.7 ± 0.2	2.4	[95]
Py / Ru	14 (at 4 K)	0.24	[96]
Py / Ru		3.8 ± 0.7	[97]
Py / Ta	1.5 ± 0.1	1.3 ± 0.4	[97]

Table 4.9.: Table of fitted values for the spin pumping effect of batch-1 samples. Values marked by W represented normal weighted non-linear regression, ODR stands for values from weighted orthogonal distance regression.

Batch-1 hard axis	Fit	λ_{sd} [nm]	error [nm]	g_{eff} [$10^{19}m^{-2}$]	error [$10^{19}m^{-2}$]
1 nm Rh Included	W	1.37	0.5	3.19	0.19
	W	0.633	0.79	2.74	0.19
	ODR	0.633	0.8	2.74	0.19
		Mean: 0.87	Std. dev: 0.42	Mean: 2.92	Std. dev: 2.61
1 nm Rh Excluded	W	2.33	1.16	3.35	0.18
	W	4.097	1.36	2.74	0.19
	ODR	2.33	1.16	2.94	0.3
		Mean: 2.92	Std. dev: 1.017	Mean: 3.08	Std. dev: 0.23
Batch-1 hard axis:		Mean: 2.15	Std. dev: 1.3	Mean: 3.03	Std. dev: 0.23
Batch-1 intermediate	Fit	λ_{sd} [nm]	error [nm]	g_{eff} [$10^{19}m^{-2}$]	error [$10^{19}m^{-2}$]
1 nm Rh Included	W	1.5	0.52	2.85	0.14
	W	0.02	0.004	2.81	0.13
	ODR	0.07	error	2.81	0.12
		Mean: 0.54	Std. dev: 0.85	Mean: 2.82	Std. dev: 0.02
1 nm Rh Excluded	W	1.76	0.4	2.914	0.13
	W	2.2	0.64	3	0.19
	ODR	1.41	0.19	2.8	0.19
		Mean: 1.73	Std. dev: 0.3	Mean: 2.9	Std. dev: 0.1
Batch-1 intermediate:		Mean: 1.13	Std. dev: 0.87	Mean: 2.86	Std. dev: 0.077

Table 4.10.: Table of fitted values for the spin pumping effect of batch-2 samples. Values marked by W represented normal weighted non-linear regression, ODR stands for values from weighted orthogonal distance regression.

Batch-2 hard axis	Fit	λ_{sd} [nm]	error [nm]	g_{eff} [$10^{19}m^{-2}$]	error [$10^{19}m^{-2}$]
15 nm Rh Included	W	5.58	1.04	3.485	0.063
	W	3.42	0.69	2.97	0.22
	ODR	3.05	0.69	2.84	0.21
		Mean: 4.01	Std. dev: 1.36	Mean: 3.1	Std. dev: 0.34
15 nm Rh Excluded	W	4.02	0.7	3.18	0.11
	W	2.34	0.48	2.58	0.16
	ODR	2.34	0.49	2.59	0.16
		Mean: 2.9	Std. dev: 0.96	Mean: 2.78	Std. dev: 0.34
Batch-2 hard axis:		Mean: 3.46	Std. dev: 1.22	Mean: 2.94	Std. dev: 0.34
Batch-2 intermediate	Fit	λ_{sd} [nm]	error [nm]	g_{eff} [$10^{19}m^{-2}$]	error [$10^{19}m^{-2}$]
15 nm Rh Included	W	5.07	1.56	2.87	0.28
	W	4.89	1.39	2.99	0.27
	ODR	4.97	0.01	3.01	0.27
		Mean: 4.97	Std. dev: 0.01	Mean: 2.96	Std. dev: 0.07
15 nm Rh Excluded	W	3.33	0.99	2.57	0.16
	W	3.19	0.77	2.62	0.16
	ODR	3.19	0.73	2.62	0.16
		Mean: 3.23	Std. dev: 0.08	Mean: 2.6	Std. dev: 0.028
Batch-2 intermediate:		Mean: 4.1	Std. dev: 0.95	Mean: 2.78	Std. dev: 0.29

5. Conclusions and outlook

The goal of this thesis was to investigate the growth and the magnetic properties of the Fe/Rh bilayer system by means of ferromagnetic resonance. The evaporation of both Fe and Rh had to be set up in a four pocket mini E-Beam evaporator in an UHV-chamber. The setup procedure took more than half-time of this thesis, as the rhodium pocket exerted all kinds of malfunctions. After a complete rebuild of the mini E-Beam evaporator the rhodium evaporation system was setup successfully and experiments to analyse the Rh growth mode could be started. For the growth mode determination, the Auger Electron Spectroscopy was used. It was found, that Rh grows epitaxially on Fe/GaAs(100), the Stranski-Krastanov growth mode for rhodium films of thicknesses below 1 nm was concluded. The finding of epitaxy is supported by several LEED patterns, suggesting a fcc rhodium, growing 45 ° rotated to the Fe lattice. Although no clear evidence was found, some AES intensity dependencies on the rhodium thickness suggest a intermixing with the Fe surface, which has been observed in literature.

In total 16 samples were produced, of which 12 were characterised in magnetic properties. The magnetic properties were investigated using the ferromagnetic resonance technique. Combining both ex-situ CPW multi-frequency and ex-situ cavity based angular dependent setups a variety of magnetic parameters could be determined at room temperature. As the average over all samples, the rhodium layer does not influence the g-factor of 5 nm Fe/GaAs(100). Both hard and intermediate in-plane orientation compare to literature, with the hard axes value $g = 2.11 \pm 0.01$ and the intermediate axis value $g = 2.10 \pm 0.01$. However, the thinner rhodium films of 1 and 2 nm show a slight deviation from this value, which in the interpretation was justified as an oxidation effect of Fe.

The magnetic anisotropy was found to vary over the Rh thickness. The effective magnetisation of the bilayer system is found to be constant over a wide range of thickness at $\mu_0 M_{eff} = 1.90 \pm 0.11$ T, with a initial increase in the low rhodium thickness region up to 2 nm. The uniaxial in-plane anisotropy $\mu_0 H_{K_{2||}}$, originating from the GaAs(100) / Fe interface was found to change. A constant offset of $\Delta\mu_0 H_{K_{2||}} = 4 \pm 1$ mT between batch-1 and batch-2 samples was found, which was attributed to the GaAs substrate quality, that changed in between the batches. From an initial reduction of $\mu_0 H_{K_{2||}}^{batch-1} = 28 \pm 1$ mT and $\mu_0 H_{K_{2||}}^{batch-2} = 24.0 \pm 0.5$ mT for 1 nm Rh the anisotropy field decreased to a minimum until 3 nm Rh with $\mu_0 H_{K_{2||}}^{batch-1} = 6 \pm 1$ mT and $\mu_0 H_{K_{2||}}^{batch-2} = 17.0 \pm 0.8$ mT, only to increase for higher thicknesses to $\mu_0 H_{K_{2||}}^{batch-1} = 25.0 \pm 0.5$ mT and $\mu_0 H_{K_{2||}}^{batch-2} = 18.0 \pm 0.8$ mT for 15 nm Rh. Furthermore, The cubic in-plane anisotropy field was found to decrease over increasing rhodium thickness with a complete reduction of $\Delta\mu_0 H_{K_{4||}} = 12\%$, starting at about $\mu_0 H_{K_{4||}} = 37 \pm 1$ mT for 1 nm Rh with a final value of $\mu_0 H_{K_{4||}} = 33.0 \pm 0.5$ mT for 15 nm.

The parameter $\mu_0 M_{eff}$ and $\mu_0 H_{K_{4||}}$ (for a value range of $\mu_0 H_{K_{4||}} = 37 \pm 4$ mT) are in good agreement to literature values, the values of $\mu_0 H_{K_{2||}}$ on the other hand show a high offset. This is attributable to the interface quality to GaAs, as most literature data points were obtained using different GaAs(100)-p(4x6) preparation recipes.

By the comparison of batch-1 1 nm rhodium sample (that due to a E-Beam evaporator malfunction adsorbed 1L of contaminants during the sample evaporation) to the 1 nm rhodium batch-2 sample, a rhodium capping layer effect could be assumed. A significant change in magnetic param-

eters of batch-1 1 nm rhodium, not occurring in 1 nm rhodium batch-2, leads to the interpretation, that 1 nm of rhodium is barely enough to protect Fe from oxidation and 3 nm Rh might be sufficient to prevent high oxidation. However the FMR data can only suggest these kinds of effects as derivations of changes in magnetic properties, only chemical analysis of the Fe layer can be used to verify the capping layer capability of rhodium.

The magnetisation damping of the Fe/Rh bilayers was investigated for up to 40 GHz. The Gilbert damping was found to increase with increasing rhodium thickness. This dependence was attributed to the appearance of the spin pumping effect from Fe into Rh, which was analysed within the model suggested by Tserkovnyak [43, 44]. By combining both batches, a mean values of spin pumping could be determined as follows:

All Hard axis: $\lambda_{sd} = 2.68 \pm 1.46$ nm and $g^{\uparrow\downarrow} = (2.96 \pm 0.30) \cdot 10^{19} m^{-2}$

All Intermediate axis: $\lambda_{sd} = 2.62 \pm 1.70$ nm and $g^{\uparrow\downarrow} = (2.82 \pm 0.15) \cdot 10^{19} m^{-2}$

While showing big deviation between batch-1 and batch-2, the batch-2 data could fit better in the present model, on which the determined parameters are:

Batch-2 Hard axis: $\lambda_{sd} = 3.46 \pm 1.20$ nm and $g^{\uparrow\downarrow} = (2.94 \pm 0.34) \cdot 10^{19} m^{-2}$

Batch-2 Intermediate axis: $\lambda_{sd} = 4.1 \pm 0.95$ nm and $g^{\uparrow\downarrow} = (2.78 \pm 0.29) \cdot 10^{19} m^{-2}$

Based on the assumption, that the same effect responsible for the uniaxial in-plane anisotropy $\mu_0 H_{K_{2||}}$, might also be applicable to damping, the spin pumping effect should also depend on the orientation. Care must be taken by this assumption, as the data shows the possible anisotropy between intermediate and hard axis within the errorbar. Nevertheless, the spin pumping parameters are found to be in close proximity to the values of platinum. The spin diffusion length λ_{sd} of rhodium, other than expected based on LS-coupling interpretations, is found to be smaller than that of palladium, while in the hard axis orientation, the spin mixing conductance lies in close proximity to platinum literature values. While no clear assumption could be made to interpret the lower spin diffusion length λ_{sd} , other than different spin relaxation mechanisms and errors due to unsaturated damping, assumption could be made for the fairly high spin mixing conductance $g^{\uparrow\downarrow}$. It is assumed, that interface alloying is reducing the potential gradient between Fe and Rh layer, which reduces the spin scattering at the interface. Furthermore the high conductivity of rhodium in comparison to platinum and palladium in the exchange coupled spin pumping approach might further enhance this behaviour.

The cavity FMR IP angular dependencies showed multiple additional effects/signals, that need to be studied further. In all of batch-1 samples an additional weak cubic signal arose, whose magnitude of anisotropy is higher, than that of the main signal, but rotated by 45° . The origin might be assumed in polarised Rh or FeRh interfacial layer, because of the 45° turned crystal lattice of rhodium relative to Fe underlying layer. It was additionally found, that this weak signal changed its anisotropy from cubic for all other samples to uniaxial with a hard axis above 0.2 T for 5 nm rhodium batch-1. The additional signal and the main signal are completely independent from each other and show no coupling effect.

Furthermore, the resonance lineshape shows a distortion dependency (asymmetry in absorption shape) on the rhodium thickness, which can be attributed to eddy currents originating in the Rh layer, gaining influence with increasing thickness. This gives rise to the usage of the complex Lorentzian or Dysonian lineshapes for compensation.

The chamber was further automated and new programs have been written in order to acquire data. This holds for LEED, AES, Chamber status (Pressure, Temperature), sample preparation, degasing/filament-conditioning and FMR data.

Outlook

Following further investigations can be done:

The saturation magnetisation of all samples needs to be determined, by techniques like SQUID or VSM.

The oxidation effect of Fe in Fe/Rh films, or in other words, the quality of Rh as capping layer can be determined by chemical analysis, XMCD or Mössbauer spectroscopy. The change of magnetic properties can also be determined via in-situ and ex-situ FMR on the same sample, or by controlled adsorption of oxygen in the vacuum chamber with a defined value of Langmuir, while each adsorption step is measured by in-situ FMR.

Bilayer films of thicker rhodium thickness greater than 15 nm need to be produced, to fully identify the point of complete saturation of Gilbert damping enhancement due to spin pumping into rhodium layer. This will rule out errors in the spin diffusion length and spin mixing conductance determination. Additionally a $1/t_{Fe}$ spin pumping dependence measurement can be conducted, to further identify the effective spin mixing conductance.

Furthermore, to completely identify the growth mode more thickness dependent AES measurements need to be done, with reduced error and without using the crystal quartz monitor as thickness determination. The growth can be further investigated in by RHEED measurements, to detect monolayer formation as RHEED oscillations, as well as IV-LEED experiments in which the surface quality and the out-of-plane lattice constant can be estimated. Both measurements should be done for ML thicknesses and thicker films, from which one might identify lattice relaxation from epitaxial stress, or interface alloying. To further investigate the surface and interface roughness of rhodium on iron, fresh samples of varying thicknesses can be analysed by MFM, AFM, SEM or STEM microscopies in in-plane or cross section orientation. Latter will also provide an information about interface alloying, which additionally could also be investigated in using Mössbauer spectroscopy and samples including Fe⁵⁷. The degree of interface polarisation of Rh should be determined as well, maybe an interface alloying is either enhancing or decreasing polarisation.

XRD measurements, if possible, should be done, to further understand the change in anisotropy of the 3 nm rhodium sample of batch-1. Additionally the crystal structure can be identified by this.

Additionally, the GaAs(100) substrate preparation must be improved to achieve a higher rate of p(4x6) superstructures. This could be done iteratively by varying parameters like, sample temperature and annealing time, while observing the changes using RHEED.

For all further experiments, new software must be written, as for example, to evaluate the RHEED oscillations in real time, or automate the deposition rate using PID regulation. Furthermore, the in-situ FMR acquisition will change, as a new magnet power supply must be integrated into the setup. In combination of a 3D printed adapter and a stepper motor, the MBE shutter movement can be automated, allowing an automatisisation of the AES growth dependence experiments as well.

A. Appendix

A.1. Additional Information

Fig. A.1, A.2 and A.3 show the effective magnetisation, in-plane uniaxial anisotropy and cubic anisotropy of 5,nm Fe/GaAs(100) as a function of Rh top layer thickness. These plots do not include many literature points and therefore present the thickness dependence in an unpolluted way.

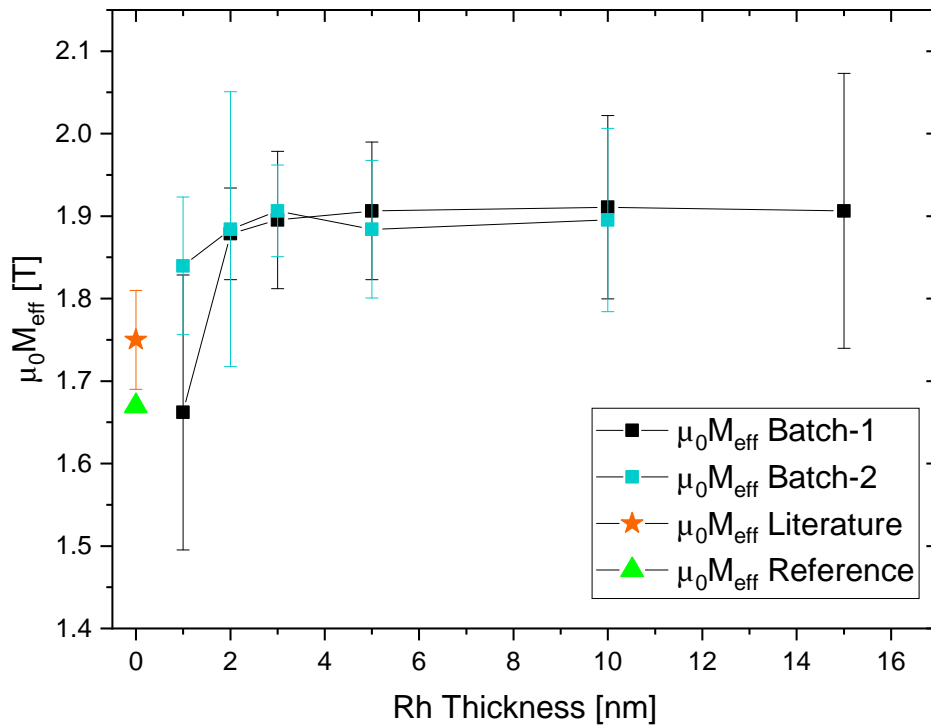


Fig. A.1.: Effective magnetisation of 5,nm Fe film as a function of Rh top layer thickness. Literature value taken from [41].

A.2. VNA-test-sample

The frequency dependence of Batch-2 samples was dependent on the magnet powersupply, that exerted several points of failure, delaying the measurements for 2 months. As a backup measurement setup, a VNA based FMR setup was quickly constructed and frequency sweep FMR measurements were taken. This has been done for 5, 10 and 15 nm Rh of batch-2. However due to a software error, only the 5 nm measurement can be used. The measurement of the VNA is not modulated, resulting in an absorption dip rather than an absorption derivative. Nevertheless the measurements should be compared to the ordinary CPW based frequency dependent field sweep measurements.

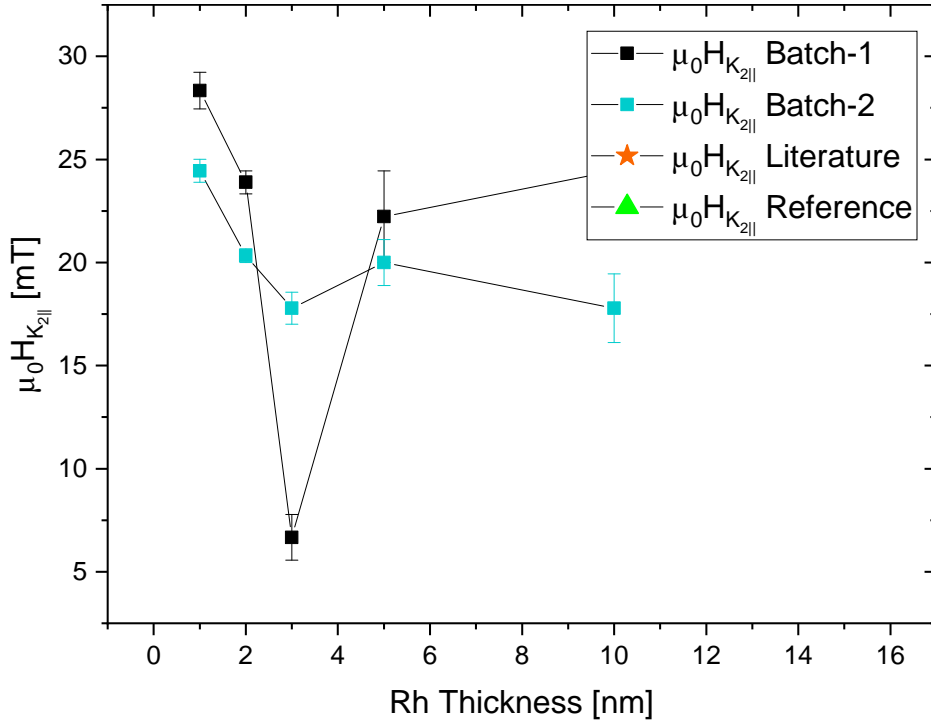


Fig. A.2.: The in-plane uniaxial anisotropy field of 5 nm Fe film as a function of Rh top layer thickness. Literature value taken from [41].

For samples 1, 5, 10 nm Rh of batch-2, the powersupply could be repaired and these samples could be measured. Therefore the 5 nm sample can be compared to the VNA setup. The direct comparison can be found in figure A.5. The same CPW was used in transmission for both measurements. In the case of the VNA (figure A.5a), a constant magnetic field of 10 mT was applied and the VNA swept the frequency from 0 to 40 GHz in 12000 points with microwaves of 0 dBm power. The signal was averaged 10 times and has a smoothening filter applied (point range = 100 points). The smoothening was chosen to not interfere with the resonance position or linewidth. Both averaging and smoothening are done by the VNA and were not applied during comparison. One spectra is obtained in less than 10 seconds, including the computational work of averaging and smoothing. As the field must be changed and the spectra needed to be saved manually, one measurement at a constant field needed about 30 seconds. The standard CPW setup, that was used in this analysis is based on the ordinary field sweep method. The field was changed in steps of 4096 points from 0 to 0.8 T at a constant frequency. Each field sweep takes about 5 minutes. Additionally microwaves at 8 GHz with 7.7 dBm were used. The spectras were chosen accordingly to their resonance position.

By identifying the noise amplitude (marked in red) as well as the FMR signal intensity, the signal-to-noise ration can be determined. For the un-modulated VNA-CPW setup, the SNR was found to be $SNR_{VNA} = 36 \pm 5$, while the standard CPW exerted a SNR of $SNR_{std} = 30 \pm 2$. Based on this observation both setups show a very similar SNR, with the modulation in mind, the VNA measurement even has potential to increase the SNR further by applying a modulation method. It would be worth investing time to further optimise this setup, as it can obtain FMR spectra extremely quick, while preserving a comparable SNR to the standard setup. By changing the CPW, higher frequencies are possible too, which reduces the error in damping constant and g-factor determination.

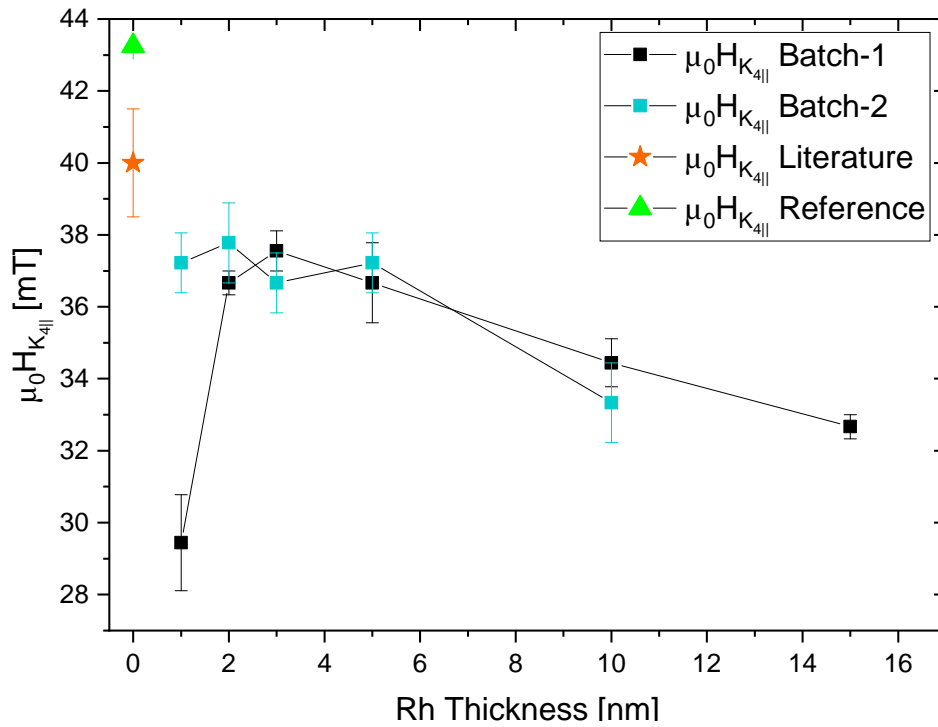


Fig. A.3.: The cubic in-plane anisotropy field of 5 nm Fe film as a function of Rh top layer thickness. Literature value taken from [41].

A.3. Restoration of the evaporation system

The E-beam evaporator can be seen in figure A.6. This picture shows the state freshly after the repair. After ruling out every error contribution, it was found, that a very high degree of contamination on both inner evaporation pocket walls and isolating aluminium oxide ceramics must have been the main cause of continuing problems with this evaporator (figure A.7).

The whole evaporator was completely disassembled and cleaned. The whole top part (copper cooling), was sanded down to bare copper and then was polished on the outside. The inner pocket walls were sanded down as well. The copper was then cleaned several times by an ultra sonic bath in isopropanol, to clean the copper surface of any residuals from sanding. It was found, that metallic films were slowly depositing on the ceramic isolators, which made them conductive and led to short circuits of the high voltage to ground. Furthermore, it was found that the high voltage isolation of the Rh rod, in the beginning was broken (figure A.8), leading to sparking inside the vacuum. Therefore all broken or metal covered ceramic parts were exchanged. The parts that could not be changed were immersed in an aqua-regia solution for several hours, to dissolve any metallic contaminations. Furthermore, the flux electrode was repaired, by replacing the flux wire and adding a second one. This will allow for future co-evaporation of two separately flux controlled materials. After cleaning and repair, some Rh growth measurements could take place, until the Rh high voltage line was shorting/sparking again. After further inspection it was found, that rhodium was depositing mainly onto the inner walls (figure A.9). Building up Rh flakes reaching the evaporation material caused single time sparking, that cooled down the Rh rod during evaporation which ruined the deposition rate or sometimes led to break-offs of the sample evaporation. The cause of this is unknown, but an assumption would be a too high evaporation rate (although the pressure and the deposition rate measured by the quartz monitor never suggested unsafe territory). With all of above fixed, several samples of batch-1 could be evaporated. After some samples it was found, that the

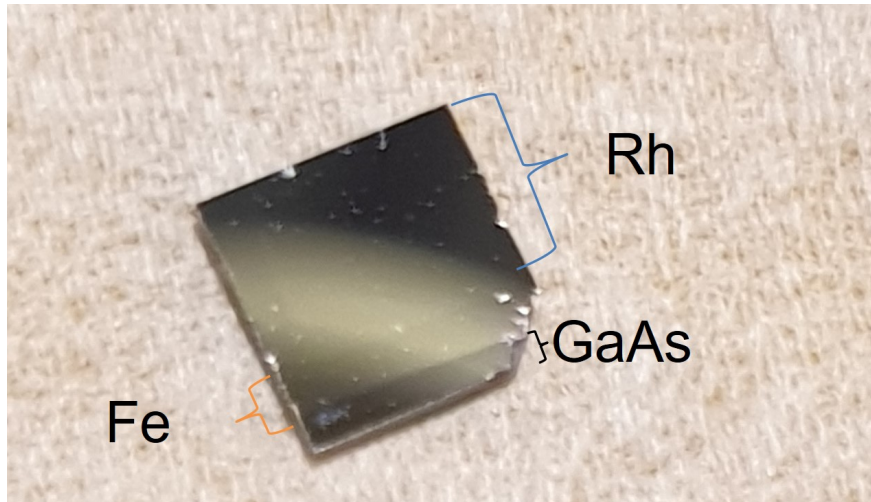


Fig. A.4.: Sample of 0.1 Å Rh per step AES growth experiment, one can see all elements. The dark bottom is uncovered GaAs, directly above a layer of Fe can be found. The rest of this sample is Rh.

Rh deposition rate was steadily decreasing. As an example, the evaporation started at an Rh rate of 0.7 Å/min with a flux of 80 nA and minutes later the rate was found to be 0.3 Å/min or less with 30 nA of flux. By increasing the filament and/or the high voltage, the rod temperature was adjusted up to the point of complete failure of evaporation. By closer inspection of the pockets it was found, that the Rh rod was loose and was tilted downwards (figure A.10), probably blocking the path for gaseous Rh to condense on the Fe substrate or the quartz monitor. Furthermore, by pulling back the isolation, some material had build up inside the ceramics, melting/reducing the steel threading as well (cone shape of the threaded rod). A possible explanation would be, that the temperature, that is needed to evaporate Rh (≈ 1900 K) is too high for the steel rod. Due to limited time, the steel rod was exchanged with a new steel rod. For future repair/upgrade one should consider using a molybdenum threaded rod, to rule out further errors.

A.4. Software used

A.4.1. FMR-Fit

The FMR fits were performed using a self written fitting interface (see figure A.11), that allows for selection and modification of derivative lineshapes. Each spectra can be fitted manually or automatised. Last one comes in handy for large angular dependencies, in which 360 spectra need to be evaluated. Each lineshape parameter can be changed in value, can be ignored/ set constant in the fit or can be bound to a specific range of values. Furthermore, there is no real limitation in the amount of lineshapes that can be used at the same time, although more than 1000 lines will crash the program due to memory errors.

The program further includes plotting capabilities for 2D plots, to either display angular or frequency dependent measurements (see figures in 4.22). Adjustments on colour range, plotting range or data filters are plotted in realtime. These operations plus plotting are found to be several times faster and easier in this program than compared to OriginPro or Mathematica, in which plotting and data manipulation can not be handled in real time speed (especially OriginPro).

Furthermore, once a dataset was fitted it can be directly analysed in terms of anisotropies. The free energy density as well as the fitting parameters can be freely modified. Both IP and OOP

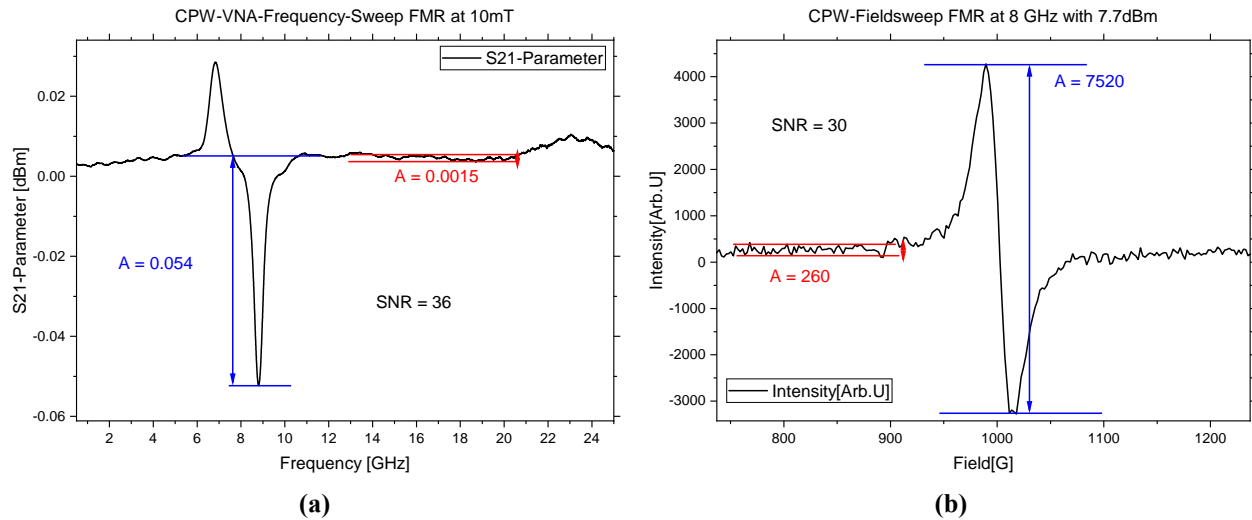


Fig. A.5.: Direct comparison between un-modulated VNA frequency sweep FMR in a) with field modulated field sweep FMR in b). The sample and the CPW was the same in both measurements. The sample was aligned in hard axis orientation, for a) this was aligned manually, a high angle error is expected. For b) the hard axis was determined using a angular dependence of 0.5° angle step. The noise level is marked in red, while the measurement is marked in blue.

angular dependence anisotropy fits can be performed. Due to a direct link to Mathematica, the same set of parameters can be fitted for anisotropies in two different approaches.

The source code can be found in <https://github.com/WiemelerJo/FMR-Fit>.

A much newer and less error prone version can be found in https://github.com/WiemelerJo/FMR_Fit_refreshed.

In addition to this GUI, several scripts for calculations were written, for example to calculate the resonance positions in various orientations and to plot these in a 3D. In total following Python libraries were used:

SciPy -> *NumPy* + *Matplotlib*, *SymEngine/Sympy*, *PyQtGraph*, *VisPy*, *Mayavi*, *PyVisa/PySerial*, *PyQt5*, *PySide2*, *lmfit* + *Blender* for the 3D model of the chamber

A.4.2. Chamber Software

Software was written to control the chamber and conduct experiments:

AES - Acquisition An AES-UI was written (figure A.12), that was used in the 0.3 \AA Rh per step dependence to obtain the data. It is a semi automatised approach, in which all Rh and Fe ranges are scanned iteratively. The sample positioning in AES and evaporation position was done by hand.

LEED Simultaneously to the AES-UI, a LEED image acquisition script was written, that could change the LEED energies of the LEED powersupply and take images using a CCD camera. In future this should enable the measurements of IV-LEED and RHEED/MEED.

Chamber Monitoring An chamber monitoring interface was written (figure A.13), that in a given time, scans all possible turbo pumps, IGP, pressure sensors and temperature sensors and plots the data in a real time plot. This was used to keep track of the chamber status over several weeks. In the future this will be expanded, to sample position manipulation by addressing ϕ - and Z-motors.



Fig. A.6.: The 4 pocket E-beam evaporator after repair.

Degasing helper UI As a quality of live improvement , the filament degasing after a bake-out was automatised and could be set to a ramp function (figure A.14), that would automatically degas the filaments over a long duration (\approx days).

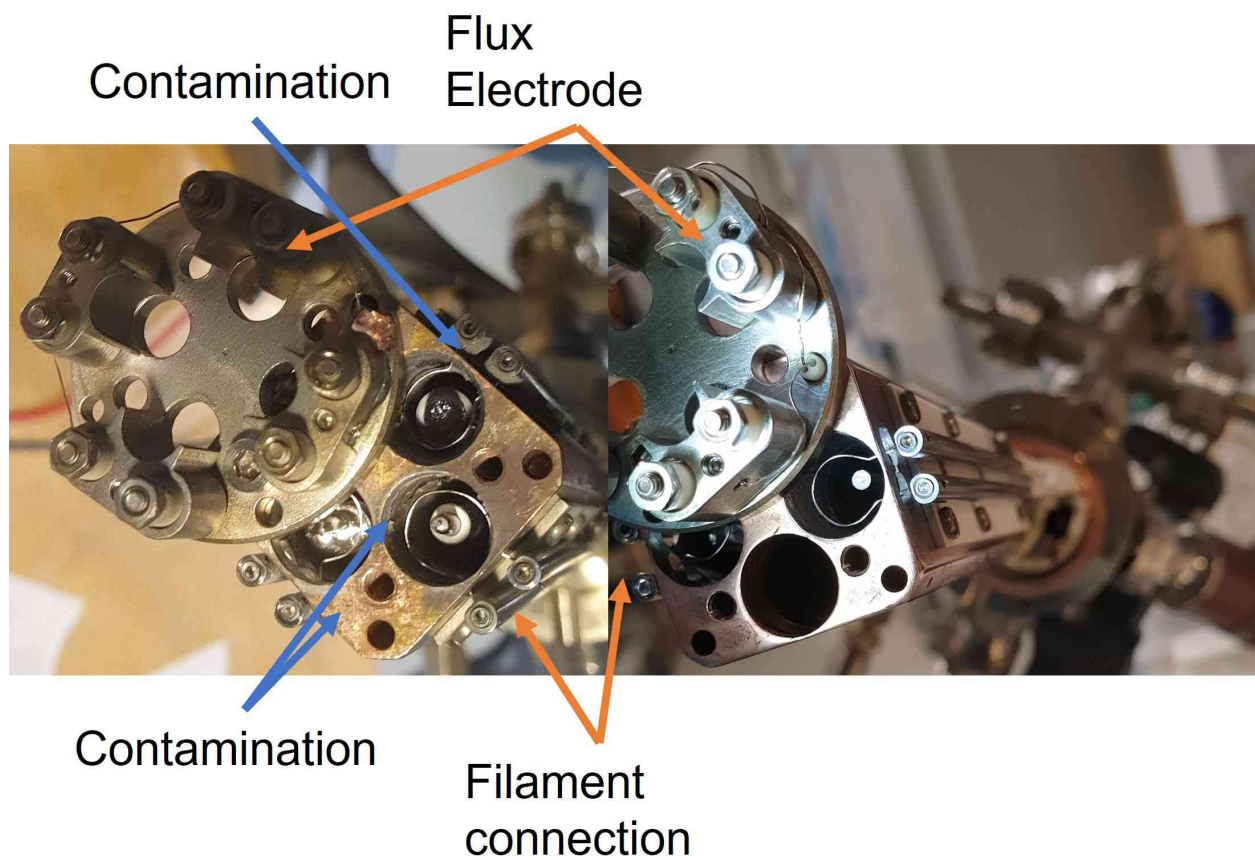
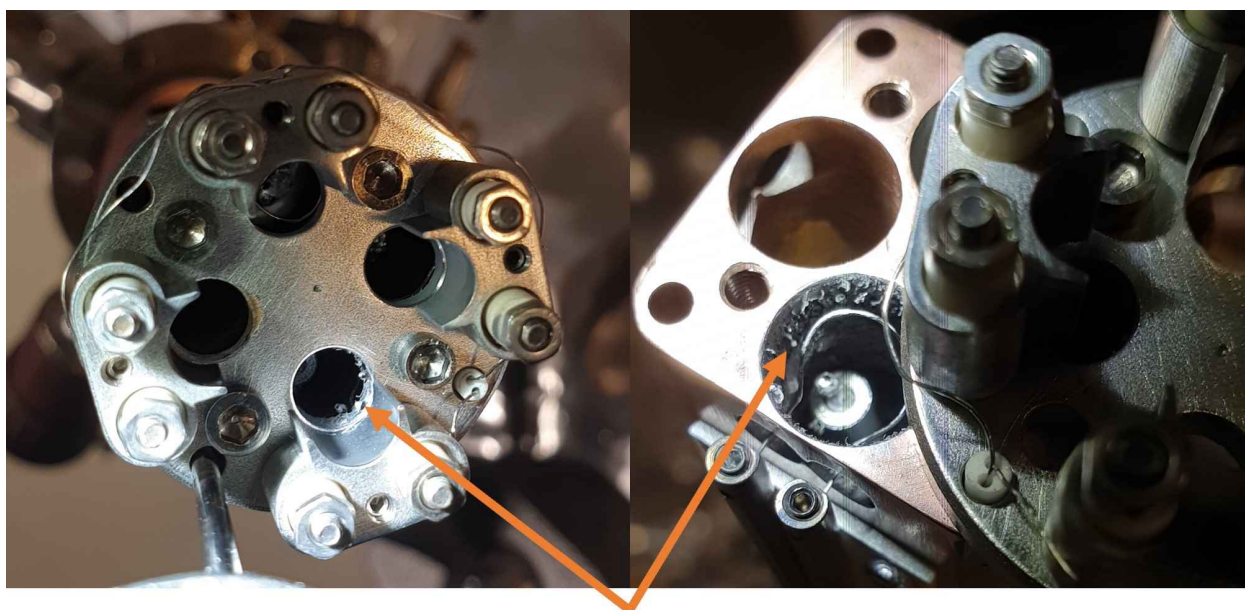


Fig. A.7.: Before and after comparison. The contaminations can be seen as flakes/sheets on the inside wall of the evaporation pockets (some were big enough to be removed by tweezers) and as random deposits of metal everywhere else as the top filament connection suggests.



Fig. A.8.: Broken isolation, that went black as sparks could hit the underlying metal.



Rhodium

Fig. A.9.: Build up Rh on the inner walls, that can be best described as flakes/sheets reaching the filament or the Rh rod itself.



Fig. A.10.: The top image, shows the how the Rh rod should have been positioned. The middle picture shows the position of the Rh rod inside the evaporator and the ceramics were pulled back revealing some build up material. The bottom image shows the detached rod, that was barely holding on to the threading. The metallic material covered the whole steel threading and was even "flowing" inside the ceramics. A lot of material can be seen on the molybdenum rod holder as well.

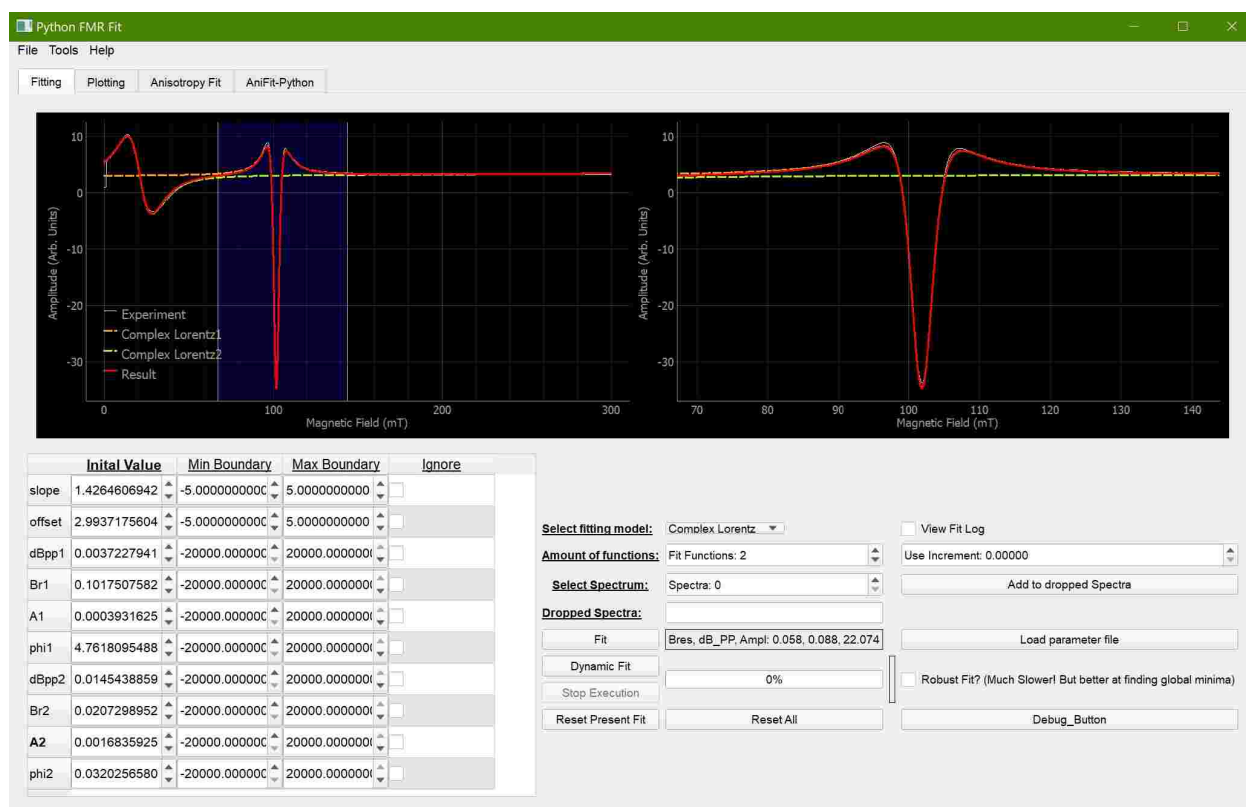


Fig. A.11.: Fitting interface, that was used and improved during this thesis. The fit of a field sweep measurement can be seen. For this two complex Lorentzian functions were used. The red line shows the fit while a white line shows the data, the individual functions are plotted as dashed lines.

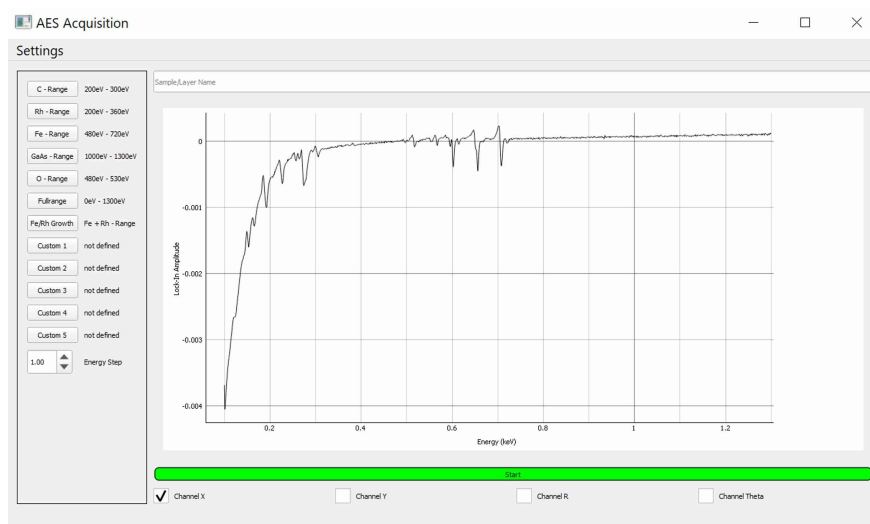


Fig. A.12.: The AES-acquisition UI, that was used to obtain AES measurements in the end of this thesis. Several different energy ranges are predefined, including a Fe/Rh mode, in which both surface and high energy regions of Rh and Fe are scanned iteratively.

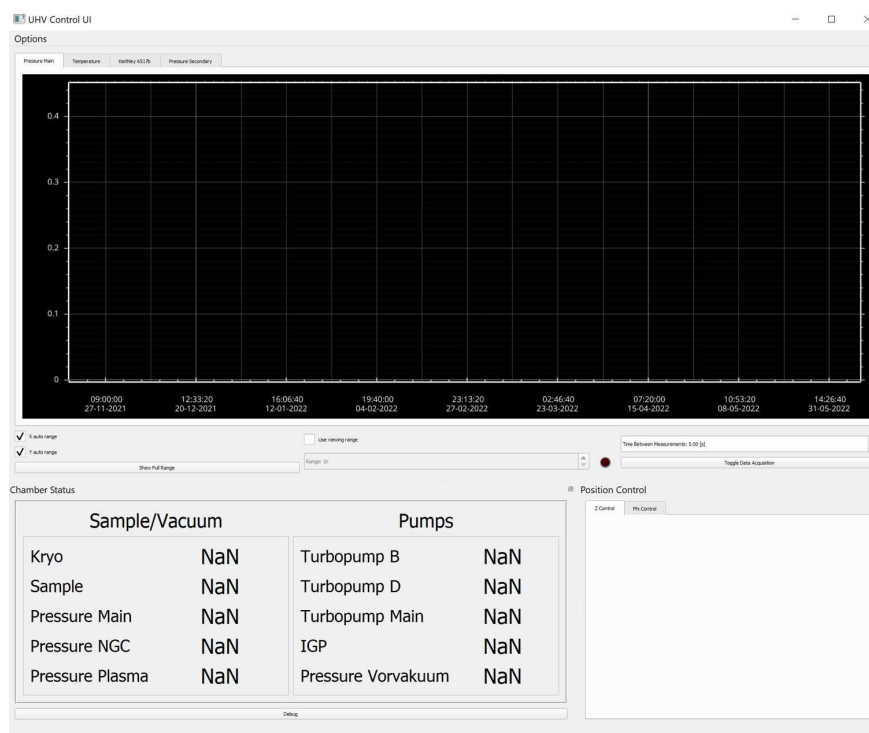


Fig. A.13.: The UHV-Chamber monitoring UI, that was specifically written, to obtain data in ranges of several months in real time.

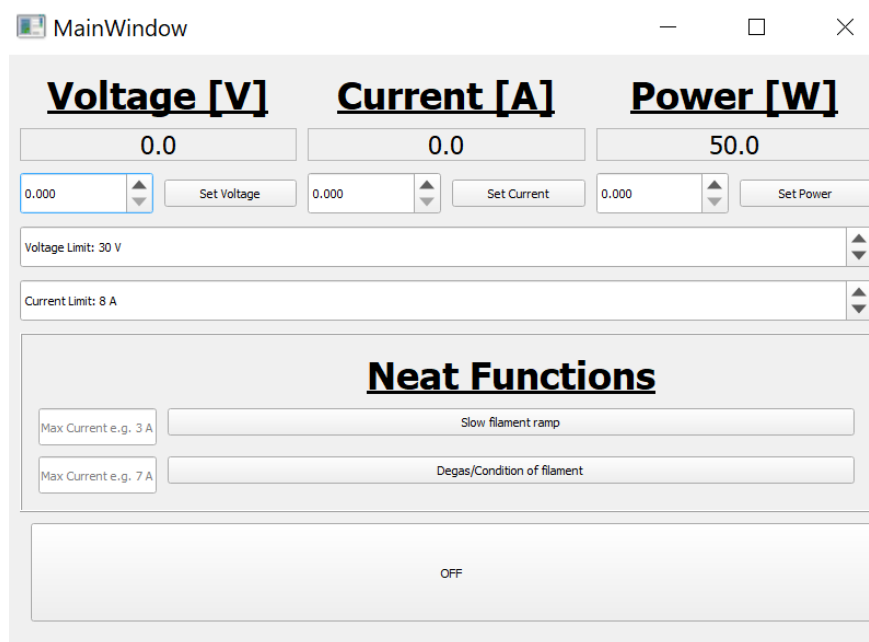


Fig. A.14.: Powersupply control, to comfortably degas filaments.

List of Figures

1.1.	Schematic representation of Fe growing on GaAs(100)-p(4x6). The picture was taken from [6].	1
2.1.	Schematic diagram of the precession of the magnetisation. The blue arrow is the damping term, that shows the spiral motion of M , if external stimulation through microwave fields is neglected. The red arrow is the precession term, driving the magnetisation around an effective magnetic field \vec{H}_{eff}	4
2.2.	This figure shows the spherical coordinate system, that is used to derive the phenomenological anisotropy. The field H is the external magnetic field and θ_H, ϕ_H describe the orientation of H . The angles θ, ϕ describe the orientation of the magnetisation M . The x axis is set along the [100] direction. A uniaxial in-plane anisotropy can be oriented with respect to the [100] direction, by the angle ϕ_u . This schematic further explains the meaning of in-plane rotation, in which the field H is varied around the z-axis with $\theta = const = 90^\circ = \pi/2$ and out-of-plane rotation in which $\phi = const$ and θ is varied. The picture is adapted from [23]	6
2.3.	Phenomenological Helmholtz free energy landscapes for different anisotropy contributions. Figure a) is a purely cubic anisotropy potential landscape. Figure b) shows a cubic anisotropy tetragonal distorted and figure c) shows a cubic anisotropy overlaid by an in-plane uniaxial anisotropy	9
2.4.	Helmholtz free energy landscape for uniaxial anisotropies F_{uni} . Figure a) shows the uniaxial anisotropy for a negative free energy density $F_{uni} < 0$ and figure b) for positive $F_{uni} > 0$	10
2.5.	Resonant response of the magnetic susceptibility for the case of ferromagnetic resonance. The susceptibility was calculated according to equations 2.39 using $M_0 = 0.0016$ T a damping of $\alpha = 0.01$, a frequency of 9.54 GHz and a g-factor $g = 2.1$. Only the resonance for positive fields is shown, in negative applied fields $H \in (-0.6, 0)$ T, due to the square law dependency on ω_H , a solution of the magnetic susceptibility can be found as well. This negative resonance mirrors the resonance of positive fields.	14

- 2.6. These figures show the free energy landscape cut **a)** and **d)**, like an in-plane, $\theta = \pi/2$, FMR measurement would produce. The values projected in 2D are presented in **b)** and **e)**. From these values the resonance field using the SBS resonance condition Eq. 2.45 seen in **c)** and **f)** can be determined. For figures a) to c), a pure cubic crystal was assumed. In figures d) to f) the cubic crystal was overlaid by an additional in-plane uniaxial anisotropy with easy axis at $\frac{3}{4}\pi$. Pictures g) and h) show a cubic anisotropy of Fe superimposed by a uniaxial anisotropy due to the growth on GaAs with ZnS structure. The magnitude of the superimposed uniaxial anisotropy becomes smaller, as Fe thickness increases. This is due to a increasing volume anisotropy, compensating the ZnS structure effect. This can be seen for a cubic anisotropy of Fe overlaid by measurement points in a polar plot in figure g). This figure reflects the situation in figures a) - c). For sufficiently thin Fe films on GaAs a additional uniaxial anisotropy is present, as seen in figure h). This figure reflects the situation of figures d) - f). Taken from Bayreuther [33]. 16
- 2.7. Calculated resonance positions for a frequency dependent FMR experiment oriented in the hard axis, for a Fe/GaAs(100) film this correlates to the [110] direction. The blue line shows the situation of the resonance positions for a very small misalignment around the hard axis of $\Delta\phi = 1.3^\circ$. Parameters of the film are given in the text. 18
- 2.8. FMR experiments for sample GaAs(100) / 4 nm Fe / 0.76 nm Rh. Based on a frequency dependence **a)**, the non-aligned modes can be made visible, following the green curve, in 9.4 GHz cavity angular dependence measurements **d)**. Following the yellow at 13 GHz **b)**, the FMR lies out of the non-aligned mode regime, resulting in undisturbed angular dependencies. From anisotropy parameters extracted from the 13 GHz measurement, the resonance loops originating from the non-aligned modes can be calculated **c)**. 20
- 2.9. Lorentzian lineshape in comparison to a Flovik/Complex-Lorentz lineshape. For the Flovik line, a high asymmetry was chosen (Complex Lorentz of $\phi = 3\pi/2$), to enhance the difference to the Lorentzian shape. The parameters chosen to plot these functions were: $A = 1$, $\Delta H_{pp} = 0.01$ mT, $H_{res} = H_R \in \{0.05, 0.15\}$ 22
- 2.10. The dragging effect of ultrathin Fe films on GaAs(100). Figure has been taken from supplementary materials of [41]. The solid light green line shows the dragging effect of a 5 nm Fe film. The green dashed line displays the situation without dragging. At hard axes points ([110], [$\bar{1}$ 10], [$\bar{1}$ 10]), the green, blue and the dashed green line are crossing, marking the points where the dragging effect vanishes in the experiment. 24
- 2.11. A quantum channel that connects two spin reservoirs A and B, which represent a ferromagnet and a regular metal, respectively. 26
- 2.12. Schematics of spin accumulation due to the precession of the magnetisation, taken from literature [47]. The magnetisation $\vec{M}_a(t)$, at a fixed time, is found to point at a specific value on the x-axis. The spin accumulation can now be described as the difference of spin polarised chemical potential $\delta\mu_s$ due to an inhomogeneous distribution of the value of the magnetisation between the present direction and its opposite site at a fixed time. In this figure the opposite site is modelled as $x < 0$. The model described by Takahashi, the blue line represents the spin accumulation δm_z for a precessing magnetisation of unfixed time. The resulting spin current is named \vec{j}_S 27

3.1.	The simplified 3D model of the ultra high vacuum chamber used in this work. . . .	31
3.2.	Approximated phase diagram of pure iron. Different crystallographic phases are present such as bcc- α -Iron, fcc- γ -Iron and bcc- δ -Iron, as well as the states of aggregation, solid, liquid and most importantly the vapour phase. The region of interest in MBE is the range around 800K, producing vapour pressures of about $10^{-10} - 10^{-8}$ mbar. The diagram was recreated with data from [52].	33
3.3.	Ewald construction for the Laue-Law at the surface of a lattice. The green vertical lines show the Laue-Rods, that are created due to missing crystal periodicity to the vacuum. Pictures were taken from [53].	34
3.4.	Auger-process: The left picture shows the excitation of energy E_{kin} . The created electron hole is filled by relaxation under photon emission of a characteristic wavelength. The right picture, begins in the excited state and displays the Auger-Process of radiationless relaxation and emission of an Auger-Electron. Picture taken from [54].	35
3.5.	Predicted and measured metal on metal growth taken from [55]. According to these calculations, Rh(001) is expected to grow parallel to Fe(001) plane.	36
3.6.	Schematic description of the growth and corresponding AES intensity dependencies, taken from [57]	37
3.7.	A collection of LEED patterns for GaAs(100) taken from literature [59]	39
3.8.	Schematic representation of a Bruker Eleksys E500 EPR setup. The EPR setup can be used for FMR experiments, as both effect can be measured by resonant absorption of microwave energy. As a microwave source, a Gunn-Diode is used. However, the present measurement arrangement of X-Band microwaves can also be achieved by using a Klystron microwave source. The thicker black lines represent the path of the microwaves, while the arrows indicate the propagation direction. Picture based on [6]	41
3.9.	Schematics of a circulator. Recreated according to [67]	42
3.10.	Schematic representation of the CPW FMR setup. On the left side, the overall setup without the magnet and the modulation coils is shown. The right picture shows a close-up of the CPW stripline with the electric and magnetic field portion distribution of the flowing signal. The right picture was taken from [23].	43
3.11.	Calibration measurement for frequency dependent FMR using either a CPW or a microwave short. Figure a) and b) show the uncalibrated diode voltage over the applied frequency with constant microwave power of 5 dBm. The red dots, that are better resolved in figure b), are the local maxima of the diode voltage for a specific frequency range. Figure c) shows the microwave power for each of the local maximum points required to achieve a constant diode voltage of -0.3 V. . . .	44
4.1.	Example of a freshly prepared Fe layer AES spectra. Impurities like Carbon and Oxygen have been marked, as well as the very surface sensitive low energy Fe peak at 47 eV and the 703 eV peak. The measurement was taken under parameters creating a sample current $> 1 \mu\text{A}$	47
4.2.	A rough estimation of the inelastic mean free path of an electron plotted and highlighted for low and higher energy peak of Fe. The graph was calculated according to data from [70].	48

- 4.3. All AES growth studies made during this thesis. The highlighted areas mark repeating patterns. The error of the intensities is determined to be the size of the symbols in the plots and lay in the area of $\pm 1\text{E-5}$. Figure **a)** shows the 0.1 Å per evaporation step dependence of AES peak to peak intensities. For this study in particular, the thickness error is significant. Figure **b)** shows the 0.2 Å Rh per step measurement. This study was performed with an increased electron beam current, resulting in higher AES intensities, reducing the noise. The 0.3 Å Rh per step measurement is shown in figure **c)**, the first three data points of the Fe intensity are missing. In the measurement of figure **d)** the Rh was evaporated in steps of 0.4 Å. After reaching 2.4 Å, the study was stopped and continued on the next day to evaporate a total Rh thickness of 5 Å. 49
- 4.4. AES surface peak intensities as a function of 0.2 Å. The intensity error is smaller or comparable to the point size of the measurement points. The Rh points in particular show large fluctuations that cannot be attributed to the noise or error of the signal. This is due to a large background that does not change the Rh value linearly. Figure **a)** shows the peak-to-peak AES intensity of Rh and Fe, while Figure **b)** shows the logarithm of the normalised Fe surface peak intensity. The linear fits are intended to highlight the areas of interpreted linear dependence. 52
- 4.5. Example picture of a perfect GaAs(100) 4x6 LEED pattern at 124 eV. Taken from literature [64] 55
- 4.6. Example LEED pictures of prepared wafer-1 and wafer-2 substrates. Figure **a)** shows the GaAs substrate for Fe the of 0.4 Å Rh AES dependence at 150 eV, In figure **b)** the GaAs substrate of the 2 nm Rh sample of Batch-2 at 118 eV is presented. 56
- 4.7. Figure **a)** shows the LEED images for prepared GaAs(100)-p(4-6) at 135 eV and Fe layers at 120 eV, taken from [76]. Example LEED pictures of a 5 nm Fe film, directly after evaporation, are found in figure **b)**. This Fe belongs to the 2 nm Rh sample of Batch-2. 58
- 4.8. Example LEED picture for Fe films with worse pattern as for 2 nm Rh sample of Batch-2 in figure 4.7b. The sample shown in the picture is the Fe layer of the 5 nm Rh Batch-2 sample at 149 eV. The picture has been enhanced in brightness and contrast, to make the dots visible 58
- 4.9. LEED images of **a)** Rh, and **b)** a comparison between Rh and Fe at the same energies of 2 nm Rh Batch-2 sample. Besides 289 eV of 15 nm Rh Batch-1 no picture was enhanced. The red box is a residual box from the LEED acquisition software used in the beginning and was not placed to focus on this area in particular. In the pictures of 5 nm Rh Batch-2 a misalignment of the sample holder is present. . . . 59
- 4.10. Analysis of the 2 nm Rh batch-2 surface using AES-spectroscopy. This measurement was done utilising a sample current of 4.5 μA 60
- 4.11. In figure **a)** a in-plane CPW-FMR frequency dependence measurement, oriented in hard axis Fe[110], is visible. Figure **b)** shows the calculated and overlaid resonance position, according to an iterative fitting method of anisotropies, misalignment and g-factor. The sample shown is 2 nm Rh of batch-1. The anisotropy was determined to be $K_{2\perp} = 340000 \pm 50000 \text{ J/m}^3$, $K_{2\parallel} = 22000 \pm 2000 \text{ J/m}^3$ and $K_{4\parallel} = 33813 \pm 1500 \text{ J/m}^3$. The g-factor is $g = 2.11 \pm 0.02$ and additionally a hard axis misalignment of $0.01 \text{ rad} \approx 0.57^\circ$ was found. 62

- 4.12. Plot of the g-factors for **hard axis** [110]. A uncapped reference sample of 5 nm Fe on GaAs(100)-(4x6) was added as the green triangle at $g = 2.12$. Furthermore, a value taken from literature $g_{lit} = 2.11 \pm 0.008$ is presented as an orange star [41] . 64
- 4.13. Plot of the g-factors for **intermediate axis** [110]. A uncapped reference sample of 5 nm Fe on GaAs(100)-(4x6) was added as the green triangle at $g = 2.1$. Furthermore, a value taken from literature $g_{lit} = 2.11 \pm 0.008$ is presented as an orange star [41] 64
- 4.14. In figure **a**) a in-plane cavity angular dependence measurement of 2 nm Rh of batch-1 is shown. The angle was varied from 0° to 359° in 1° steps. For each step the external field was varied from 0 to 0.3 T in steps of 2048 points and a microwave frequency of $f = 9.543$ GHz was used. The hard axes at 45° and 225° correspond to Fe [110] and $\bar{1}\bar{1}0$ directions. Figure **b**) shows the calculated resonance position as white dots; the non-aligned mode loops are calculated as well. The anisotropy was determined to be $K_{2\perp} = 340000 \pm 50000 J/m^3$, $K_{2\parallel} = 22000 \pm 2000 J/m^3$ and $K_{4\parallel} = 33800 \pm 1500 J/m^3$. The g-factor is $g = 2.11 \pm 0.02$ 66
- 4.15. This 3D plot shows the angular and frequency dependence on the resonance position. The field was varied between 0 to 0.6 T in steps of 0.001 T. The resonance frequencies were calculated for each field step. This was done for angles from 0° to 359° in steps of 0.2° . As anisotropy parameters, the anisotropies of 2 nm Rh of batch-1 were taken. If one keeps the frequency constant, which would create a 2D plane in the XY orientation, the intersections with this plane would correspond to the angular dependence matching the constant frequency. For the case of non-aligned modes, multiple intersections are found, corresponding to multiple resonance positions at one angle, creating the resonance loops. One could explain this 3D plot as the angular dependence of the frequency dependence of the FMR as seen in figure 2.7. The minima positions (cones) at 0° and 180° show the hard axis non aligned modes. For 90° and 270° the intermediate axis can be found. . . 67
- 4.16. High field angular dependent measurement from 1.0 T to 2.2 T of 2 nm Rh batch-1. The resonance position was fitted and plotted as the black point. The error of the fit lays in the size of the points. Additionally from a set of anisotropies, $K_{2\perp} = 340000 \pm 50000 J/m^3$, $K_{2\parallel} = 22000 \pm 2000 J/m^3$, $K_{4\parallel} = 33800 \pm 1500 J/m^3$, $K_{4\perp} = -20000 \pm 10000 J/m^3$ and $g = 2.11 \pm 0.02$, the resonance position was calculated and plotted as green points. 68
- 4.17. Out of plane anisotropy fit of 2 nm Rh. The angle $\phi_H = \pi/4$ was set constant and θ was varied. The black line is the calculated value of the resonance position, while the red points show the fitted resonance position. This measurement is a combination of 2 measurements. The magnetic field can only be varied in sweep ranges of 1.2 T. For the higher field portion a second measurement was done only around one hard axis, this measurement is visible in figure 4.16. From both measurements the resonance position was extracted and overlaid. Because the hard axis needs higher fields than the magnet can create, the resonance positions in the distinct hard axis orientation $\theta \in (0, \pi)$ is just an estimate. A value of $K_{4\perp} = -20000 \pm 10000 J/m^3$, which corresponds to a anisotropy field of $\mu_0 H_{K_{4\perp}} = -22 \pm 11$ mT, was found . . 69

4.18. Comparison of effective magnetisation M_{eff} values between data from this work and literature. The bottom x-axis shows the origin of the literature data and the black points the corresponding value, while the top x-axis shows the Rh-thickness and the green symbols show the values of batch-1 samples, while the orange symbols show the values of batch-2. Furthermore, the literature is split in: In-Situ, marked by the blue region, and Ex-Situ, marked by the green region.	70
4.19. This figure presents the IP uniaxial anisotropy field $\mu_0 H_{K_{2 }}$ in [mT]. As for the effective magnetisation (figure 4.18), the literature is shown in black and the measurement data is presented in orange for batch-1 and green for batch-2.	72
4.20. The figure shows the cubic in-plane anisotropy field $\mu_0 H_{K_{4 }}$. The colour coding follows the same structure as previous comparisons.	73
4.21. The colour plot of the angular dependent cavity based FMR measurement for 3 nm Rh of batch-1. The data was obtained in in-plane orientation at room temperature and at a frequency of 9.54 GHz. The colourbar on the right sets a colour value to the FMR intensities. The light blue region defines the colour mapping, in which a histogram of the intensities is plotted.	76
4.22. Additional signals, that were found in in-plane cavity angular dependent FMR experiments on batch-1 samples and samples with the same wafer as batch-1. All measurements were performed at room temperature in an X-Band cavity. Figure a) shows the measurement of 0.76 nm Rh on 4 nm Fe using the GaAs from wafer-1. In figure b) the measurement of 3 nm Rh batch-1, focused on a very tiny intensity range. For figure c) , the measurement of 5 nm Rh batch-1 can be found, while figure d) shows the angular dependence of 15 nm Rh batch-1.	78
4.23. Gilbert damping in hard axis orientation of batch-1 and batch-2.	80
4.24. Gilbert damping in intermediate axis orientation of batch-1 and batch-2.	80
4.25. Comparison of the Gilbert damping in between the batches. The x-axis additionally is scaled using the natural logarithm. Figure a) shows the samples of batch-1, while figure b) shows the samples of batch-2	81
4.26. In homogeneous broadening of batch-1 a) and batch-2 b) . This value is obtained, as the constant linewidth offset in the linear damping fit.	81
4.27. Evaluation of the spin pumping parameters for hard and intermediate axes of both batches. Figure a) shows the hard axis spin pumping, overlaid with a model evaluation of presented parameters. Figure b) shows the the spin pumping data of the intermediate axis, overlaid by the evaluated model of same parameters. By the assumption of isotropic spin pumping, one set of parameters should fit both intermediate and hard axis direction.	84
A.1. Effective magnetisation of 5,nm Fe film as a function of Rh top layer thickness. Literature value taken from [41].	91
A.2. The in-plane uniaxial anisotropy field of 5 nm Fe film as a function of Rh top layer thickness. Literature value taken from [41].	92
A.3. The cubic in-plane anisotropy field of 5 nm Fe film as a function of Rh top layer thickness. Literature value taken from [41].	93
A.4. Sample of 0.1 Å Rh per step AES growth experiment, one can see all elements. The dark bottom is uncovered GaAs, directly above a layer of Fe can be found. The rest of this sample is Rh.	94

A.5. Direct comparison between un-modulated VNA frequency sweep FMR in a) with field modulated field sweep FMR in b). The sample and the CPW was the same in both measurements. The sample was aligned in hard axis orientation, for a) this was aligned manually, a high angle error is expected. For b) the hard axis was determined using a angular dependence of 0.5° angle step. The noise level is marked in red, while the measurement is marked in blue.	95
A.6. The 4 pocket E-beam evaporator after repair.	96
A.7. Before and after comparison. The contaminations can be seen as flakes/sheets on the inside wall of the evaporation pockets (some were big enough to be removed by tweezers) and as random deposits of metal everywhere else as the top filament connection suggests.	97
A.8. Broken isolation, that went black as sparks could hit the underlying metal.	97
A.9. Build up Rh on the inner walls, that can be best described as flakes/sheets reaching the filament or the Rh rod itself.	98
A.10. The top image, shows the how the Rh rod should have been positioned. The middle picture shows the position of the Rh rod inside the evaporator and the ceramics were pulled back revealing some build up material. The bottom image shows the detached rod, that was barely holding on to the threading. The metallic material covered the whole steel threading and was even "flowing" inside the ceramics. A lot of material can be seen on the molybdenum rod holder as well.	98
A.11. Fitting interface, that was used and improved during this thesis. The fit of a field sweep measurement can be seen. For this two complex Lorentzian functions were used. The red line shows the fit while a white line shows the data, the individual functions are plotted as dashed lines.	99
A.12. The AES-acquisition UI, that was used to obtain AES measurements in the end of this thesis. Several different energy ranges are predefined, including a Fe/Rh mode, in which both surface and high energy regions of Rh and Fe are scanned iteratively.	99
A.13. The UHV-Chamber monitoring UI, that was specifically written, to obtain data in ranges of several months in real time.	100
A.14. Powersupply control, to comfortably degas filaments.	100

List of Tables

4.1.	The g-factors for all samples in hard axis [110] orientation evaluated as a fit of the frequency dependence of the resonance field according to the Kittel equation 2.50. The 15 nm Rh sample of batch-2 could not be measured in a frequency dependence. The g-factor is assumed to be constant over all samples, therefore the g-factor of 15 nm was assumed to be $g = 2.11$ for further angular dependent anisotropy estimation.	63
4.2.	The g-factors for all samples in intermediate axis $[1\bar{1}0]$ orientation evaluated as a fit of the frequency dependence of the resonance field according to the Kittel equation 2.50. The 15 nm Rh sample of batch-2 could not be measured in a frequency dependence. The g-factor is assumed to be constant over all samples, therefore the g-factor of 15 nm was assumed to be $g = 2.1$ for further angular dependent anisotropy estimation.	65
4.3.	Anisotropy fields for two methods of anisotropy estimation. The values belong to sample 2 nm batch-1. As the names suggest, $\mu_0 H_{K_{2,4\parallel}}$ are the anisotropy field of anisotropy parameters $K_{2,4\parallel}$. The parameter $K_{2\perp}$, as described in chapter 2.1.2, is described in term of M_{eff} . Cavity ϕ -Fit stands for the anisotropy of the cavity angular dependence, while CPW f-Fit stands for the anisotropies obtained through aligning the resonance frequency to the measurement data.	67
4.4.	Time dependence of the anisotropy parameter of 1 nm Rh batch-1.	71
4.5.	All anisotropy fields used in the discussion.	75
4.6.	Literature damping values for bulk or 5 nm thick Fe layers.	79
4.7.	From fitting obtained Gilbert damping values for all samples. The values are given in $[10^{-3}]$.	81
4.8.	Table of values for spin pumping in different systems.	86
4.9.	Table of fitted values for the spin pumping effect of batch-1 samples. Values marked by W represented normal weighted non-linear regression, ODR stands for values from weighted orthogonal distance regression.	86
4.10.	Table of fitted values for the spin pumping effect of batch-2 samples. Values marked by W represented normal weighted non-linear regression, ODR stands for values from weighted orthogonal distance regression.	87

Bibliography

- [1] L H Lewise. In: *J. Phys. D: Appl. Phys* 49.32 (2016), p. 323002.
- [2] Heidarian A. “Tuning the antiferromagnetic to ferromagnetic phase transition in FeRh thin films by means of low-energy/low fluence ion irradiation.” In: *Nuclear Instruments and Methods in Physics Research Section B: Beam Interactions with Materials and Atoms* 358 (2015), pp. 251–254. issn: 0168583X. doi: [10.1016/j.nimb.2015.06.027](https://doi.org/10.1016/j.nimb.2015.06.027).
- [3] Thiele J. “FeRh/FePt exchange spring films for thermally assisted magnetic recording media.” In: *Applied Physics Letters* 82.17 (2003), pp. 2859–2861. issn: 0003-6951. doi: [10.1063/1.1571232](https://doi.org/10.1063/1.1571232).
- [4] Wang Y. “Spin pumping during the antiferromagnetic–ferromagnetic phase transition of iron–rhodium.” In: *Nature Communications* 11.1 (2020), p. 275. issn: 2041-1723. doi: [10.1038/s41467-019-14061-w](https://doi.org/10.1038/s41467-019-14061-w).
- [5] I. Suzuki. In: *APPLA* 105.17 (2014), p. 172401.
- [6] Zakeri K. “Magnetic monolayers on semiconducting substrates: an in situ FMR study of Fe-based heterostructures.” PhD thesis. 2007.
- [7] Gordon R.A. “In-plane structural anisotropy of ultrathin Fe films on GaAs(001)–4 × 6: X-ray absorption fine-structure spectroscopy measurements.” In: *Physical Review B* 74.16 (2006). PRB, p. 165405. doi: [10.1103/PhysRevB.74.165405](https://doi.org/10.1103/PhysRevB.74.165405).
- [8] Cox A.J. “Experimental observation of magnetism in rhodium clusters.” In: *Physical Review Letters* 71.6 (1993). PRL, pp. 923–926. doi: [10.1103/PhysRevLett.71.923](https://doi.org/10.1103/PhysRevLett.71.923).
- [9] Kachel T. “Ferromagnetic order in ultrathin Rh layers on Fe(100).” In: *Physical Review B* 46.19 (1992). PRB, pp. 12888–12891. doi: [10.1103/PhysRevB.46.12888](https://doi.org/10.1103/PhysRevB.46.12888).
- [10] M.Busch. “Spin polarization, structure and chemical composition of the Rh/Fe(1 0 0) interface.” In: *Surface Science* 582.1-3 (2005), pp. 31–41. doi: <https://doi.org/10.1016/j.susc.2005.02.046>.
- [11] R. Gross. *Festkörperphysik*. 2014. isbn: 978-3-11-035869-8. doi: [10.1524/9783110358704](https://doi.org/10.1524/9783110358704).
- [12] Abo G. “Definition of Magnetic Exchange Length.” In: *IEEE Transactions on Magnetics* 49.8 (2013), pp. 4937–4939. issn: 1941-0069. doi: [10.1109/TMAG.2013.2258028](https://doi.org/10.1109/TMAG.2013.2258028).
- [13] Heinrich B. “Ultrathin metallic magnetic films: magnetic anisotropies and exchange interactions.” In: *Advances in Physics* 42.5 (1993). doi: 10.1080/00018739300101524, pp. 523–639. issn: 0001-8732. doi: [10.1080/00018739300101524](https://doi.org/10.1080/00018739300101524).
- [14] G. Woltersdorf. “SPIN-PUMPING AND TWO-MAGNON SCATTERING IN MAGNETIC MULTILAYERS.” PhD thesis. 2004. url: <https://epub.uni-regensburg.de/14960/1/Woltersdorf-PhD04.pdf>.

- [15] Kittel C. "ON THE THEORY OF FERROMAGNETIC RESONANCE ABSORPTION." In: *Physical Review* 73.2 (1948). ISI Document Delivery No.: UB293 Times Cited: 1488 Cited Reference Count: 12 Kittel, c 1499 9 135 American physical soc College pk, pp. 155–161. issn: 0031-899X. doi: [10.1103/PhysRev.73.155](https://doi.org/10.1103/PhysRev.73.155).
- [16] Gurevich A.G. *Magnetization Oscillations and Waves*. Vol. 1. 1996. isbn: 9780138748487. doi: <https://doi.org/10.1201/9780138748487>.
- [17] Bennett L. H. *Magnetic Multilayers*. World Scientific, 1994.
- [18] Van-Vleck. "Ferromagnetic resonance." In: *Physica* 17.3 (1951), pp. 234–252. issn: 0031-8914. doi: [https://doi.org/10.1016/0031-8914\(51\)90063-8](https://doi.org/10.1016/0031-8914(51)90063-8).
- [19] Farle M. "Ferromagnetic resonance of ultrathin metallic layers." In: *Rep. Prog. Phys.* 61 (1998), p. 755.
- [20] Rado G. "Magnetic Resonance and Electromagnetic Wave Propagation in Materials Having *g*-Factor Anisotropies." In: *Physical Review B* 5.3 (1972). PRB, pp. 1021–1031. doi: [10.1103/PhysRevB.5.1021](https://doi.org/10.1103/PhysRevB.5.1021).
- [21] Gilbert T.L. "A phenomenological theory of damping in ferromagnetic materials." In: *IEEE Transactions on Magnetics* 40.6 (2004), pp. 3443–3449. issn: 0018-9464. doi: [10.1109/TMAG.2004.836740](https://doi.org/10.1109/TMAG.2004.836740).
- [22] Baberschke K. "Investigation of Ultrathin Ferromagnetic Films by Magnetic Resonance." In: *Handbook of Magnetism and Advanced Magnetic Materials*. 2007. doi: <https://doi.org/10.1002/9780470022184.hmm314>.
- [23] Körner M. "Morphology-Induced Magnetic Phenomena Studied by Broadband Ferromagnetic Resonance." Thesis. 2013.
- [24] Nolting W. *Grundkurs Theoretische Physik 6*. 2014. isbn: 978-3-642-25392-8. doi: [10.1007/978-3-642-25393-5](https://doi.org/10.1007/978-3-642-25393-5).
- [25] Coey J.M.D. *Magnetism and Magnetic Materials*. Cambridge: Cambridge University Press, 2010. isbn: 9780521816144. doi: [DOI:10.1017/CB09780511845000](https://doi.org/10.1017/CB09780511845000).
- [26] Vonsovskij S.V. *Ferromagnetic resonance : the phenomenon of resonant absorption of a high-frequency magnetic field in ferromagnetic substances*. 1. Engl. ed. International series of monographs in solid state physics. Oxford [u.a.]: Pergamon Press, 1966.
- [27] Morrish A.H. *The physical principles of magnetism*. New York: IEEE Press, 2001. isbn: 0470546581.
- [28] Poole Ch. P. jr. "Electron-Spin-Resonance, 2nd Edition, A Comprehensive Treatise on Experimental Techniques, John Wiley and Sons, New York, Chichester, Brisbane, Toronto, Singapore 1983. 780 Seiten, Preis: £ 61.—." In: *Berichte der Bunsengesellschaft für physikalische Chemie* 87.12 (1983). <https://doi.org/10.1002/bbpc.19830871245>, pp. 1230–1230. issn: 0005-9021. doi: <https://doi.org/10.1002/bbpc.19830871245>.
- [29] Suhl H. "Ferromagnetic Resonance in Nickel Ferrite Between One and Two Kilomegacycles." In: *Physical Review* 97.2 (1955). PR, pp. 555–557. doi: [10.1103/PhysRev.97.555](https://doi.org/10.1103/PhysRev.97.555).
- [30] Smit J. "Ferromagnetic resonance absorption in BaFe₁₂O₁₉, a highly anisotropic crystal." In: *Philips Res. Rep.* 10 (1955), pp. 113–130.

- [31] Gupta S. “Important role of magnetization precession angle measurement in inverse spin Hall effect induced by spin pumping.” In: *Applied Physics Letters* 110.2 (2017). doi: 10.1063/1.4973704, p. 022404. issn: 0003-6951. doi: 10.1063/1.4973704.
- [32] Baselgia L. “Derivation of the resonance frequency from the free energy of ferromagnets.” In: *Physical Review B* 38.4 (1988). PRB, pp. 2237–2242. doi: 10.1103/PhysRevB.38.2237.
- [33] Bayreuther G. “Uniaxial magnetic anisotropy in Fe/GaAs(001): Role of magnetoelastic interactions.” In: *Phys. Rev. B* 86 (5 Aug. 2012), p. 054418. doi: 10.1103/PhysRevB.86.054418. url: <https://link.aps.org/doi/10.1103/PhysRevB.86.054418>.
- [34] Shaw J.M. “Precise determination of the spectroscopic g-factor by use of broadband ferromagnetic resonance spectroscopy.” In: *Journal of Applied Physics* 114.24 (2013), p. 243906. doi: 10.1063/1.4852415.
- [35] G. Breit and E. Wigner. “Capture of Slow Neutrons.” In: *Phys. Rev.* 49 (7 Apr. 1936), pp. 519–531. doi: 10.1103/PhysRev.49.519. url: <https://link.aps.org/doi/10.1103/PhysRev.49.519>.
- [36] Flovik V. “Eddy current interactions in a ferromagnet-normal metal bilayer structure, and its impact on ferromagnetic resonance lineshapes.” In: *Journal of Applied Physics* 117.14 (2015), p. 143902. doi: 10.1063/1.4917285.
- [37] Dyson F.J. “Electron Spin Resonance Absorption in Metals. II. Theory of Electron Diffusion and the Skin Effect.” In: *Phys. Rev.* 98 (2 Apr. 1955), pp. 349–359. doi: 10.1103/PhysRev.98.349. url: <https://link.aps.org/doi/10.1103/PhysRev.98.349>.
- [38] Popovych V. “Dyson line and modified Dyson line in the EPR measurements.” In: *Nukleonika* 60.3 (2015), pp. 385–388. doi: doi: 10.1515/nuka-2015-0068. url: <https://doi.org/10.1515/nuka-2015-0068%20https://www.sciendo.com/article/10.1515/nuka-2015-0068>.
- [39] Nembach H.T. “Perpendicular ferromagnetic resonance measurements of damping and Landé g -factor in sputtered $(\text{Co}_2\text{Mn})_{1-x}\text{Ge}_x$ thin films.” In: *Physical Review B* 84.5 (2011). PRB, p. 054424. doi: 10.1103/PhysRevB.84.054424. url: <https://link.aps.org/doi/10.1103/PhysRevB.84.054424%20https://journals.aps.org/prb/pdf/10.1103/PhysRevB.84.054424>.
- [40] Li Y. “Isotropic non-local Gilbert damping driven by spin pumping in epitaxial Pd/Fe films on MgO(001) substrates.” In: *New Journal of Physics* 21.10 (2019), p. 103040. issn: 1367-2630. doi: 10.1088/1367-2630/ab4c8d.
- [41] Chen L. “Emergence of anisotropic Gilbert damping in ultrathin Fe layers on GaAs(001).” In: *Nature Physics* 14.5 (2018), pp. 490–494. issn: 1745-2481. doi: 10.1038/s41567-018-0053-8. url: <https://doi.org/10.1038/s41567-018-0053-8%20https://www.nature.com/articles/s41567-018-0053-8.pdf>.
- [42] Yakata S. “Temperature Dependences of Spin-Diffusion Lengths of Cu and Ru layers.” In: *Japanese Journal of Applied Physics* 45.5A (2006), pp. 3892–3895. issn: 0021-4922 1347-4065. doi: 10.1143/jjap.45.3892. url: <http://dx.doi.org/10.1143/JJAP.45.3892%20https://iopscience.iop.org/article/10.1143/JJAP.45.3892/pdf>.
- [43] Tserkovnyak Y. “Enhanced Gilbert Damping in Thin Ferromagnetic Films.” In: *Physical Review Letters* 88.11 (2002). PRL, p. 117601. doi: 10.1103/PhysRevLett.88.117601.
-

- [44] Tserkovnyak Y. "Spin pumping and magnetization dynamics in metallic multilayers." In: *Physical Review B* 66.22 (2002). PRB, p. 224403. doi: [10.1103/PhysRevB.66.224403](https://doi.org/10.1103/PhysRevB.66.224403).
- [45] M.O. Härtinger. "Untersuchung magnetischer Materialien mit Methoden der Ferromagnetischen Resonanz." PhD thesis. 2016.
- [46] M. Obstbaum. "Inverse spin Hall effect in metallic heterostructures." PhD thesis. 2015.
- [47] Takahashi S. "Physical Principles of Spin Pumping." In: *Handbook of Spintronics*. Ed. by Yongbing Xu, David D. Awschalom, and Junsaku Nitta. Dordrecht: Springer Netherlands, 2016, pp. 1–31. isbn: 978-94-007-7604-3. doi: [10.1007/978-94-007-7604-3_51-2](https://doi.org/10.1007/978-94-007-7604-3_51-2). url: https://doi.org/10.1007/978-94-007-7604-3_51-2.
- [48] Foros J. "Scattering of spin current injected in Pd(001)." In: *Journal of Applied Physics* 97.10 (2005). doi: 10.1063/1.1853131, 10A714. issn: 0021-8979. doi: [10.1063/1.1853131](https://doi.org/10.1063/1.1853131).
- [49] E. Montoya. "Spin pumping and spin transport in magnetic heterostructures." PhD thesis. 2016. url: <http://summit.sfu.ca/item/16131>.
- [50] Berger L. "Emission of spin waves by a magnetic multilayer traversed by a current." In: *Physical Review B* 54.13 (1996). PRB, pp. 9353–9358. doi: [10.1103/PhysRevB.54.9353](https://doi.org/10.1103/PhysRevB.54.9353).
- [51] Nehasil V. "Miniature electron bombardment evaporation source: evaporation rate measurement." In: *Czechoslovak Journal of Physics* 47.3 (1997), pp. 261–268. issn: 1572-9486. doi: [10.1023/A:1022842115104](https://doi.org/10.1023/A:1022842115104).
- [52] G.W. Pearsall W.G. Moffatt and J. Wulff. *The Structure and Properties of Materials*. 1964. isbn: 978-0471612650.
- [53] F.M. Römer. "Breitbandige in situ Ferromagnetische Resonanz und niederfrequente Suszeptibilitätsmessungen an Eisen auf III-V Halbleitern." PhD thesis. Mar. 2013. url: <https://nbn-resolving.org/urn:nbn:de:hbz:464-20130320-104827-0>.
- [54] Demtröder W. *Experimentalphysik 3*. 2016. doi: <https://doi.org/10.1007/978-3-662-49094-5>.
- [55] Bruce L.A. "Geometric factors in f. c. c. and b. c. c. metal-on-metal epitaxy IV. Deposits of Rh, Ir, Pd and Pt on (001)W and (001)Mo." In: *Philosophical Magazine A* 40.1 (1979). doi: 10.1080/01418617908234835, pp. 97–109. issn: 0141-8610. doi: [10.1080/01418617908234835](https://doi.org/10.1080/01418617908234835).
- [56] Bauer E. "Epitaxy of metals on metals." In: *Applications of Surface Science* 11-12 (1982), pp. 479–494. issn: 0378-5963. doi: [https://doi.org/10.1016/0378-5963\(82\)90094-0](https://doi.org/10.1016/0378-5963(82)90094-0).
- [57] Bryant K.W. "Monolayer growth modes of Re and Nb on 4H-SiC(0001) and 4H-SiC(0001̄)." In: *Journal of Applied Physics* 97.2 (2004), p. 024904. issn: 0021-8979. doi: [10.1063/1.1831548](https://doi.org/10.1063/1.1831548).
- [58] Ossicini W. "AES analysis of the growth mechanism of metal layers on metal surfaces." In: *Journal of Vacuum Science & Technology A* 3.2 (1985), pp. 387–391. doi: [10.1116/1.573226](https://doi.org/10.1116/1.573226).
- [59] W. Ranke and K. Jacobi. "Structure and reactivity of GaAs surfaces." In: *Progress in Surface Science* 10.1 (1981), pp. 1–52. issn: 0079-6816. doi: [https://doi.org/10.1016/0079-6816\(81\)90005-8](https://doi.org/10.1016/0079-6816(81)90005-8). url: <https://www.sciencedirect.com/science/article/pii/0079681681900058>.

- [60] Xue Q. “Structures of the Ga-Rich 4×2 and 4×6 Reconstructions of the GaAs(001) Surface.” In: *Physical Review Letters* 74.16 (1995). PRL, pp. 3177–3180. doi: [10.1103/PhysRevLett.74.3177](https://doi.org/10.1103/PhysRevLett.74.3177).
- [61] Mirbt S. “First-principles calculations of Fe on GaAs(100).” In: *Physical Review B* 67.15 (2003). PRB, p. 155421. doi: [10.1103/PhysRevB.67.155421](https://doi.org/10.1103/PhysRevB.67.155421).
- [62] Filipe A. “Structure and magnetism of the Fe/GaAs interface.” In: *Applied Physics Letters* 70.1 (1997). doi: 10.1063/1.119284, pp. 129–131. issn: 0003-6951. doi: [10.1063/1.119284](https://doi.org/10.1063/1.119284).
- [63] Zölfl M. “Magnetic films epitaxially grown on semiconductors.” In: *Journal of Magnetism and Magnetic Materials* 175.1 (1997), pp. 16–22. issn: 0304-8853. doi: [https://doi.org/10.1016/S0304-8853\(97\)00209-6](https://doi.org/10.1016/S0304-8853(97)00209-6).
- [64] Nefedov A. “Growth and structure of L1₀ ordered FePt films on GaAs(001).” In: *Journal of Physics: Condensed Matter* 14.47 (2002), pp. 12273–12286. issn: 0953-8984. doi: [10.1088/0953-8984/14/47/304](https://doi.org/10.1088/0953-8984/14/47/304).
- [65] Moosbühler R. “Epitaxial Fe films on GaAs(001): Does the substrate surface reconstruction affect the uniaxial magnetic anisotropy?” In: *Journal of Applied Physics* 91.10 (2002). doi: 10.1063/1.1447205, pp. 8757–8759. issn: 0021-8979. doi: [10.1063/1.1447205](https://doi.org/10.1063/1.1447205).
- [66] Monchesky T.L. “Magnetoresistance and magnetic properties of Fe/Cu/Fe/GaAs(100).” In: *Physical Review B* 60.14 (1999). PRB, pp. 10242–10251. doi: [10.1103/PhysRevB.60.10242](https://doi.org/10.1103/PhysRevB.60.10242).
- [67] Dinc T. “Synchronized conductivity modulation to realize broadband lossless magnetic-free non-reciprocity.” In: *Nature Communications* 8.1 (2017), p. 795. issn: 2041-1723. doi: [10.1038/s41467-017-00798-9](https://doi.org/10.1038/s41467-017-00798-9). url: <https://doi.org/10.1038/s41467-017-00798-9>.
- [68] R. Meckenstock. “Untersuchung der magnetischen Eigenschaften von Fe/Ag-Schichtsystemen mit der konventionellen und der orts aufgelösten ferromagnetischen Resonanz.” PhD thesis. 1997.
- [69] url: <https://tectra.de/>.
- [70] Seah M.P. “Quantitative electron spectroscopy of surfaces: A standard data base for electron inelastic mean free paths in solids.” In: *Surface and Interface Analysis* 1.1 (1979). <https://doi.org/10.1002/sia.740010103>, pp. 2–11. issn: 0142-2421. doi: <https://doi.org/10.1002/sia.740010103>.
- [71] Davis L.E. *Handbook of Auger Electron Spectroscopy: A Reference Book of Standard Data for Identification and Interpretation of Auger Electron Spectroscopy Data*. Physical Electronics Industries, 1976.
- [72] url: https://webelements.com/rhodium/crystal_structure.html.
- [73] Hanisch K. “Interface alloying and magnetic properties of Fe/Rh multilayers.” In: *Journal of Applied Physics* 76.10 (1994). doi: 10.1063/1.358213, pp. 6528–6530. issn: 0021-8979. doi: [10.1063/1.358213](https://doi.org/10.1063/1.358213).
- [74] Pfandzelter R. “GROWTH OF ULTRATHIN Rh FILMS ON Fe(100).” In: *Surface Review and Letters* 10.01 (2003), pp. 117–120. issn: 0218-625X. doi: [10.1142/S0218625X03004615](https://doi.org/10.1142/S0218625X03004615).
- [75] Takeshita H. “Scanning Tunneling Microscopy Study of Ultrathin Fe Films Grown on GaAs(001) Surface.” In: *Japanese Journal of Applied Physics* 34.Part 1, No. 2B (1995), pp. 1119–1122. doi: [10.1143/jjap.34.1119](https://doi.org/10.1143/jjap.34.1119). url: <https://doi.org/10.1143/jjap.34.1119>.
-

- [76] Xu Y. B. “Evolution of the ferromagnetic phase of ultrathin Fe films grown on GaAs(100)- 4×6 .” In: *Phys. Rev. B* 58 (2 1998), pp. 890–896. doi: [10.1103/PhysRevB.58.890](https://doi.org/10.1103/PhysRevB.58.890). url: <https://link.aps.org/doi/10.1103/PhysRevB.58.890>.
- [77] B. Bhagat. “To be submitted.” PhD thesis. 2022.
- [78] Zakeri K. “Magnetic anisotropy of Fe/GaAs(001) ultrathin films investigated by in situ ferromagnetic resonance.” In: *Journal of Magnetism and Magnetic Materials* 299.1 (2006), pp. L1–L10. issn: 0304-8853. doi: <https://doi.org/10.1016/j.jmmm.2005.03.079>.
- [79] Wendtland Paul. Thesis. 2017.
- [80] Madami M. “In situ Brillouin scattering study of the thickness dependence of magnetic anisotropy in uncovered and Cu-covered Fe/GaAs(100) ultrathin films.” In: *Physical Review B* 69.14 (2004). PRB, p. 144408. doi: [10.1103/PhysRevB.69.144408](https://doi.org/10.1103/PhysRevB.69.144408).
- [81] McPhail S. “Interface bonding versus strain-induced magnetic anisotropy in epitaxial Fe/semiconductor structures.” In: *Physical Review B* 67.2 (2003). PRB, p. 024409. doi: [10.1103/PhysRevB.67.024409](https://doi.org/10.1103/PhysRevB.67.024409).
- [82] Kebe T. “Magnetization and magnetic anisotropy energy of ultrathin Fe films on GaAs(001) exposed to oxygen.” In: *Journal of Physics: Condensed Matter* 18.39 (2006), pp. 8791–8802. issn: 0953-8984 1361-648X. doi: [10.1088/0953-8984/18/39/010](https://doi.org/10.1088/0953-8984/18/39/010).
- [83] Kardasz B. “Magnetic anisotropies in GaAs/Fe(001) structures.” In: *Journal of Physics: Conference Series* 200.7 (2010), p. 072046. issn: 1742-6596. doi: [10.1088/1742-6596/200/7/072046](https://doi.org/10.1088/1742-6596/200/7/072046).
- [84] Frait Z. “Ferromagnetic resonance and surface anisotropy in iron single crystals.” In: *Journal of Magnetism and Magnetic Materials* 15-18 (1980), pp. 1081–1082. issn: 0304-8853. doi: [https://doi.org/10.1016/0304-8853\(80\)90895-1](https://doi.org/10.1016/0304-8853(80)90895-1).
- [85] Bhagat S.M. “Ferromagnetic Resonance in Nickel and Iron.” In: *Journal of Applied Physics* 37.1 (1966). doi: 10.1063/1.1707805, pp. 194–197. issn: 0021-8979. doi: [10.1063/1.1707805](https://doi.org/10.1063/1.1707805).
- [86] Chouairi A. “Spin-Polarization in Ultrathin Rh Layers on Fe (001).” In: *MRS Proceedings* 313 (1993), p. 595. issn: 0272-9172. doi: [10.1557/PROC-313-595](https://doi.org/10.1557/PROC-313-595).
- [87] Chouairi A. “Rh polarization in ultrathin Rh layers on Fe(001).” In: *Physical Review B* 48.10 (1993). PRB, pp. 7735–7738. doi: [10.1103/PhysRevB.48.7735](https://doi.org/10.1103/PhysRevB.48.7735).
- [88] Goldoni. “Experimental Evidence of Magnetic Ordering at the Rh(100) Surface.” In: *Physical Review Letters* 82.15 (1999). PRL, pp. 3156–3159. doi: [10.1103/PhysRevLett.82.3156](https://doi.org/10.1103/PhysRevLett.82.3156).
- [89] Tao X. “Self-consistent determination of spin Hall angle and spin diffusion length in Pt and Pd: The role of the interface spin loss.” In: *Science Advances* 4.6 (2018), eaat1670. doi: [10.1126/sciadv.aat1670](https://doi.org/10.1126/sciadv.aat1670). url: <https://doi.org/10.1126/sciadv.aat1670%20https://www.ncbi.nlm.nih.gov/pmc/articles/PMC6014716/pdf/aat1670.pdf>.
- [90] Cahaya A.B. “Crystal field effects on spin pumping.” In: *Physical Review B* 96.14 (2017). PRB, p. 144434. doi: [10.1103/PhysRevB.96.144434](https://doi.org/10.1103/PhysRevB.96.144434).
- [91] Kumar A. “Spin transfer torque ferromagnetic resonance induced spin pumping in the Fe/Pd bilayer system.” In: *Physical Review B* 95.6 (2017). PRB, p. 064406. doi: [10.1103/PhysRevB.95.064406](https://doi.org/10.1103/PhysRevB.95.064406).

-
- [92] Huo Y. “Spin pumping and the inverse spin hall effect in single crystalline Fe/Pt heterostructure.” In: *AIP Advances* 7.5 (2017). doi: 10.1063/1.4976957, p. 056024. doi: [10.1063/1.4976957](https://doi.org/10.1063/1.4976957).
- [93] Conca A.Kardasz. “Study of fully epitaxial Fe/Pt bilayers for spin pumping by ferromagnetic resonance spectroscopy.” In: *Physical Review B* 93.13 (2016). PRB, p. 134405. doi: [10.1103/PhysRevB.93.134405](https://doi.org/10.1103/PhysRevB.93.134405).
- [94] Kardasz B. “Ferromagnetic resonance studies of accumulation and diffusion of spin momentum density in Fe/Ag/Fe/GaAs(001) and Ag/Fe/GaAs(001) structures.” In: *Physical Review B* 81.9 (2010), p. 094409. doi: [10.1103/PhysRevB.81.094409](https://doi.org/10.1103/PhysRevB.81.094409). url: <https://link.aps.org/doi/10.1103/PhysRevB.81.094409> <https://journals.aps.org/prb/pdf/10.1103/PhysRevB.81.094409>.
- [95] Azevedo A. “Spin pumping and anisotropic magnetoresistance voltages in magnetic bilayers: Theory and experiment.” In: *Physical Review B* 83.14 (2011), p. 144402. doi: [10.1103/PhysRevB.83.144402](https://doi.org/10.1103/PhysRevB.83.144402). url: <https://link.aps.org/doi/10.1103/PhysRevB.83.144402> <https://journals.aps.org/prb/pdf/10.1103/PhysRevB.83.144402>.
- [96] Behera N. “Effect of Ru thickness on spin pumping in Ru/Py bilayer.” In: *Journal of Applied Physics* 117.17 (2015), 17A714. issn: 0021-8979. doi: [10.1063/1.4913510](https://doi.org/10.1063/1.4913510). url: <https://doi.org/10.1063/1.4913510> <https://aip.scitation.org/doi/pdf/10.1063/1.4913510>.
- [97] Gómez J.E. “Spin transport parameters in Ni₈₀Fe₂₀/Ru and Ni₈₀Fe₂₀/Ta bilayers.” In: *Physical Review B* 90.18 (2014), p. 184401. doi: [10.1103/PhysRevB.90.184401](https://doi.org/10.1103/PhysRevB.90.184401). url: <https://link.aps.org/doi/10.1103/PhysRevB.90.184401> <https://journals.aps.org/prb/pdf/10.1103/PhysRevB.90.184401>.
-

Danksagung

Ich möchte mich ausdrücklich bei den folgenden Personen für die Zusammenarbeit und Hilfestellungen während meiner Arbeit bedanken:

Zunächst möchte ich mich bei Prof. Dr. Michael Farle bedanken, der es mir ermöglicht hat meine Masterarbeit in seiner Arbeitsgruppe zu schreiben und mich dabei auf die Ressourcen und Köpfe seiner Arbeitsgruppe zurückgreifen ließ.

Des Weiteren möchte Ich mich bei Anna Semisalova bedanken, die mich während meiner Arbeit betreut hat und meinen unzähligen Fragen standhalten musste.

Ein besonderer Dank gebührt Ali Can Aktas, Tim Salzmann und Anna Semisalova, die mir bei Messungen und der Arbeit an der UHV-Kammer geholfen haben.

Ich möchte mich weiterhin bedanken bei Ralf Meckenstock der mir immer fragen zur FMR und besonders beim Aufbau des VNA-FMR setups geholfen hat.

Außerdem Bedanke Ich mich bei Tanja Strusch für die Diskussionen und den Informationsaustausch zum Thema Spin Pumping.

Ich möchte mich insbesondere bei Detlef Spoddig und Michael Vennemann bedanken, die mich immer tatkräftig bei Reparaturen jeglicher Art unterstützten.

Und natürlich gebührt mein Dank dem restlichen Teil der Arbeitsgruppe Farle für die Gespräche, Interpretationen und Unterstützungen welche eine freundschaftliche Arbeitsatmosphäre erschaffen.

Selbstständigkeitserklärung

Hiermit erkläre ich, Jonas Wiemeler, dass ich die vorliegende Arbeit selbstständig angefertigt und keine anderen als die angegebenen Hilfsmittel verwendet habe. Sämtliche wesentlich verwendete Textausschnitte, Zitate oder Inhalte anderer Verfasser wurden ausdrücklich als solche gekennzeichnet.

Ort, Datum

Unterschrift